Integrated optoelectronic terahertz receivers

Iñigo Belio-Apaolaza

A dissertation submitted in partial fulfillment

of the requirements for the degree of

Doctor of Philosophy

of

University College London.

Department of Electrical and Electronic Engineering

University College London

August 11, 2025

I, Iñigo Belio-Apaolaza, confirm that the work presented in this thesis is my own. Where information has been derived from other sources, I confirm that this has been indicated in the work.

Abstract

Photonic technologies offer intrinsic advantages in terahertz generation and detection, making them key enablers for a wide range of applications. In terahertz receivers, these advantages are imparted to local oscillator (LO) generation and distribution, providing ultra-high-frequency tunability, remote signal distribution, and compatibility with existing 1550 nm equipment. Wireless communications at 300 GHz, fully enabled by photonics, can leverage these features for efficient and seamless convergence with fibre networks. However, current photonic-based terahertz receivers exhibit higher conversion loss compared to state-of-the-art electronic solutions.

This thesis introduces an alternative optoelectronic terahertz receiver concept based on photonically pumped Schottky mixers. By integrating low-barrier Schottky barrier diodes (SBDs) with uni-travelling-carrier photodiodes (UTC-PDs), this approach combines high-performance down-conversion efficiency with the advantages of photonic LO signal generation and distribution. The modelling, design, and characterisation of such receivers are presented. The study first focuses on integrating UTC-PDs and SBDs, designing three subharmonic receivers operating at 220–330 GHz. The first is a monolithic receiver using InP Schottky contacts with a standard UTC-PD epitaxy. The second and third explore hybrid integration with InGaAs air-bridged SBDs: a quasi-optical receiver and a rectangular waveguide (WR3) receiver.

The quasi-optical receiver was fabricated and tested, along with a non-integrated receiver used to validate the concept and provide a performance comparison. Results indicate a minimum conversion loss of approximately 14 dB for

the non-integrated and 18 dB for the integrated receiver, approaching the state-of-the-art in this frequency band. The UTC-PD is shown to provide sufficient LO power to saturate the mixer response, and the modelling and design process is validated through agreement between simulations and measurements. To showcase the receiver's potential for wireless communications, a multi-channel 300 GHz link was demonstrated, achieving an aggregate data rate of 180 Gbps.

Impact statement

This work represents a breakthrough in bridging the performance gap between optoelectronic and electronic terahertz receivers. Current optoelectronic receivers, based on GaAs/InGaAs photoconductors, exhibit conversion losses of approximately 30 dB or higher at 300 GHz. Here, we demonstrate, to the best of authors' knowledge, photonically-pumped Schottky mixer receivers at 300 GHz for the first time, achieving at least an order-of-magnitude improvement. Three novel integrated receiver designs are presented with predicted performance approaching the state-of-the-art down-conversion efficiency of GaAs Schottky mixers. Additionally, we propose and describe a modelling and design methodology capable of predicting receiver performance, enabling future designs with improvements and targeting higher frequency bands.

The successful experimental demonstration of an integrated receiver highlights its strong potential for applications such as wireless communications, as confirmed by the multi-channel link using the proposed optoelectronic receiver. We achieve a line rate of 180 Gbps, significantly surpassing previously demonstrated fully optoelectronic links. This improvement is a direct consequence of the enhanced signal-to-noise ratio (SNR) enabled by superior down-conversion efficiency. The unprecedented data rates demonstrated here establish the proposed concept as a strong candidate for 6G front-haul and backhaul applications, facilitating seamless integration between fibre and wireless networks.

This work has been disseminated through journal publications and presentations at international conferences.

Acknowledgements

I would like to start by thanking my supervisor, Prof. Cyril C. Renaud, for giving me the opportunity to join this project, for his support and guidance, and for teaching me to become an independent researcher. I am also grateful to my former supervisor, Dr. Katarzyna Balakier, for providing me with this opportunity.

I am deeply grateful to my secondary supervisor, Dr. James Seddon, for his invaluable knowledge in modelling, simulation, and experiments, as well as for his unwavering support from the very beginning. His motivation and assistance were instrumental to my success, and without him, the outcome and impact of this thesis would not have been the same. I am also very grateful to Dr. Chris Graham for fabricating the photodiodes used in this work, which were essential for all my experiments.

To my colleagues and friends in the Ultrafast Photonics Group—Alexis, Sarah, Christina, Fasil, Euan, Sam, Alex, Rob, and others—thank you for making every day enjoyable and for creating an environment where I always felt excited to come to work.

I would also like to thank the Department of Optoelectronics at the University of Duisburg-Essen, especially Prof. Andreas Stöhr, for giving me the opportunity to work in his lab on the communications experiments. I am deeply grateful to Jonas, Jose, and Marcel for their support during my stay, as well as for the insightful discussions and the time we shared in Duisburg.

My sincere thanks to the Millimetre-Wave Group at the Rutherford Appleton Laboratory—Dr. Peter Huggard, Dr. Hui Wang, Dr. Byron Alderman, and Nick Brewster. Thank you for the opportunity to work with you, for fabricating and as-

sembling the hybrid mixer circuit, and for the technical discussions that contributed to a successful outcome.

I would also like to express my sincere gratitude to Prof. Iñigo Ederra and Dr. Jose Manuel Pérez-Escudero for giving me the opportunity to undertake a short stay and for their warm welcome at the Public University of Navarra (UPNA), where I significantly expanded my understanding of THz Schottky mixer design.

To my colleagues and friends in the Marie Curie TERAOPTICS training network, thank you for making our events such an enjoyable experience, for the valuable discussions, and for your advice. I would like to extend special thanks to Javier Martinez-Gil for his constant and unconditional support throughout the project and for all the great moments we have shared—and will continue to share in the future. To the friends I made in London, thank you for making these past three and a half years so enjoyable.

Finally, I cannot end without expressing my deep gratitude to my family. To my parents, Javier and Ana, thank you for the education and values you instilled in me, and for your unconditional support in everything I have done. The person I am today is a reflection of the incredible parents you are. To my sister, Helena, thank you for always supporting me—whether through proofreading, editing, offering perspectives, or countless other things. You have always been an inspiration and someone I deeply admire. Thank you for motivating me to be ambitious and pursue a PhD.

Contents

List of Publications

Journal publications

- **I. Belio-Apaolaza** et al., "Photonically-driven Schottky diode based 0.3 THz heterodyne receiver", Opt. Express, vol. 30, no. 24, pp. 43223–43236, Nov. 2022.
- **I. Belio-Apaolaza** et al., "Fully-optoelectronic 300 GHz multi-channel wireless link using a photonically-pumped low-barrier mixer for up to 180 Gbps", J. Lightwave Technol., vol. 43, pp. 19–28, Jan. 2025.
- **I. Belio-Apaolaza** et al., "Integrated 300 GHz Optoelectronic Mixer Based on Photonically-Pumped Low-Barrier Schottky Diodes", J. Lightwave Technol., pp. 1–10, 2025.
- **I. Belio-Apaolaza**, J. Seddon, and C. C. Renaud, "Fermi-level-managed multi-barrier heterojunction diodes for terahertz detection", Sci Rep, vol. 15, no. 1, July 2025.
- J. Martinez-Gil, **I. Belio-Apaolaza** et al., "Performance Evaluation of GaAs and InGaAs Schottky Mixers at 0.3 THz: A Comparative Analysis Between Optical and Electrical Pumping in THz Wireless Communication Systems", Electronics, vol. 14, no. 10, p. 1957, May 2025.

Conference presentations and proceedings

- **I. Belio-Apaolaza**, J. Seddon, J. M. Pérez-Escudero, I. Ederra, and C. C. Renaud, "High-performance terahertz optoelectronic receivers enabled by

monolithic integration of SBDs and UTC-PDs: modelling and design," in 2023 48th International Conference on Infrared, Millimeter, and Terahertz Waves (IRMMW-THz), 2023, pp. 1–2.

- **I. Belio-Apaolaza** et al., "Integrated 220-330 GHz quasi-optical receiver based on low-barrier Schottky diodes and UTC photodiodes," in 2024 49th International Conference on Infrared, Millimeter, and Terahertz Waves (IRMMW-THz), Perth, Australia, 2024, pp. 1–2.

- **I. Belio-Apaolaza** et al., "Optical-THz-Optical bridge at 5Gbps with a photonically-driven Schottky mixer at the receiver," in Advanced Properties and Processes in Optoelectronic Materials and Systems APROPOS 18, Vilnius, Lithuania, 5-7 October, 2022.

- **I. Belio-Apaolaza** et al.,"Optoelectronic terahertz receiver based on the hybrid integration of Schottky diodes and UTC photodiodes in a rectangular waveguide block," in German Microwave Conference (GeMiC), Duisburg, Germany, 11-13 March, 2024.

List of Figures

List of Tables

List of Abbreviations

5G-NR 5G new radio

ACP air co-planar

ADS Advanced Design System

ALMA Atacama Large Millimeter/Submillimeter Array

BBU baseband unit

BER bit-error-rate

BTE Boltzmann transport equation

CMA constant modulus algorithm

CMOS complementary metal-oxide semiconductor

CPW co-planar waveguide

CPE carrier phase estimation

CVD chemical vapour deposition

CW continuous wave

DAC digital-to-analogue converter

DD drift-diffusion

DSB double-side-band

DSO digital storage oscilloscope

DSP digital signal processing

ECL external cavity laser

EDFA erbium-doped fibre amplifier

ESA electrical spectrum analyser

EVM error vector magnitude

FEC forward error correction

FIR far infrared

FMBD Fermi-level-managed barrier diode

FPGA field-programmable gate array

FSPL free-space path loss

GSG ground-signal-ground

HB harmonic balance

HD hard decision

HEB hot electron bolometer

HEMT high electron mobility transistor

HBT heterojunction bipolar transistor

IC integrated circuit

IF intermediate-frequency

IMPATT impact ionization avalanche transit-time

LCN London Centre of Nanotechnology

LMS-DDE least mean square decision-directed equalizer

LNA low-noise amplifier

LO local oscillator

LSB lower sideband

MAC medium access control

MBE molecular beam epitaxy

MUTC-PD modified UTC-PD

MZM Mach-Zehnder modulator

NDC negative differential conductance

NDR negative differential resistance

NEP noise equivalent power

OSA optical spectrum analyser

OWC optical wireless communication

PCB printed circuit board

PC polarization controller

PEC perfect electric conductor

PHY physical

PIN-PD p-i-n photodiode

pin-PD p-i-n photodiode

PTFE polytetrafluoroethylene

QAM quadrature amplitude modulation

QCL quantum cascade laser

RAL Rutherford Appleton Laboratory

RC raised-cosine

RDE radius-directed equalizer

RF radio-frequency

RIE reactive ion etching

RoF radio-over-fibre

RRH remote radio head

RTA rapid thermal annealing

RTD resonant tunnelling diode

SBD Schottky barrier diode

SD soft decision

SEM scanning electron microscopy

SIS superconductor-insulator-superconductor

SNR signal-to-noise ratio

SSB single-side-band

SS-MBE solid source molecular beam epitaxy

TDS time-domain spectroscopy

THz terahertz

ToF terahertz-over-fibre

TUNNETT tunnelling transit-time

UTC-PD uni-travelling-carrier photodiode

USB upper sideband

UV ultraviolet

VNA vector network analyser

VOA variable optical attenuator

WDM wavelength-division multiplexing

Chapter 1

Introduction

1.1 Background

1.1.1 The terahertz region

The terahertz (THz) frequency band, ranging from 0.1 to 30 THz [1-1], [1-2], bridges the gap between infrared light and microwave radiation. Interest in this field has grown exponentially over the last few decades, as evidenced by the increasing number of publications. According to Web of Science [1-3], published articles featuring the terms ‘terahertz’, ‘THz’ or ‘submillimetre wave’ in their abstract or title have increased from 1,230 during 1990–1994 to 33,996 in 2020–2024, as seen in Figure 1.1.

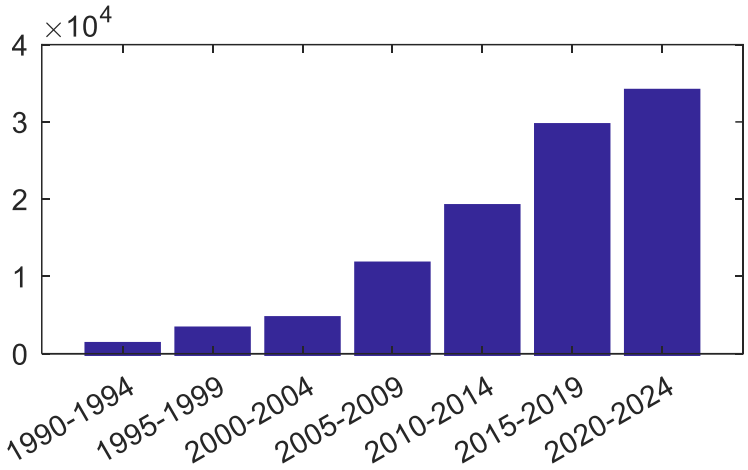

Figure 1.1: Occurrences of articles including the terms ‘THz’, ‘terahertz’, or ‘submillimetre wave’ in their title or abstract, according to the Web of Science database, grouped into five-year intervals from 1990 to 2024.

Although radioastronomical research on the terahertz band has been conducted for many decades [1-4], these frequencies have remained largely unexplored in terms of applications due to limited technological development [1-1], [1-2]. In the microwave/millimetre wave and infrared/optical regimes, excellent sources and detectors are widely available, relying typically on electronic and photonic technologies, respectively. In contrast, in the terahertz band these two worlds converge and the performance of traditional electronic or photonic solutions is not sufficient, resulting in the lack of high-power sources and efficient detectors, often referred to as the 'terahertz gap'. In recent decades, significant breakthroughs have been made in THz emission and detection through the combination of advances in electronic, photonic, and material science [1-2], [1-5]. As a result, new applications are being unlocked that include communications [1-6]–[1-8], security imaging [1-9], [1-10], biological and biomedical [1-11]–[1-13], and material characterisation [1-14], [1-15], among others. Some of these have already been transferred from research to the industrial world, e.g. automotive paint control [1-16]–[1-18] or semiconductor integrated circuits (ICs) inspection [1-19], [1-20]. Figure 1.2 collects a few insights on some emerging THz applications.

1.1.2 Terahertz photonics

In this context of emerging trends, photonic-based THz technologies are playing an important role in the generation, detection, processing, and transportation of THz signals, which make up the so-called field of THz photonics [1-24], [1-25]. Optical devices and techniques are particularly attractive for THz applications because they offer four main intrinsic advantages: (1) ultra-wide tuneability, (2) low-loss signal distribution, (3) reuse of mature 1550 nm technology, and (4) potentially lower signal phase noise. Some of the applications where photonic technologies have great potential due to these benefits are spectroscopy, radio astronomy, and wireless communications. An overview of the use of photonics in these applications is provided next, with a special focus on wireless communications, which is the target application of this work.

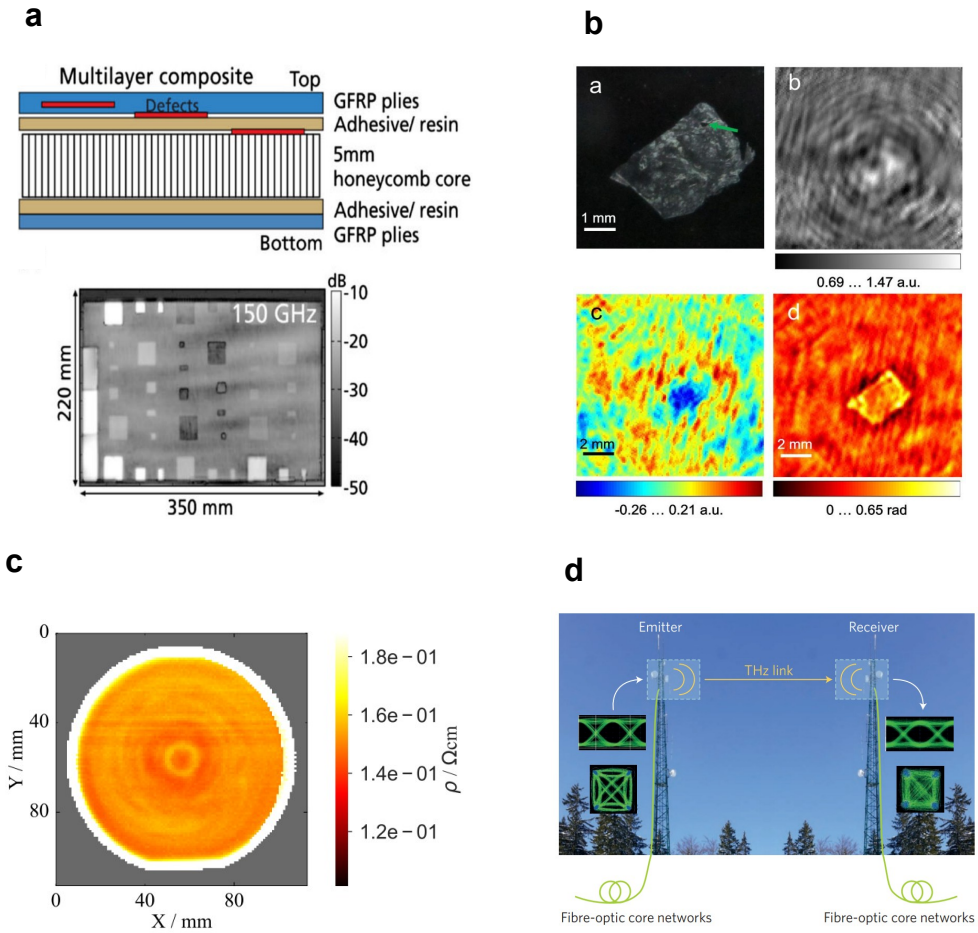

Figure 1.2: THz emerging applications. **a** Automotive and aviation quality control: Schematic and reflection image at 150 GHz of a composite structure with different layers used in radomes, adapted from [1-18]. **b** Medical imaging: Terahertz in-line measurements of human hepatocellular carcinoma tissue, reproduced from [1-21]. **c** Semiconductor characterisation: Terahertz spectroscopy performed on an n-doped silicon wafer to obtain its resistivity, adapted from [1-22]. **d** Wireless communications: Seamless connection between two base stations via a THz wireless bridge, adapted from [1-23].

Spectroscopy and radio astronomy

In the THz spectral domain, many chemical and biological materials exhibit unique signatures as a result of crystalline lattice vibrations, hydrogen bonding stretches, and other intermolecular vibrations [1-10]. THz spectroscopy systems can operate in either the time or frequency domain, but in both cases, photonic technologies are employed. In time-domain spectroscopy (TDS) systems, ultra-fast optical femtosecond lasers pump either photoconductive switches or non-linear crystals to generate the THz wave, and the detector is typically based on a photoconduc-

tor, for which the best systems attain a peak dynamic range of more than 100 dB and a bandwidth of 6.5 THz [1-26]. A schematic of a typical THz-TDS system is shown in Figure 1.3**b**. The main drawback of these systems lies in the requirement complex setups with difficult assembly, adjustment, and electronic control schemes [1-27], [1-28]. CW frequency-domain spectroscopy systems (Figure 1.3**a**) on the other hand are much simpler and inexpensive, providing excellent resolution and bandwidth, but with a limited acquisition time. Nevertheless, recent reported CW systems have demonstrated 200 Hz of acquisition speed [1-29], being comparable to state-of-the-art TDS systems. Up to 5.5 THz bandwidth with a peak dynamic range of 132 dB was achieved recently [1-30]. These systems are a great example of the capabilities of photonic technologies to enable immense frequency tuneability.

In THz radio astronomy, spectral signatures primarily of hydrogen, helium, oxygen, carbon and nitrogen are studied, which gives valuable information about star and planet formation, galaxy evolution, chemistry of gas clouds, etc [1-4]. In this sense, photonics can also play a key role, particularly when dealing with telescope arrays. The most relevant case is the Atacama Large Millimeter/Submillimeter Array (ALMA). Located in the Atacama dessert in Chile at 5000 m of altitude, it consists of 64 distributed antennas that operate synchronously and span from 27 to 938 GHz [1-31]. Figure 1.3**b** shows a photograph of the radio-observatory. The heterodyne receivers of each array element, require a low-noise LO signal, and here is where photonics are essential. The low-loss distribution of optical signals via an optical fibre, allows the realization of a photonic local oscillator system that is remotely operated at a centralised generation and distribution point [1-32]. Thus, the antenna receiver systems are greatly simplified, as only levelling electronics and a photomixer are required. This reduces cost, complexity and improves reliability and scalability. In addition, compared to electronic local oscillators, the resulting phase noise does not suffer from the penalty associated with multiplier chains, where the phase noise increases by 20log(N), where N is the factor of frequency multiplication. A schematic of the photonic LO system of the ALMA observatory [1-33]–[1-35] is depicted in Figure 1.3**d**.

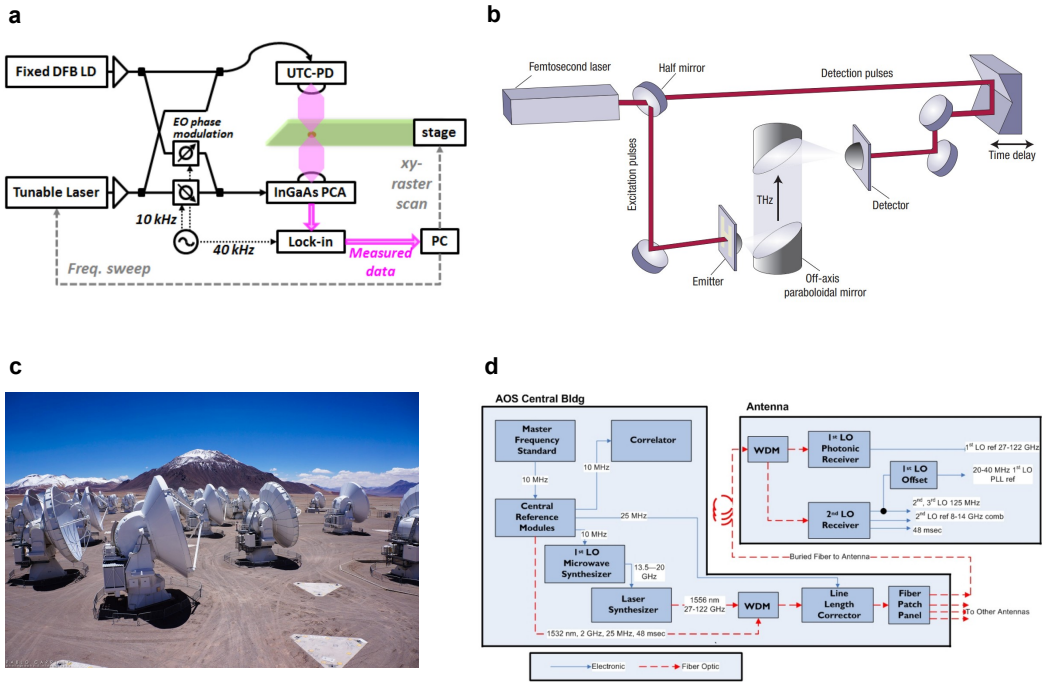

Figure 1.3: THz photonics for spectroscopy and radioastronomy. **a** Schematic of a THz-CW system, reproduced from [1-36]. **b** Schematic of a THz-TDS system with a femtosecond laser source, reproduced from [1-37]. **c** Photograph of the ALMA observatory, reproduced from [1-38]. **d** Schematic of the ALMA's photonics local oscillator system, reproduced from [1-34].

Wireless communications

In the current 5G new radio (5G-NR) standard, frequencies up to 71 GHz are considered, Frequency Range 2 (FR2) section, with a maximum channel bandwidth of 2 GHz is allocated at the 57-71 GHz band [1-39]. Although this is a major step compared to 4G networks, the ever-growing demand for high-speed data transmission makes the available bandwidth at these frequencies insufficient to meet the expected demands at 6G and future generations, where links with over 100 Gbps capacity are expected to be deployed [1-40]. To meet these demands, two potential solutions are (1) to move higher in frequency beyond 100 GHz exploiting the available bandwidth in the THz range, and (2) to use optical frequencies to implement optical wireless communications (OWCs) systems. These two are currently considered as potential 6G enablers, although THz communications are arguably more versatile considering some intrinsic OWC limitations. For example, OWC is less tolerant to atmospheric effects and more sensitive to misalignment than THz [1-41].

Existing regulations cover frequency allocation up to 275 GHz with 10 windows reserved for fixed and mobile communications above 100 GHz [1-42]. In contrast to sub-100 GHz frequencies, the THz band is characterised for exhibiting high free-space path loss (FSPL), which can be compensated through beam collimation, and considerable molecular absorption from water vapour. This leads to several transmission windows that can be utilised for communications depending on the range of the link. In Figure 1.4, the propagation loss in dB is depicted at the 0.1-1 THz range for distances up to 1 km, using the Recommendation ITU-R P.67 model [1-43] for atmospheric attenuation. Among this terahertz range, the 200-320 GHz window is particularly interesting because it offers immense bandwidth at a relatively low THz range, where more power is available and the advances on key technologies are significant. These prospects materialised in the first standardization efforts in the IEEE 802.15.3d amendment, defined between 252 and 325 GHz and ratified in 2017 [1-44].

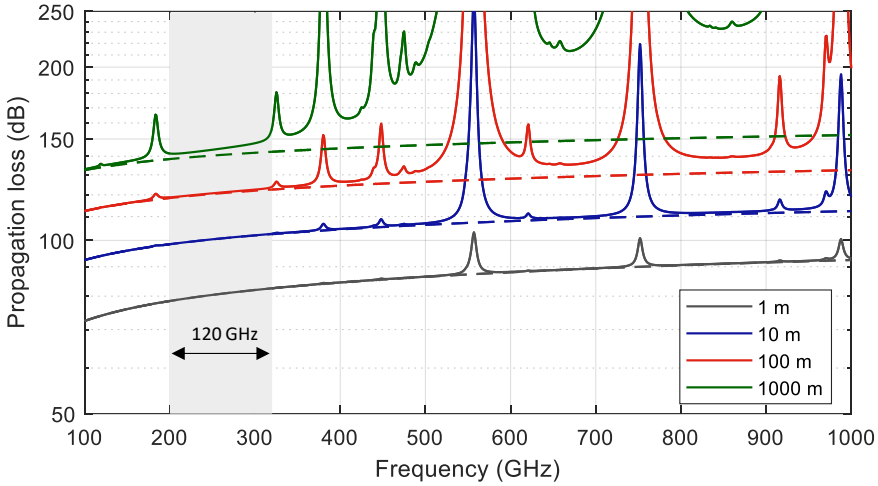

Figure 1.4: Propagation loss from 0.1 to 1 THz including FSPL and atmospheric attenuation, according to Recommendation ITU-R P.676. Dotted lines show the attenuation considering FSPL only. Values are calculated for an ambient temperature of 293 K, an atmospheric pressure of 101,300 kPa, and a water vapour density of 7.5 g/m^3.

The standard primarily addresses physical (PHY) and medium access control (MAC) layer specifications, defining channel bandwidths from 2.16 GHz up to 69.12 GHz, depending on the application, enabling data rates up to 315.39 Gbps using 64-QAM format in THz-SC mode. Targeted applications are: (1) fronthaul

and backhaul links, (2) data centres, (3) kiosk downloads, and (4) intra-device communications. In this work our primary focus is on fronthaul and backhaul links, which are increasingly critical as the number of deployed cells and connections grows exponentially. Dense networks will not depend exclusively on optical fibre for fronthaul and backhaul, particularly where fibre deployment is cost-inefficient or impractical [1-45]–[1-47]. Wireless THz connections can meet these needs by delivering ultra-fast links and complementing optical networks where necessary, and achieving convergence between fibre and wireless technologies will be essential for enabling high-speed, low-latency, and energy-efficient communications [1-48], [1-49].

To implement such THz wireless links, a wide variety of technologies and methods compete to offer the higher data rates. These systems can be broadly categorised in electronic and photonic types. In Figure 1.5, an overview of single-channel data rates demonstrated with photonic and electronic approaches in real-time and offline systems at 300 GHz and above is shown. We see that over 100 Gbps links have been achieved, and photonics mainly dominates the field. In addition, utilizing multi-channel/multi-lines systems, photonics-based demonstrations have achieved aggregated data rates of up to 1 Tbps [1-50], and long range transmissions of up to 200 Gbps for a distance of 4,600 m [1-51].

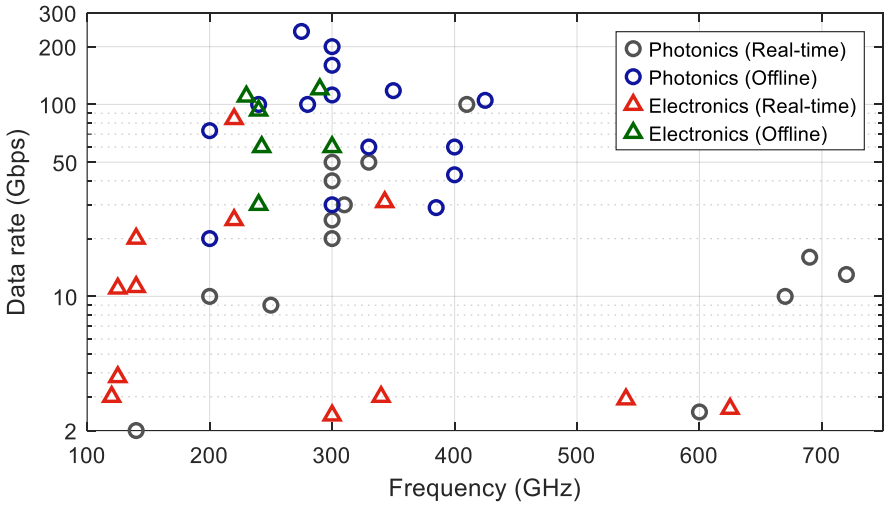

Figure 1.5: Single-channel transmission rates of THz communications demonstrations using photonics and electronics, adapted from [1-40] with added data from [1-52]–[1-57].

Photonics are mainly utilised in the transmitter of these systems, facilitating the optical generation and transport of data, which is then converted to THz frequencies via a high-speed photomixer. In contrast, the receiver side generally relies on electronic receivers, as their superior sensitivity outperforms that of photonic receivers. This results in improved signal-to-noise ratio (SNR) and supports higher data rates. This will be discussed in detail in section 1.2. A simplified schematic of a common photonic-based THz wireless link is depicted in Figure 1.6.

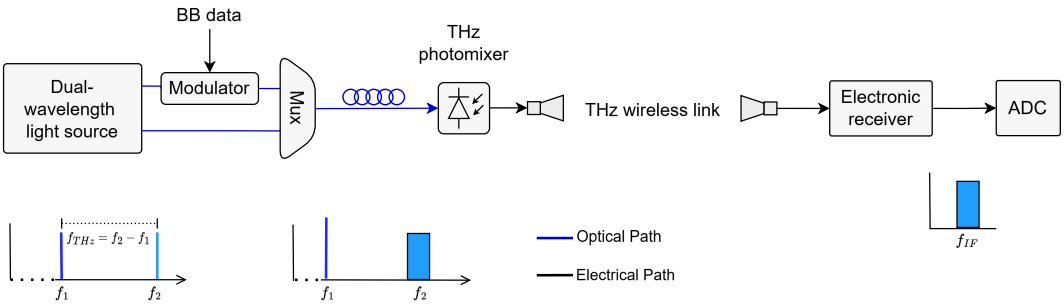

Figure 1.6: Simplified schematic of a common photonics-based single-channel THz wireless link. ADC: analogue-to-digital converter

In this context, photonic-based THz links are potentially the best suited to be deployed in 6G networks, not only for offering ultra-high data rates, but for the intrinsic advantages and ease of integration with current fibre technologies. The concept of distribution of radio signals over fibre networks to operate a remote station is known as radio-over-fibre (RoF), and it has been extensively studied for its use in 5G networks [1-58]–[1-60]. The use of optical fibres, enables long-distance distribution of radio signals, centralizing the generation and simplifying the front-ends. Currently deployed RoF systems at microwave frequencies can be extrapolated to terahertz-over-fibre (ToF), inheriting the same advantages from photonics [1-23], [1-25]. For instance, frequency division multiplexing multichannel systems can be easily implemented using multi-wavelength phase/frequency locked sources [1-61]–[1-63] and optical filters/multiplexers developed for optical wavelength-division multiplexing (WDM) networks. To illustrate the potential of THz photonics in wireless communications, a simplified concept of a future 6G network fully enabled by photonics is depicted in Figure 1.7. The baseband units (BBUs)

include optical engines responsible of generating the different THz channels and the THz LOs to operate in full-duplex mode. This is distributed via the local fibre network to the remote radio heads (RRHs), serving small cell links, fronthaul, or backhaul links. Each RRH may operate in single-channel or multi-channel modes, covering multiple THz bands with the same optical engine at the BBU. The RRHs include a 'colourless' coherent THz photonic transceiver operating with the optical signals distributed over the fibre network. The optoelectronic transmitter is based on a high-speed THz photomixer that performs optical-to-THz down-conversion. In contrast to typical photonic-based THz systems, the receiver here is also optoelectronic, which fully exploits the advantages of photonics.

Despite the promise of terahertz wireless communications, whether photonics-based or otherwise, numerous challenges remain. Some of these are (1) the efficiency and performance of THz transceivers, (2) beam alignment requirements and associated technology, (3) the impact of weather and atmospheric conditions, (4) hardware complexity and integration, (5) the definition of network protocols, (6) channel modelling and estimation, and (7) interference management in dense networks [1-7], [1-8], [1-46], [1-64]–[1-66]. This work focuses specifically on addressing challenge (1) as will be discussed next.

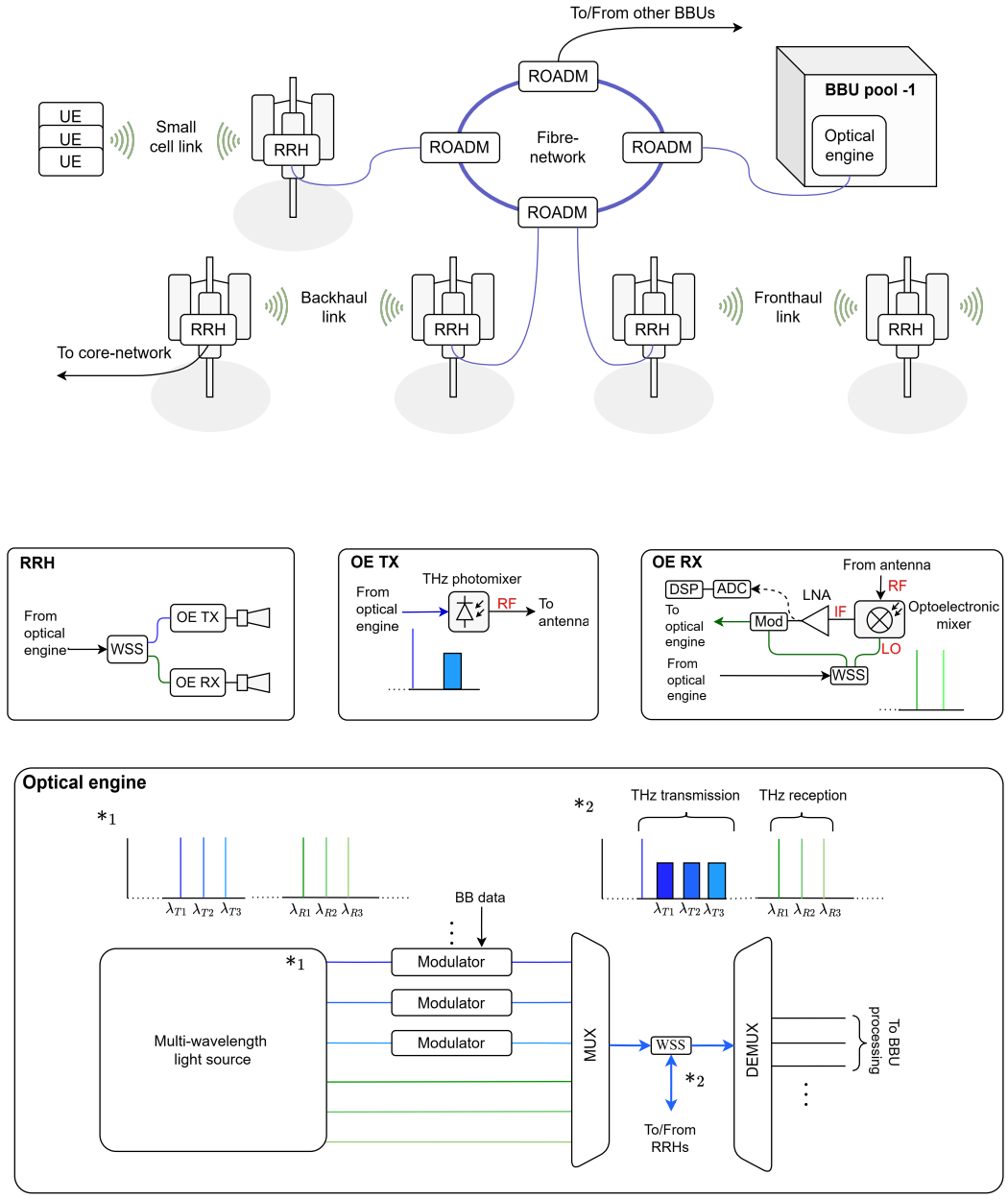

Figure 1.7: THz photonics for wireless communications. **a** Simplified concept of a future terahertz 6G network enabled by photonics. **b.** Insights on the RRHs based on a coherent THz photonic transceiver. WSS: Wavelength selective switch, ROADM: Reconfigurable optical add and drop multiplexer, UE: User equipment, ADC: analogue to digital converter, DSP: Digital signal processing, LNA: Low-noise amplifier, OE: Optoelectronic.

1.2 Literature review

The previous section has introduced the terahertz field and emphasised the critical role of photonics in enabling diverse applications. As highlighted, one of the fundamental challenges in the terahertz field is to develop efficient detectors, which is the main focus of this thesis. A wide range of THz systems are based on heterodyne detection, down-converting to a much lower IF, by mixing the THz wave with a reference signal, i.e. the local oscillator. This scheme has been used for decades in microwave and THz systems, with well-known advantages such as an improvement in sensitivity, frequency channel selection, IF amplification and processing, and coherent detection. Broadly, a terahertz heterodyne receiver consists of (1) a mixer, and (2) a source to generate local reference signal (see Figure 1.8). This section reviews the state-of-the-art in terahertz sources and mixers, providing the context and motivation for this work.

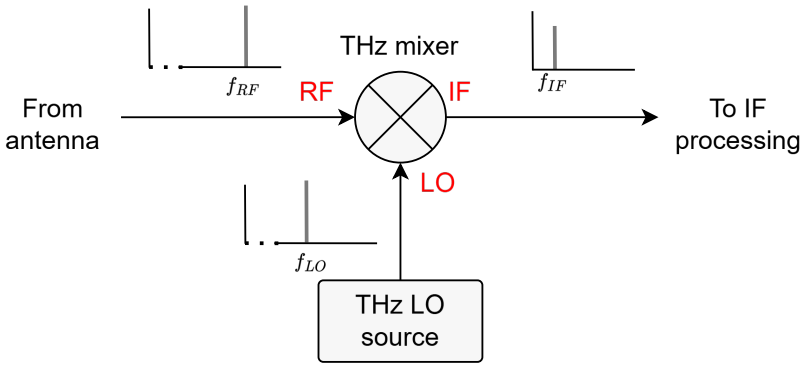

Figure 1.8: THz heterodyne receiver concept.

1.2.1 Terahertz sources

The earliest technology for generating CW terahertz radiation was the far infrared (FIR) gas laser based on CO_2, developed in the 1960s [1-67]. These lasers can achieve power levels in the milliwatt range, even at frequencies up to 5 THz [1-68]. While the existence of such sources might suggest the 'terahertz gap' is overstated, this concept inherently considers factors such as practicality, complexity, and compactness, i.e. areas where FIR gas sources face significant limitations.

This review focuses on the output power of compact solid-state terahertz

sources, excluding vacuum-based devices such as klystrons [1-69], free-electron lasers [1-70], and gyrotrons [1-71]. Although other figures of merit like phase noise are important, they are beyond the scope of this review, which aims to benchmark source power for driving a THz mixer.

Electronic sources

Electronic terahertz sources are generally based on producing electron oscillation by exploiting either negative differential conductance (NDC) or negative differential resistance (NDR) [1-72]. This is the case of Gunn, impact ionization avalanche transit-time (IMPATT), tunnelling transit-time (TUNNETT), and resonant tunnelling diodes (RTDs). The Gunn diode is a widely available option for low terahertz range generation that exploits the NDR of certain materials when a critical electric field is reached [1-73], [1-74]. Typically, InP is used as the active material, reaching powers in the milliwatt range up to about 300 GHz. The maximum reported frequency of oscillation is 455 GHz, generating an output power of 23 µW [1-75]. IMPATT diodes are also classic terahertz sources, which exploit NDR caused via avalanche and transit-time effects when high reverse voltage is applied to semiconductors like GaAs, InP or Si [1-76]. The TUNNET diode was proposed to improve the IMPATT diode performance by using quantum tunnelling instead of the avalanche effect, achieving lower noise levels [1-77]. The output power levels and maximum oscillation frequency is similar in these two, being limited to about 300-400 GHz, with milliwatt output power up to about 300 GHz. A more recent terahertz oscillator is the RTD, which is based on achieving resonant tunnelling in a quantum well with an ultra-low transit time [1-78], also resulting in NDR. In contrast to IMPATT and TUNNETT diodes, the RTD can achieve higher cut-off frequencies. In addition, a high integration density of RTDs is possible, and arrays with multiple RTDs have been developed. For example, in [1-79] a 6x6 array was demonstrated reaching up to 12 mW at 450 GHz. Also, in [1-80] an output power of 0.73 mW was reported at 1 THz with an 89 element array, which results in 8.2 µW per element. A maximum oscillation frequency of about 2 THz has been achieved, with an output power of less than 0.1 µW for a single RTD [1-81].

Terahertz transistors have also been extensively investigated for signal generation, including complementary metal-oxide semiconductor (CMOS) transistors, heterojunction bipolar transistors (HBTs), and high electron mobility transistors (HEMTs). CMOS THz transistors are particularly interesting because they can benefit from the high integration density, and scalability potential of CMOS processes. Recent progress have shown their remarkable performance, implementing NDR oscillators but also multiplier-chains [1-82]. For example, output powers of 31 and 5.4 µW have been demonstrated at 607.5, and 1330 GHz [1-83], [1-84], respectively. Silicon germanium (SiGe) HBT transistors have the advantage of exhibiting higher cut-off frequency (300 GHz) compared to CMOS [1-85]. Up to 1 THz radiation has been demonstrated, achieving 20 µW at 823 GHz [1-86], 18.6 µW at 928 GHz [1-87], and 81.3 µW at 1.01 THz with an array of 42 coherent radiators [1-88]. An important semiconductor parameter that limits the maximum frequency of Silicon-based THz transistors is the low electron mobility. For this reason, HEMTs based in high electron mobility materials like the InP material system have been demonstrated with maximum frequencies up to 1.2 THz [1-89]. These are typically used to implement power amplifiers and multiplier chains, reaching for example saturated powers of 19.9 mW at 300 GHz [1-90], 1.7 mW at 640 GHz [1-91], 1.8 mW at 680 GHz [1-92], and 0.6 mW at 847 GHz [1-93].

Despite the promising results of the aforementioned sources, GaAs SBD multipliers remain the most widely available technology for compact and efficient terahertz generation [1-94]–[1-96]. To achieve frequency multiplication, the modulation of the non-linear diode capacitance is typically used, operating the diode in varactor mode [1-5]. Initially demonstrated in the 1960s using whisker-contact diodes [1-97], they achieved exceptionally low parasitics but were limited in integration and reproducibility. These challenges were overcome in the 1990s with the advent of planar Schottky diodes [1-98], which are now widespread and commercially accessible [1-99]. Figure 1.9 shows SEM images of planar SBDs utilised in terahertz multipliers. Recent advancements in on-chip power combining modules have achieved record output powers of 500, 110, 35, 30, 2, and 0.7 mW at 180, 220,

330, 550, 1003, and 1640 GHz, respectively [1-100].

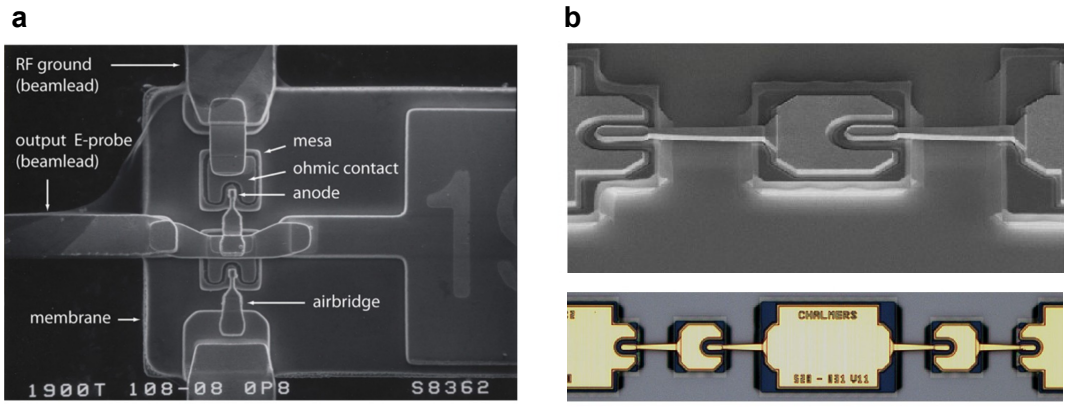

Figure 1.9: Planar GaAs Schottky barrier diodes for THz multipliers. **a** SEM picture of a 1.9 THz tripler chip, reproduced from [1-95]. **b** Balanced doubler chip, adapted from [1-101].

Photonic sources

An intuitive approach to generate electromagnetic radiation using photonics consists of implementing a laser. At infrared and optical frequencies, this can be achieved straightforwardly by exploiting interband transitions in semiconductors with energy bandgaps in the optical/infrared range [1-102]. However, at THz frequencies, the photon energy is too low for semiconductor interband transitions. To address this, the quantum cascade laser (QCL) was proposed, which uses quantum wells to enable intersubband transitions at THz photon energies [1-103], first demonstrated in 2002 [1-104]. QCLs typically emit in the mW range between 1–5 THz [1-105], with up to 1 W demonstrated at 3.7 THz [1-106], competing with or surpassing electronic technologies. However, their practicality is limited by the need for extremely low operating temperatures (typically below 50 K) due to intrinsic scattering processes that prevent efficient operation at room temperature [1-107].

An alternative mature approach involves direct optical-to-THz heterodyning downconversion in a high-speed photodiode. Unlike QCLs, photodiodes operate at room temperature, offering greater practicality. Conventional p-i-n photodiodes (pin-PDs) have been investigated for terahertz photomixing [1-108]–[1-112], and achieving recently saturated output powers of 885, 62, 12 and 1.4 µW at 115, 300, 500 and 1000 GHz, respectively [1-112]. However, the limited hole mobility

in pin-PDs constrains their maximum frequency and power-handling capabilities. To overcome these limitations, the UTC-PD was introduced in 1997 [1-113], [1-114]. This device typically employs a thin p-type quasi-neutral InGaAs layer as the absorber, enabling photogenerated majority holes to respond within the dielectric relaxation time. Consequently, only electrons contribute to the UTC-PD response, benefiting from drift velocities an order of magnitude higher than those of holes [1-115]. This higher drift velocity reduces space-charge effects, resulting in improved saturation power. THz UTC-PD photomixers have been commercially available for over a decade, enabling THz communication systems with record transmission rates [1-40].

Several variants of the basic vertically-illuminated UTC-PD structure have been proposed and demonstrated to further improve the frequency-response, saturation power, and responsivity such as waveguide-feed structures [1-116] or travelling-wave type devices [1-117]. Initial demonstrations achieved over 10 mW power at 50-100 GHz by implementing quarter-wavelength and stub matching circuits optimised for the frequency of interest[1-118]–[1-121]. Integration with resonant and wide-band planar antennas have been extensively studied, demonstrating over 1 μW power levels up to 1 THz [1-117], [1-122]–[1-125], as well as packaging on rectangular-waveguides [1-126]. Power combining approaches have achieved a record output power of 1.2 mW at 300 GHz [1-127]. Further examples of UTC-PD photomixers include modified UTC-PD (MUTC-PD) type structures [1-128]–[1-130], resonant-cavity enhanced devices with 750 μW at 300GHz [1-131], and hybrid integration on SiC to enhance power dissipation, achieving 2 mW at 300 GHz [1-132]. Figure 1.10 depicts some examples of UTC-PD photomixers for terahertz generation.

1.2.2 Terahertz mixers

Three figures of merit that are typically used to evaluate the mixer's performance are (1) the noise temperature, (2) conversion loss, and (3) the local oscillator power required to pump the mixer. In the same manner as with THz sources, THz mixers can be classified into electronic and optoelectronic types.

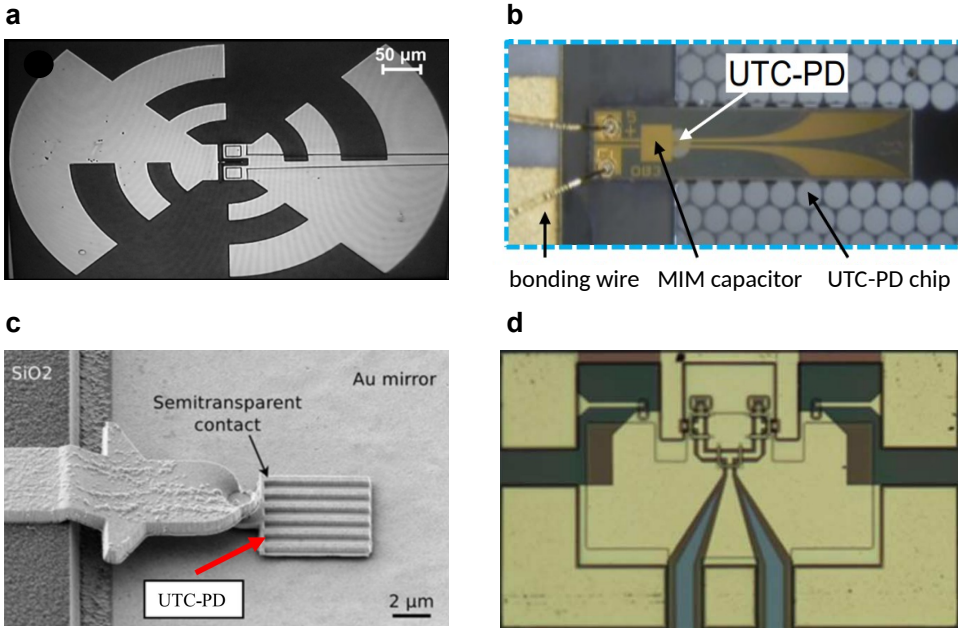

Figure 1.10: UTC-PDs for terahertz generation. **a** SEM photograph of an antenna-integrated (log-periodic) device, adapted from [1-133]. **b** Photograph of a packaged UTC-PD module fabricated in SiC substrate, adapted from [1-132]. **c** SEM photograph of a resonant-cavity-enhanced UTC-PD, reproduced from [1-131]. **d** Photograph of a 300 GHz power-combining UTC-PD chip, reproduced from [1-127].

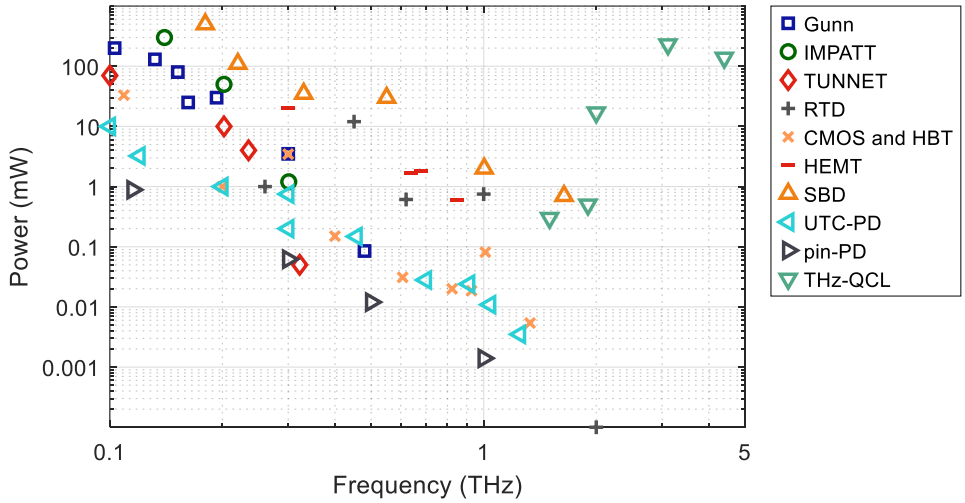

Figure 1.11: State-of-the-art THz peak output power of compact CW electronic and photonic sources. The data is taken from the following references: Gunn[1-134]–[1-136], TUNNET[1-134], [1-137], [1-138], RTD[1-79]–[1-81], [1-139], IMPATT[1-140], [1-141], CMOS and HBT[1-83], [1-84], [1-86], [1-87], [1-142]–[1-145],HEMT[1-90]–[1-93], pin-PD[1-112], UTC-PD[1-116], [1-117], [1-127], [1-129], [1-131], [1-133], QCL[1-146]–[1-150].

Electronic mixers

The most sensitive terahertz mixers are based on a superconductor-insulator-superconductor (SIS) junction, consisting of two superconductors separated by a thin insulator. Due to photo-assisted tunnelling of quasi-particles through the insulating material, the I-V curve is non-linear and can be exploited for frequency mixing [1-151]–[1-153]. The superconducting electrodes are typically made of Nb or NbTiN, with junction areas of the order of 1 µm, and SiO_2 as insulating layer [1-151]. RC constant and energy gap frequency of the superconducting material are the two main frequency limiting factors, leading to a maximum frequency of around 1.4 THz for all-Nb junctions [1-151]–[1-153]. These kind of mixers are relevant because the theory predicts quantum-limited sensitivity with low LO power. In practice, SIS mixers achieve a noise temperature trend of 2 to 10 times the quantum limit (hf/k) with about $\sim$100 µW of LO power [1-154]–[1-158]. This makes SIS mixers an excellent option for THz heterodyne receivers at the low THz regime, being used in many radio-observatories, e.g in ALMA [1-158]. However, the biggest limitation is the requirement of cryogenic cooling ($\sim 2-4\,K$), which is impractical in many scenarios such as space-based missions. In addition, significant IF impedance tuning and matching is required to compensate the large junction capacitance of about 60-100 $\mu F \cdot \mu m^{-2}$ [1-153], therefore limiting the attainable IF bandwidth (typical IF band is 4-8 GHz).

Unlike SIS mixers, bolometers are thermal detectors that sense THz radiation by a temperature dependent resistance when photons are absorbed in the active area of the device [1-152]. hot electron bolometers (HEBs) are a compelling alternative to SIS mixers because their maximum frequency is not limited by the energy gap of the material, enabling mixing up to several THz [1-151], [1-152]. The active material can be made of semiconductors [1-159] (typically InSb) or superconductors [1-157], [1-158], [1-160]–[1-164]. The first case does not have many practical applications as the IF bandwidth is limited to a few MHz only [1-159]. Superconducting HEBs however, have demonstrated frequency mixing up to 5 THz with excellent sensitivity (close to a $10hf/k$ trend) [1-151]. In comparison to SIS mixers,

they require even lower LO power, of the order of 1 µW, but also cryogenic cooling to achieve optimum performance. The IF bandwidth is however limited to a few GHz, being 7-8 GHz the maximum achieved [1-162], [1-163].

At room temperature, Schottky THz mixers are currently the dominant solution [1-95], [1-96]. In contrast to frequency multipliers, here the non-linear I-V characteristic is used to achieve frequency mixing, operating the diode in varistor mode [1-165], [1-166]. Planar GaAs Schottky technology has been also successfully applied to mixers, achieving reliable and reproducible contacts of a few μm^2 and even submicron areas. This enables diodes with series resistance of a few Ohms and junction capacitance of less than 1 fF, achieving cut-off frequencies of a few THz. Although the sensitivity is significantly lower than SISs and HEBs mixers (close to a $50hf/k$ trend) [1-151], they operate at room-temperature, are highly compact and the IF bandwidth can be of tens of GHz. Their main limitation is the high driving LO power, which is of the order of a few mW. This arises from the significant barrier height of 0.8-0.9 eV [1-167]. To mitigate this, subharmonic mixers where the LO is provided at a lower harmonic of the incoming signal can be implemented [1-95]. Figure 1.12 shows pictures of planar SBDs chips utilised in subharmonic terahertz mixers, and in table 1.1, the performance and LO power requirements of representative GaAs Schottky mixers is shown, from 200 GHz to 2.5 THz.

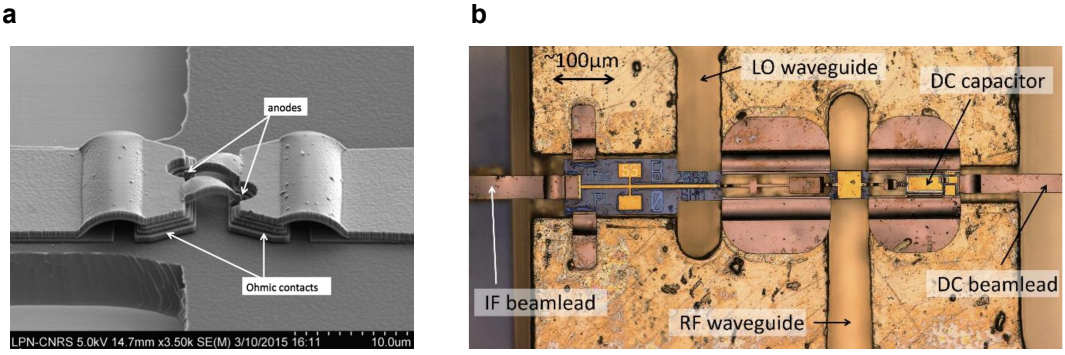

Figure 1.12: Planar GaAs Schottky barrier diodes for THz mixers. **a** SEM picture of 520-620 GHz antiparallel SBD mixer diodes, reproduced from [1-168]. **b** Photograph of a 2 THz mixer packaged chip, reproduced from [1-169].

To further reduce the LO power requirements, 'InP-based' materials can be used to make Schottky contacts with reduced barrier height. By 'InP-based' we

Year	Ref.	Type	f_{RF}(GHz)	T_{DSB}(K)	L_{DSB}(dB)	P_{LO}(mW)	C_j(fF)	R_s(Ω)
1993	[1-170]	SHM	195-230	795	5.7	5.7	3	12
1993	[1-171]	FM-S	230-280	1310	7.2	2	11	3
2005	[1-172]	SHM	300-365	700	6.3	4.5	1.3	15
1991	[1-173]	FM-S	300-365	1640	4.2	-	2.3	14
2008	[1-174]	SHM	368-392	1625	8	1.5	2.5	10
1999	[1-175]	SHM	380-425	1120	8	5	1.3	18
2010	[1-176]	FM-B	520-590	2500	8.5	1.5	-	-
2016	[1-168]	SHM	520-620	1284	5.5	3	1.1	32
2010	[1-177]	FM-B	835-900	2660	9.25	1	1	30
2014	[1-178]	SHM	1120-1280	2800	12	2.5	-	-
2009	[1-179]	FM-B	1250-1650	3000	10	1.5	-	-
2024	[1-169]	SHM	1900-2060	4000	11.5	1.3	0.25	49
1999	[1-180]	FM-S	2500	9000	16.9	5	-	20

Table 1.1: Performance of representative example of planar schottky diode THz mixers. FM-S: Fundamental mixer, single-ended. FM-B: Fundamental mixer, balanced. SHM: Subharmonic mixer, antiparallel configuration, f_{RF}: RF frequency. T_{DSB}: DSB noise temperature. P_{LO}: LO power. C_j: junction capacitance. R_s: series resistance.

refer to material layers that can be grown effectively, by molecular beam epitaxy (MBE) for example, in InP substrates. This is the case for instance of InP, InGaAs, and InGaAsP [1-181]–[1-183]. Barrier heights of about 0.5 eV are achieved for InP Schottky diodes [1-184], [1-185], and about 0.2-0.3 eV with InGaAs [1-186], which is considerably lower than GaAs Schottky contacts. Despite their promising characteristics, there are not many studies or demonstrations of InP-based THz Schottky mixers [1-187]–[1-191]. We can find several studies predicting a theoretical excess of 1-2 dB of conversion loss for InGaAs mixers compared to GaAs with an LO power about 0.1 mW [1-187], [1-190], which is an order of magnitude lower. Regarding experimental work, we can highlight a DSB conversion loss as low as 6.6 dB and noise temperature of 700 K was demonstrated at 183 GHz [1-189], with only 0.34 mW of LO power. Then in [1-191], a single-side-band (SSB) conversion loss of 15 dB and a noise temperature of 9,000 K is demonstrated up to 330 GHz, with an LO power of 0.5 mW.

A recently proposed alternative for low-barrier Schottky diodes is the Fermi-level-managed barrier diode (FMBD) [1-192]. Metal-semiconductor Schottky contacts encounter two intrinsic limitations: (1) the barrier height cannot be controlled

or further reduced without a lattice mismatch, and (2) the effect of surface-states compromises the reproducibility of the contact. To address these limitations, an all-semiconductor rectifying diode based on an n-type InGaAs-InP heterojunction was proposed for terahertz detection, the FMBD. By adjusting the doping of the InGaAs layer at the heterointerface, the barrier height can be reduced by shifting the Fermi-level above the conduction band. The FMBD was initially demonstrated as a zero-bias terahertz detector, but considerable amount of work has followed using the FMBD as a heterodyne receiver [1-193]–[1-198]. We can highlight achieved NEPs and LO powers at 300 GHz as low as $4{\cdot}10^{-19}$ W/Hz$^{-1/2}$ with 160 μW for a subharmonic mixer [1-194], and $2{\cdot}10^{-19}$ W/Hz$^{-1/2}$ with 400 μW for a balanced mixer [1-198]. Conversion loss and noise temperature has not been reported yet for FMBDs, although the achieved noise equivalent power (NEP) suggest a performance comparable to GaAs/InGaAs Schottky mixers.

Finally, silicon-based CMOS and SiGe HBT THz mixers have shown promising potential, particularly at lower frequencies in the terahertz range [1-199] ($\sim$ 300 GHz). A notable example is a 65 nm CMOS mixer with a reported noise temperature of 8,073-25,556 K at 220-320 GHz [1-200]. However, at higher frequencies, performance deteriorates, with significantly increased conversion loss and noise temperatures. For instance, a 65 nm CMOS mixer exhibited a noise temperature of 695,371 K at 410 GHz [1-201], while a 130 nm SiGe HBT chipset showed a noise temperature of 4,595,900 K at 823 GHz [1-202].

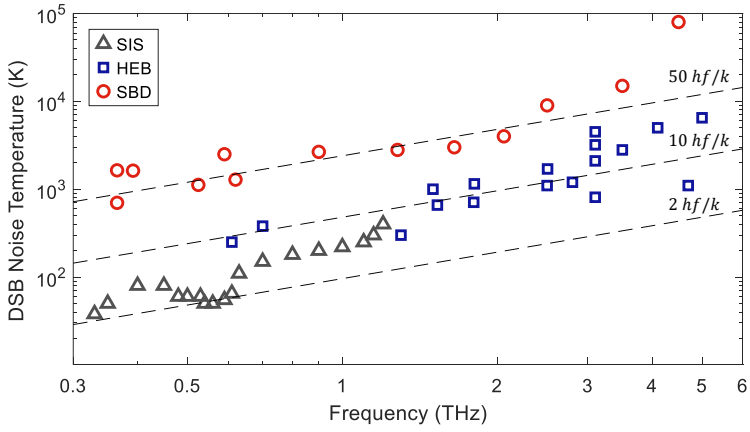

Figure 1.13: DSB noise temperature of state-of-the-art SIS, HEB, and SBD mixers, adapted from [1-151] with added data from [1-157], [1-203]–[1-206] and Table 1.1.

Optoelectronic mixers

The most common optoelectronic mixers utilize planar, interdigitated electrodes fabricated on short carrier lifetime photoconductive materials such as GaAs or InGaAs [1-207], [1-208]. When the active region of a photoconductor is illuminated with light at its absorption wavelength, free carriers (electrons and holes) are generated, increasing the material's conductivity (photoconductance) [1-5]. With incoming THz radiation, if the electric field is confined between the electrodes and the photoconductive material, photocarriers are accelerated accordingly. If the generation of photocarriers is also modulated by a beat note between two optical frequencies, frequency mixing occurs between the incoming THz radiation and the beat note producing a down-converted signal.

Photoconductor mixers are typically used in spectroscopy systems, since they can operate continuously up to a few THz. However, compared to electronic mixers, these are highly limited in conversion loss, with a minimum reported value of $\sim$ 27 dB at 300 GHz using a GaAs photoconductor [1-209]. This limitation is mainly related to the very high photoconductance, of the order of kΩs [1-5], which imposes a significant impedance mismatch with output electronics. To use telecom wavelengths, InGaAs-based photoconductors are required, with a minimum reported conversion loss of $\sim$ 30 dB at 300 GHz, using a plasmonic microcavity to enhance field interaction and iron doping to increase the dark resistivity and shorten the carrier lifetime [1-210]. Nevertheless, photoconductors are key to enable ultra-wide bandwidth spectroscopy systems [1-29], [1-30], [1-211], [1-212], achieving a record of 132 dB peak dynamic range with up to 5.5 THz bandwidth in a CW system[1-30].

Some additional technologies that have been proposed for optoelectronic THz mixing are UTC-PDs [1-124], [1-213], [1-214] and graphene-based transistors or heterostructures [1-215]–[1-217]. However, their reported performance is far from optimal, exhibiting conversion loss typically above 40 dB. Table 1.2 summarises the performance of relevant examples of optoelectronic THz mixers.

Year	Ref.	Type	f_{RF}(GHz)	L_{SSB}(dB)	P_{opt} (mW)	λ_{opt} (nm)
2023	[1-217]	hBN-graphene	94	44	20	1550
2012	[1-214]	InGaAs UTC-PD	100	32	33	1550
2013	[1-209]	LTG-GaAs PC	300	27	117	800
2014	[1-213]	InGaAs UTC-PD	300	66	-	1550
2023	[1-210]	Fe-doped InGaAs PC	320	30	35	1550

Table 1.2: Performance of representative optoelectronic terahertz mixers. LTG: low-temperature-grown. PC: photonductor. UTC-PD: uni-travelling-carrier-photodiode. f_{RF}: RF frequency. L_{SSB}: SSB conversion loss. P_{opt}: optical power. λ_{opt}: optical wavelength.

1.3 Research gap and contributions

The literature review highlights that electronic-based solutions currently outperform photonics-based technologies in terms of source power and mixer sensitivity. However, the discussed inherent advantages of photonic technologies, help bridge this performance gap to make photonics-based solutions the preferred option in some areas. Wireless communications, the target application of this work, exemplifies this dynamic: the highest data rates have been achieved using UTC-PD-based transmitters. These demonstrations, however, rely on electronic-based receivers, where the performance disparity with optoelectronic mixers is more pronounced and the mixer sensitivity is of major importance to increase the overall system SNR and achieve greater data rates. In this sense, optoelectronic mixers have been significantly less developed compared to SIS, HEB, and SBD technologies, with sensitivities lagging by one or more orders of magnitude. This highlights a clear research gap in advancing optoelectronic receivers to state-of-the-art performance levels, to fully exploit the advantages of photonics at the transmitter and receiver of THz systems.

This work aims to bridge the performance gap by investigating a hybrid solution: photonically-pumped electronic mixers. This solution seeks to combine the strengths of both electronics and photonics by integrating a high-performance electronic mixer with a photonic LO generator. The choice of technologies for this purpose depends on three key factors: (1) operating temperature, (2) integration ease, and (3) available LO power. Since room-temperature operation is a require-

ment for the target application, SISs and HEBs are excluded as mixer options, along with QCLs for the LO source. Among the remaining alternatives, a promising solution involves combining SBD-based mixers with UTC-PD-based sources, which has seen minimal research. For instance, [1-218] reports a 180 GHz subharmonic Schottky mixer pumped by a UTC-PD at 90 GHz, achieving a noise temperature of 2000 K. Nevertheless, the use of GaAs Schottky mixers imposes a significant challenge related to the LO power required, which is above 1 mW (see Table 1.1). Although UTC-PDs can generate milliwatt-level power up to about 300 GHz, these are record-breaking demonstrations, usually referring to on-chip power, and are difficult to replicate. The development of repeatable UTC-PD-based LO sources for pumping GaAs Schottky mixers at higher THz frequencies remains highly constrained.

To overcome this limitation, the use of alternative materials like InP and InGaAs to make SBDs can significantly reduce the LO power required, with a moderate penalty in mixer sensitivity. Furthermore, the use of these material systems enables the monolithic integration of the mixer and the UTC-PD parts due to epitaxial compatibility. An example is described in [1-183], where an InGaAsP SBD was fabricated using the UTC-PD epitaxy, but never integrated together in a receiver. Here, we propose the integration of InP-based Schottky mixers with UTC-PDs to implement high-performance optoelectronic THz receivers. This concept is illustrated in Figure 1.14.

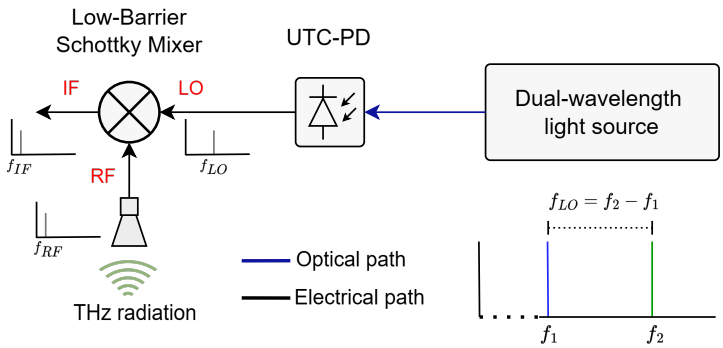

Figure 1.14: Optoelectronic receiver concept based on a low-barrier Schottky mixer pumped by a photonic local oscillator generated with a UTC-PD.

It is worth noting that the complete receiver system includes a dual-wavelength light source for performing optical heterodyning in the UTC-PD. Functionally, integrating this component may not be desired, as one of the primary advantages of the receiver is the ability to distribute the optical LO signal through an optical fibre link. This work focuses exclusively on the integration of the low-barrier mixer and the UTC-PD, and the applicability of this technology to wireless communications at 300 GHz. The key contributions of this work can be summarised as follows:

- The first demonstration of an optoelectronic receiver based on a photonically-pumped low-barrier mixer, utilizing non-integrated components.
- The demonstration of a high-speed 300 GHz wireless link using the optoelectronic receiver, achieving data rates comparable to systems with state-of-the-art electronic receivers.
- The design of a 300 GHz monolithically-integrated optoelectronic receiver, incorporating InP SBDs within the standard UTC-PD epitaxial structure, with state-of-the-art predicted performance.
- The design, fabrication, and characterisation of a 300 GHz hybrid-integrated optoelectronic receiver, featuring low-barrier InGaAs SBDs and a UTC-PD in a quasi-optical package, achieving an order-of-magnitude improvement over existing optoelectronic receivers.

1.4 Thesis overview

This thesis is structured as follows: Chapter 2 provides the theoretical background for designing the proposed optoelectronic receivers, including SBD, UTC-PD, and resistive mixer theory. Chapter 3 details the design of InP-based SBDs using the UTC-PD epitaxial structure, along with their monolithic integration into a 300 GHz quasi-optical receiver. Chapter 4 presents the design hybrid integration solution, including the development of a quasi-optical 300 GHz receiver and a rectangular-waveguide WR3 receiver. Chapter 5 discusses experimental results for photonically-pumped SBD-based receivers, focusing on receiver performance and

demonstrations of 300 GHz wireless links. Chapter 6 concludes the thesis with a summary of key findings and future research directions.

References

[1-1] S. S. Dhillon, M. S. Vitiello, E. H. Linfield, *et al.*, "The 2017 terahertz science and technology roadmap," en, *J. Phys. D Appl. Phys.*, vol. 50, no. 4, p. 043 001, Feb. 2017.

[1-2] A. Leitenstorfer, A. S. Moskalenko, T. Kampfrath, *et al.*, "The 2023 terahertz science and technology roadmap," *J. Phys. D Appl. Phys.*, vol. 56, no. 22, p. 223 001, Jun. 2023.

[1-3] *Web of science, clarivate*, :https://www.webofscience.com/, Accessed: 2024-11-30.

[1-4] C. K. Walker, *Terahertz Astronomy*, en. CRC Press, Oct. 2015.

[1-5] D. Pavlidis, *Fundamentals of Terahertz Devices and Applications*, en. John Wiley & Sons, Aug. 2021.

[1-6] T. Kleine-Ostmann and T. Nagatsuma, "A review on terahertz communications research," en, *J. Infrared Millim. Terahertz Waves*, vol. 32, no. 2, pp. 143–171, Feb. 2011.

[1-7] Z. Chen, X. Ma, B. Zhang, *et al.*, "A survey on terahertz communications," *China Communications*, vol. 16, no. 2, pp. 1–35, Feb. 2019.

[1-8] H.-J. Song and N. Lee, "Terahertz communications: Challenges in the next decade," *IEEE Transactions on Terahertz Science and Technology*, vol. 12, no. 2, pp. 105–117, Mar. 2022.

[1-9] M. C. Kemp, P. F. Taday, B. E. Cole, J. A. Cluff, A. J. Fitzgerald, and W. R. Tribe, "Security applications of terahertz technology," en, in *Terahertz for Military and Security Applications*, vol. 5070, SPIE, Jul. 2003, pp. 44–52.

[1-10] H.-B. Liu, H. Zhong, N. Karpowicz, Y. Chen, and X.-C. Zhang, "Terahertz spectroscopy and imaging for defense and security applications," *Proc. IEEE*, vol. 95, no. 8, pp. 1514–1527, Aug. 2007.

[1-11] J.-H. Son, S. J. Oh, and H. Cheon, "Potential clinical applications of terahertz radiation," *J. Appl. Phys.*, vol. 125, no. 19, p. 190 901, May 2019.

[1-12] A. Gong, Y. Qiu, X. Chen, Z. Zhao, L. Xia, and Y. Shao, "Biomedical applications of terahertz technology," *Appl. Spectrosc. Rev.*, vol. 55, no. 5, pp. 418–438, May 2020.

[1-13] A. G. Markelz and D. M. Mittleman, "Perspective on terahertz applications in bioscience and biotechnology," *ACS Photonics*, vol. 9, no. 4, pp. 1117–1126, Apr. 2022.

[1-14] R. R. Hartmann, J. Kono, M. Portnoi, and M. Portnoi, "Terahertz science and technology of carbon nanomaterials," *Nanotechnology*, vol. 25, Nov. 2013.

[1-15] M. Yu Glyavin, G. G. Denisov, V. E. Zapevalov, M. A. Koshelev, M. Yu Tretyakov, and A. I. Tsvetkov, "High-power terahertz sources for spectroscopy and material diagnostics," en, *Phys.-Usp.*, vol. 59, no. 6, p. 595, Jun. 2016.

[1-16] F. Ospald, W. Zouaghi, R. Beigang, *et al.*, "Aeronautics composite material inspection with a terahertz time-domain spectroscopy system," en, *Organ. Ethic.*, vol. 53, no. 3, p. 031 208, Dec. 2013.

[1-17] S. Krimi, J. Klier, J. Jonuscheit, G. von Freymann, R. Urbansky, and R. Beigang, "Highly accurate thickness measurement of multi-layered automotive paints using terahertz technology," *Appl. Phys. Lett.*, vol. 109, no. 2, p. 021 105, Jul. 2016.

[1-18] F. Ellrich, M. Bauer, N. Schreiner, *et al.*, "Terahertz quality inspection for automotive and aviation industries," en, *J. Infrared Millim. Terahertz Waves*, vol. 41, no. 4, pp. 470–489, Apr. 2020.

[1-19] Y. Lu, Q. Mao, and J. Liu, "A deep transfer learning model for packaged integrated circuit failure detection by terahertz imaging," *IEEE Access*, vol. 9, pp. 138 608–138 617, 2021.

[1-20] J. True, C. Xi, N. Jessurun, K. Ahi, and N. Asadizanjani, "Review of THz-based semiconductor assurance," *Opt. Eng.*, vol. 60, no. 06, Jun. 2021.

[1-21] L. Rong, T. Latychevskaia, C. Chen, *et al.*, "Terahertz in-line digital holography of human hepatocellular carcinoma tissue," en, *Sci. Rep.*, vol. 5, no. 1, p. 8445, Feb. 2015.

[1-22] J. Hennig, J. Klier, S. Duran, *et al.*, "Wide-range resistivity characterization of semiconductors with terahertz time-domain spectroscopy," en, *Opt. Express*, vol. 32, no. 12, pp. 21 028–21 041, Jun. 2024.

[1-23] T. Nagatsuma, G. Ducournau, and C. C. Renaud, "Advances in terahertz communications accelerated by photonics," *Nat. Photonics*, vol. 10, no. 6, pp. 371–379, 2016.

[1-24] D. Saeedkia and S. Safavi-Naeini, "Terahertz photonics: Optoelectronic techniques for generation and detection of terahertz waves," *J. Lightwave Technol.*, vol. 26, no. 15, pp. 2409–2423, Aug. 2008.

[1-25] A. J. Seeds, M. J. Fice, K. Balakier, *et al.*, "Coherent terahertz photonics," en, *Opt. Express*, vol. 21, no. 19, pp. 22 988–23 000, Sep. 2013.

[1-26] U. Nandi, J. C. Norman, A. C. Gossard, H. Lu, and S. Preu, "1550-nm driven ErAs:In(Al)GaAs photoconductor-based terahertz time domain system with 6.5 THz bandwidth," *J. Infrared Millim. Terahertz Waves*, vol. 39, no. 4, pp. 340–348, Apr. 2018.

[1-27] J. Neu and C. A. Schmuttenmaer, "Tutorial: An introduction to terahertz time domain spectroscopy (THz-TDS)," *J. Appl. Phys.*, vol. 124, no. 23, p. 231 101, Dec. 2018.

[1-28] R. I. Hermans, J. Seddon, H. Shams, L. Ponnampalam, A. J. Seeds, and G. Aeppli, "Ultra-high-resolution software-defined photonic terahertz spectroscopy," en, *Optica*, vol. 7, no. 10, p. 1445, Oct. 2020.

[1-29] L. Liebermeister, S. Nellen, R. B. Kohlhaas, *et al.*, "Optoelectronic frequency-modulated continuous-wave terahertz spectroscopy with 4 THz bandwidth," *Nat. Commun.*, vol. 12, no. 1, 2021.

[1-30] M. Deumer, S. Breuer, S. Berrios, *et al.*, "Continuous wave THz receivers with rhodium-doped InGaAs enabling 132 dB dynamic range," en, *Opt. Express*, vol. 32, no. 17, p. 29 855, Aug. 2024.

[1-31] *Atacama large millimetre array (ALMA)*, www.almaobservatory.org, Accessed: 2024-11-30.

[1-32] J. M. Payne and W. P. Shillue, "Photonic techniques for local oscillator generation and distribution in millimeter-wave radio astronomy," in *International Topical Meeting on Microwave Photonics MWP-02*, IEEE, 2002, pp. 9–12.

[1-33] B. Shillue, "Atacama large millimeter array photonic local oscillator: Femtosecond-level synchronization for radio astronomy," in *2010 IEEE International Frequency Control Symposium*, IEEE, Jun. 2010, pp. 569–571.

[1-34] W. Shillue, W. Grammer, C. Jacques, *et al.*, "The ALMA photonic local oscillator system," in *2011 XXXth URSI General Assembly and Scientific Symposium*, IEEE, Aug. 2011, pp. 1–4.

[1-35] I. C. Mayorga, A. Schmitz, T. Klein, C. Leinz, and R. Gusten, "First in-field application of a full photonic local oscillator to terahertz astronomy," *IEEE Trans. Terahertz Sci. Technol.*, vol. 2, no. 4, pp. 393–399, Jul. 2012.

[1-36] J.-Y. Kim, H.-J. Song, M. Yaita, A. Hirata, and K. Ajito, "CW-THz vector spectroscopy and imaging system based on 1.55-μm fiber-optics," en, *Opt. Express*, vol. 22, no. 2, pp. 1735–1741, Jan. 2014.

[1-37] M. Tonouchi, "Cutting-edge terahertz technology," *Nature Photonics*, vol. 1, pp. 97–105, Feb. 2007.

[1-38] *National radio astronomy observatory*, https://public.nrao.edu/news/alma-and-the-event-horizon-telescope-tip-sheet/, Accessed: 2024-12-1.

[1-39] 3GPP, *TS 38.101-2, technical specification part 2: Range 2 standalone (release 18)*, Sep. 2024.

[1-40] T. Kürner, D. M. Mittleman, and T. Nagatsuma, *THz Communications: Paving the Way Towards Wireless Tbps*, en. Springer Nature, Dec. 2021.

[1-41] M. Shehata, Y. Wang, J. He, S. Kandeepan, and K. Wang, "Optical and terahertz wireless technologies: The race to 6G communications," *IEEE Wirel. Commun.*, vol. 30, no. 5, pp. 10–18, Oct. 2023.

[1-42] *UK frequency allocation table (UKFAT)*, https://static.ofcom.org.uk/static/spectrum/fat.html, Accessed: 2024-12-1.

[1-43] Radiocommunication Sector of International Telecommunication Union, *Recommendation ITU-R P.676-10: Attenuation by atmospheric gases*, 2022.

[1-44] V. Petrov, T. Kurner, and I. Hosako, "IEEE 802.15.3d: First standardization efforts for sub-terahertz band communications toward 6G," *IEEE Commun. Mag.*, vol. 58, no. 11, pp. 28–33, Nov. 2020.

[1-45] H. Saarnisaari, A. Chaoub, M. Heikkilä, A. Singhal, and V. Bhatia, "Wireless terrestrial backhaul for 6G remote access: Challenges and low power solutions," *Frontiers in Communications and Networks*, vol. 2, 2021.

[1-46] H. Cho, S. Mukherjee, D. Kim, T. Noh, and J. Lee, "Facing to wireless network densification in 6G: Challenges and opportunities," *ICT Express*, vol. 9, no. 3, pp. 517–524, Jun. 2023.

[1-47] G. Kalfas, C. Vagionas, A. Antonopoulos, *et al.*, "Next generation fiber-wireless fronthaul for 5G mmWave networks," *IEEE Commun. Mag.*, vol. 57, no. 3, pp. 138–144, Mar. 2019.

[1-48] A. Kanno, P. Tien Dat, N. Sekine, *et al.*, "High-speed coherent transmission using advanced photonics in terahertz bands," *IEICE Trans. Electron.*, vol. E98.C, no. 12, pp. 1071–1080, 2015.

[1-49] T. Kawanishi, "THz and photonic seamless communications," *J. Lightwave Technol.*, vol. 37, no. 7, pp. 1671–1679, 2019.

[1-50] M. Zhu, J. Zhang, X. Liu, *et al.*, "Photonics-assisted THz wireless transmission with air interface user rate of 1-tbps at 330–500 GHz band," *Information Sciences*, vol. 66, no. 199302, pp. 1–199 302, 2023.

[1-51] Y. Wei, J. Yu, X. Zhao, *et al.*, "Demonstration of a photonics-aided 4,600-m wireless transmission system in the sub-THz band," *J. Lightwave Technol.*, vol. 42, no. 24, pp. 1–13, 2024.

[1-52] K. Liu, Y. Feng, C. Han, *et al.*, "High-speed 0.22 THz communication system with 84 Gbps for real-time uncompressed 8K video transmission of live events," en, *Nat. Commun.*, vol. 15, no. 1, p. 8037, Sep. 2024.

[1-53] K. Maekawa, T. Nakashita, T. Yoshioka, T. Hori, A. Rolland, and T. Nagatsuma, "Single-channel 240-Gbit/s sub-THz wireless communications using ultra-low phase noise receiver," en, *IEICE Electron. Express*, vol. 21, no. 3, pp. 20 230 584–20 230 584, Feb. 2024.

[1-54] J. Dittmer, J. Tebart, C. Füllner, C. Koos, A. Stöhr, and S. Randel, "200 Gbit/s wireless THz transmission over 52m using optoelectronic signal generation," pp. 134–137, Sep. 2023.

[1-55] H. Zhang, L. Zhang, Z. Yang, *et al.*, "Single-lane 200 Gbit/s photonic wireless transmission of multicarrier 64-QAM signals at 300 GHz over 30 m," *Chin. Opt. Lett.*, vol. 21, no. 2, p. 023 901, 2023.

[1-56] J. Zhang, M. Zhu, B. Hua, *et al.*, "Real-time demonstration of 100 GbE THz-wireless and fiber seamless integration networks," *J. Lightwave Technol.*, vol. 41, no. 4, pp. 1129–1138, Feb. 2023.

[1-57] S. Nellen, S. Lauck, E. Peytavit, *et al.*, "Coherent wireless link at 300 GHz with 160 Gbit/s enabled by a photonic transmitter," *J. Lightwave Technol.*, vol. 40, no. 13, pp. 4178–4185, Jul. 2022.

[1-58] S. Iezekiel, "Radio-over-fiber technology and devices for 5G: An overview," *Broadband access communication technologies X*, vol. 9772, pp. 50–56, 2016.

[1-59] P. T. Dat, A. Kanno, T. Umezawa, N. Yamamoto, and T. Kawanishi, "Millimeter- and terahertz-wave radio-over-fiber for 5G and beyond," in *2017 IEEE Photonics Society Summer Topical Meeting Series (SUM)*, IEEE, Jul. 2017, pp. 165–166.

[1-60] S. Rommel, D. Dodane, E. Grivas, *et al.*, "Towards a scaleable 5G fronthaul: Analog radio-over-fiber and space division multiplexing," *J. Lightwave Technol.*, vol. 38, no. 19, pp. 5412–5422, Oct. 2020.

[1-61] T. Fortier and E. Baumann, "20 years of developments in optical frequency comb technology and applications," *Commun. Phys.*, vol. 2, Sep. 2019.

[1-62] L. Chang, S. Liu, and J. Bowers, "Integrated optical frequency comb technologies," *Nat. Photonics*, vol. 16, pp. 95–108, Feb. 2022.

[1-63] E. J. Tough, M. J. Fice, G. Carpintero, C. C. Renaud, A. J. Seeds, and K. Balakier, "InP integrated optical frequency comb generator using an amplified recirculating loop," *Opt. Express, OE*, vol. 30, no. 24, pp. 43 195–43 208, Nov. 2022.

[1-64] C. Han, Y. Wu, Z. Chen, and X. Wang, "Terahertz communications (TeraCom): Challenges and impact on 6G wireless systems," *arXiv [eess.SP]*, Dec. 2019.

[1-65] C.-X. Wang, J. Wang, S. Hu, Z. H. Jiang, J. Tao, and F. Yan, "Key technologies in 6G terahertz wireless communication systems: A survey," *IEEE Veh. Technol. Mag.*, vol. 16, no. 4, pp. 27–37, Dec. 2021.

[1-66] W. Jiang, Q. Zhou, J. He, *et al.*, "Terahertz communications and sensing for 6G and beyond: A comprehensive review," *IEEE Commun. Surv. Tutor.*, vol. 26, no. 4, pp. 2326–2381, 2024.

[1-67] A. Crocker, H. A. Gebbie, M. F. Kimmitt, and I. E. S. Mathias, "Stimulated emission in the far infrared," *Nature*, 1964.

[1-68] G. P. Gallerano and S. Biedron, "Overview of terahertz radiation sources," in *Proceedings of the 2004 FEL Conference*, vol. 1, 2004, pp. 216–221.

[1-69] A. Roitman, D. Berry, and B. Steer, "State-of-the-art W-band extended interaction klystron for the CloudSat program," *IEEE Trans. Electron Devices*, vol. 52, no. 5, pp. 895–898, May 2005.

[1-70] C. Sung, S. Y. Tochitsky, S. Reiche, J. B. Rosenzweig, C. Pellegrini, and C. Joshi, "Seeded free-electron and inverse free-electron laser techniques for radiation amplification and electron microbunching in the terahertz range," *Phys. Rev. ST Accel. Beams*, vol. 9, no. 12, p. 120 703, Dec. 2006.

[1-71] V. L. Bratman, Y. K. Kalynov, and V. N. Manuilov, "Large-orbit gyrotron operation in the terahertz frequency range," en, *Phys. Rev. Lett.*, vol. 102, no. 24, p. 245 101, Jun. 2009.

[1-72] D. Chattopadhyay and P. C. Rakshit, *Electronics Fundamentals and Applications*, 7th ed. New Delhi, India: New Age International, Dec. 2006.

[1-73] J. B. Gunn, "Microwave oscillations of current in III–V semiconductors," *Solid State Commun.*, 1963.

[1-74] A. Khalid, N. J. Pilgrim, G. M. Dunn, *et al.*, "A planar Gunn diode operating above 100 GHz," *IEEE Electron Device Lett.*, vol. 28, no. 10, pp. 849–851, Oct. 2007.

[1-75] H. Eisele, "Third-harmonic power extraction from InP Gunn devices up to 455 GHz," *IEEE Microw. Wirel. Compon. Lett.*, vol. 19, no. 6, pp. 416–418, Jun. 2009.

[1-76] A. Acharyya and J. P. Banerjee, "Prospects of IMPATT devices based on wide bandgap semiconductors as potential terahertz sources," en, *Appl. Nanosci.*, vol. 4, no. 1, pp. 1–14, Jan. 2014.

[1-77] G. I. Haddad, J. R. East, and C. Kidner, "Tunnel transit-time (tunnett) devices for terahertz sources," en, *Microw. Opt. Technol. Lett.*, vol. 4, no. 1, pp. 23–29, Jan. 1991.

[1-78] E. R. Brown, J. R. Söderström, C. D. Parker, L. J. Mahoney, K. M. Molvar, and T. C. McGill, "Oscillations up to 712 GHz in InAs/AlSb resonant-tunneling diodes," en, *Appl. Phys. Lett.*, vol. 58, no. 20, pp. 2291–2293, May 1991.

[1-79] Y. Koyama, Y. Kitazawa, K. Yukimasa, *et al.*, "A high-power terahertz source over 10 mW at 0.45 THz using an active antenna array with integrated patch antennas and resonant-tunneling diodes," *IEEE Trans. Terahertz Sci. Technol.*, vol. 12, no. 5, pp. 510–519, Sep. 2022.

[1-80] K. Kasagi, S. Suzuki, and M. Asada, "Large-scale array of resonant-tunneling-diode terahertz oscillators for high output power at 1 THz," *J. Appl. Phys.*, Mar. 2019.

[1-81] R. Izumi, S. Suzuki, and M. Asada, "1.98 THz resonant-tunneling-diode oscillator with reduced conduction loss by thick antenna electrode," in *2017 42nd International Conference on Infrared, Millimeter, and Terahertz Waves (IRMMW-THz)*, IEEE, Aug. 2017, pp. 1–2.

[1-82] E. Seok, D. Shim, C. Mao, *et al.*, "Progress and challenges towards terahertz CMOS integrated circuits," *IEEE J. Solid-State Circuits*, vol. 45, no. 8, pp. 1554–1564, Aug. 2010.

[1-83] B. Khamaisi, S. Jameson, and E. Socher, "A 0.58-0.61THz single on-chip antenna transceiver based on active X30 LO chain on 65nm CMOS," in *2016 11th European Microwave Integrated Circuits Conference (EuMIC)*, IEEE, Oct. 2016, pp. 97–100.

[1-84] Z. Ahmad, M. Lee, and K. O. Kenneth, "20.5 1.4THz, -13dBm EIRP frequency multiplier chain using symmetric- and asymmetric-CV varactors in 65nm CMOS," in *2016 IEEE International Solid-State Circuits Conference (ISSCC)*, IEEE, Jan. 2016, pp. 350–351.

[1-85] B. Saha, S. Fregonese, B. Heinemann, *et al.*, "Reliable technology evaluation of SiGe HBTs and MOSFETs: *fmax* estimation from measured data," *IEEE Electron Device Lett.*, vol. 42, no. 1, pp. 14–17, Jan. 2021.

[1-86] E. Ojefors, J. Grzyb, Y. Zhao, B. Heinemann, B. Tillack, and U. R. Pfeiffer, "A 820GHz SiGe chipset for terahertz active imaging applications," in *2011 IEEE International Solid-State Circuits Conference*, IEEE, Feb. 2011, pp. 224–226.

[1-87] H. Aghasi, A. Cathelin, and E. Afshari, "A 0.92-THz SiGe power radiator based on a nonlinear theory for harmonic generation," *IEEE J. Solid-State Circuits*, vol. 52, no. 2, pp. 406–422, Feb. 2017.

[1-88] Z. Hu, M. Kaynak, and R. Han, "High-power radiation at 1 THz in silicon: A fully scalable array using a multi-functional radiating mesh structure," *IEEE J. Solid-State Circuits*, vol. 53, no. 5, pp. 1313–1327, May 2018.

[1-89] A. M. Arabhavi, F. Ciabattini, S. Hamzeloui, *et al.*, "InP/GaAsSb double heterojunction bipolar transistor emitter-fin technology with *fmax* = 1.2 THz," *IEEE Trans. Electron Devices*, vol. 69, no. 4, pp. 2122–2129, Apr. 2022.

[1-90] L. John, A. Tessmann, A. Leuther, P. Neininger, T. Merkle, and T. Zwick, "Broadband 300-GHz power amplifier MMICs in InGaAs mHEMT technology," *IEEE Trans. Terahertz Sci. Technol.*, vol. 10, no. 3, pp. 309–320, May 2020.

[1-91] V. Radisic, K. M. K. H. Leong, X. Mei, S. Sarkozy, W. Yoshida, and W. R. Deal, "Power amplification at 0.65 THz using InP HEMTs," *IEEE Trans. Microw. Theory Tech.*, vol. 60, no. 3, pp. 724–729, Mar. 2012.

[1-92] A. Zamora, K. M. K. H. Leong, G. Mei, *et al.*, "A high efficiency 670 GHz x36 InP HEMT multiplier chain," in *2017 IEEE MTT-S International Microwave Symposium (IMS)*, IEEE, Jun. 2017, pp. 977–979.

[1-93] K. M. K. H. Leong, X. Mei, W. H. Yoshida, *et al.*, "850 GHz receiver and transmitter front-ends using InP HEMT," *IEEE Trans. Terahertz Sci. Technol.*, vol. 7, no. 4, pp. 466–475, Jul. 2017.

[1-94] J. Ward, E. Schlecht, G. Chattopadhyay, *et al.*, "Capability of THz sources based on schottky diode frequency multiplier chains," in *2004 IEEE MTT-S International Microwave Symposium Digest (IEEE Cat. No.04CH37535)*, vol. 3, IEEE, 2004, 1587–1590 Vol.3.

[1-95] A. Maestrini, B. Thomas, H. Wang, *et al.*, "Schottky diode-based terahertz frequency multipliers and mixers," *Comptes Rendus Physique*, vol. 11, no. 7-8, pp. 480–495, 2010.

[1-96] I. Mehdi, J. V. Siles, C. Lee, and E. Schlecht, "THz diode technology: Status, prospects, and applications," *Proceedings of the IEEE*, vol. 105, no. 6, pp. 990–1007, 2017.

[1-97] D. T. Young and J. C. Irvin, "Millimeter frequency conversion using Au-n-type GaAs Schottky barrier epitaxial diodes with a novel contacting technique," *Proc. IEEE Inst. Electr. Electron. Eng.*, vol. 53, no. 12, pp. 2130–2131, 1965.

[1-98] J. W. Archer, R. A. Batchelor, and C. J. Smith, "Low-parasitic, planar schottky diodes for millimeter-wave integrated circuits," *IEEE Trans. Microw. Theory Tech.*, vol. 38, no. 1, pp. 15–22, 1990.

[1-99] *Custom transmitters/sources (AMC and Tx)*, https://www.vadiodes.com/en/products/custom-transmitters, Accessed: 2024-12-20.

[1-100] J. Siles, K. Cooper, C. Lee, R. Lin, G. Chattopadhyay, and I. Mehdi, "A new generation of room-temperature frequency-multiplied sources with up to 10× higher output power in the 160-GHz–1.6-THz range," *IEEE Trans. Terahertz Sci. Technol.*, vol. 8, no. 6, pp. 596–604, Oct. 2018.

[1-101] A.-Y. Tang, "Modelling and characterisation of terahertz planar schottky diodes," en, Ph.D. dissertation, Chalmers Tekniska Hogskola (Sweden), Ann Arbor, United States, 2013.

[1-102] G. P. Agrawal and N. K. Dutta, *Semiconductor lasers*, en, 2nd ed. New York, NY: Springer, Nov. 2013.

[1-103] J. Faist, F. Capasso, D. L. Sivco, C. Sirtori, A. L. Hutchinson, and A. Y. Cho, "Quantum cascade laser," en, *Science*, vol. 264, no. 5158, pp. 553–556, Apr. 1994.

[1-104] R. Köhler, A. Tredicucci, F. Beltram, *et al.*, "Terahertz semiconductor-heterostructure laser," en, *Nature*, vol. 417, no. 6885, pp. 156–159, May 2002.

[1-105] B. Williams, "Terahertz quantum-cascade lasers," *Nature photonics*, 2007.

[1-106] L. Li, L. Chen, J. Zhu, *et al.*, "Terahertz quantum cascade lasers with >1 W output powers," en, *Electron. Lett.*, vol. 50, no. 4, pp. 309–311, Feb. 2014.

[1-107] M. S. Vitiello and A. Tredicucci, "Physics and technology of terahertz quantum cascade lasers," en, *Adv. Phys. X.*, vol. 6, no. 1, p. 1 893 809, Jan. 2021.

[1-108] H.-G. Bach, "Ultrafast waveguide-integrated pin-photodiodes and photonic mixers from GHz to THz range," in *33rd European Conference and Exhibition on Optical Communication - ECOC 2007*, IEE, 2007, pp. 1–4.

[1-109] E. S. Lee, N. Kim, S.-P. Han, *et al.*, "SOA-integrated dual-mode laser and a PIN-photodiode for compact CW terahertz system," *ETRI J.*, Mar. 2016.

[1-110] M. Ali, L. E. G. Munoz, G. Carpintero, S. Nellen, and B. Globisch, "Millimetre-wave photonic emitter integrating a PIN-PD and planar high gain antenna," in *2020 Third International Workshop on Mobile Terahertz Systems (IWMTS)*, IEEE, Jul. 2020, pp. 1–5.

[1-111] J. Zhang, J. Zhang, Q. Wang, *et al.*, "Experimental comparison of commercial PIN-PD and UTC-PD for THz power and transmission performance in the 370GHz-430GHz," in *2023 Opto-Electronics and Communications Conference (OECC)*, IEEE, Jul. 2023, pp. 1–4.

[1-112] M. Deumer, S. Nellen, S. Lauck, *et al.*, "Ultra-wideband PIN-PD THz emitter with > 5.5 THz bandwidth," en, *J. Infrared Millim. Terahertz Waves*, vol. 45, no. 9-10, pp. 831–840, Oct. 2024.

[1-113] T. Ishibashi, N. Shimizu, S. Kodama, H. Ito, T. Nagatsuma, and T. Furuta, "Uni-traveling-carrier photodiodes," in *Ultrafast Electronics and Optoelectronics*, Optica Publishing Group, Mar. 1997, UC3.

[1-114] T. Ishibashi, S. Kodama, N. S. N. Shimizu, and T. F. T. Furuta, "High-speed response of uni-traveling-carrier photodiodes," *Japanese journal of applied physics*, vol. 36, no. 10R, p. 6263, 1997.

[1-115] S. Adachi, *Physical Properties of III-V Semiconductor Compounds*, en. John Wiley & Sons, Nov. 1992.

[1-116] C. C. Renaud, D. Moodie, M. Robertson, and A. J. Seeds, "High output power at 110 GHz with a waveguide uni-travelling carrier photodiode," in *LEOS 2007 - IEEE Lasers and Electro-Optics Society Annual Meeting Conference Proceedings*, Oct. 2007, pp. 782–783.

[1-117] E. Rouvalis, C. C. Renaud, D. G. Moodie, M. J. Robertson, and A. J. Seeds, "Traveling-wave uni-traveling carrier photodiodes for continuous wave THz generation," en, *Opt. Express*, vol. 18, no. 11, pp. 11 105–11 110, May 2010.

[1-118] H. Ito, T. Ohno, H. Fishimi, T. Furuta, S. Kodama, and T. Ishibashi, "60 GHz high output power uni-travelling-carrier photodiodes with integrated bias circuit," *Electronics Letters*, vol. 36, no. 8, p. 747, 2000.

[1-119] H. Ito, Y. Hirota, A. Hirata, T. Nagatsuma, and T. Ishibashi, "11 dBm photonic millimetre-wave generation at 100 GHz using uni-travelling-carrier photodiodes," *Electronics Letters*, vol. 37, no. 20, p. 1225, 2001.

[1-120] T. Nagatsuma, T. Ishibashi, A. Hirata, *et al.*, "Characterisation of uni-travelling-carrier photodiode monolithically integrated with matching circuit," en, *Electronics Letters; Stevenage*, vol. 37, no. 20, pp. 1–2, Sep. 2001.

[1-121] H. Ito, T. Nagatsuma, A. Hirata, *et al.*, "High-power photonic millimetre wave generation at 100 GHz using matching-circuit-integrated uni-travelling-carrier photodiodes," *IEE Proceedings - Optoelectronics*, vol. 150, no. 2, pp. 138–142, Apr. 2003.

[1-122] H. Ito, T. Furuta, Y. Hirota, *et al.*, "Photonic millimetre-wave emission at 300 GHz using an antenna-integrated uni-travelling-carrier photodiode," *Electronics Letters*, vol. 38, no. 17, p. 989, 2002.

[1-123] H. Ito and T. Ishibashi, "Photonic terahertz-wave generation using slot-antenna-integrated uni-traveling-carrier photodiodes," *IEEE J. Sel. Top. Quantum Electron.*, vol. 23, no. 4, pp. 1–7, Jul. 2017.

[1-124] C. C. Renaud, M. Natrella, C. Graham, J. Seddon, F. Van Dijk, and A. J. Seeds, "Antenna integrated THz uni-traveling carrier photodiodes," *IEEE J. Sel. Top. Quantum Electron.*, vol. 24, no. 2, pp. 1–11, Mar. 2018.

[1-125] J. P. Seddon, M. Natrella, X. Lin, C. Graham, C. C. Renaud, and A. J. Seeds, "Photodiodes for terahertz applications," *IEEE J. Sel. Top. Quantum Electron.*, vol. 28, no. 2, pp. 1–12, 2022.

[1-126] H. Ito, T. Furuta, Y. Muramoto, T. Ito, and T. Ishibashi, "Photonic millimetre- and sub-millimetre-wave generation using J-band rectangular-waveguide-output uni-travelling-carrier photodiode module," *Electronics Letters*, vol. 42, no. 24, p. 1424, 2006.

[1-127] H.-J. Song, K. Ajito, Y. Muramoto, A. Wakatsuki, T. Nagatsuma, and N. Kukutsu, "Uni-travelling-carrier photodiode module generating 300 GHz power greater than 1 mW," *IEEE Microwave Compon. Lett.*, vol. 22, no. 7, pp. 363–365, Jul. 2012.

[1-128] A. Beling, J. C. Campbell, K. Li, *et al.*, "High-power photodiodes for analog applications," in *Microwave Photonics (MWP) and the 2014 9th Asia-Pacific Microwave Photonics Conference (APMP) 2014 International Topical Meeting on*, Oct. 2014, pp. 412–414.

[1-129] G. Zhou, W. Ebert, S. Mutschall, *et al.*, "High-power waveguide integrated modified uni-traveling-carrier (UTC) photodiode with 5 dBm RF output power at 120 GHz," in *Optical Fiber Communication Conference*, Washington, D.C.: OSA, 2016.

[1-130] Q. Li, K. Li, Y. Fu, *et al.*, "High-power flip-chip bonded photodiode with 110 GHz bandwidth," *J. Lightwave Technol.*, vol. 34, no. 9, pp. 2139–2144, May 2016.

[1-131] P. Latzel, F. Pavanello, M. Billet, *et al.*, "Generation of mW level in the 300-GHz band using resonant-cavity-enhanced unitraveling carrier photodiodes," *IEEE Transactions on Terahertz Science and Technology*, vol. 7, no. 6, pp. 800–807, Nov. 2017.

[1-132] T. Ohara, T. Ishibashi, Y. Kawamoto, M. Tojo, K. Maekawa, and T. Nagatsuma, "2-mW-output power uni-traveling-carrier photodiodes in 300-GHz-band," in *2023 Asia-Pacific Microwave Conference (APMC)*, IEEE, Dec. 2023, pp. 676–678.

[1-133] E. Rouvalis, C. C. Renaud, D. G. Moodie, M. J. Robertson, and A. J. Seeds, "Continuous wave terahertz generation from ultra-fast InP-based photodiodes," *IEEE Trans. Microw. Theory Tech.*, vol. 60, no. 3, pp. 509–517, Mar. 2012.

[1-134] H. Eisele, A. Rydberg, and G. I. Haddad, "Recent advances in the performance of InP Gunn devices and GaAs TUNNETT diodes for the 100-300-GHz frequency range and above," *IEEE Trans. Microw. Theory Tech.*, vol. 48, no. 4, pp. 626–631, Apr. 2000.

[1-135] H. Eisele and R. Kamoua, "Submillimeter-wave InP Gunn devices," *IEEE Trans. Microw. Theory Tech.*, vol. 52, no. 10, pp. 2371–2378, Oct. 2004.

[1-136] H. Eisele, "480 GHz oscillator with an InP Gunn device," en, *Electron. Lett.*, vol. 46, no. 6, p. 422, 2010.

[1-137] H. Eisele and G. I. Haddad, "GaAs TUNNETT diodes on diamond heat sinks for 100 GHz and above," *IEEE Trans. Microw. Theory Tech.*, vol. 43, no. 1, pp. 210–213, 1995.

[1-138] P. Plotka, J. Nishizawa, T. Kurabayashi, and H. Makabe, "240-325-GHz GaAs CW fundamental-mode TUNNETT diodes fabricated with molecular layer epitaxy," *IEEE Trans. Electron Devices*, vol. 50, no. 4, pp. 867–873, Apr. 2003.

[1-139] A. Al-Khalidi, K. H. Alharbi, J. Wang, *et al.*, "Resonant tunneling diode terahertz sources with up to 1 mW output power in the *J*-band," *IEEE Trans. Terahertz Sci. Technol.*, vol. 10, no. 2, pp. 150–157, Mar. 2020.

[1-140] T. Ishibashi and M. Ohmori, "200-GHz 50-mW CW oscillation with silicon SDR IMPATT (short papers)," *IEEE Trans. Microw. Theory Tech.*, vol. 24, no. 11, pp. 858–859, Nov. 1976.

[1-141] M. Wollitzer, J. Buechler, F. Schäffler, and J.-F. Luy, "D-band Si-IMPATT diodes with 300 mW CW output power at 140 GHz," en, *Electron. Lett.*, vol. 32, no. 2, p. 122, 1996.

[1-142] S. Jameson, E. Halpern, and E. Socher, "20.4 a 300GHz wirelessly locked 2×3 array radiating 5.4dBm with 5.1% DC-to-RF efficiency in 65nm CMOS," in *2016 IEEE International Solid-State Circuits Conference (ISSCC)*, IEEE, Jan. 2016, pp. 348–349.

[1-143] I. Momson, S. Lee, S. Dong, and K. O. Kenneth, "425-to-25-GHz CMOS-integrated downconverter," *IEEE Solid-state Circuits Lett.*, vol. 4, pp. 80–83, 2021.

[1-144] A. Standaert and P. Reynaert, "A 400-GHz 28-nm TX and RX with chip-to-waveguide transitions used in fully integrated lensless imaging system," *IEEE Trans. Terahertz Sci. Technol.*, vol. 9, no. 4, pp. 373–382, Jul. 2019.

[1-145] H. S. Son, J. Y. Jang, D. M. Kang, H. J. Lee, and C. S. Park, "A 109 GHz CMOS power amplifier with 15.2 dBm Psat and 20.3 dB gain in 65-nm CMOS technology," *IEEE Microw. Wirel. Compon. Lett.*, vol. 26, no. 7, pp. 510–512, Jul. 2016.

[1-146] S. Kumar, B. Williams, Q. Hu, and J. Reno, "1.9 THz quantum-cascade lasers with one-well injector," *Applied Physics Letters*, vol. 88, p. 121 123, Mar. 2006.

[1-147] B. S. Williams, S. Kumar, Q. Hu, and J. L. Reno, "High-power terahertz quantum cascade lasers," in *2006 Conference on Lasers and Electro-Optics and 2006 Quantum Electronics and Laser Science Conference*, IEEE, 2006, pp. 1–2.

[1-148] C. Worrall, J. Alton, M. Houghton, *et al.*, "Continuous wave operation of a superlattice quantum cascade laser emitting at 2 THz," en, *Opt. Express*, vol. 14, no. 1, pp. 171–181, Jan. 2006.

[1-149] C. Walther, M. Fischer, G. Scalari, R. Terazzi, N. Hoyler, and J. Faist, "Quantum cascade lasers operating from 1.2 to 1.6 THz," en, *Appl. Phys. Lett.*, vol. 91, no. 13, p. 131 122, Sep. 2007.

[1-150] X. Wang, C. Shen, T. Jiang, *et al.*, "High-power terahertz quantum cascade lasers with 0.23 W in continuous wave mode," *AIP Advances*, vol. 6, p. 075 210, Jul. 2016.

[1-151] H.-W. Hubers, "Terahertz heterodyne receivers," *IEEE J. Sel. Top. Quantum Electron.*, vol. 14, no. 2, pp. 378–391, Mar. 2008.

[1-152] K. H. Gundlach and M. Schicke, "SIS and bolometer mixers for terahertz frequencies," en, *Supercond. Sci. Technol.*, vol. 13, no. 12, R171, Dec. 2000.

[1-153] J. Zmuidzinas and P. L. Richards, "Superconducting detectors and mixers for millimeter and submillimeter astrophysics," *Proc. IEEE Inst. Electr. Electron. Eng.*, vol. 92, no. 10, pp. 1597–1616, Oct. 2004.

[1-154] A. Karpov, J. Blondel, M. Voss, and K.-H. Gundlach, "A three photon noise SIS heterodyne receiver at submillimeter wavelength," *IEEE Trans. Appl. Supercond.*, vol. 9, no. 2, pp. 4456–4459, Jun. 1999.

[1-155] J. W. Kooi, "A low noise NbTiN-based 850 GHz SIS receiver for the caltech submillimeter observatory," *Int. J. Infrared Millimeter Waves*, vol. 21, no. 9, pp. 1357–1373, 2000.

[1-156] S. V. Shitov, B. D. Jackson, A. M. Baryshev, *et al.*, "A low-noise double-dipole antenna SIS mixer at 1 THz," en, *Physica C Supercond.*, vol. 372-376, pp. 374–377, Aug. 2002.

[1-157] A. Karpov, D. Miller, F. Rice, *et al.*, "Low noise 1 THz–1.4 THz mixers using nb/al-AlN/NbTiN SIS junctions," *IEEE Trans. Appl. Supercond.*, vol. 17, no. 2, pp. 343–346, Jun. 2007.

[1-158] D. Meledin, A. Pavolotsky, V. Desmaris, *et al.*, "A 1.3-THz balanced waveguide HEB mixer for the APEX telescope," *IEEE Trans. Microw. Theory Tech.*, vol. 57, no. 1, pp. 89–98, Jan. 2009.

[1-159] T. Phillips and K. B. Jefferts, "A low temperature bolometer heterodyne receiver for millimeter wave astronomy," *Review of Scientific Instruments*, vol. 44, pp. 1009–1014, Aug. 1973.

[1-160] L. Jiang, S. Shiba, K. Shimbo, *et al.*, "Development of THz waveguide NbTiN HEB mixers," *IEEE Trans. Appl. Supercond.*, vol. 19, no. 3, pp. 301–304, Jun. 2009.

[1-161] W. Zhang, P. Khosropanah, J. R. Gao, *et al.*, "Quantum noise in a terahertz hot electron bolometer mixer," *Appl. Phys. Lett.*, vol. 96, no. 11, p. 111 113, Mar. 2010.

[1-162] F. Rodriguez-Morales, K. S. Yngvesson, and D. Gu, "Wideband IF-integrated terahertz HEB mixers: Modeling and characterization," *IEEE Trans. Microw. Theory Tech.*, vol. 58, no. 5, pp. 1140–1150, May 2010.

[1-163] I. Tretyakov, S. Ryabchun, M. Finkel, *et al.*, "Low noise and wide bandwidth of NbN hot-electron bolometer mixers," *Appl. Phys. Lett.*, vol. 98, no. 3, p. 033 507, Jan. 2011.

[1-164] F. Boussaha, J. Kawamura, J. Stern, and C. Jung-Kubiak, "2.7 THz balanced waveguide HEB mixer," *IEEE Trans. Terahertz Sci. Technol.*, vol. 4, no. 5, pp. 545–551, Sep. 2014.

[1-165] S. A. Maas, *Microwave mixers*. ui.adsabs.harvard.edu, Jan. 1986.

[1-166] S. A. Maas, *Nonlinear microwave and RF circuits*, en, 2nd ed. Norwood, MA: Artech House, Jan. 2003.

[1-167] J. R. Waldrop, "Electrical properties of ideal metal contacts to GaAs: Schottky-barrier height," en, *J. Vac. Sci. Technol. B Microelectron. Nanometer Struct. Process. Meas. Phenom.*, vol. 2, no. 3, pp. 445–448, Jul. 1984.

[1-168] J. Treuttel, L. Gatilova, A. Maestrini, *et al.*, "A 520–620-GHz Schottky receiver front-end for planetary science and remote sensing with 1070 K–1500 K DSB noise temperature at room temperature," *IEEE Transactions on Terahertz Science and Technology*, vol. 6, no. 1, pp. 148–155, Jan. 2016.

[1-169] A. E. Maestrini, J. V. Siles, C. Lee, R. Lin, and I. Mehdi, "A 2 THz room temperature bias-able Schottky mixer," *IEEE Transactions on Terahertz Science and Technology*, vol. 15, no. 2, pp. 169–180, 2025.

[1-170] P. H. Siegel, R. J. Dengler, I. Mehdi, *et al.*, "Measurements on a 215-GHz subharmonically pumped waveguide mixer using planar back-to-back air-bridge Schottky diodes," *IEEE Trans. Microw. Theory Tech.*, vol. 41, no. 11, pp. 1913–1921, Nov. 1993.

[1-171] W. Y. Ali-Ahmad, W. L. Bishop, T. W. Crowe, and G. M. Rebeiz, "A submillimeter-wave planar low noise Schottky receiver," in *1993 IEEE MTT-S International Microwave Symposium Digest*, ieeexplore.ieee.org, Jun. 1993, 527–530 vol.2.

[1-172] B. Thomas, A. Maestrini, and G. Beaudin, "A low-noise fixed-tuned 300-360-GHz sub-harmonic mixer using planar Schottky diodes," *IEEE Microw. Wirel. Compon. Lett.*, vol. 15, no. 12, pp. 865–867, Dec. 2005.

[1-173] T. Newman and K. T. Ng, "A submillimeter-wave planar diode mixer-design and evaluation," in *1991 IEEE MTT-S International Microwave Symposium Digest*, ieeexplore.ieee.org, Jul. 1991, 1293–1296 vol.3.

[1-174] B. Thomas, B. Alderman, D. Matheson, and P. de Maagt, "A combined 380 GHz mixer/doubler circuit based on planar Schottky diodes," *IEEE Microwave Compon. Lett.*, vol. 18, no. 5, pp. 353–355, May 2008.

[1-175] T. W. Crowe and R. M. Weikle, Eds., *A Fixed-Tuned 400 GHz Subharmonic Mixer Using Planar Schottky Diodes*, Tenth International Symposium on Space Terahertz Technology, ui.adsabs.harvard.edu, Mar. 1999.

[1-176] E. T. Schlecht, J. J. Gill, R. H. Lin, R. J. Dengler, and I. Mehdi, "A 520–590 GHz crossbar balanced fundamental Schottky mixer," *IEEE Microwave Compon. Lett.*, vol. 20, no. 7, pp. 387–389, Jul. 2010.

[1-177] B. Thomas, A. Maestrini, J. Gill, *et al.*, "A broadband 835–900-GHz fundamental balanced mixer based on monolithic GaAs membrane Schottky diodes," *IEEE Trans. Microw. Theory Tech.*, vol. 58, no. 7, pp. 1917–1924, Jul. 2010.

[1-178] E. Schlecht, J. V. Siles, C. Lee, *et al.*, "Schottky diode based 1.2 THz receivers operating at room-temperature and below for planetary atmospheric sounding," *IEEE Trans. Terahertz Sci. Technol.*, vol. 4, no. 6, pp. 661–669, Nov. 2014.

[1-179] N. R. Erickson and T. M. Goyette, "Terahertz Schottky-diode balanced mixers," en, in *Terahertz Technology and Applications II*, vol. 7215, SPIE, Feb. 2009, pp. 41–45.

[1-180] P. H. Siegel, R. P. Smith, M. C. Graidis, and S. C. Martin, "2.5-THz GaAs monolithic membrane-diode mixer," *IEEE Trans. Microw. Theory Tech.*, vol. 47, no. 5, pp. 596–604, May 1999.

[1-181] G. Y. Robinson, "Schottky diodes and Ohmic contacts for the III-V semiconductors," in *Physics and Chemistry of III-V Compound Semiconductor Interfaces*, C. W. Wilmsen, Ed., Boston, MA: Springer US, 1985, pp. 73–163.

[1-182] E. H. Rhoderick and R. H. Williams, *Metal-semiconductor Contacts*, en. Clarendon Press, 1988.

[1-183] H. Ito, F. Nakajima, T. Ohno, T. Furuta, T. Nagatsuma, and T. Ishibashi, "InP-based planar-antenna-integrated Schottky-barrier diode for millimeter- and submillimeter-wave detection," en, *Jpn. J. Appl. Phys.*, vol. 47, no. 8R, p. 6256, Aug. 2008.

[1-184] Z. Pang, "Schottky contacts to indium phosphide and their applications," Ph.D. dissertation, McMaster University, 1997.

[1-185] Z. J. Horvath, V. Rakovics, B. Szentpali, S. Puspoki, and K. Zdansky, "InP Schottky junctions for zero bias detector diodes," *Vacuum*, vol. 71, no. 1, pp. 113–116, May 2003.

[1-186] S. Khanal, T. Kiuru, M. Hoefle, *et al.*, "Characterisation of low-barrier Schottky diodes for millimeter wave mixer applications," in *2016 Global Symposium on Millimeter Waves (GSMM) & ESA Workshop on Millimetre-Wave Technology and Applications*, IEEE, Jun. 2016, pp. 1–4.

[1-187] U. Bhapkar, T. Brennan, and R. Mattauch, "InGaAs Schottky barrier mixer diodes for minimum conversion loss and low lo power requirements at terahertz frequencies," in *Second International Symposium on Space Terahertz Technology*, 1991, pp. 371–388.

[1-188] P. Marsh, D. Pavlidis, and K. Hong, "MOVPE-grown millimeter-wave InGaAs mixer diode technology and characteristics," *IEEE Trans. Electron Devices*, vol. 44, no. 7, pp. 1066–1075, Jul. 1997.

[1-189] I. Oprea, A. Walber, O. Cojocari, H. Gibson, R. Zimmermann, and H. L. Hartnagel, "183 GHz mixer on InGaAs Schottky diodes," en, *21st International Symposium on Space Terahertz Technology*, 2010.

[1-190] D. Pardo, H. Wang, H. Sanghera, *et al.*, "Ingaas Schottky technology for thz mixers," in *Proceedings of the 28th International Symposium*, 2017.

[1-191] J. Martinez Gil, D. Moro-Melgar, A. Negrus, I. Oprea, and O. Cojocari, "Efficiency assessment of traditional GaAs and low-power InGaAs Schottky diodes in full-band mixers at 0.3 THz," en, *Electronics*, vol. 12, no. 21, p. 4518, Nov. 2023.

[1-192] H. Ito and T. Ishibashi, "InP/InGaAs Fermi-level managed barrier diode for broadband and low-noise terahertz-wave detection," en, *Jpn. J. Appl. Phys.*, vol. 56, no. 1, p. 014 101, Dec. 2016.

[1-193] T. Nagatsuma, M. Sonoda, T. Higashimoto, R. Kimura, L. Yi, and H. Ito, "300-GHz-band wireless communication using Fermi-level managed barrier diode receiver," in *2019 IEEE MTT-S International Microwave Symposium (IMS)*, Jun. 2019, pp. 762–765.

[1-194] H. Ito and T. Ishibashi, "Highly sensitive terahertz-wave detection by Fermi-level managed barrier diode," en, in *Optical Sensing, Imaging, and Photon Counting: From X-Rays to THz 2019*, vol. 11088, SPIE, Sep. 2019, pp. 15–22.

[1-195] T. Nagatsuma, F. Ayano, K. Toichi, *et al.*, "Wireless communication using Fermi-level-managed barrier diode receiver with J-band waveguide-input port," in *2020 IEEE/MTT-S International Microwave Symposium (IMS)*, Aug. 2020, pp. 631–634.

[1-196] H. Ito and T. Ishibashi, "Low-noise sub-harmonic-mixing in 300-GHz band by Fermi-level managed barrier diode," en, *Appl. Phys. Express*, vol. 14, no. 10, p. 104 001, Sep. 2021.

[1-197] H. Ito and T. Ishibashi, "Low-noise terahertz-wave detection by Fermi-level managed barrier diode," en, in *Terahertz Emitters, Receivers, and Applications XIII*, vol. 12230, SPIE, Sep. 2022, pp. 8–19.

[1-198] H. Ito, Y. Kawamoto, T. Ohara, T. Nagatsuma, and T. Ishibashi, "Low-noise balanced mixer for 300-GHz band based on Fermi-level managed barrier diode on SiC platform," *IEICE Electronics Express*, vol. 20, no. 21, pp. 20 230 395–20 230 395, 2023.

[1-199] D. Kissinger, G. Kahmen, and R. Weigel, "Millimeter-wave and terahertz transceivers in SiGe BiCMOS technologies," *IEEE Trans. Microw. Theory Tech.*, vol. 69, no. 10, pp. 4541–4560, Oct. 2021.

[1-200] C. Wang, B. Perkins, Z. Wang, and R. Han, "Molecular detection for unconcentrated gas with ppm sensitivity using 220-to-320-GHz dual-frequency-comb spectrometer in CMOS," en, *IEEE Trans. Biomed. Circuits Syst.*, vol. 12, no. 3, pp. 709–721, Jun. 2018.

[1-201] W. Choi, Z. Ahmad, A. Jha, J.-Y. Lee, I. Kim, and K. O. Kenneth, "410-GHz CMOS imager using a 4^{th} sub-harmonic mixer with effective NEP of 0.3 fW/Hz$^{0.5}$ at 1-kHz noise bandwidth," in *2015 Symposium on VLSI Circuits (VLSI Circuits)*, IEEE, Jun. 2015, pp. C302–C303.

[1-202] J. Zhou and X. Luo, "An 820-GHz down-converter with fourth subharmonic mixer in 40-nm CMOS technology," *IEEE Microwave Compon. Lett.*, vol. 31, no. 10, pp. 1146–1149, Oct. 2021.

[1-203] S. Shiba, Y. Irimajiri, T. Yamakura, *et al.*, "3.1-THz heterodyne receiver using an NbTiN hot-electron bolometer mixer and a quantum cascade laser," *IEEE Trans. Terahertz Sci. Technol.*, vol. 2, no. 1, pp. 22–28, Jan. 2012.

[1-204] D. Buchel, P. Putz, K. Jacobs, *et al.*, "4.7-THz superconducting hot electron bolometer waveguide mixer," *IEEE Trans. Terahertz Sci. Technol.*, vol. 5, no. 2, pp. 207–214, Mar. 2015.

[1-205] Y. Irimajiri, A. Kawakami, I. Morohashi, *et al.*, "Development of a superconducting low-noise 3.1-THz hot electron bolometer receiver," *IEEE Trans. Terahertz Sci. Technol.*, vol. 5, no. 6, pp. 1154–1159, Nov. 2015.

[1-206] S. Krause, D. Meledin, V. Desmaris, A. Pavolotsky, H. Rashid, and V. Belitsky, "Noise and IF gain bandwidth of a balanced waveguide NbN/GaN hot electron bolometer mixer operating at 1.3 THz," *IEEE Trans. Terahertz Sci. Technol.*, vol. 8, no. 3, pp. 365–371, May 2018.

[1-207] Y. C. Shen, P. C. Upadhya, H. E. Beere, *et al.*, "Generation and detection of ultrabroadband terahertz radiation using photoconductive emitters and receivers," en, *Appl. Phys. Lett.*, vol. 85, no. 2, pp. 164–166, Jul. 2004.

[1-208] E. Castro-Camus and M. Alfaro, "Photoconductive devices for terahertz pulsed spectroscopy: A review [invited]," *Photon. Res., PRJ*, vol. 4, no. 3, A36–A42, Jun. 2016.

[1-209] E. Peytavit, F. Pavanello, G. Ducournau, and J.-F. Lampin, "Highly efficient terahertz detection by optical mixing in a GaAs photoconductor," *Appl. Phys. Lett.*, vol. 103, no. 20, p. 201 107, 2013.

[1-210] C. Tannoury, V. Merupo, G. Di Gioia, *et al.*, "Photonic THz mixers based on iron-doped InGaAs embedded in a plasmonic microcavity," *APL Photonics*, vol. 8, p. 116 101, Nov. 2023.

[1-211] S. Hisatake, G. Kitahara, K. Ajito, Y. Fukada, N. Yoshimoto, and T. Nagatsuma, "Phase-sensitive terahertz self-heterodyne system based on photodiode and low-temperature-grown GaAs photoconductor at 1.55 μm," *IEEE Sensors Journal*, vol. 13, no. 1, pp. 31–36, 2013.

[1-212] M. Deumer, S. Breuer, R. Kohlhaas, *et al.*, "Continuous wave terahertz receivers with 4.5 THz bandwidth and 112 dB dynamic range," en, *Opt. Express*, vol. 29, no. 25, pp. 41 819–41 826, Dec. 2021.

[1-213] S. Hisatake, J.-Y. Kim, K. Ajito, and T. Nagatsuma, "Self-heterodyne spectrometer using uni-traveling-carrier photodiodes for terahertz-wave generators and optoelectronic mixers," *J. Lightwave Technol.*, vol. 32, no. 20, pp. 3683–3689, Oct. 2014.

[1-214] E. Rouvalis, M. J. Fice, C. C. Renaud, and A. J. Seeds, "Millimeter-wave optoelectronic mixers based on uni-traveling carrier photodiodes," *IEEE Trans. Microw. Theory Tech.*, vol. 60, no. 3, pp. 686–691, Mar. 2012.

[1-215] X. Mao, C. Cheng, B. Huang, *et al.*, "Optoelectronic mixer based on graphene FET," *IEEE Electron Device Lett.*, vol. 36, no. 3, pp. 253–255, Mar. 2015.

[1-216] L. Hamidouche, A. Montanaro, M. Rosticher, *et al.*, "Optoelectronic mixing in high-mobility graphene," *ACS Photonics*, vol. 8, no. 1, pp. 369–375, Jan. 2021.

[1-217] A. Montanaro, G. Piccinini, V. Mišeikis, *et al.*, "Sub-THz wireless transmission based on graphene-integrated optoelectronic mixer," en, *Nat. Commun.*, vol. 14, no. 1, pp. 1–14, Oct. 2023.

[1-218] P. G. Huggard, B. N. Ellison, B. Alderman, *et al.*, "1.55 μm photomixer sources for mm-wave heterodyne detection and frequency conversion with Schottky diodes," in *Digest of the LEOS Summer Topical Meetings, 2005.*, IEEE, Jul. 2005, pp. 105–106.

Chapter 2

Theory and modelling

The key components of the optoelectronic receiver concept targeted in this thesis are (1) the Schottky barrier diode, (2) the high-speed photodiode, and (3) the terahertz mixer integrating these two. In this chapter, the theoretical fundamentals and modelling approaches used for these components are introduced, while more details are given in the next chapters. These are used ultimately to design the optoelectronic receiver and to predict the overall receiver performance. Figure 2.1 summarises of the modelling and simulation process followed in this work.

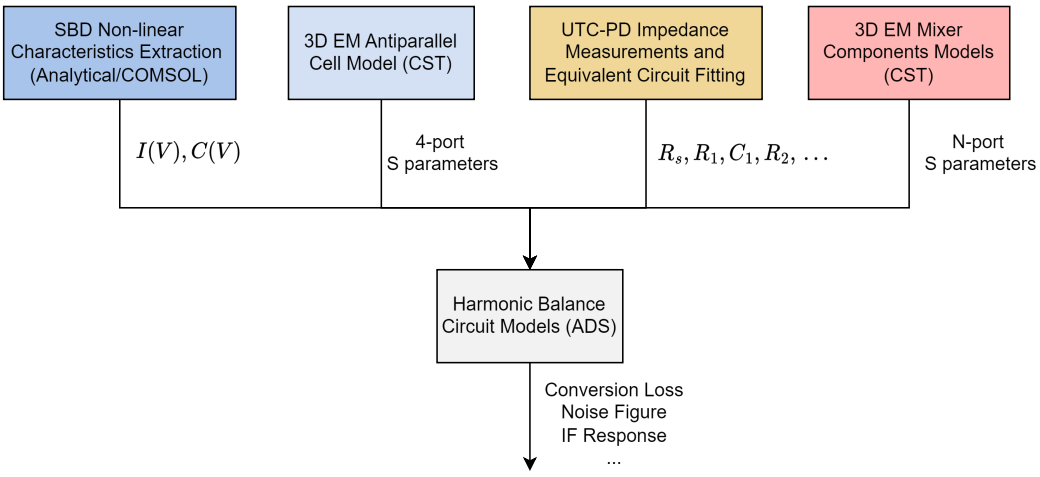

Figure 2.1: Summary of the modelling and simulation process to predict performance and design the optoelectronic receiver.

2.1 THz Schottky barrier diodes

2.1.1 Schottky barrier physics

The non-linear properties of the Schottky diode emerge from the metal-semiconductor contact physics. Figure 2.2 illustrates the energy diagrams of a Schottky contact, specifically for an n-type semiconductor. In these diagrams, E_0, E_C, E_V, and E_F correspond to the free-space, conduction band, valence band, and Fermi-level energies respectively.

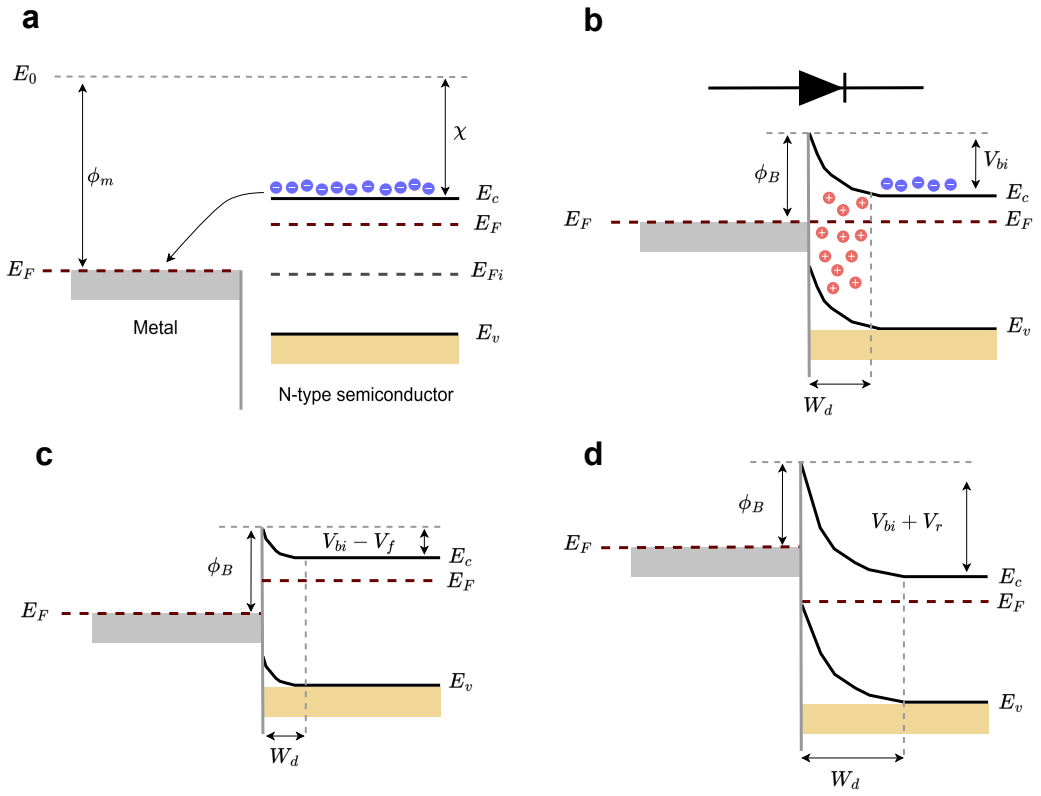

Figure 2.2: Schottky barrier contact physics described by energy diagrams with an n-type semiconductor. **a** Before making contact. **b** After making contact without applying bias. **c** Under forward bias. **d** Under reverse bias.

Prior to contact, there is a difference in the Fermi level energies which is determined by the metal workfunction ϕ_m and the semiconductor electron affinity χ (Figure 2.2**a**). These parameters represent the energy required to remove an electron from the metal or semiconductor conduction band to free space [2-1], [2-2]. When the contact is made (Figure 2.2**b**), higher energy electrons in the conduction band migrate into the metal until equilibrium is reached, aligning the Fermi levels

on both sides. Consequently, a potential barrier ϕ_B from metal to semiconductor is formed which is equal to

$$\phi_B = \phi_m - \chi \tag{2.1}$$

This is known as the Schottky-Mott rule [2-3], [2-4], which is frequently not observed in many metal-semiconductor systems. This discrepancy is primarily attributed to surface states in the semiconductor, which result in Fermi-level pinning, making the Schottky barrier height independent of the metal workfunction [2-5], [2-6]. The barrier formation chemistry of Schottky contacts is a complex process that is still not fully understood [2-7], and the barrier of a particular metal-semiconductor system is often determined by experimental data. The barrier height seen from the semiconductor is typically denoted as the built-in potential V_{bi}, which is equal to

$$V_{bi} = \phi_B - (E_C - E_F) \tag{2.2}$$

Due to electron migration, a region with positively charged ions is created in the semiconductor, typically denoted as the depletion region. Using the abrupt depletion approximation, the width of the depletion region W_d is given by [2-8]

$$W_{d0} = \sqrt{\frac{2\varepsilon_0 \varepsilon_r V_{bi}}{qN_d}} \tag{2.3}$$

where ε_0, ε_r, q, and N_d are the vacuum permittivity, relative permittivity, electron charge, and semiconductor doping respectively. The base energy diagram of a Schottky contact is perturbed when an external voltage is applied to the junction. Under an applied voltage (Figure 2.2**c**) the barrier seen from the semiconductor and the depletion region width can be adjusted. Electrons can only flow freely when the potential barrier from the semiconductor is overcome under forward bias. Therefore, the Schottky contact has a rectifying behaviour allowing current to flow in one direction.

2.1.2 Conduction mechanisms

The main transport mechanism that governs current-voltage characteristics in a Schottky diode is thermionic emission through the barrier [2-9]. This refers to electrons that reach enough energy to overcome the potential barrier from the semiconductor to the metal. Since the current transport is dominated by electrons, the Schottky diode is referred to as a majority carrier device, not limited by hole transport. The thermionic emission theory [2-9] leads to the following expression for the junction current

$$I_j(V_j) = I_0 \left(e^{\frac{qV_j}{k_B T}} - 1 \right) \tag{2.4}$$

where V_j is the junction voltage, I_0 is the reverse saturation current, k_B is the Boltzmann's constant, T is the operation temperature. The reverse saturation current I_0 can be expressed as

$$I_0 = AA^* T^2 e^{\frac{-q\phi_B}{k_B T}} \tag{2.5}$$

where A is the Schottky contact area, and A^* is the Richardson's constant, which is material dependent [2-6], [2-10] and can be estimated by

$$A^* = \frac{4\pi m_n^* k_B^2 q}{h^3} \tag{2.6}$$

where m_n^* is the effective electron mass, and h is the Planck constant. The second most relevant transport mechanism in a Schottky diode is quantum-mechanical tunnelling through the barrier [2-11]–[2-13]. Electrons near the Fermi level in the semiconductor can tunnel through the potential barrier with a certain probability. This is also known as field emission effect and it is prominent at low temperatures and high doping levels [2-8]. As temperature is raised, more electrons have enough energy to go over the barrier (thermionic emission), making the tunnelling effect less significant [2-8]. Since this work focuses on room-temperature operation and the used semiconductor doping levels are low, tunnelling is not considered as a relevant mechanism and it is not included in the simulations. Tunnelling or other

effects deviating from ideal thermionic emission (Equation 2.4), are often included by adding an ideality factor η

$$I_j(V_j) = I_0 \left(e^{\frac{qV_j}{\eta k_B T}} - 1 \right) \tag{2.7}$$

Deviation from ideal behaviour may also result from image-force barrier lowering, recombination effects, or fabrication imperfections [2-1], [2-2], [2-7], [2-12], [2-14].

2.1.3 Equivalent circuit model

The general n-type Schottky diode structure is depicted in Figure 2.3**a**. It comprises the epitaxial layer or epilayer with a moderate doping level (typically $< 5 \cdot 10^{17} cm^{-3}$), a highly-doped buffer layer (typically $> 1 \cdot 10^{18} cm^{-3}$) for Ohmic contact and to prevent diffusion of impurities from the substrate [2-15], and a supporting substrate.

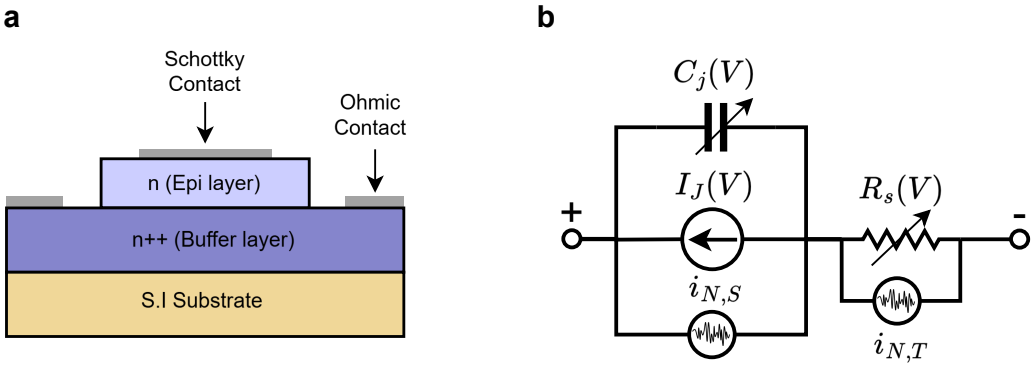

Figure 2.3: Circuit modelling of Schottky diodes. **a** General structure of an n-type Schottky diode. **b** Simple equivalent circuit model of a Schottky diode.

To model this structure electrically, a simple analytical lumped equivalent circuit is often used to implement the non-linear characteristics of the device [2-15]–[2-17]. Such a model is shown in Figure 2.4**b**, consisting of a voltage-dependent current source $I_j(V)$, a voltage-dependent capacitance $C_j(V)$, and a voltage-dependent series resistance $R_s(V)$. The current source corresponds to the junction current in Equation 2.7. Since there is a charge storage in the depletion region that changes with W_d, this effect can be essentially modelled as a voltage-

dependent capacitance. The expression of junction capacitance is obtained from the derivative of the charge in the depletion region [2-8], [2-15]

$$C_j(V_j) = \frac{C_{j0}}{\sqrt{1-\frac{V_j}{V_{bi}}}} \tag{2.8}$$

where C_{j0} is the capacitance at zero bias, given by

$$C_{j0} = A\sqrt{\frac{q\varepsilon_0\varepsilon_r N_d}{2V_{bi}}} \tag{2.9}$$

This formulation is only valid for a regime where $V_j < V_{bi}$ (flat-band). Beyond flat-band, where the depletion width is zero, the model is no longer applicable. In addition, the model assumes that the depletion width is smaller than the epilayer thickness. If the depletion width exceeds the epilayer thickness, the charge storage effect is influenced by the buffer layer, which has higher doping levels, leading to an increase in junction capacitance. This effect can be analytically modelled as described in [2-18].

$$C_j(V_j) = \begin{cases} A\sqrt{\frac{q\varepsilon_0\varepsilon_r N_d}{2}}\frac{1}{\sqrt{\frac{V_{bi}-V_j}{N_d}}} & \text{if } V_j > V_{dw} \\ A\sqrt{\frac{q\varepsilon_0\varepsilon_r N_d}{2}}\frac{1}{\sqrt{\frac{V_{bi}-V_{dw}}{N_d}+\frac{V_{dw}-V_j}{N_b}}} & \text{if } V_j < V_{dw} \end{cases} \tag{2.10}$$

where N_b is the buffer layer doping and V_{dw} is the voltage for which the depletion width equals the epilayer thickness. Note that the equation when $V_j < V_{dw}$ is the same as Equation 2.8. The series resistance, related to the power loss in the Schottky diode, has three main contributions: (1) the undepleted epilayer ($R_{s,epi}$), (2) the spreading resistance in the buffer layer ($R_{s,spr}$), and (3) the Ohmic contact ($R_{s,contact}$). The resistance from the undepleted epilayer can be approximated by

$$R_{s,epi}(V_j) = \frac{t_{epi} - W_d(V_j)}{A\sigma_{epi}} \tag{2.11}$$

where t_{epi} is the thickness of the epilayer, and σ_{epi} is the layer conductivity is given by

$$\sigma_{epi} = q\mu_{n,epi}N_d \tag{2.12}$$

where $\mu_{n,epi}$ is the low-field electron mobility of the epilayer. While this is a voltage-dependent quantity, the value of R_s when the epilayer is undepleted is typically considered. The spreading resistance in the buffer layer is intrinsically diode geometry-dependent [2-19]. Although analytical expressions exist for calculating this resistance, in this work, a physics-based model is used, as discussed later. Finally, the series resistance due to the Ohmic contact is given by

$$R_{s,contact} = \frac{\rho_{ohm}}{A_{ohm}} \tag{2.13}$$

where ρ_{ohm} is the specific contact resistivity (typically $< 10^{-6}\,\Omega \cdot cm^2$), and A_{ohm} is the area of the Ohmic contact. Due to the majority carrier nature of the Schottky diode, the current and capacitance change virtually instantaneously with an applied voltage (quasistatic assumption) [2-17]. Therefore, the DC expressions are valid even at several hundred GHz. The cut-off frequency, a commonly used figure of merit for evaluating the maximum frequency capabilities of the diode, is defined by

$$f_{3dB} = \frac{1}{2\pi R_s C_{j0}} \tag{2.14}$$

In this sense, the choice of material is crucial for achieving THz operation. Only materials with high electron mobility are suitable, as they allow for a small contact area, reducing capacitance while maintaining moderate series resistance. For this reason, III-V semiconductors like GaAs are employed in THz Schottky diodes [2-20]–[2-22].

2.1.4 Physics-based modelling

The analytical models described here present two main limitations: (1) they rely on abrupt approximations with limited accuracy, and (2) they fail to account for important effects at higher frequencies such as velocity saturation or non-local effects

such as velocity overshoot [2-23]–[2-25]. To overcome these, different physics-based models can be applied to Schottky diodes, which are generally based on solving the Boltzmann transport equation (BTE) [2-25]. The solution to the BTE consists of the distribution function of carriers $f(\vec{r},\vec{k},t)$, where $\vec{r}$ and $\vec{k}$ are position and momentum spaces. Obtaining an exact solution of the BTE exactly is highly complex. To solve this, the equation can be multiplied by weight functions and integrated over the momentum space, considering a finite number of moments [2-26], [2-27]. To address limitation (1) and obtain a more accurate I-V and C-V prediction, a 2D physics-based model is implemented in this work using the commercial drift-diffusion (DD) solver in the software COMSOL Multiphysics. This model is based on the Poisson's equation and the first two moments of the BTE [2-25]. Further details are provided in Appendix A.

2.1.5 Parasitics and embedding impedance

The models described so far address the intrinsic behaviour of the Schottky diode. To design Schottky-based THz receivers, paying attention to the parasitics and embedding impedance of the specific diode geometry is crucial for accurate modelling [2-28], [2-29]. In Figure 2.4, top and cross-section views of simplified planar air-bridged Schottky diodes are shown. This technology is well established due to its low parasitics and reliable fabrication when compared to whisker-type contact diodes [2-30], [2-31].

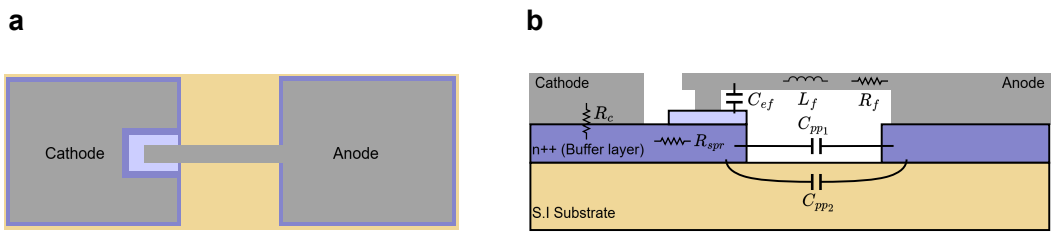

Figure 2.4: Planar air-bridged Schottky diodes. **a** Top view. **b** Cross-section with most relevant parasitics

In Figure 2.4**b**, the most relevant parasitics for this structure are displayed, including finger resistance and inductance (R_f and L_f), finger to epilayer capacitance (C_{ef}), pad-to-pad capacitance (C_{pp}), and high-frequency spreading resistance

(R_{spr}). These parasitics, along with the specific diode chip geometry, determine the embedding impedance of the diode. To account for this, a typical approach is to simulate the diode structure in a full-wave 3D EM simulator with appropriate material parameters (relative permittivity and conductivity) [2-28], [2-29]. In this work, we use CST Studio Suite for this purpose. By doing this, we can obtain the S-parameters of the specific designed structure which are then used in the mixer circuit design step.

2.1.6 Noise in Schottky diodes

Noise in Schottky diodes has been extensively studied [2-5], [2-32]–[2-36], with Shot and thermal (Johnson-Nyquist) being the two main mechanisms. Shot noise arises from random fluctuations of the electrons passing through the barrier, and the mean squared value of the current spectral density is given by [2-37]

$$\frac{\langle i_{N,S}^2 \rangle}{B} = 2qI \tag{2.15}$$

where I is the average current through the junction and B is the bandwidth. The thermal noise is also known as Johnson-Nyquist noise, and it originates from thermal agitations of the electric charges [2-38], [2-39]. In Schottky diodes this is associated to the series resistance, and the noise current spectral density can be modelled as [2-38]

$$\frac{\langle i_{N,T}^2 \rangle}{B} = \frac{4kT}{R_s} \tag{2.16}$$

These two contributions can be added to the Schottky diode circuit model as shown in Figure 2.3**b**. In addition to Shot and thermal noise mechanisms, the second most relevant noise contribution is the hot-electron noise, also referred as excess noise [2-40], [2-41]. This becomes relevant at high current densities or low temperatures, and will not be considered in the analysis.

This completes the modelling considerations for the Schottky diode part of the receiver design covering (1) non-linear I-V and C-V characteristics, (2) high-frequency diode chip parasitics and embedding impedance, and (3) diode noise contributions.

2.2 Uni-travelling-carrier photodiodes

2.2.1 Uni-travelling-carrier photodiode physics

The conventional p-i-n photodiode (PIN-PD) is the most commonly used photodiode structure, in which the intrinsic layer provides the function of both absorption of photons and collection of the generated electrical carriers [2-42], [2-43]. The basic energy band diagram is depicted in Figure 2.5**b**.

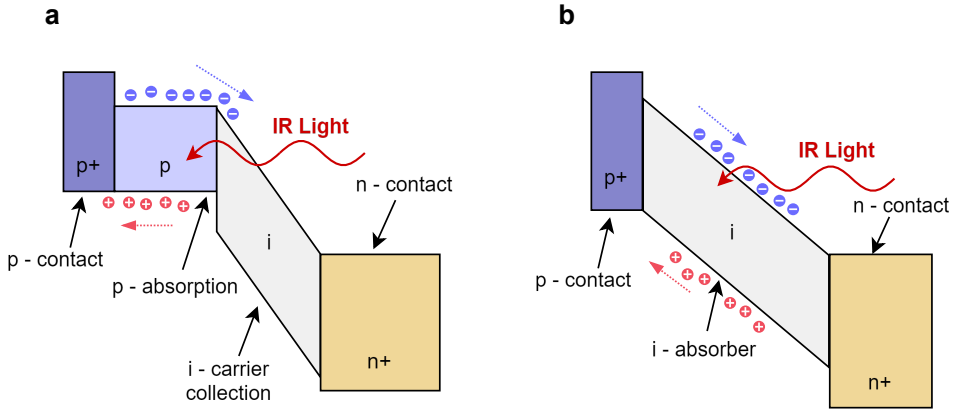

Figure 2.5: Energy band structure of **a** UTC-PDs and **b** p-i-n PDs.

Under reverse bias, photogenerated electrons and holes travel through the intrinsic layer to be collected by n-type and p-type sides respectively. This means that both carriers contribute to the overall device response. Due to the significantly lower hole mobility, which is about an order of magnitude lower than electrons, the hole transit time limits the maximum frequency of PIN-PD operation. Moreover, the band profile is altered under high-excitation conditions, as photogenerated carriers accumulate in the absorption layer. This reduction in the electric field significantly slows the carrier velocity, increases charge storage, and ultimately leads to saturation of the output current [2-44]. PIN-PD are strongly influenced by this effect due to the hole-limited carrier mobility.

These challenges can be mitigated by using the structure of a UTC-PD, depicted in Figure 2.5**a**. In contrast to the PIN-PD, the functions of absorption and carrier collection are separated in two layers [2-45]–[2-47]. A quasi-neutral p-type layer is used an as absorber, leading the photogenerated holes to contribute almost instantaneously to the device response, limited only by the dielectric relaxation time

[2-48]. Only electrons travel through the intrinsic carrier collection layer, which means that the UTC-PD can be treated as a majority carrier device. The consequence of this is that transit-time and space-charge effects previously discussed are now mitigated due to the faster carrier mobility of electrons. This makes the UTC-PD an excellent option to generate THz radiation, acting as a photomixer.

2.2.2 Photomixing in a photodiode

The concept of THz generation via optical heterodyning or photomixing in a photodiode is depicted in Figure 2.6.

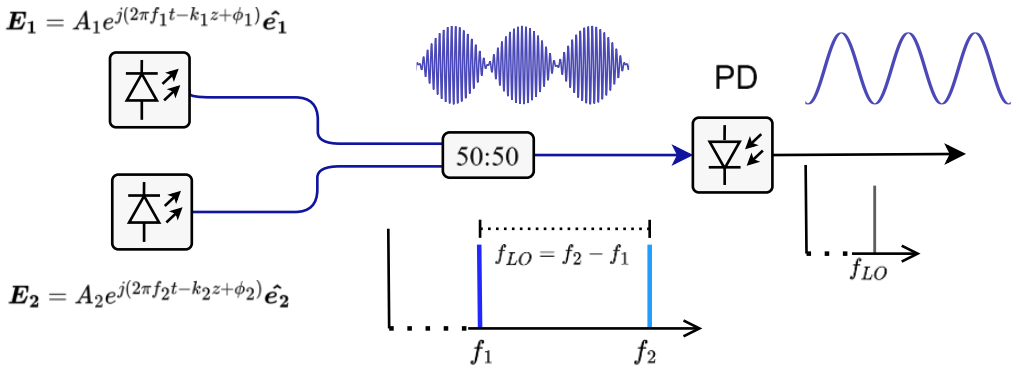

Figure 2.6: Illustration schematic of the concept of photomixing in a photodiode for THz generation.

To illustrate this process, we can consider two monochromatic optical waves at frequencies f_1 and f_2. For simplicity, we assume plane waves linearly polarised and propagating in the +z direction. The complex electrical field vectors E_1, E_2 can be written as [2-49]

$$E_1 = A_1 e^{j(2\pi f_1 t - k_1 z + \phi_1)} \hat{e_1} \tag{2.17}$$

$$E_2 = A_2 e^{j(2\pi f_2 t - k_2 z + \phi_2)} \hat{e_2} \tag{2.18}$$

Where A_1, A_2 are the field amplitudes, k_1 and k_2 the wave numbers, ϕ_1 and ϕ_2 the wave phases, and $\hat{e_1}$ and $\hat{e_2}$ the unitary vectors determining the field orientation. If the waves have the same polarization ($\hat{e_1} = \hat{e_2}$), the resulting electrical field when both waves are combined is $E_0 = E_1 + E_2$. The UTC-PD functions as a power

detector, so the output current is proportional to $|E_0|^2$. If the amplitudes of both waves are equal ($A_1 = A_2$), the output photocurrent I_{ph} for the conditions described above can be written as [2-49]

$$I_{ph} = 2s_{DC}P_{opt} + 2s_{fc}P_{opt}cos(2\pi f_c t + \Delta\phi) \tag{2.19}$$

where f_c is the separation given by $f_2 - f_1$, s_{DC} and s_{fc} are the responsivity of the UTC-PD at DC and high frequency respectively, $\Delta\phi$ is the phase difference given by $\phi_2 - \phi_1$, and P_{opt} is the optical wave power ($P_{opt} = P_1 = P_2$).

Beyond the current or power level, phase noise is a key parameter in optically generated THz signals. It arises from instabilities in the optical source and can be significant with free-running lasers. However, digital signal processing (DSP) techniques can mitigate this in THz links [2-50], and frequency-locked sources can achieve phase noise comparable to leading electronic sources [2-51]. In the context of this work, phase noise is not included in the modelling of the LO source.

2.2.3 Structure and equivalent circuit

In this work, the UTC-PD serves as the LO signal generator. In the context of the receiver design, which integrates the photodiode, the focus is on determining the device's impedance and assessing the power it can deliver to a specified load under a given driving photocurrent. For that purpose, a possible approach is to use an equivalent circuit [2-52] such as the one depicted in Figure 2.7.

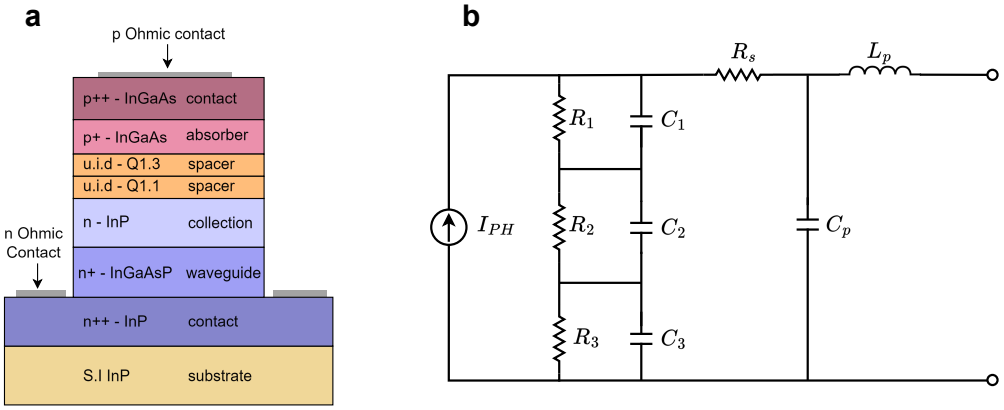

Figure 2.7: UTC-PDs. **a** Cross-section view of UCL's UTC-PDs with simplified structure. **b** Equivalent circuit to model the UTC-PD impedance at high frequencies.

To understand the equivalent circuit, the UTC-PD structure must be examined. UCL's UTC-PD simplified epitaxial structure is shown in Figure 2.7**a** [2-53]. The epitaxial structure is based on solid source molecular beam epitaxy (SS-MBE) growth on a semi-insulating InP substrate. The absorber, made of lattice matched p-type InGaAs, maximises absorption at 1550 nm. The collector layer, formed from unintentionally doped n-type InP, is followed by a quaternary (InGaAsP) layer adjusted for a wavelength of 1300 nm, which is used to build the optical waveguide to couple light into the UTC-PD. To mitigate abrupt conduction band transitions at the InGaAs-InP heterojunction interface, two thin spacer layers of quaternary material with bandgaps of 1300 nm and 1100 nm are incorporated. Finally, the top and bottom contact layers are composed of highly doped p-type InGaAs and n-type InP, respectively.

Under reverse bias, when the collection layer is depleted, the UTC-PD can be treated as a capacitor in parallel with high resistance in the order of $k\Omega s$. In the equivalent circuit, this refers to C_3 and R_3. The resistance arising from the p and n Ohmic contacts and the bulk semiconductor can be modelled as the series resistance R_s. These are the two base contributions considered in any photodiode circuit model. However, in order to match experimental data to the equivalent circuit of a UTC-PD, it is necessary to add the contribution from the spacer layers. These two can be modelled as well as a parallel RC circuit, by including C_1, R_1, C_2, and R_2. Finally, C_p and L_p represent the parasitic capacitance and inductance from the contact pads. The model is completed by adding a current source with the appropriate photocurrent value.

2.2.4 Transit-time frequency response

The equivalent circuit addresses the complex impedance of the photodiode, which is linked to the RC bandwidth limitation of the PD. To complete the PD modelling and be able to estimate the power delivered to a load, we need to pay attention to the transit-time limited response. The photocurrent response as a function of frequency $I_{ph}(f)$ can be approximated by[2-54], [2-55]

$$I_{ph}(f) = I_{ph0}\frac{1}{1+j2\pi f\tau_{abs}}\frac{sin(\frac{2\pi f\tau_{coll}}{2})}{\frac{2\pi f\tau_{coll}}{2}}e^{-j\frac{2\pi f\tau_{coll}}{2}} \tag{2.20}$$

where I_{ph0} is the reference DC photocurrent, and τ_{abs} and τ_{coll} are the transit times through the absorber and collector layer respectively. These can be calculated by [2-55]

$$\tau_{abs} = \frac{W_{abs}^2}{3D_e} + \frac{W_{abs}}{v_{th}} \tag{2.21}$$

$$\tau_{coll} = \frac{W_{coll}}{v_{coll}} \tag{2.22}$$

where W_{abs} is the absorber thickness, D_e is the diffusion constant of electrons in the absorber, v_{th} is the thermionic emission velocity at the absorber-collector interface, W_{coll} is the collector layer thickness, and v_{coll} is the carrier saturation velocity in the collector. The derivation of the UTC-PD photocurrent response is included in Appendix B.

2.3 THz resistive mixers

2.3.1 Mixer theory

A frequency mixer is a device that translates an input RF signal into a different frequency, either higher or lower, depending on whether upconversion or downconversion is desired. To do this, the mixer uses a local signal often denoted as the local oscillator. An ideal mixer can be represented by the multiplication operation as illustrated in Figure 2.8**a**.

If we consider two sinusoidal voltage signals v_{LO} and v_{RF}, with frequencies f_{LO} and f_{RF}, the output mixer signal can be written as

$$\begin{aligned} v_{out} &= [(A_{LO}cos(2\pi f_{LO}t)] \cdot [A_{RF}cos(2\pi f_{RF}t)] \\ &= \frac{A_{LO}A_{RF}}{2}[cos(2\pi(f_{LO}-f_{RF})t) + cos(2\pi(f_{LO}+f_{RF})t)] \end{aligned} \tag{2.23}$$

where A_{LO} and A_{RF} are the amplitudes of the LO and RF signal respectively.

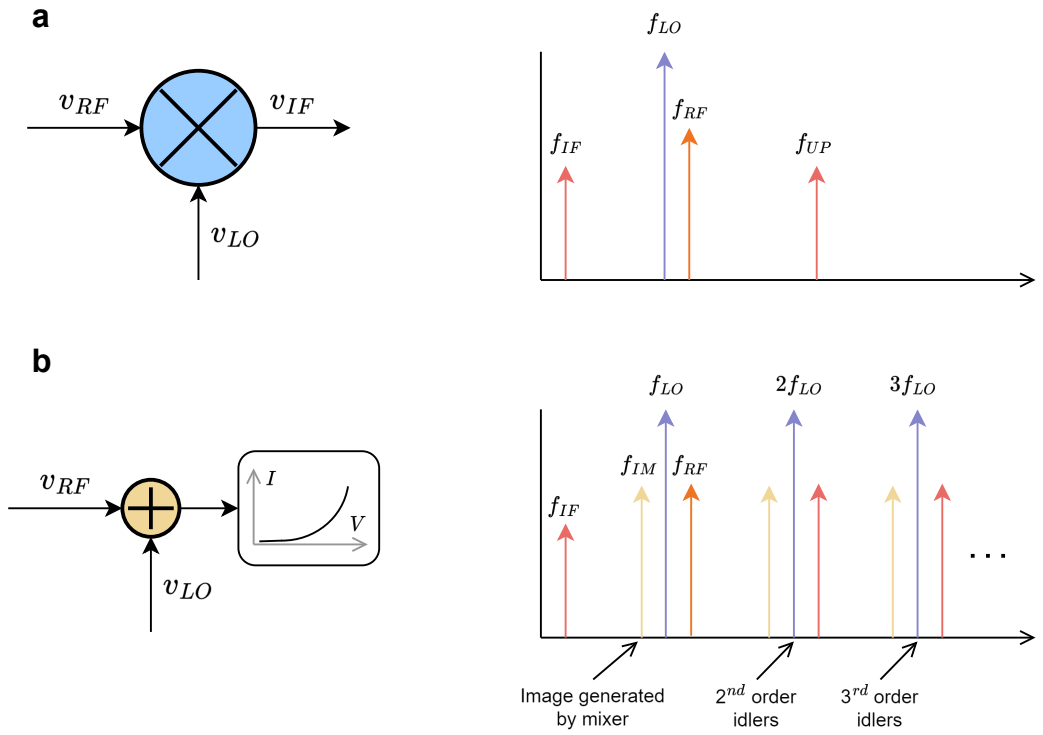

Figure 2.8: Frequency mixers. **a** Ideal mixer under local-oscillator excitation producing only down-converted and up-converted terms. **b** Practical resistive mixer under local oscillator excitation producing multiple order idlers.

The output signal has two components with translated frequencies $f_{IF} = f_{LO} - f_{RF}$ and $f_{UP} = f_{LO} + f_{RF}$. The lower frequency component is commonly referred as the IF signal v_{IF}, and it is the desired output signal in a receiver. This scenario, illustrated in Figure 2.8**a**, is known as SSB conversion. When the RF signal has an image around the LO signal, this is also down-converted or up-converted and it is referred to as double-side-band (DSB) conversion.

A practical mixer uses a non-linear device as the mixing element, which generates not only down-converted and up-converted terms but also a series of mixing products (idlers) [2-17], [2-56]. In diode-based mixers, this is achieved by modulating the non-linear conductance of the diode. This mixer approach is known as a resistive mixer [2-57], with the mixing products defined by [2-56]

$$v_{out} = v_{RF} \sum_{n=1}^{\infty} [k_n \cos(n2\pi(f_{LO} - f_{RF})t) + k_n \cos(n2\pi(f_{LO} + f_{RF})t)] \qquad (2.24)$$

where n is the order of the idler, and k_n is the coefficient associated to each idler. This solution is valid if the input RF signal power is significantly lower than the LO. The resulting frequency spectrum in this scenario is depicted in Figure 2.8**b**. To evaluate the mixer's performance in down-conversion mode, the key figure of merit is the conversion loss. This refers to the ratio of the input RF power and the IF power

$$L_c = \frac{P_{RF}}{P_{IF}} \tag{2.25}$$

According to resistive mixer theory, a theoretical limit of 3 dB of conversion loss for the first order term (fundamental mixing) is achieved [2-56]. This considers that no power is dissipated in other idlers. In the scenario where idlers are matched to a load, the theoretical limit increases to 3.92 dB [2-56], [2-58], independent of the mixer configuration. The second most important figure of merit is the noise figure of a mixer F_m, which can be defined as the SNR degradation [2-59]

$$F_m = \frac{SNR_i}{SNR_o} \tag{2.26}$$

where SNR_i and SNR_o are the SNR at the input and output of the device. A related concept is the noise temperature of the mixer T_m, which represents the equivalent thermal noise power from a resistor to produce the same SNR degradation and is defined by

$$T_m = \frac{P_n}{B}\frac{1}{k} \tag{2.27}$$

where P_n is the noise power and B is the bandwidth. These two figures of merit are related by

$$F_m = 1 + \frac{T_m}{T_0} \tag{2.28}$$

where T_0 is by definition 290 K.

2.3.2 Subharmonic mixing

The analysis so far has focused on fundamental mixing, i.e. selecting the first order idler $f_{LO} - f_{RF}$ in down-conversion mode. However, to generate a down-converted IF signal at the desired frequency, one can select different mixing products $|mf_{LO} - nf_{RF}|$, where $m+n$ defines the order. A common example is the product $2f_{LO} - f_{RF}$, referred to as subharmonic mixing. This approach is widely used in THz Schottky mixers because due to two key advantages: (1) the LO frequency is halved relative to the RF frequency, making more LO power available at lower frequencies, and (2) it simplifies the isolation of LO and RF signals, facilitating on-chip integration. In addition, a subharmonic mixer has only a slight conversion loss penalty of 1.5 dB compared to a fundamental mixer [2-60]. For these reasons, in this work we focus on developing subharmonic optoelectronic receivers. To achieve this mixing mode in diode-based mixers, the antiparallel topology is commonly employed [2-17], [2-60], depicted in Figure 2.9**b**.

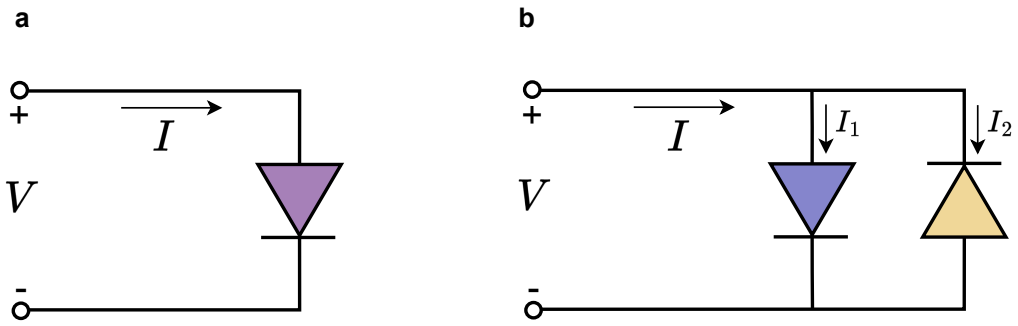

Figure 2.9: Basic diode topologies. **a** Single-ended. **b** Antiparallel.

To illustrate how this is achieved in a simplified manner, we first consider the current of a single-ended diode, as illustrated in Figure 2.9**a**. The current I in the diode which is an exponential function (Equation 2.7), can be expanded into a Taylor series

$$I_1 = f(V) = c_1V + c_2V^2 + c_3V^3 + c_4V^4 + c_4V^5... \tag{2.29}$$

where c_n are the n-th order Taylor series coefficients. This configuration produces every order of mixing products. By placing a second diode in parallel with

opposite polarity, the current becomes

$$I_2 = -f(-V) = c_1V - c_2V^2 + c_3V^3 - c_4V^4 + -c_5V^5... \tag{2.30}$$

The total current flowing through the antiparallel cell will be

$$I = I_1 + I_2 = 2c_1V + 2c_3V^3 + 2c_5V^5... \tag{2.31}$$

In this configuration, only odd-degree components can escape the diode cell. This means that only odd order $m+n$ mixing products will be produced by this configuration, which includes the target mixing product $|2f_{LO} - f_{RF}|$.

2.3.3 Harmonic balance simulations

The receiver components can be categorised as either linear or non-linear. Linear components include passive RF circuitry such as filters, impedance matching networks, and waveguide transitions. The non-linear component in this case is the SBD which produces the mixing products. To accurately predict receiver performance, it is crucial to simulate both linear and non-linear components together. A widely used method for integrating these two domains is the harmonic balance (HB) technique [2-15], [2-17], [2-61]. Figure 2.10 illustrates the basic case of a single-tone input interacting with a non-linear element.

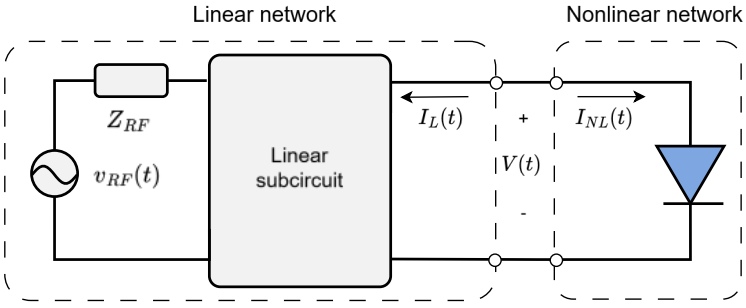

Figure 2.10: Harmonic balance technique for a single tone simulation and single non-linear component.

The goal is to determine the steady-state solution of $V(t)$ by minimising an error function, in this example $I_L - I_{NL} = 0$. This process involves estimating a solution and refining it iteratively using numerical methods until the desired con-

vergence is achieved. The steady-state solution of $V(t)$ has the form

$$v(t) = \Re\left\{\sum_{k=0}^{K} V_k e^{j2\pi k f t}\right\} \tag{2.32}$$

where f is the source frequency, V_k is the k-th complex Fourier series coefficient, and K represents the number of harmonics considered in the calculation, also known as the order. In case, multiple sources with different frequencies are considered, the steady-state solution can be written as

$$v(t) = \Re\left\{\sum_{k_1=0}^{K_1}\sum_{k_2=0}^{K_2}\ldots\sum_{k_n=0}^{K_n} V_{k_1,k_2,\ldots k_n} e^{j2\pi(k_1 f_1 + k_2 f_2 + \ldots k_n f_n)t}\right\} \tag{2.33}$$

where n is the number of sources, while f_n and K_n represent the frequency and the number of harmonics for each source, respectively. Consequently, in the case of a mixer, two frequency sources must be taken into account: the LO and RF. In this work, we use the software Advanced Design System (ADS) which incorporates a HB simulator. Different steps are followed to be able to predict the final receiver performance (conversion loss and noise figure) based on subharmonic mixing. The circuits used for HB simulations in each step are summarised in Figure 2.11.

- The first step (Figure 2.11**a**) consists of simulating the ideal mixer by including the antiparallel diodes circuit model. Ideal filters are included to separate RF, LO, IF, and higher frequency harmonics. The IF impedance Z_{IF} is set to the standard 50Ω which is typically required for external connections, and the higher harmonics are terminated with $Z_H = 1000\Omega$. The RF and LO impedances Z_{RF}, Z_{LO} are optimised to minimise conversion loss.

- Next, the S-parameters of the simulated diode chip are included in the mixer simulation (Figure 2.11**b**). This enables determining the embedding impedance of the diode chip, including the effects of parasitics.

- Using this information, the mixer circuit is designed. This includes replacing ideal filters with real ones, implementing impedance matching sections, transitions, and other components. The S-parameters of the complete mixer

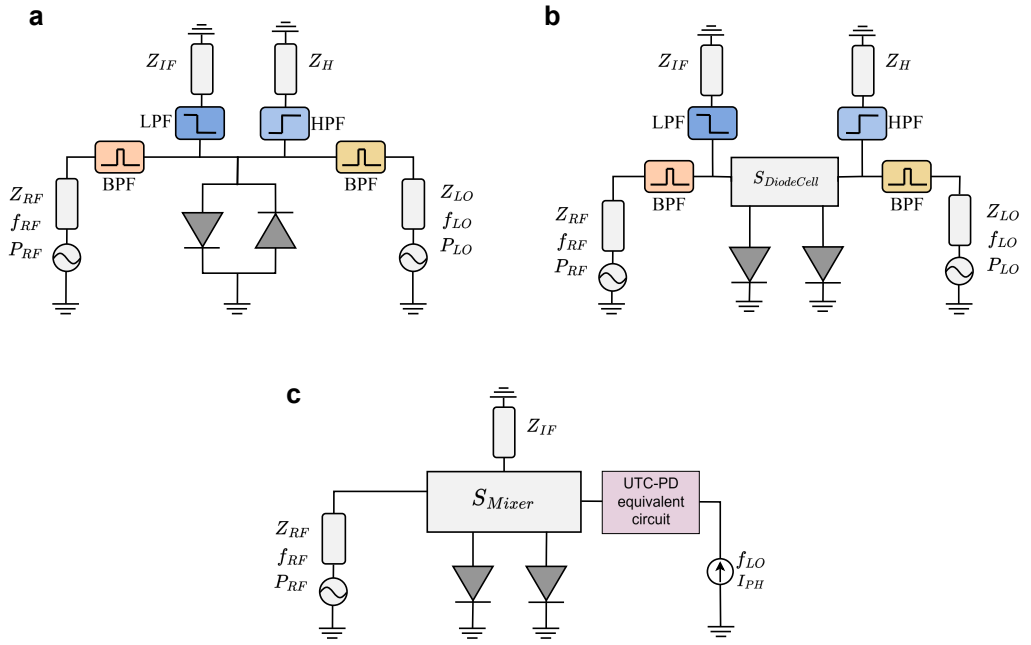

Figure 2.11: Harmonic balance circuits used for subharmonic mixer simulations. **a** Ideal mixer and filters to separate RF, LO, and IF signals. **b** Ideal mixer but including the S-parameters of the SBD cell implementation. **c** Practical mixer by including the S-parameters of the full designed mixer circuit, and the UTC-PD equivalent circuit.

circuit and the UTC-PD equivalent circuit are included in the final HB simulation (Figure 2.11**c**).

Following this approach, the final mixer performance can be predicted, including (1) the non-linear characteristics of the SBD, (2) the impedance and frequency response of the UTC-PD, and (3) the S-parameters of the mixer circuit.

References

[2-1] E. H. Rhoderick and R. H. Williams, *Metal-semiconductor Contacts*, en. Clarendon Press, 1988.

[2-2] B. L. Sharma, *Metal-Semiconductor Schottky Barrier Junctions and Their Applications*, en. Springer Science & Business Media, Nov. 2013.

[2-3] W. Schottky, "Zur halbleitertheorie der sperrschicht- und spitzengleichrichter," de, *Eur. Phys. J. A*, vol. 113, no. 5-6, pp. 367–414, May 1939.

[2-4] N. F. Mott, "The theory of crystal rectifiers," en, *Proc. R. Soc. Lond.*, vol. 171, no. 944, pp. 27–38, May 1939.

[2-5] A. Cowley and S. M. Sze, "Surface states and barrier height of metal-semiconductor systems," *Journal of Applied Physics*, vol. 36, pp. 3212–3220, Oct. 1965.

[2-6] C. R. Crowell and G. I. Roberts, "Surface state and interface effects on the capacitance-voltage relationship in Schottky barriers," en, *J. Appl. Phys.*, vol. 40, no. 9, pp. 3726–3730, Aug. 1969.

[2-7] R. T. Tung, "The physics and chemistry of the Schottky barrier height," *Applied physics reviews*, vol. 1, p. 011 304, Mar. 2014.

[2-8] M. T. Faber, J. Chramiec, and M. Adamski, *Microwave and Millimeter-wave Diode Frequency Multipliers*. Artech House, Jan. 1995.

[2-9] S. M. Sze, Y. Li, and K. K. Ng, *Physics of semiconductor devices*, en, 4th ed. Nashville, TN: John Wiley & Sons, May 2021.

[2-10] C. R. Crowell, "The Richardson constant for thermionic emission in Schottky barrier diodes," en, *Solid State Electron.*, vol. 8, no. 4, pp. 395–399, Apr. 1965.

[2-11] C. Y. Chang and S. M. Sze, "Carrier transport across metal-semiconductor barriers," *Solid-State Electronics*, 1970.

[2-12] V. L. Rideout and C. R. Crowell, "Effects of image force and tunneling on current transport in metal-semiconductor (Schottky barrier) contacts," *Solid State Electron.*, vol. 13, no. 7, pp. 993–1009, Jul. 1970.

[2-13] F. Padovani and R. Stratton, "Field and thermionic-field emission in Schottky barriers," *Solid-state Electronics*, vol. 9, pp. 695–707, Jul. 1966.

[2-14] C. Crowell and M. Beguwala, "Recombination velocity effects on current diffusion and imref in Schottky barriers," *Solid-state electronics*, vol. 14, no. 11, pp. 1149–1157, 1971.

[2-15] S. A. Maas, *Nonlinear microwave and RF circuits*, en, 2nd ed. Norwood, MA: Artech House, Jan. 2003.

[2-16] K. S. Champlin, D. B. Armstrong, and P. D. Gunderson, "Charge carrier inertia in semiconductors," *Proc. IEEE Inst. Electr. Electron. Eng.*, vol. 52, no. 6, pp. 677–685, 1964.

[2-17] S. A. Maas, *Microwave mixers*. ui.adsabs.harvard.edu, Jan. 1986.

[2-18] D. M. Melgar, "Design and optimization at the highest frequency of a heterodyne receiver at 1.2 THz for the JUICE-SWI instrument," en, Ph.D. dissertation, Université Pierre et Marie Curie-Paris VI, 2017.

[2-19] R. H. Cox and H. Strack, "Ohmic contacts for GaAs devices," en, *Solid State Electron.*, vol. 10, no. 12, pp. 1213–1218, Dec. 1967.

[2-20] T. W. Crowe, R. J. Mattauch, H. P. Roser, W. L. Bishop, W. C. B. Peatman, and X. Liu, "GaAs Schottky diodes for THz mixing applications," *Proc. IEEE*, vol. 80, no. 11, pp. 1827–1841, Nov. 1992.

[2-21] P. H. Siegel, R. P. Smith, M. C. Graidis, and S. C. Martin, "2.5-THz GaAs monolithic membrane-diode mixer," *IEEE Trans. Microw. Theory Tech.*, vol. 47, no. 5, pp. 596–604, May 1999.

[2-22] I. Mehdi, J. V. Siles, C. Lee, and E. Schlecht, "THz diode technology: Status, prospects, and applications," *Proceedings of the IEEE*, vol. 105, no. 6, pp. 990–1007, 2017.

[2-23] W. L. Schroeder and I. Wolff, "Monte-Carlo study of high-frequency, large-signal transport parameters for physics based device simulation," *IEEE Trans. Electron Devices*, vol. 42, no. 5, pp. 819–827, May 1995.

[2-24] M. S. Lundstrom, "Fundamentals of carrier transport, 2nd edn," *Measurement Science and Technology*, vol. 13, pp. 230–230, Feb. 2002.

[2-25] S. Selberherr, *Analysis and simulation of semiconductor devices*, en, 1984th ed. Vienna, Austria: Springer, Dec. 2012.

[2-26] D. Pardo Santos, "Analysis and design of multipliers and mixers via Monte Carlo modelling at THZ bands," en, Ph.D. dissertation, 2019.

[2-27] S. Selberherr, *Analysis and simulation of semiconductor devices*, en. Vienna, Austria: Springer, Dec. 2011.

[2-28] J. L. Hesler, "Planar Schottky diodes in submillimeter-wavelength waveguide receivers," en, Ph.D. dissertation, University of Virginia, Ann Arbor, United States, 1996.

[2-29] A.-Y. Tang, "Modelling and characterisation of terahertz planar Schottky diodes," en, Ph.D. dissertation, Chalmers Tekniska Hogskola (Sweden), Ann Arbor, United States, 2013.

[2-30] W. L. Bishop, K. McKinney, R. J. Mattauch, T. W. Crowe, and G. Green, "A novel whiskerless Schottky diode for millimeter and submillimeter wave application," in *1987 IEEE MTT-S International Microwave Symposium Digest*, vol. 2, MTT005, 1987, pp. 607–610.

[2-31] J. W. Archer, R. A. Batchelor, and C. J. Smith, "Low-parasitic, planar Schottky diodes for millimeter-wave integrated circuits," *IEEE Trans. Microw. Theory Tech.*, vol. 38, no. 1, pp. 15–22, 1990.

[2-32] T. Kleinpenning, "Low-frequency noise in Schottky barrier diodes," *Solid-state Electronics*, vol. 22, pp. 121–128, Feb. 1979.

[2-33] J. Nougier, "Fluctuations and noise of hot carriers in semiconductor materials and devices," *IEEE Transactions on Electron Devices*, vol. 41, pp. 2034–2049, Nov. 1994.

[2-34] T. González, D. Pardo, L. Reggiani, and L. Varani, "Microscopic analysis of electron noise in GaAs Schottky barrier diodes," *Journal of Applied Physics*, vol. 82, pp. 2349–2358, Sep. 1997.

[2-35] S. Perez, T. Gonzalez, P. Shiktorov, *et al.*, "Noise in Schottky-barrier diodes: From static to large-signal operation," in *Noise in Devices and Circuits II*, F. Danneville, F. Bonani, M. J. Deen, and M. E. Levinshtein, Eds., SPIE, May 2004.

[2-36] J. Graffeuil, R. A. Liman, J. L. Muraro, and O. Llopis, "Cyclostationary shot-noise measurements in RF Schottky-barrier diode detectors," *IEEE Electron Device Lett.*, vol. 31, no. 1, pp. 74–76, Jan. 2010.

[2-37] A. M. Cowley and R. A. Zettler, "Shot noise in silicon Schottky barrier diodes," *IEEE Trans. Electron Devices*, vol. 15, no. 10, pp. 761–769, Oct. 1968.

[2-38] J. B. Johnson, "Thermal agitation of electricity in conductors," *Physical review*, vol. 32, no. 1, pp. 97–109, 1928.

[2-39] H. Nyquist, "Thermal agitation of electric charge in conductors," *Physical review*, vol. 32, no. 1, pp. 110–113, 1928.

[2-40] G. M. Hegazi, A. Jelenski, and K. S. Yngvesson, "Limitations of microwave and millimeter-wave mixers due to excess noise," *IEEE Trans. Microw. Theory Tech.*, vol. 33, no. 12, pp. 1404–1409, Dec. 1985.

[2-41] T. Gonzalez, D. Pardo, L. Varani, and L. Reggiani, "A microscope interpretation of hot-electron noise in Schottky barrier diodes," *Semicond. Sci. Technol.*, vol. 9, no. 5S, pp. 580–583, May 1994.

[2-42] M. DiDomenico and O. Svelto, "Solid-state photodetection: A comparison between photodiodes and photoconductors," *Proc. IEEE Inst. Electr. Electron. Eng.*, vol. 52, no. 2, pp. 136–144, Feb. 1964.

[2-43] J. Bowers and C. Burrus, "Ultrawide-band long-wavelength p-i-n photodetectors," *Journal of Lightwave Technology*, vol. 5, no. 10, pp. 1339–1350, Oct. 1987.

[2-44] P.-L. Liu, K. J. Williams, M. Y. Frankel, and R. D. Esman, "Saturation characteristics of fast photodetectors," *IEEE Trans. Microw. Theory Tech.*, vol. 47, no. 7, pp. 1297–1303, Jul. 1999.

[2-45] T. Ishibashi, N. Shimizu, S. Kodama, H. Ito, T. Nagatsuma, and T. Furuta, "Uni-traveling-carrier photodiodes," in *Ultrafast Electronics and Optoelectronics*, Optica Publishing Group, Mar. 1997, UC3.

[2-46] T. Ishibashi, S. Kodama, N. S. N. Shimizu, and T. F. T. Furuta, "High-speed response of uni-traveling-carrier photodiodes," *Japanese journal of applied physics*, vol. 36, no. 10R, p. 6263, 1997.

[2-47] T. Ishibashi, T. Furuta, H. Fushimi, *et al.*, "InP/InGaAs uni-traveling-carrier photodiodes," *IEICE transactions on electronics*, vol. 83, no. 6, pp. 938–949, 2000.

[2-48] H. Ito, S. Kodama, Y. Muramoto, T. Furuta, T. Nagatsuma, and T. Ishibashi, "High-speed and high-output InP–InGaAs unitraveling-carrier photodiodes," en, *IEEE J. Sel. Top. Quantum Electron.*, vol. 10, no. 4, pp. 709–727, Jul. 2004.

[2-49] S. Iezekiel, *Microwave Photonics: Devices and Applications*, en. John Wiley & Sons, Mar. 2009.

[2-50] J. Dittmer, J. Tebart, C. Füllner, C. Koos, A. Stöhr, and S. Randel, "200 Gbit/s wireless THz transmission over 52m using optoelectronic signal generation," pp. 134–137, Sep. 2023.

[2-51] D.-C. Shin, B. Kim, H. Jang, Y.-j. Kim, and S.-W. Kim, "Photonic comb-rooted synthesis of ultra-stable terahertz frequencies," *Nat. Commun.*, vol. 14, Feb. 2023.

[2-52] M. Natrella, C.-P. Liu, C. Graham, *et al.*, "Accurate equivalent circuit model for millimetre-wave UTC photodiodes," en, *Opt. Express*, vol. 24, no. 5, pp. 4698–4713, Mar. 2016.

[2-53] X. Lin, M. Natrella, J. Seddon, *et al.*, "High performance waveguide uni-travelling carrier photodiode grown by solid source molecular beam epitaxy," en, *Opt. Express*, vol. 27, no. 25, pp. 37 065–37 086, Dec. 2019.

[2-54] T. Ishibashi and H. Ito, "Uni-traveling-carrier photodiodes," en, *J. Appl. Phys.*, vol. 127, no. 3, p. 031 101, Jan. 2020.

[2-55] D. Guendouz, "Development of the first compact model for ultra-fast UTC (uni-travelling carrier) photodiodes towards monolithic integration of photonic and nanoelectronic technologies," Ph.D. dissertation, Universite de Bordeaux, 2022.

[2-56] A. J. Kelly, "Fundamental limits on conversion loss of double sideband resistive mixers," *IEEE Trans. Microw. Theory Tech.*, vol. 25, pp. 867–869, 1977.

[2-57] A. Saleh, "Theory of resistive mixers," Ph.D. dissertation, Massachusetts Institute of Technology, 1970.

[2-58] K. Yhland, "Simplified analysis of resistive mixers," *IEEE Microw. Wirel. Compon. Lett.*, vol. 17, pp. 604–606, Aug. 2007.

[2-59] D. M. Pozar, *Microwave engineering, international adaptation*, en, 4th ed. Nashville, TN: John Wiley & Sons, Feb. 2021.

[2-60] M. Cohn, J. E. Degenford, and B. A. Newman, "Harmonic mixing with an antiparallel diode pair," *IEEE Transactions on Microwave Theory and Techniques*, vol. 23, no. 8, pp. 667–673, 2003.

[2-61] R. J. Gilmore and M. B. Steer, "Nonlinear circuit analysis using the method of harmonic balance—a review of the art. part I. introductory concepts," *International Journal of Microwave and Millimeter-Wave Computer-Aided Engineering*, vol. 1, no. 1, pp. 22–37, 1991.

Chapter 3

Monolithic integration

The idea of monolithically integrated SBDs and UTC-PDs to implement terahertz receivers was originally conceived by C.C. Renaud, J. Seddon and I. Belio-Apaolaza. All the content shown in this Chapter was produced by I. Belio-Apaolaza, including the simulation and design and InP-based Schottky diodes, and the terahertz mixer.

Building on the modelling framework introduced in Chapter 2, this chapter presents the design and simulation of a monolithically integrated receiver that incorporates a UTC-PD and an SBD. The process starts with the design of the InP-based SBD using the standard UTC-PD epitaxy, followed by the design of a 220–330 GHz subharmonic integrated receiver in CPW.

3.1 InP THz Schottky diodes

3.1.1 Epitaxial layers and planar structure

In Table 3.1, the epitaxial structure of the UTC-PDs used in this work is presented, including the doping levels, materials, functions, and thicknesses of each layer. The goal here is to design an SBD using this structure without any modifications that could alter the performance of the UTC-PD. First, because the SBD is intended to be used as a frequency mixer at THz frequencies, it must be implemented in *n*-type layers with high electron mobility. Therefore, the first eight layers are excluded, leaving the collector and waveguide layers for consideration. The remaining layers resembles the standard structure of a typical THz SBD, with an *n*-type layer for the

Schottky contact followed by a highly doped semiconductor. To form the Schottky contact, the collector or waveguide layer can be employed, but the high doping level of the waveguide layer introduces two issues: (1) it may cause the Schottky contact to degrade into an Ohmic contact during the fabrication process, and (2) micron or submicron contact areas would be required to reduce the junction capacitance to achieve THz operation. Typical THz SBD epilayers have a doping level of the order of $1 \cdot 10^{17}\,\mathrm{cm}^{-3}$ [3-1], which provides an optimum balance between series resistance (R_s) and junction capacitance (C_j) for contact areas of few μm^2. While lower doping levels result in an increase of R_s, the collector layer is the most practical and effective choice for fabricating the SBD.

Doping ($1/cm^{-3}$)	Material	Function	Thickness (nm)
$> 1 \cdot 10^{19}$	$p^{++} - Q_{1.3}$	p contact	200
$2.5 \cdot 10^{18}$	$p^{+} - In_{0.53}Ga_{0.47}As$	absorber	30
$1 \cdot 10^{18}$	$p^{+} - In_{0.53}Ga_{0.47}As$	absorber	30
$5 \cdot 10^{17}$	$p - In_{0.53}Ga_{0.47}As$	absorber	30
$2.5 \cdot 10^{17}$	$p - In_{0.53}Ga_{0.47}As$	absorber	30
u.i.d	$u - In_{0.53}Ga_{0.47}As$	absorber	10
u.i.d	$u - Q_{1.3}$	spacer	10
u.i.d	$u - Q_{1.1}$	spacer	10
$1 \cdot 10^{16}$	$n - InP$	collector	300
$2.5 \cdot 10^{18}$	$n^{+} - Q_{1.3}$	waveguide	300
$> 1 \cdot 10^{19}$	$n^{++} - InP$	n contact	600
S.I. Substrate	Fe-doped InP	substrate	$300 \cdot 10^3$

Table 3.1: UTC-PD epitaxial layers structure [3-2]. u.i.d: unintentionally doped. $Q_{1.3} - Q_{1.1}$: quaternary material (InGaAsP) lattice-matched to InP with a centre wavelength of 1.3-1.1μm.

The cross-sectional illustration of the planar InP-based SBD implemented with these layers is shown in Figure 3.1. The Ohmic contact is assumed to be fabricated in the n^{+}- $Q_{1.3}$ layer although it could alternatively be implemented in the n^{++}- InP layer. This assumption is based on the typical fabrication approach for UTC-PDs. For the purposes of SBD design, this distinction is not critical, as the primary contributors to series resistance and capacitance are the thickness and area of the Schottky contact at the epilayer (collector layer). Instead of employing an air-bridged structure, the SBD is embedded in silicon oxynitride (SiON), with Schottky

and Ohmic contacts accessed using through vias. This approach aligns with the fabrication method of the UTC-PD [3-2], as both devices must be fabricated together. The fabrication process for the SBD and UTC-PD is discussed in section 3.2.6.

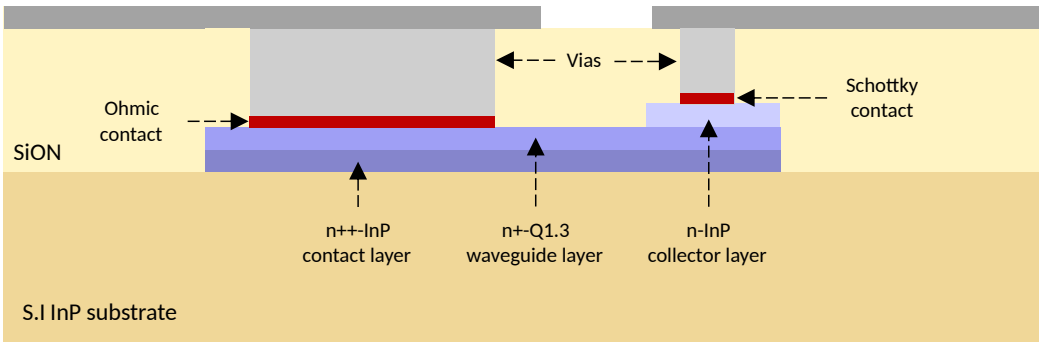

Figure 3.1: Cross-section schematic of planar InP-based Schottky diodes based on the UTC-PD standard epitaxy. S.I: semi insulating.

3.1.2 Contact area and epilayer thickness optimisation

As outlined in Chapter 2, the barrier height is the fundamental parameter of a Schottky contact. Due to Fermi-level pinning, the Schottky-Mott rule does not hold in InP, and the barrier height is independent of the contact metal. In this sense, InP Schottky contacts exhibit a barrier height in the range of 0.4–0.5 eV [3-3]. For this work, a value of 0.45 eV was assumed. Using the equations introduced in Chapter 2, the I-V and C-V characteristics of the diode can be determined analytically. This requires appropriate semiconductor parameters, which are specific to the layer material, including: bandgap, relative permittivity, effective density of states in the conduction band, effective electron mass, electron affinity, and electron mobility. These parameters, obtained from literature sources [3-4]–[3-9], are detailed in Appendix C. Figure 3.2 illustrates the analytically calculated series resistance and zero-bias junction capacitance as a function of epilayer thickness and contact area. The calculated depletion width is 218 nm, which reflects in the junction capacitance rate of change (Equation 2.10).

The optimisation of R_s and C_{j0} was performed by analysing the conversion loss of an ideal subharmonic mixer using the test bench depicted in Figure 2.11**a**. The modelled I-V and C-V characteristics of the InP SBDs were employed in ADS diode

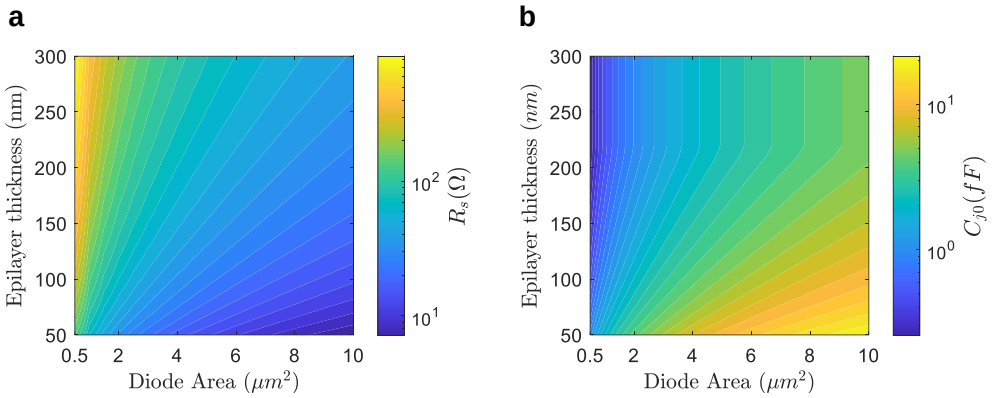

Figure 3.2: Series resistance (**a**) and zero-bias junction capacitance (**b**) of the InP Schottky diode as a function of contact area and epilayer thickness.

model, with an effective Richardson constant (A^{**}) of $93,735\,\mathrm{m^2K^2}$. The resulting conversion loss at 300 GHz for optimised RF and LO impedances is depicted in Figure 3.3 for LO powers of -13, -10, and -7 dBm. At higher LO powers, the impact of increased capacitance from larger contact areas can be compensated, enabling lower series resistance if the thickness of the epilayer is reduced. In contrast, for lower LO powers, minimising the contact area is critical to maintain acceptable conversion loss.

Based on these considerations, a contact area of $3\,\mu\mathrm{m}^2$ and an epilayer thickness of 110 nm were selected for the SBD to be used in the monolithically integrated receiver, resulting in $R_s = 52\,\Omega$, $C_{j0} = 3\,\mathrm{fF}$, and a cut-off frequency of 1.02 THz. The selected area represents a compromise between minimising capacitance, supporting low-power operation and preserving the reliability of the fabrication process. A contact area of $3\,\mu\mathrm{m}^2$ corresponds to a contact diameter of approximately $2\,\mu\mathrm{m}$, which remains within the resolution limits of standard photolithography. As for the epilayer, its thickness was minimised motivated by experimental evidence showing that thinner epilayers, of the order of 100 nm, are typically necessary to reach optimal THz Schottky mixer performance. With these diode characteristics, the simulated conversion losses are 26.47, 15.87, and 13.16 dB for LO powers of -13, -10, and -7 dBm, respectively.

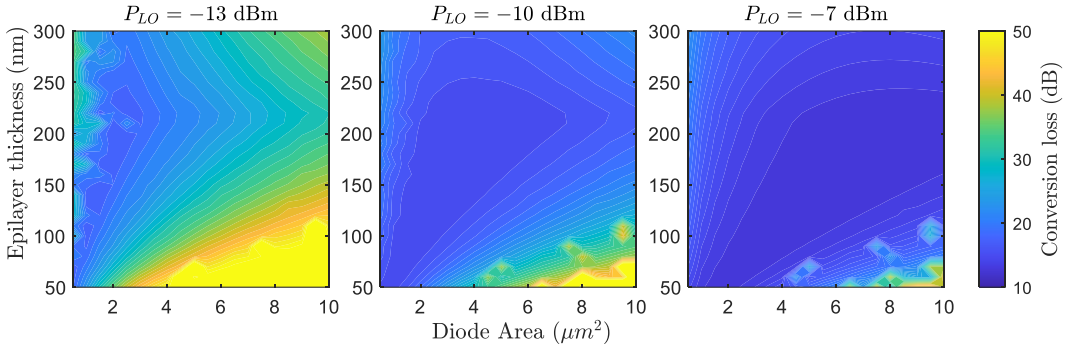

Figure 3.3: Ideal mixer performance of InP-based SBD at 300 GHz as a function of contact area and epilayer thickness for an LO power of -13 (**a**), -10 (**a**), and -7 (**a**) dBm.

3.1.3 2D physics-based modelling

The analytical expressions for calculating series resistance and capacitance have limited accuracy due to simplifications and assumptions, as discussed in Chapter 2. In addition, only the epilayer's series resistance is considered in this calculation, which excludes the spreading resistance from the buffer layer to the Ohmic contact. To achieve more accurate I-V and C-V characteristics of the InP SBD, the 2D physics-based (DD) model developed in COMSOL was used. Figure 3.4 provides insights into this model, defining the 2D model region (Figure 3.4**a**), and the layers, materials, and contacts (Figure 3.4**b**). Further details about the fundamentals of DD semiconductor models are provided in Appendix A, with the employed material parameters detailed in Appendix C.

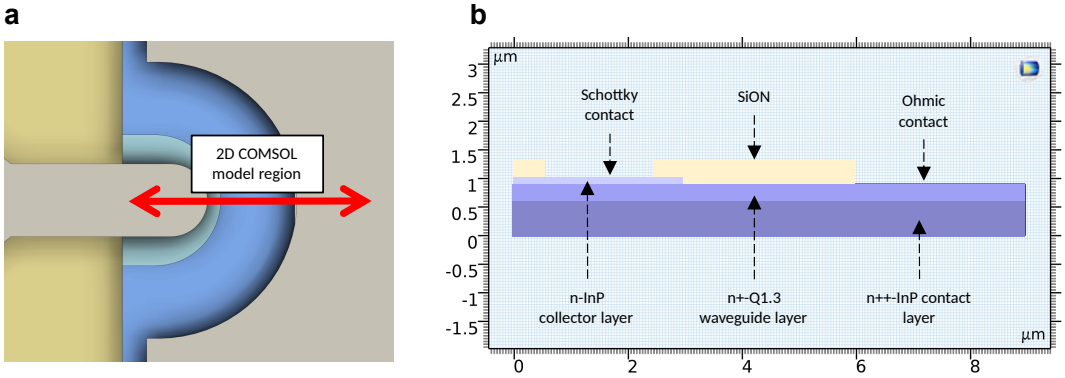

Figure 3.4: 2D physics-based COMSOL SBD model. **a** Top view of the planar InP SBD indicating the model region. **b** Geometry of the model indicating layers, materials, and contacts.

The electron concentration for an applied voltage of 0 V is shown in Figure 3.5, highlighting the depletion region gradient within the epilayer. The concentration in the epilayer varies from $2.88 \cdot 10^{10}\,\mathrm{cm}^{-3}$ at the Schottky contact edge to $7.89 \cdot 10^{16}\,\mathrm{cm}^{-3}$ at the epilayer-waveguide interface. This behaviour differs from the depletion region approximation used in analytical calculations, influencing the I-V and C-V characteristics. Figure 3.6 presents the energy band diagram along a vertical cut of the SBD. At the Schottky contact, the energy barrier is 0.45 eV, gradually decreasing across the epilayer. Notice that the n^{++}- InP layer, as well as the n^{+}- $Q_{1.3}$ layer are in degeneracy, evidenced by the Fermi level position with respect to the conduction band.

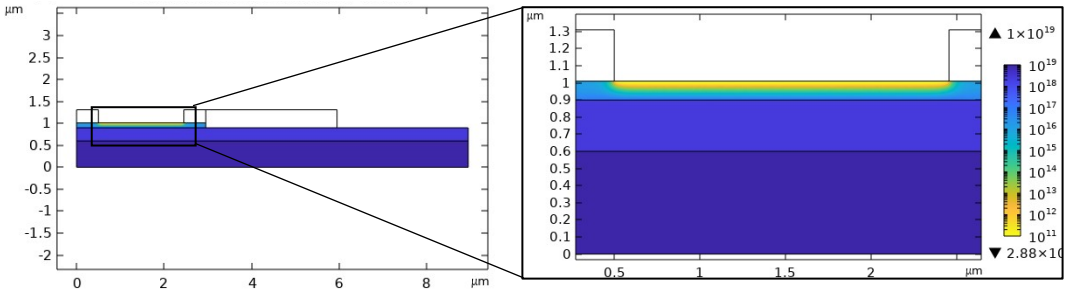

Figure 3.5: Carrier distribution of the InP-based SBD obtained from the 2D COMSOL model.

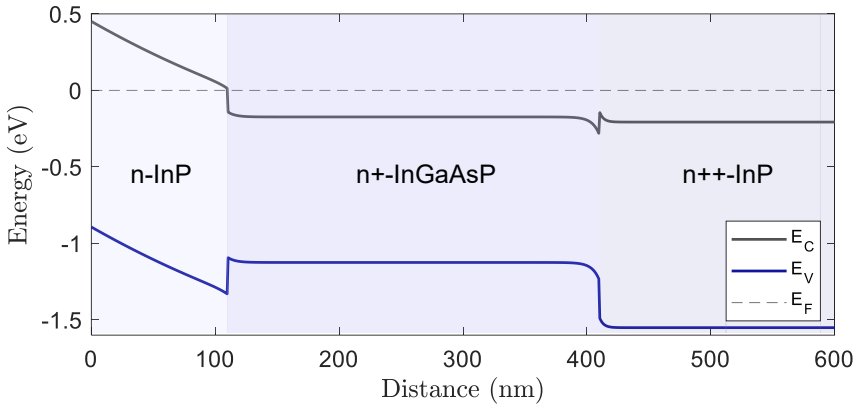

Figure 3.6: Energy bands diagram of the InP-based SBD obtained from the 2D COMSOL model.

Using this model, the I-V and C-V curves were obtained, depicted in Figure 3.7. The I-V characteristics (Figure 3.7**a**) reveal consistent behaviour between the analytical and physics-based models at low voltages, diverging beyond the built-

in potential (0.35 V). Interestingly, the 2D model predicts a lower series resistance than the analytical calculation, despite including spreading resistance, which was omitted in the analytical model. This discrepancy arises from approximations in the analytical approach, which assumes a fully depleted region and a uniformly doped undepleted epilayer with a level of $1 \cdot 10^{16}\,\mathrm{cm}^{-3}$. However, higher electron concentrations near the layer interface, due to carrier migration, reduce the overall series resistance. By adjusting the analytical model's series resistance to 32 Ω, the DD model matches the analytical calculation. With the adjusted series resistance and junction capacitance, the new cut-off frequency is 1.61 THz.

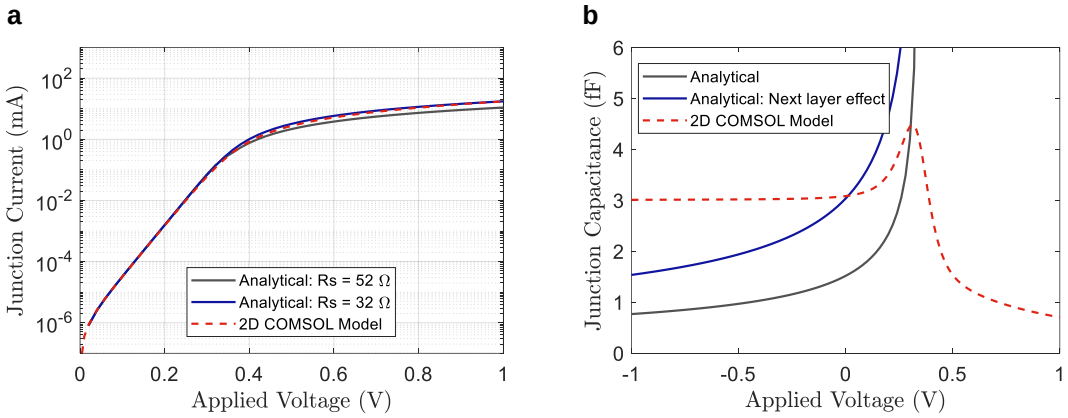

Figure 3.7: I-V (**a**) and C-V (**b**) characteristics obtained with analytical model presented in Chapter 2, and with the 2D COMSOL model.

Figure 3.7**b** shows the C-V characteristics, including analytically calculated curves for voltages from -1 to 1 V. At zero bias, the DD model predicts a junction capacitance of 3.08 fF, while the analytical calculations estimate 3.03 fF. The thinner epilayer (110 nm) compared to the depletion width (218 nm) causes the next layer to significantly influence the junction capacitance (Equation 2.10). Ignoring this effect and applying Equation 2.8 leads to an underestimated capacitance of 1.51 fF at 0 V. The DD model indicates capacitance saturation at about 3 fF for negative voltages and provides estimates beyond the built-in potential. Analytical equations, however, are constrained to the built-in potential (flat band), beyond which they exhibit a singularity.

Therefore, the DD model enables a more precise estimation of the I-V and C-V curves. These results were employed to refine the ADS diode model, incorporat-

ing the observed behaviour to evaluate the intrinsic performance of a subharmonic mixer using the designed InP SBDs in an antiparallel configuration. The achieved conversion loss, as a function of RF frequency for various LO power levels, is presented in Figure 3.8**a**. For an LO power of -13 dBm, a conversion loss below 20 dB is maintained across the 220–330 GHz band, with fixed RF and LO impedances optimised at 300 GHz ($Z_{LO} = (44 + j160)\,\Omega$; $Z_{RF} = (41 + j64)\,\Omega$). Near-optimum conversion loss values of 12.30 dB and 10.80 dB are achieved for -10 dBm and -7 dBm, respectively. Figure 3.8**b** illustrates the conversion loss at 300 GHz as a function of LO power, showing an optimum power of approximately -3 dBm, where a minimum conversion loss of 10.50 dB is achieved. Beyond this point, overpumping the SBDs leads to a deterioration in performance.

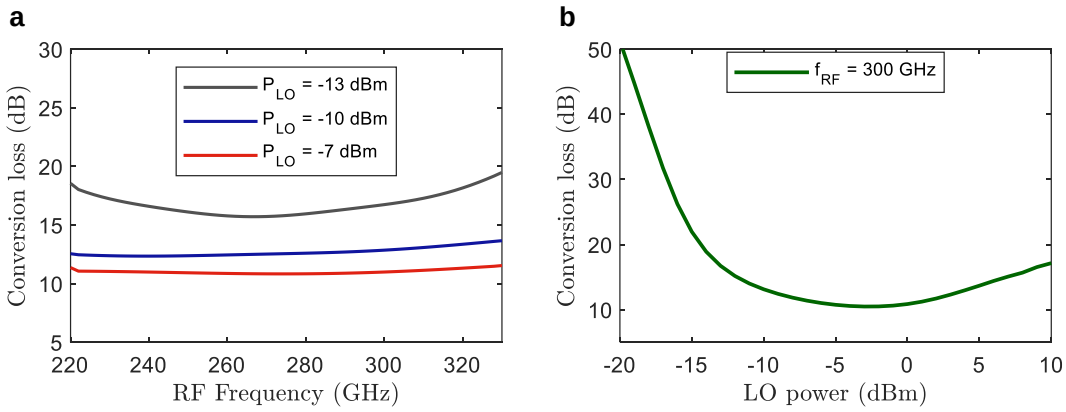

Figure 3.8: Ideal mixer performance using the InP-based SBD. **a** Conversion loss as a function of RF frequency for LO powers of -7, -10, and -13 dBm. **b** Conversion loss as a function of LO power at a frequency of 300 GHz.

3.2 220-330 GHz CPW monolithic receiver

3.2.1 Co-planar waveguide on InP

Once the basic design of the InP SBD was completed, the monolithically integrated receiver design was carried out. For this purpose, the first consideration is the high-frequency waveguide technology to be used. This choice is influenced by several factors, including fabrication constraints, cost-effectiveness, and ease of implementation. In this context, CPW represents a logical choice, especially considering that the fabrication process of the UTC-PDs is designed for CPW devices. Figure 3.9

illustrates key aspects of the CPW technology employed in the monolithic receiver. The metallisation layer consists of sputtered gold with a thickness of 0.5 µm, deposited on top of a 2 µm SiON layer, which serves as a passivation layer. This is supported on a 150 µm thick Fe-doped InP substrate. A 50 Ω line utilising this structure is depicted in Figure 3.9**b**, and the quasi-TEM mode simulated in CST is shown in Figure 3.9**c**, which represents the fundamental mode of a CPW line. Figure 3.9**d** presents the equivalent line attenuation in dB/mm across the frequency range of 1 to 500 GHz. The pronounced increase in attenuation with frequency is primarily attributed to the excitation of higher-order modes and, more critically, substrate modes. These substrate modes are triggered by the significant contrast between the relative permittivity of air ($\varepsilon_r = 1$) and InP ($\varepsilon_r = 12.5$).

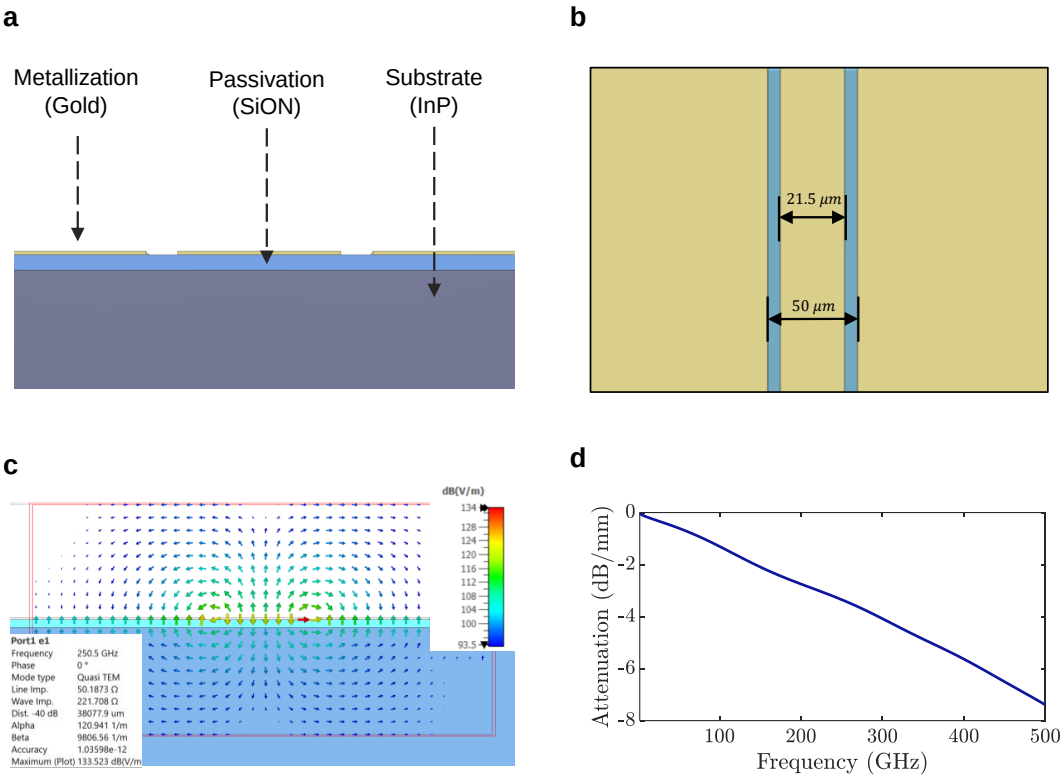

Figure 3.9: Insights on the CPW waveguide used for the monolithically integrated mixer. **a** Cross-section view indicating metallisation, passivation, and substrate layers. **b** Dimensions of the CPW line designed for 50 Ω. **c** CPW quasi TEM mode distribution for a 50 Ω line. **d** CPW line attenuation in dB/mm

3.2.2 Antiparallel shunt SBD on CPW

After defining the CPW line to be employed in the mixer circuits, the next step consists of implementing the SBD in this waveguide technology. For this purpose, two possible configuration can be used: (1) series diodes, and (2) shunt diodes. By using CPW, the diodes can be easily grounded by using a shunt configuration, which makes this an interesting topology. Following this consideration, the SBD antiparallel cell was designed. The EM model of the designed cell is depicted in Figure 3.10**a**, highlighting the different SBD layers. The electrical parameters corresponding to the materials used in the model are provided in Appendix C. The structure comprises four ports to compute S-parameters, including two discrete ports at each SBD junction, and two waveguide ports at each CPW access line. Using this model, high-frequency parasitics of the diode cell are accounted for, and the diode cell's embedding impedance can be extracted. The geometry was optimised by minimising the subharmonic mixer's conversion loss by including the S-parameters of the diode cell in ADS simulation. Figure 3.10**b** presents the simulated E-field distribution when the structure is excited by the CPW input port, showing effective coupling of the field into the SBD active area (discrete port).

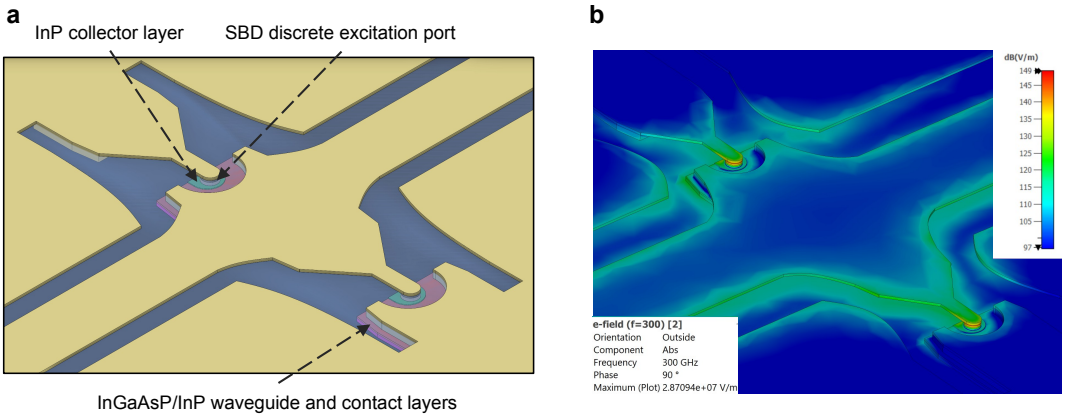

Figure 3.10: Antiparallel InP-based pair of diodes (shunt configuration) in CPW. **a** EM model highlighting the SBD layers and discrete excitation port. **b** E-field when exciting the diode cell from the input port.

Figure 3.11 compares the conversion loss of the ideal mixer to that of the mixer including the diode cell, with results shown as functions of RF frequency and LO power. At an LO power of -7 dBm, the conversion loss increases across the full

band, with an offset of approximately 2-3 dB. The minimum conversion loss is now 13 dB, achieved at 269 GHz. It should be noted that these values are obtained with RF and LO impedances optimised for 300 GHz ($Z_{LO} = (11 + j58)\,\Omega$; $Z_{RF} = (14 + j19)\,\Omega$). More detailed behaviour is depicted in Figure 3.11**b**, where the conversion loss is plotted as a function of LO power at 300 GHz. The curves show that the diode cell increases the LO power requirement, due to coupling losses and high-frequency parasitics introduced by the cell. Despite this, the designed antiparallel shunt diodes in CPW provide acceptable performance for a THz mixer in this frequency band, as the deviation from the ideal mixer is moderate.

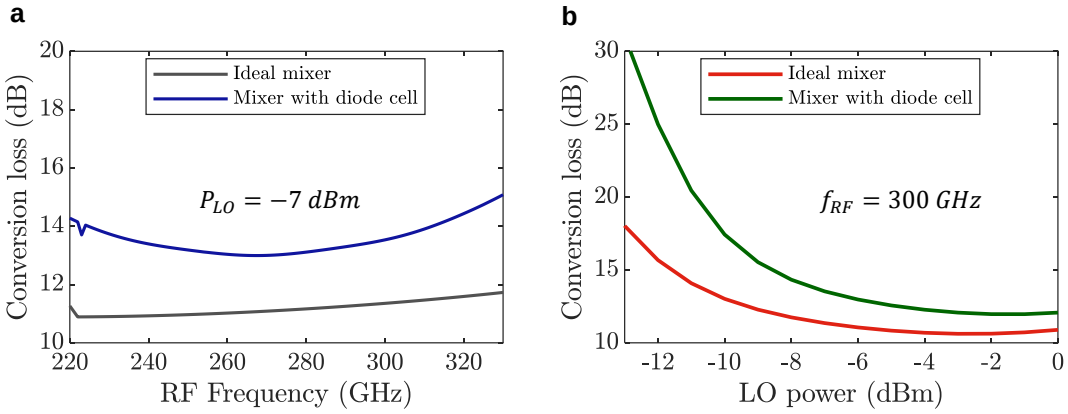

Figure 3.11: Mixer performance with and without the influence of the antiparallel shunt diodes cell in CPW. **a** Conversion loss as a function of RF frequency for a fixed LO power of -7 dBm. **b** Conversion loss as a function of LO power for a fixed RF frequency of 300 GHz.

3.2.3 UTC-PD model for mixer design

To incorporate the UTC-PD into the mixer design process, the equivalent circuit presented in Chapter 2 must first be fitted to measured impedance data. For this, previously available CPW ground-signal-ground (GSG) devices with an active area of 3x10 µm^2 were used, which were fabricated in the London Centre of Nanotechnology (LCN). The 3D structure of the UTC-PDs employed in this work is shown in Fig.3.12**a**. Note that the devices are fabricated using a SiON layer for passivation, which is why we used the same approach for the SBD design (Figure 3.1). The vector network analyser (VNA) measured impedance of a 3x10 µm^2 device up to 67 GHz was compared to the impedance derived from the fitted equivalent

circuit. Using Equations 2.20-2.22, the transit-time frequency response was calculated based on the absorber and collector thickness provided in Table 3.1, and the parameters in Appendix C. Figure 3.12**c** presents the normalised power response considering RC, transit-time, and their combined effects, obtained by connecting the equivalent circuit to a 50 Ω load. The resulting 3 dB bandwidth of the device referring to RC, transit-time, and their combination is approximately 133, 170, and 96 GHz, respectively. To demonstrate the model's ability to predict absolute output power, Figure 3.12**d** shows the model-predicted output power compared to measurements [3-10] at 135-145 GHz, revealing close agreement between the two. We see that the device can deliver a power of about 0 dBm at these frequencies.

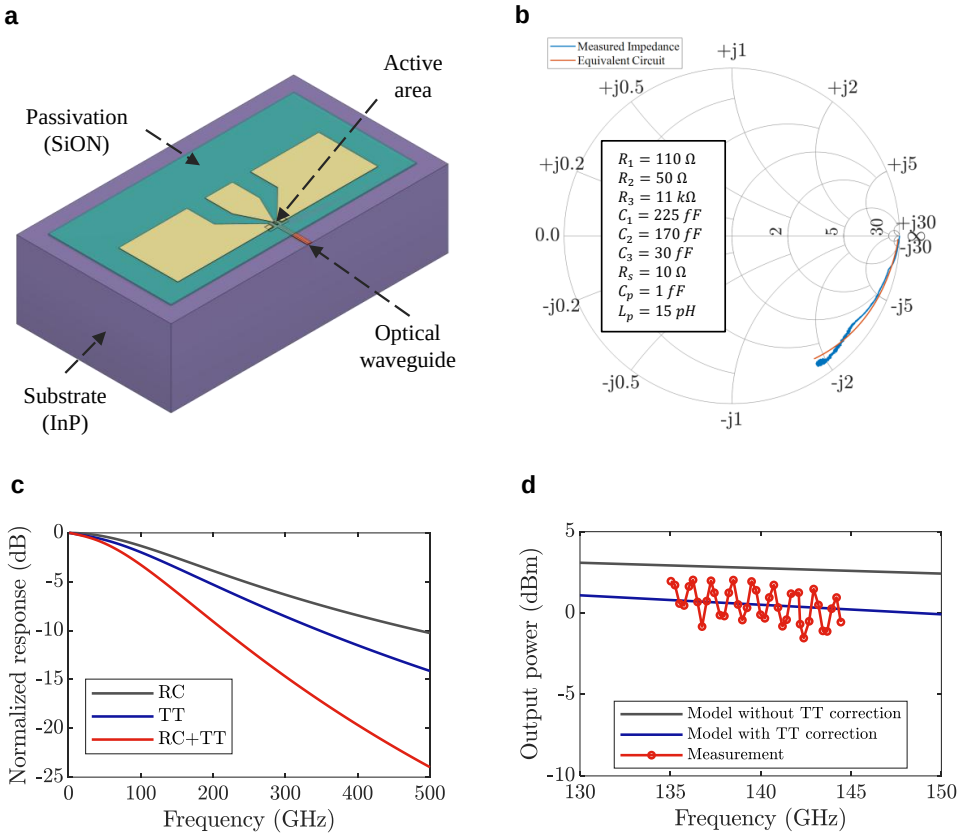

Figure 3.12: UTC-PDs for terahertz generation. **a** 3D illustration of a waveguide-integrated UTC-PD with GSG pads. **b** Measured impedance of a 3x10 μm^2 device compared to the equivalent circuit with fitted values. **c** Normalised power response of RC, transit-time, and combined effects. **d** Output power at around 140 GHz predicted by the model with and without transit-time limitation, and measured power of a real device between 135 and 145 GHZ.

In the mixer design process, we employed the 3D EM model shown in Figure 3.13. This simplified model defines the UTC active area and contacts using a perfect electric conductor (PEC) while embedding a discrete excitation port in the active area of the device. That port is then linked to the equivalent circuit, which is reduced to the components representing the active area of the UTC-PD ($R_s, R_1, C_1, R_2, C_2, R_3, C_3$). This approach allows us to model the impedance of the UTC-PD and predict the output power that a device of the same intrinsic characteristics as the measured 3x10 μm^2 will provide to the SBDs for frequency mixing.

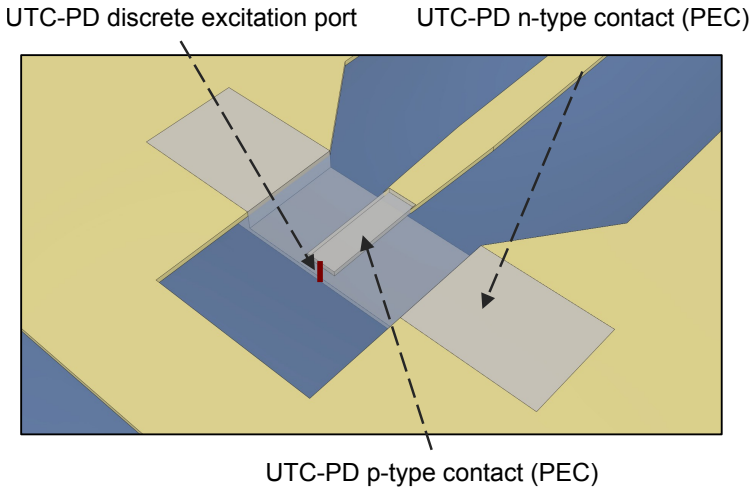

Figure 3.13: EM model of the UTC-PD for mixer simulations with discrete excitation port.

3.2.4 Mixer design

Figure 3.14 shows the mixer architecture, depicting the critical components necessary for isolating and handling the DC, RF, LO, and IF signals. Firstly, as the antiparallel SBDs are arranged in a shunt topology, open circuits at RF, LO, and IF frequencies are required to provide signal grounding paths. Secondly, a key requirement is to provide a reverse bias voltage to the UTC-PD. Therefore, a bias-T circuit is required, which comprises a 'DC block' and an 'LO block' to isolate the DC path. The down-converted IF signal is extracted via a dedicated T-junction, with an additional 'LO block' to isolate the IF path.

Taking these considerations into account, the mixer circuit was designed and optimised. This required careful and non-trivial geometric design of the filters, T-junction, and antenna. Typically, the requirements for the RF, LO, and IF bands

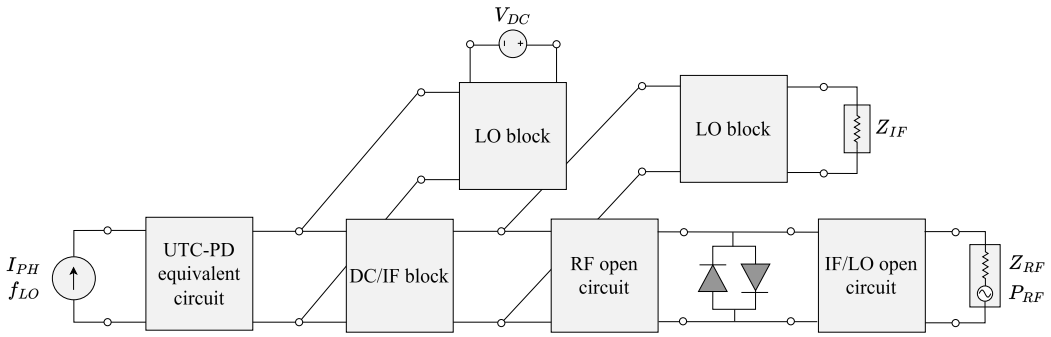

Figure 3.14: Circuit schematic of the mixer architecture used in the monolithically integrated mixer.

are first defined, after which the optimisation process begins. In this work, the goal is to maximise the operational bandwidth to cover the full 220–330 GHz range. To achieve this, broadband structures are selected and then optimised to provide the best possible performance across the entire RF and LO bands. Each component is first designed and optimised individually by combining S-parameter simulations in CST with HB simulations in ADS to minimise conversion loss and required LO power. The complete mixer is then simulated and reoptimised in CST to improve the accuracy of the overall performance prediction.

The final design, illustrated in Figure 3.15, highlights its key components. Two main filtering structures were employed to block RF, LO, and DC signals. A hammerhead-type low-pass filter [3-11] functions as the LO block in the bias T and simultaneously blocks the LO and RF signals to enable IF extraction. The simulated S-parameters, shown in Figure 3.16**b**, indicate a rejection greater than 15 dB between 123.5 GHz and 353.2 GHz.

The DC block in the bias T circuit was implemented using an open-ended series stub [3-12], which also isolates the DC and LO path from the RF and IF signals. The S-parameters shown in Figure 3.16**a** indicate an insertion loss below 2 dB within the LO band (110–165 GHz). To ensure the RF reflection coefficient seen by the SBDs approximates an open circuit, a matching section was included between the antiparallel diode cell and the first T-junction. This section also provides additional LO impedance matching. A key feature is the use of cross-track bridges in the T-junction. Discontinuities in the CPW ground excite the undesired

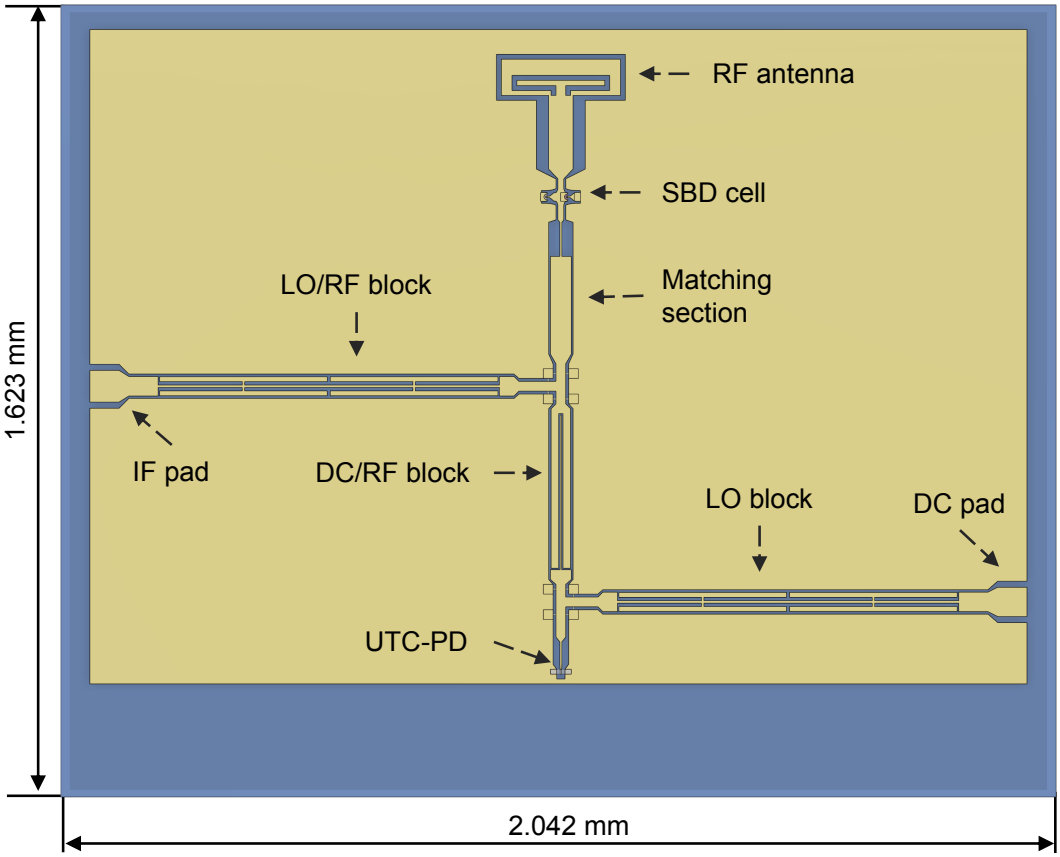

Figure 3.15: Top view of the complete monolithically integrated mixer indicating the key components.

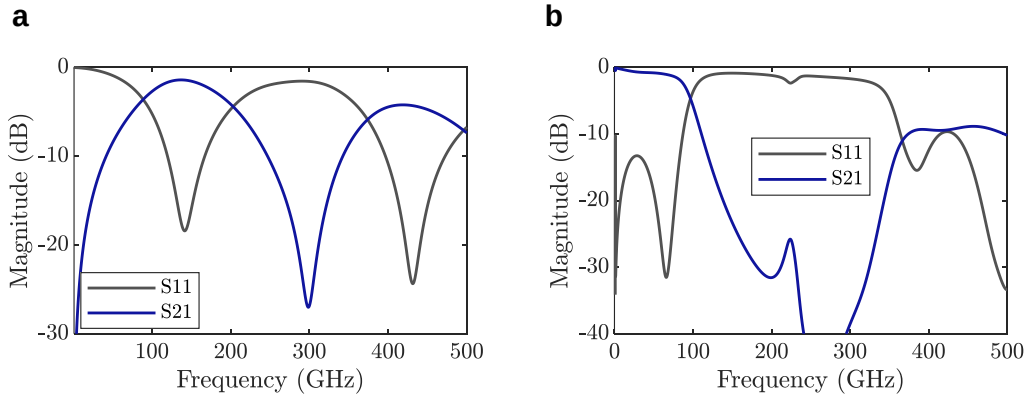

Figure 3.16: Simulated S-parameters of open-ended series stub (**a**) and hammerhead-type low-pass filter (**b**).

odd mode, which is mitigated by implementing these bridges [3-12]. The bridges were placed under the passivation layer, as shown in Figure 3.17, for fabrication simplicity, connecting them to the top metallisation through vias, in the same way as in the device fabrication processes. The resulting S-parameters are displayed in

Figure 3.18**a**, where the theoretical ideal behaviour is observed at low frequencies: S11 of -9.5 dB and S21 of -3.5 dB. However, this performance deteriorates with increasing frequency, particularly for S31 due to the perpendicular orientation of port 3 to the junction input ports 1 and 2. Figure 3.18**b** illustrates the energy balance, demonstrating near lossless performance at 1 GHz when using bridges, compared to 0.93 without them. The energy loss offset is directly attributed to the excitation of the odd mode. At higher frequencies, losses increase due to metallic and dielectric losses and, more significantly, the excitation of substrate modes. Within the LO band, the energy balance ranges between 0.97 and 0.96.

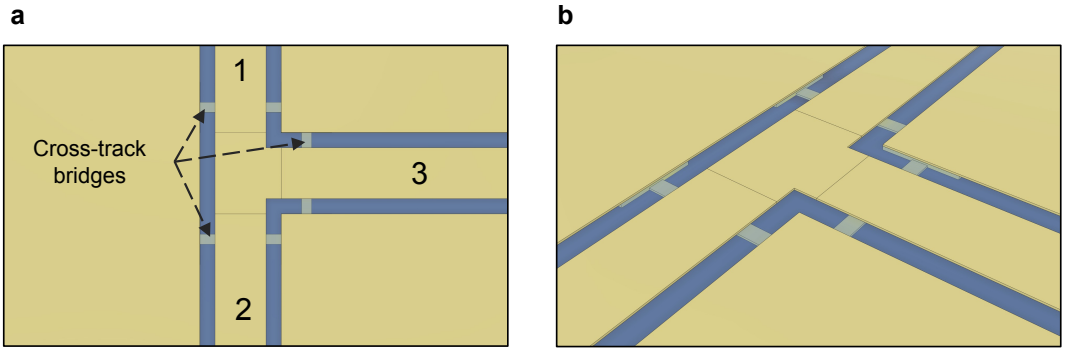

Figure 3.17: T-junctions with cross-track bridges bellow passivation. **a** Top view. **b** Perspective view.

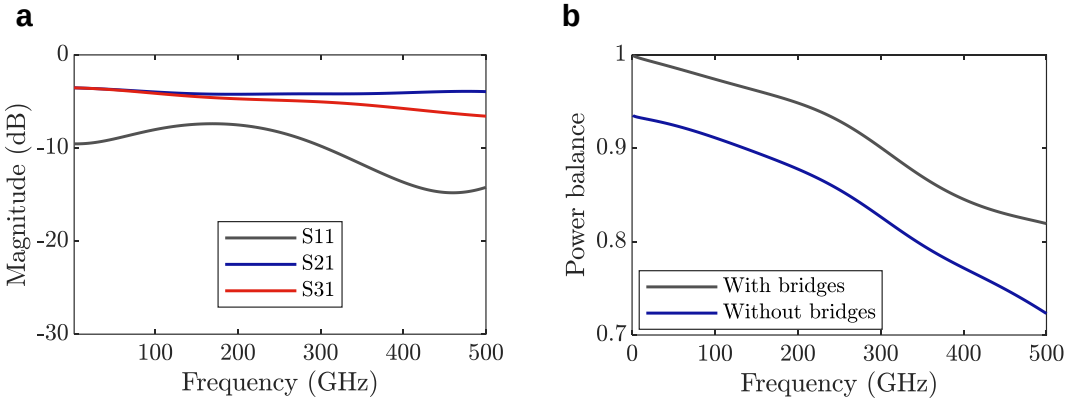

Figure 3.18: T-junction simulations. **a** S-parameters of the T-junction with cross-track bridges below the passivation layer. **b** Energy balance comparison with and without cross-track bridges.

The RF antenna implements two functions: coupling the incoming THz radiation and providing grounding for the IF and LO signals. The second function is achieved by carefully adjusting the distance between the SBDs and the antenna. The antenna's S11, simulated from the output of the SBDs, is shown in Figure 3.19**a**. The antenna S11 presents high return loss, exceeding 17.2 dB across the RF band (220–330 GHz). At lower frequencies, up to the edge of the LO band, the antenna acts as a reflective element with an S11 greater than -2.5 dB. Further analysis is presented in Figure 3.19**b**, where the S11 is plotted on a Smith chart. At 1 GHz, the antenna behaves as an open circuit, shifting with increasing frequency and becoming a short circuit at 70 GHz. This results in the main limitation on the mixer's IF bandwidth. Within the LO band, the antenna provides near open-circuit conditions again. However, deviations from an ideal open-circuit result in the requirement for higher LO power compared to the ideal case.

The intrinsic mixer performance was evaluated using HB simulations in ADS, based on the complete circuit's S-parameters using the test bench described in Chapter 2. Figure 3.20**a** shows the conversion loss versus RF frequency for UTC-PD photocurrents of 4, 6, 8, and 10 mA, at a fixed IF of 1 GHz. Best LO matching occurs at 246 GHz, achieving 16.55 dB loss with 4 mA. At 6 mA, loss stays below 20 dB over most of the band, with optimal performance at 8 mA.

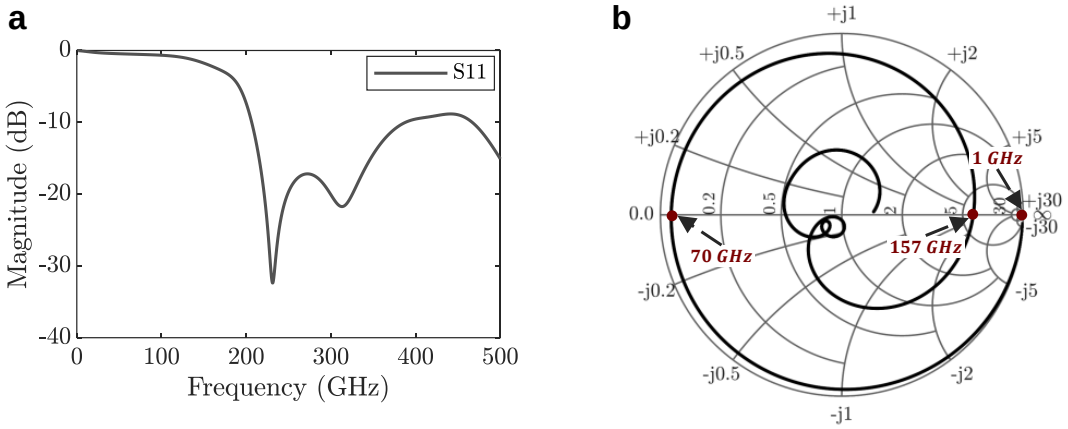

Figure 3.19: S11 of the RF antenna shown in dB units (**a**) and in Smith chart format (**b**).

A minimum conversion loss of 12.63 dB is found at 246 GHz with 8 mA of photocurrent, and a maximum of 17.33 dB at 330 GHz with 10 mA. In the context

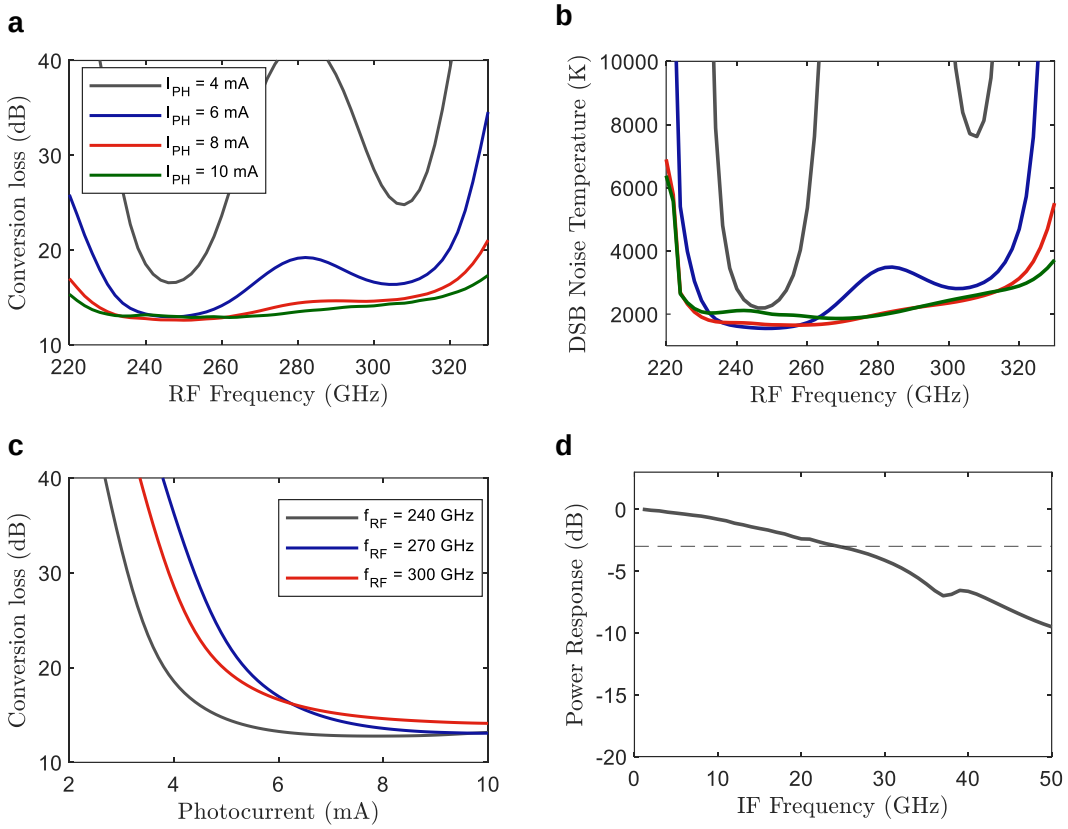

Figure 3.20: Predicted mixer performance. **a**-**b** Conversion loss and DSB noise temperature as a function of RF frequency for different pumping photocurrents. **c** Conversion loss as a function of pumping photocurrent for different RF frequencies. **d** IF response.

of wireless communications, the variation of conversion loss across the RF band would imply a lower SNR for certain channels, reducing the total achievable data rate compared to an ideal mixer with flat conversion loss.

HB simulations also enable extraction of the DSB noise temperature, considering the contributions from SBD Shot and thermal noise. Even at a photocurrent of 4 mA, the simulated noise temperature reaches a low value of 2194 K at 246 GHz. For 6 mA, the minimum noise temperature, 1548 K, is observed at 248 GHz. Notably, the optimum noise temperature is achieved at lower photocurrents than the optimal conversion loss due to the Shot noise contribution, which is directly proportional to the diode current and increases with higher pumping levels. Figure 3.20**c** shows the conversion loss as a function of photocurrent at 240, 270, and 300 GHz. At 240 GHz, near-optimum performance is achieved at approximately 6 mA, com-

pared to 8 mA at 270 and 300 GHz. Finally, the IF response, shown in Figure 3.20**d**, reveals an IF 3 dB bandwidth of approximately 25 GHz.

3.2.5 Antenna-lens simulations

Planar antennas in CPW emit or receive radiation through the substrate (downwards) due to the substrate's high permittivity compared to air. This also causes beam trapping within the substrate due to strong reflections at the substrate-air interface, exciting surface-wave modes [3-13]–[3-15]. Moreover, planar antennas at THz frequencies intrinsically exhibit low directivity. To mitigate these issues, a common solution consists of mounting the antenna on a hyper-hemispherical lens, which focuses the beam, enhances directivity, and reduces reflections [3-16]. Ideally, the lens must have the same dielectric constant as the substrate. Typically high-resistivity silicon is used due to its high dielectric constant and low dielectric losses at THz frequencies.

In this work, we used this approach by employing a 6 mm diameter silicon lens with an offset distance (L) of 0.87 mm. The optimum setback thickness was calculated by using $L = r_{lens}/\sqrt{\varepsilon_r}$, where r_{lens} is the radius of the lens, and ε_r is the substrate relative permittivity [3-16]. In Figure 3.21**a**, a cross-sectional illustration of using a hyper-hemispherical lens with a planar antenna is shown. The antenna and lens were simulated together to analyse their performance in terms of reflections, radiation pattern, and coupling efficiency. The simulation model, illustrated in Figure 3.21**b**, includes the full 6 mm diameter silicon lens and the antenna on an InP substrate, excited via a discrete port. The optimum offset distance of 0.87 mm includes the silicon lens and the InP substrate with a thickness of 0.15 mm. Since silicon and InP have similar relative permittivity values (12.5 and 11.9, respectively), the offset thickness of the silicon lens from the centre of the sphere can be determined as the difference, which is 0.72 mm.

The resulting S11 is shown in Figure 3.22**a**. A key difference compared to the simulated S-parameters without the lens is the appearance of ripples, caused by reflections at the substrate-lens and lens-air interfaces. These reflections also lead to a deterioration in return loss at the RF band. Nevertheless, the return loss remains

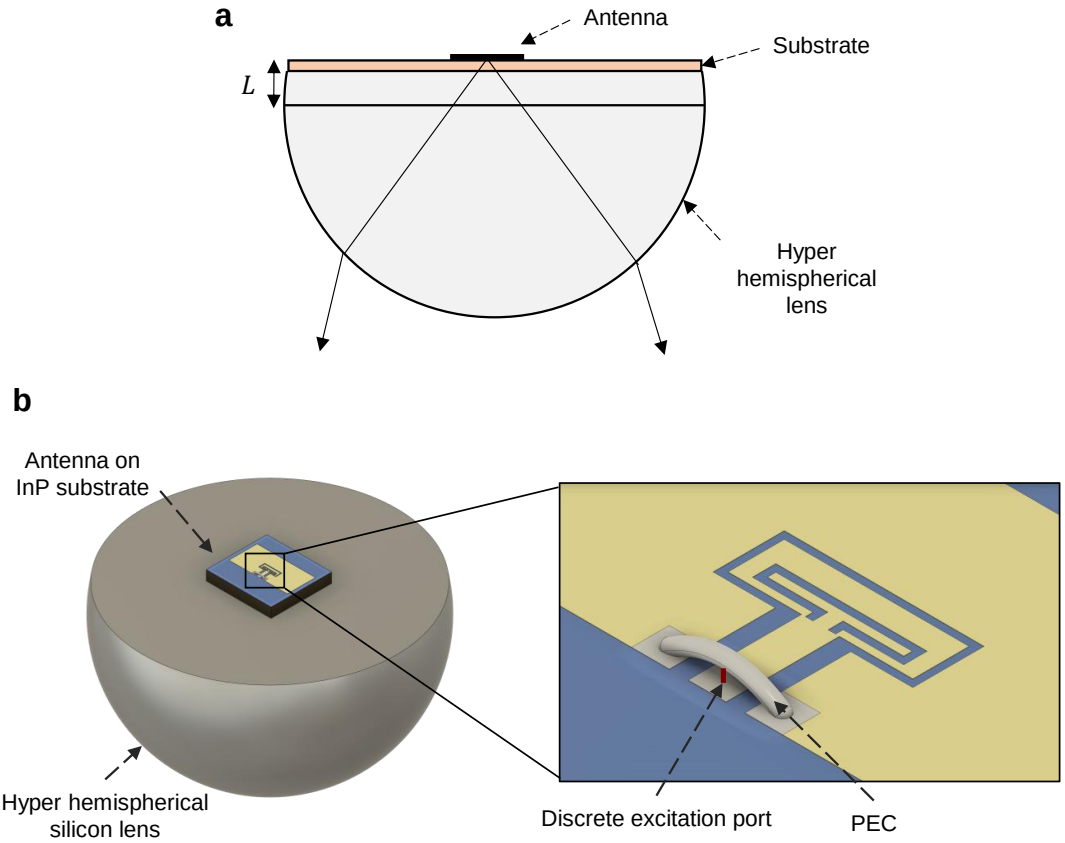

Figure 3.21: Antenna-lens system. **a** Cross-sectional illustration of a planar antenna mounted on a hyper-hemispherical lens to prevent reflected rays and enhance the radiation pattern. **b** Model used for simulations, including the 'stand-alone' antenna on InP substrate excited by a discrete port, and a 6 mm hyper-hemispherical silicon lens.

better than 10 dB across the entire RF band. The calculated radiation efficiency, based on the emitted power directed towards the lens (downwards), is shown in Figure 3.22**b**. The coupling loss varies between a maximum of 1.69 dB at 320 GHz and a minimum of 1.04 dB at 270 GHz. This introduces additional loss compared to the intrinsic mixer performance shown in Figure 3.20. The radiation patterns at 240, 270, and 300 GHz are depicted in Figure 3.23. As expected, the maximum radiation occurs in the +z-direction, corresponding to the downward direction towards the lens. The calculated directivities are 17.04, 17.07, and 17.54 dBi at 240, 270, and 300 GHz, respectively. The radiation patterns show significant variability with frequency, which is an inherent limitation of using a lens. Additionally, the presence of an undesired sidelobe can be attributed to parasitic radiation aris-

ing from substrate mode excitation and multiple reflections at the silicon-air and substrate-silicon interfaces.

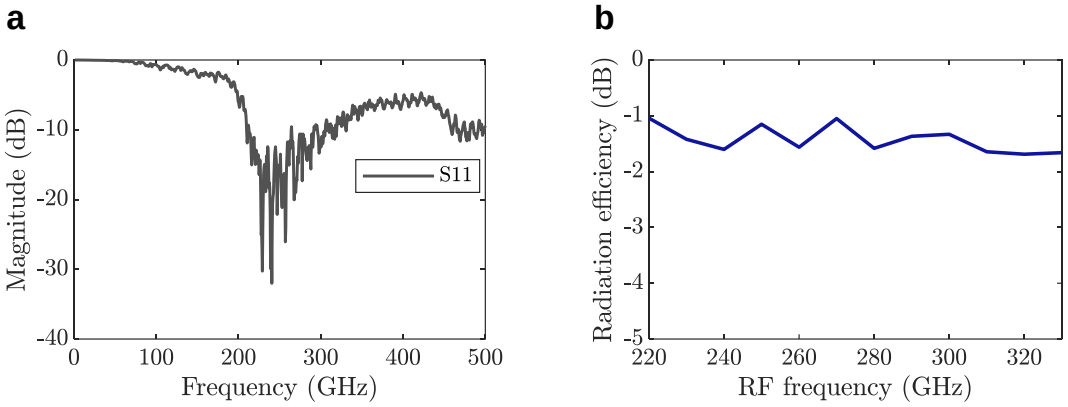

Figure 3.22: Results of antenna-lens simulations. **a** S11. **b** Radiation efficiency calculated considering the hemisphere space towards the lens.

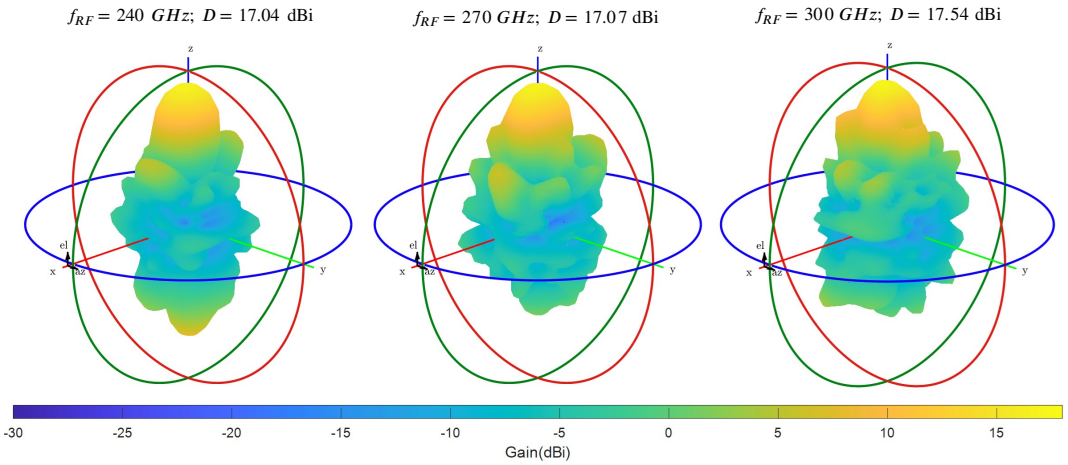

Figure 3.23: 3D radiation patterns of the antenna-lens system at 240, 270, and 300 GHz.

3.2.6 Fabrication

The fabrication of the monolithically integrated receiver is out of the scope of this work, being limited to the design and simulation content presented in this chapter. However, in this section we briefly present a possible fabrication procedure, based on the UTC-PD process [3-2]. The simplified proposed steps for fabrication are illustrated in Figure 3.24.

The wafers are first prepared for fabrication, removing the InP capping layer with HCl:H_3PO_4 (1:1) (**a**). Then, the UTC-PD p-contact is deposited by sputtering

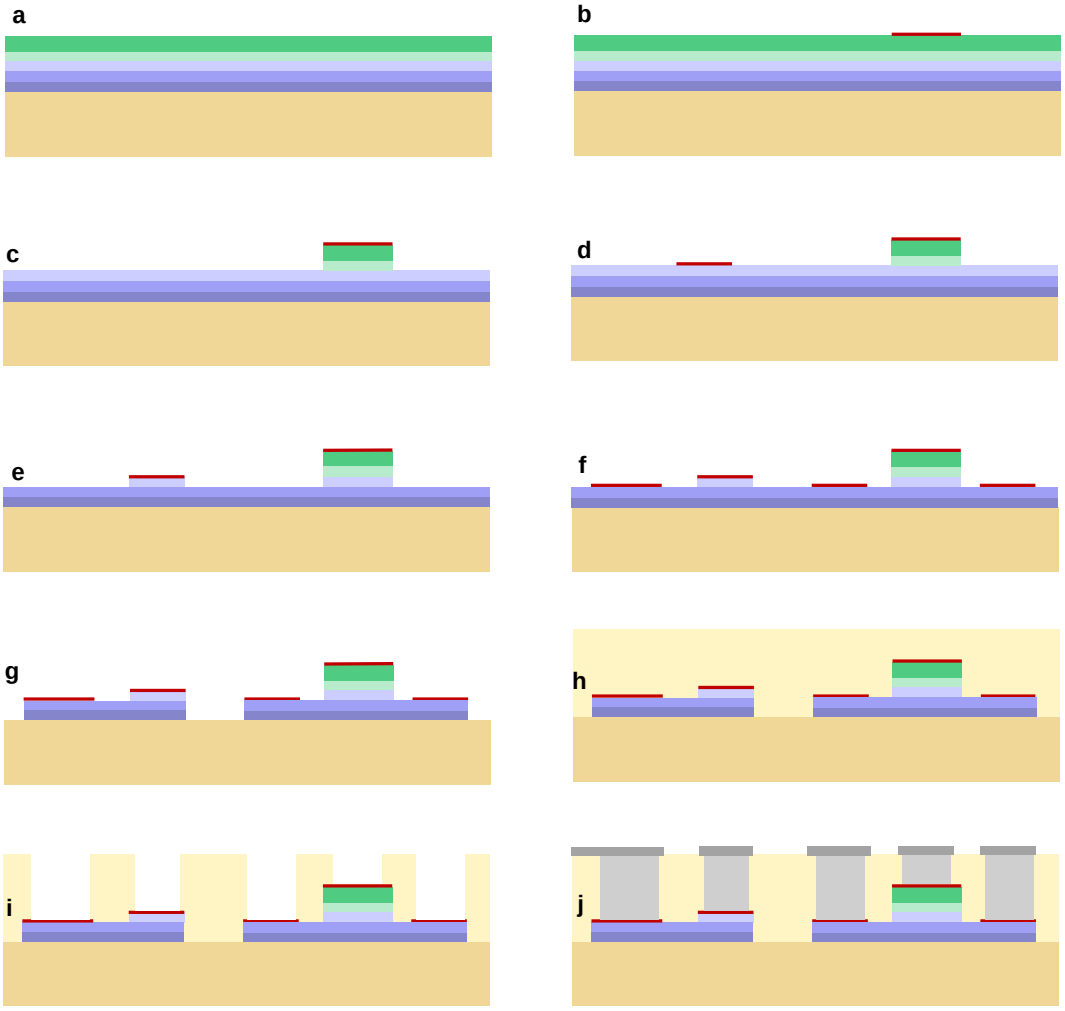

Figure 3.24: Proposed fabrication steps for the monolithically-integrated receiver. **a** Wafer preparation. **b** p-contact deposition. **c** Etching of p-type layers. **d** Schottky contact deposition. **e** Etching of n-type collector layer. **f** n-contact deposition, followed by thermal annealing. **g** Etching of final device features. **h** SiON passivation layer deposition. **i** Etching of vias. **j** Deposition of vias and top metallisation.

a metal stack of Ti/Pt/Au (75/50/400 nm) (**b**). The next step is to remove the p-type layers and expose the n-type collector layer, which is achieved by employing reactive ion etching (RIE) (**c**). From now on, every etching step is done with RIE. In comparison to wet-etching processes, RIE etches in a mostly vertical direction with minimal undercutting, resulting in better aspect-ratio and well-defined features [3-17]. The etching pattern is defined using ultraviolet (UV) lithography. After depositing the Schottky contact metal stack, the n-type collector layer is removed (**e**) and the same metal stack is deposited to make the ohmic n-contacts for the UTC-PD

and the SBD. To reduce the contact resistivity, rapid thermal annealing (RTA) must be performed, which must be carefully adjusted to avoid damaging the Schottky contact. After this step, the final device features are created (**g**), removing the rest of layers down to the substrate and defining the UTC-PD optical waveguide. An important consideration is to ensure the leakage current is minimised. If the devices are left exposed to air, a natural oxide layer grows, increasing the leakage current. To solve this, the oxide layer is removed with a 10 % HCl solution, followed by the deposition of a SiON passivation layer of 2 µm using chemical vapour deposition (CVD) (**h**). To access the devices, vias are etched exposing the Schottky and ohmic contacts, and gold is deposited (**i**). The top metallisation defining the mixer circuit can be deposited in the same step, or in a separate procedure employing for example electroplating (**j**).

3.3 Summary and discussion

This chapter has presented the design of InP SBD using the standard UTC-PD epitaxial structure and their monolithic integration to realise a subharmonic 220–330 GHz receiver. The designed diodes achieve intrinsic conversion loss close to the state-of-the-art for SBD-based mixers, demonstrating their suitability for terahertz operation. However, using the weakly doped InP collector layer for the Schottky contact introduces high series resistance, which limits performance. To improve this, the UTC-PD epitaxy could be modified to include an optimally doped layer for terahertz Schottky contacts, though such changes must be carefully evaluated as they also affect the UTC-PD response. Further improvements could be achieved by using alternative materials to lower the barrier height. While InP Schottky contacts already reduce LO power requirements compared to GaAs, making the contact on an InGaAsP layer could further enhance high-frequency operation. Some design choices, such as embedding the InP diodes in SiON, were made to align with the existing UTC-PD fabrication process, though alternative approaches, like air-bridged diodes, could improve parasitics and cut-off frequency.

Regarding the monolithic receiver, we have introduced a novel CPW-based

design with predicted performance approaching the state-of-the-art for SBD-based mixers in this frequency band, demonstrating the potential of the proposed optoelectronic receiver concept. However, the high CPW loss due to substrate mode excitation and odd-mode propagation at T-junctions suggests that alternative designs should be explored, particularly for higher frequency applications. The use of InP as a supporting substrate presents challenges due to its poor thermal conductivity, dielectric losses, and fragility, which prevent further thinning to mitigate dielectric loading and substrate mode excitation. Techniques such as micro-transfer printing [3-18] offer a promising solution by enabling the transfer of devices onto more suitable substrates and waveguide platforms for high-frequency operation [3-19]. The mixer architecture could also be improved, for instance, by increasing the IF bandwidth beyond the current 25 GHz, which would be particularly beneficial for high-speed wireless communications. Additionally, narrow-band designs could be explored to reduce LO power requirements and improve impedance matching, rather than targeting the full 220–330 GHz range. A key outcome is that the modelling approach presented in Chapter 2 allows accurate prediction of the complete performance of the optoelectronic receiver.

References

[3-1] A. Maestrini, B. Thomas, H. Wang, *et al.*, "Schottky diode-based terahertz frequency multipliers and mixers," *Comptes Rendus Physique*, vol. 11, no. 7-8, pp. 480–495, 2010.

[3-2] X. Lin, M. Natrella, J. Seddon, *et al.*, "High performance waveguide uni-travelling carrier photodiode grown by solid source molecular beam epitaxy," en, *Opt. Express*, vol. 27, no. 25, pp. 37 065–37 086, Dec. 2019.

[3-3] Z. Pang, "Schottky contacts to indium phosphide and their applications," Ph.D. dissertation, McMaster University, 1997.

[3-4] S. Adachi, *Physical Properties of III-V Semiconductor Compounds*, en. John Wiley & Sons, Nov. 1992.

[3-5] K. Tappura, "Electrical and optical properties of GaInAsP grown by gas-source molecular beam epitaxy," en, *J. Appl. Phys.*, vol. 74, no. 7, pp. 4565–4570, Oct. 1993.

[3-6] Y. A. Goldberg and N. M. Shmidt, "Gallium Indium Arsenide Phosphide ($Ga_xIn_{1-x}As_yP_{1-y}$)," in *Handbook Series on Semiconductor Parameters*, World Scientific, Nov. 1996, pp. 153–179.

[3-7] N. M. Shmidt, "Indium Phosphide (InP)," in *Handbook Series on Semiconductor Parameters*, World Scientific, Nov. 1996, pp. 169–190.

[3-8] M. Sotoodeh, A. H. Khalid, and A. A. Rezazadeh, "Empirical low-field mobility model for III–V compounds applicable in device simulation codes," *J. Appl. Phys.*, vol. 87, no. 6, pp. 2890–2900, 2000.

[3-9] J. C. Li, M. Sokolich, T. Hussain, and P. M. Asbeck, "Physical modeling of degenerately doped compound semiconductors for high-performance HBT design," *Solid State Electron.*, vol. 50, no. 7, pp. 1440–1449, Jul. 2006.

[3-10] I. Belio-Apaolaza, J. Seddon, D. Moro-Melgar, *et al.*, "Photonically-driven schottky diode based 0.3 THz heterodyne receiver," en, *Opt. Express*, vol. 30, no. 24, pp. 43 223–43 236, Nov. 2022.

[3-11] C. Wang, Y. He, B. Lu, *et al.*, "Robust sub-harmonic mixer at 340 GHz using intrinsic resonances of hammer-head filter and improved diode model," en, *J. Infrared Millim. Terahertz Waves*, vol. 38, no. 11, pp. 1397–1415, Nov. 2017.

[3-12] R. N. Simons, *Coplanar Waveguide Circuits, Components, and Systems* (Wiley Series in Microwave and Optical Engineering), en. New York, NY: Wiley-IEEE Press, Apr. 2004.

[3-13] N. G. Alexopoulos, P. B. Katehi, and D. B. Rutledge, "Substrate optimization for integrated circuit antennas," *IEEE Trans. Microw. Theory Tech.*, vol. 31, no. 7, pp. 550–557, 1983.

[3-14] D. Pozar, "Considerations for millimeter wave printed antennas," *IRE Trans. Antennas Propag.*, vol. 31, no. 5, pp. 740–747, Sep. 1983.

[3-15] P. Katehi and N. Alexopoulos, "On the effect of substrate thickness and permittivity on printed circuit dipole properties," *IRE Trans. Antennas Propag.*, vol. 31, no. 1, pp. 34–39, Jan. 1983.

[3-16] G. M. Rebeiz, "Millimeter-wave and terahertz integrated circuit antennas," *Proc. IEEE Inst. Electr. Electron. Eng.*, vol. 80, no. 11, pp. 1748–1770, 1992.

[3-17] M. Huff, "Recent advances in reactive ion etching and applications of high-aspect-ratio microfabrication," en, *Micromachines (Basel)*, vol. 12, no. 8, p. 991, Aug. 2021.

[3-18] J. Yoon, S.-M. Lee, D. Kang, M. A. Meitl, C. A. Bower, and J. A. Rogers, "Heterogeneously integrated optoelectronic devices enabled by micro-transfer printing," en, *Adv. Opt. Mater.*, vol. 3, no. 10, pp. 1313–1335, Oct. 2015.

[3-19] T. Nagatsuma, W. Gao, Y. Kawamoto, T. Ohara, H. Ito, and T. Ishibashi, "Si- and SiC-based integration platforms for generation, transmission, and detection of THz signals," in *2024 International Topical Meeting on Microwave Photonics (MWP)*, IEEE, Sep. 2024, pp. 1–4.

Chapter 4

Hybrid integration

The idea of hybrid integration of UTC-PDs and SBDs for terahertz reception was originally conceived by C.C. Renaud, J. Seddon, and I. Belio-Apaolaza. The InGaAs SBDs models used for the mixers presented in this chapter were provided by the Rutherford Appleton Laboratory (RAL) and Teratech Components. The remaining designs and simulations presented in this chapter were carried out by I. Belio-Apaolaza.

This chapter explores the design of 220–330 GHz optoelectronic receivers enabled by hybrid integration, using existing UTC-PDs and SBDs. It begins by introducing InGaAs antiparallel SBDs, which are then employed to develop two different 300 GHz hybrid integrated mixers. The first mixer is based on CPW with quasi-optical coupling, while the second employs microstrip and rectangular waveguide. The CPW-based receiver was designed with a complete packaging solution, incorporating DC and IF connections. This receiver was fabricated and tested, with the results presented in Chapter 5. Some results and figures referring to this receiver have been adapted from [4-1] and are reproduced here under the terms of a CC-BY license.

4.1 Air-bridged antiparallel InGaAs SBDs

As discussed in Chapter 1, Schottky contacts on InGaAs have great potential for use in terahertz mixers with low LO power requirements. Compared to InP, electron mobility is about twice as high [4-2], resulting in lower series resistance, which

in turn improves the conversion loss of an SBD-based mixer. In addition, the lower barrier height further reduces the required LO power. Therefore, using InGaAs SBDs is optimum for developing the optoelectronic receiver concept targeted in this work via hybrid integration. To implement a subharmonic mixer, THz InGaAs antiparallel SBDs provided by RAL and Teratech Components were used. The 3D structure of the antiparallel diodes is illustrated in Figure 4.1**a**. These are planar air-bridged diodes with a Schottky contact diameter of less than 1 µm. The chip dimensions are 120 µm by 75 µm, with a substrate thickness of approximately 15 µm, achieved by chemical thinning [4-3]. This design offers very low parasitics, enabling operation at THz frequencies.

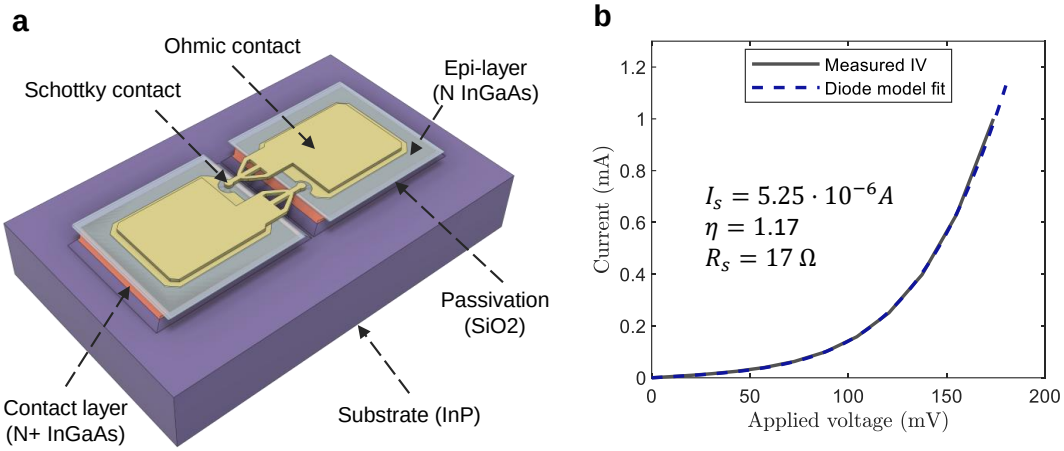

Figure 4.1: Planar air-bridged antiparallel InGaAs SBDs for terahertz mixing. **a** 3D model highlighting the different layers. **b** Forward I-V curve with fitted parameters to the standard thermionic diode equation. Adapted from [4-1], under a CC-BY license.

An example of a measured I-V curve is shown in Figure 4.1**b**, along with the fitted value from the diode equation. The curve reveals a very low barrier height, with a turn-on voltage of less than 0.15 V, and the fitted series resistance is 17 Ω. The junction capacitance cannot be measured for being in the sub-fF magnitude, but the theoretically calculated zero-bias capacitance is 0.83 fF. This results in a cut-off frequency of 11.42 THz, roughly an order of magnitude higher than the InP diodes presented in the previous chapter. This improvement is caused by a combination of higher electron mobility and optimum epilayer doping in the range of $10^{17} cm^{-3}$. As a first step, the intrinsic conversion loss with respect to RF frequency and LO

power is shown in Figure 4.2. The optimum LO power is found to be -7 dBm, achieving a conversion loss of 10.13 dB. Even with reduced LO power of -20 dBm, a conversion loss of 24 dB is achieved. The optimum RF and RF impedances to obtain this performance are $Z_{LO} = (140 - j26)\,\Omega$ and $Z_{RF} = (77 + j15)\,\Omega$.

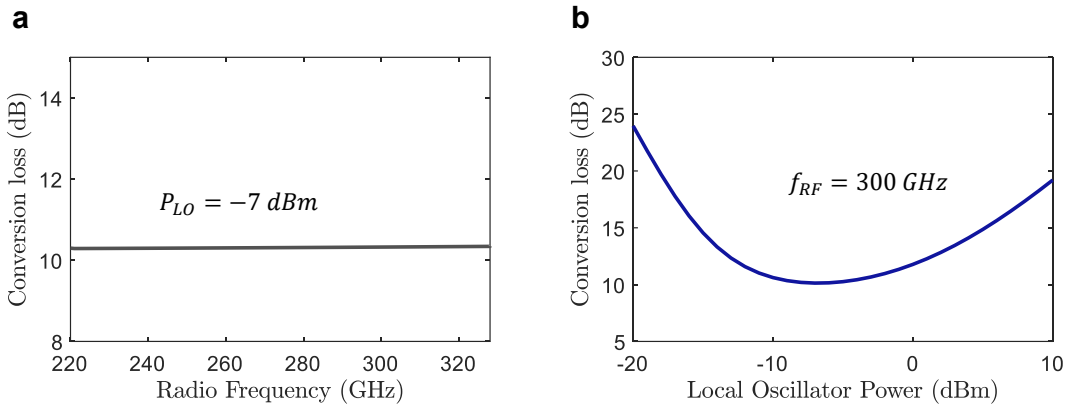

Figure 4.2: Ideal 220-330 GHz mixer performance by using InGaAs SBDs. **a** Conversion loss as function of RF frequency. **b** Conversion loss as a function of LO power. Adapted from [4-1], under a CC-BY license.

4.2 220-330 GHz quasi-optical receiver

4.2.1 Co-planar waveguide on quartz

Following the same approach as for the monolithic receiver, we designed a hybrid integrated receiver in which the RF signal is coupled to the mixer circuit via a planar antenna mounted on a silicon lens (quasi-optical coupling). Therefore, a CPW waveguide was used to implement the mixer circuit, including the planar antenna. The substrate was chosen so that its dielectric properties are optimal at THz frequencies. We selected fused silica, i.e., quartz, which has a lower dielectric constant than InP, minimising the excitation of substrate modes, and very low dielectric losses at THz frequencies. In addition, quartz presents good thermal stability and robustness, making it a typical material for use in THz circuits [4-4].

Figure 4.3 provides insights into the CPW on a 75 µm-thick quartz substrate with 3 µm-thick gold. The signal line width for a 50 Ω line is 80 µm, with a signal-to-ground gap of 10 µm. While further miniaturisation is possible, the gap is limited to approximately 10 µm due to the optical lithography method used for the mixer

circuit. Figure 4.3**c** depicts a fundamental CPW mode, with the simulated attenuation shown in Figure 4.3**d**. Compared to CPW on InP technology, this design exhibits lower attenuation at high frequencies, remaining below 3 dB/mm even at 500 GHz.

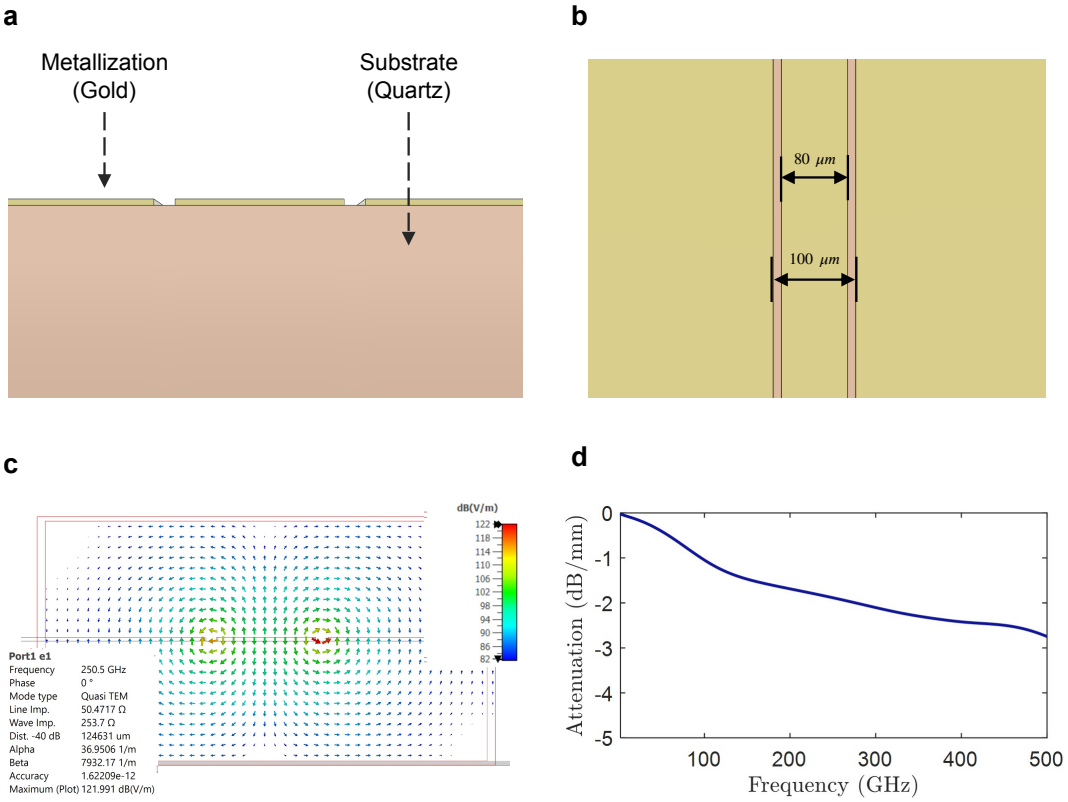

Figure 4.3: Insights on the CPW waveguide used for the hybrid integrated mixer. **a** Cross-sectional view. **b** Dimensions of a 50 Ω line. **c** Quasi-TEM CPW mode distribution for a 50 Ω line. **d** Attenuation in dB/mm.

4.2.2 Flip-chip antiparallel series SBDs on CPW

To integrate the antiparallel InGaAs SBDs into the CPW on quartz, flip-chip bonding was employed, as illustrated in Figure 4.4**a**. This figure shows the 3D model used in EM simulations to obtain the S-parameters of the diode cell. Like the monolithic receiver, the model includes four ports: two discrete ports at the SBDs active areas and two waveguide ports at the CPW inputs. Unlike wire bonding, the flip-chip approach avoids introducing additional inductance, making it well suited for terahertz operation. Figure 4.4**b** presents the simulated E-field distribution at 300 GHz when excited from a CPW input port.

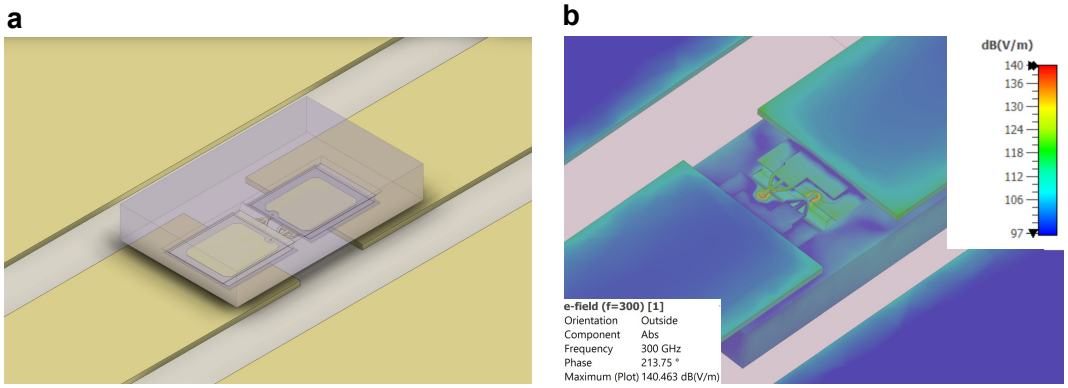

Figure 4.4: Flip-chip antiparallel series SBDs on CPW. **a** 3D model to obtain the S-parameters of the diode cell. **b** Simulated E-field distribution when exciting from a CPW port.

After obtaining the S-parameters of the diode cell, the subharmonic mixer performance can be evaluated, taking into account the cell parasitics and circuit losses. Figure 4.5 shows the conversion loss as a function of RF frequency and LO power, incorporating the S-parameters of the diode cell and comparing them to the ideal mixer case. The performance is very similar in both cases, with only a minimal degradation in conversion loss of about 1 dB. This contrasts with the InP shunt diodes presented in Chapter 3. The improvement is attributed to the lower parasitics of these diodes, as they are air-bridged rather than buried in a dielectric material, and to the use of a series topology, which enhances power coupling to the active area of the SBD and ensures the diodes are perfectly balanced [4-5]. The optimum RF and LO embedding impedances $Z_{LO} = (29 + j51)\,\Omega$ and $Z_{RF} = (36 + j14)\,\Omega$.

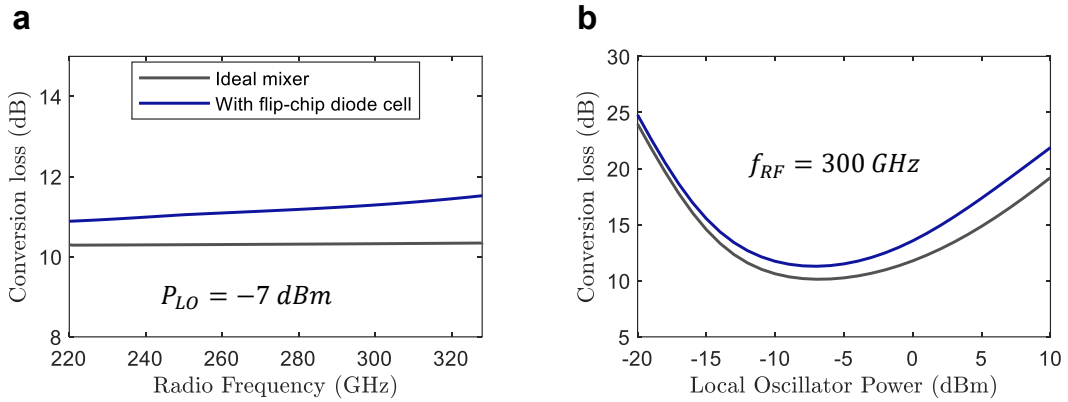

Figure 4.5: 220-330 GHz mixer performance by using flip-chip InGaAs SBDs compared to the ideal mixer. **a** Conversion loss as function of RF frequency. **b** Conversion loss as a function of LO power.

4.2.3 Mixer design

The subharmonic mixer architecture is shown in Figure 4.6. Compared to the monolithically integrated mixer, the key difference is the series topology of the SBDs. This requires short-circuit conditions for the RF, LO, and IF signals, represented by the circuit blocks 'RF short circuit' and 'IF/LO short circuit'. The rest of the mixer architecture remains unchanged, with the IF impedance fixed at 50 Ω.

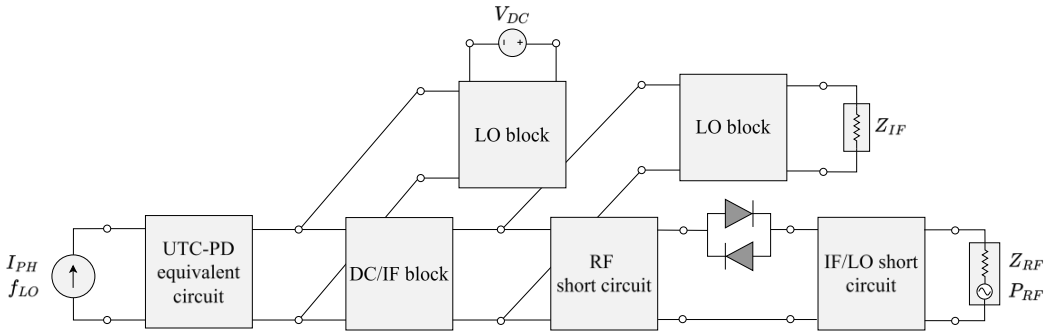

Figure 4.6: Circuit schematic of the mixer architecture used in the hybrid integrated mixer. Adapted from [4-1], under a CC-BY license.

The mixer circuit was designed and optimised based on these considerations, using the same procedure and as described in Chapter 3. The final optimised design is shown in Figure 4.7. The filtering structures used in this design are the same type as those in the monolithically integrated mixer, i.e. hammerhead-type low-pass filters for the 'LO block' and an open-ended series stub for the 'DC block'.

The S-parameters of these two components are depicted in Figure 4.8**a-c**. The 'DC block' exhibits an insertion loss of less than 2 dB across the entire LO band, while the 'LO block' provides a rejection ratio greater than 15 dB. In contrast to the monolithic receiver, to recirculate the RF signal, an 'RF block' component was incorporated using a hammerhead-type low-pass filter, with a rejection ratio typically greater than 20 dB at the RF band. This addition aims to reduce RF losses associated with this section of the circuit, as the T-junction introduces additional losses. The S-parameters of the T-junction excited from port 1 are shown in Figure 4.8**d**, from which the power balance at 150 GHz and 300 GHz is calculated as 0.7 and 0.36, respectively. Here, the cross-track bridges were implemented using 50 µm wide ribbons. Same ribbons were employed to connect the UTC-PD to the

quartz circuit, as seen in Figure 4.7.

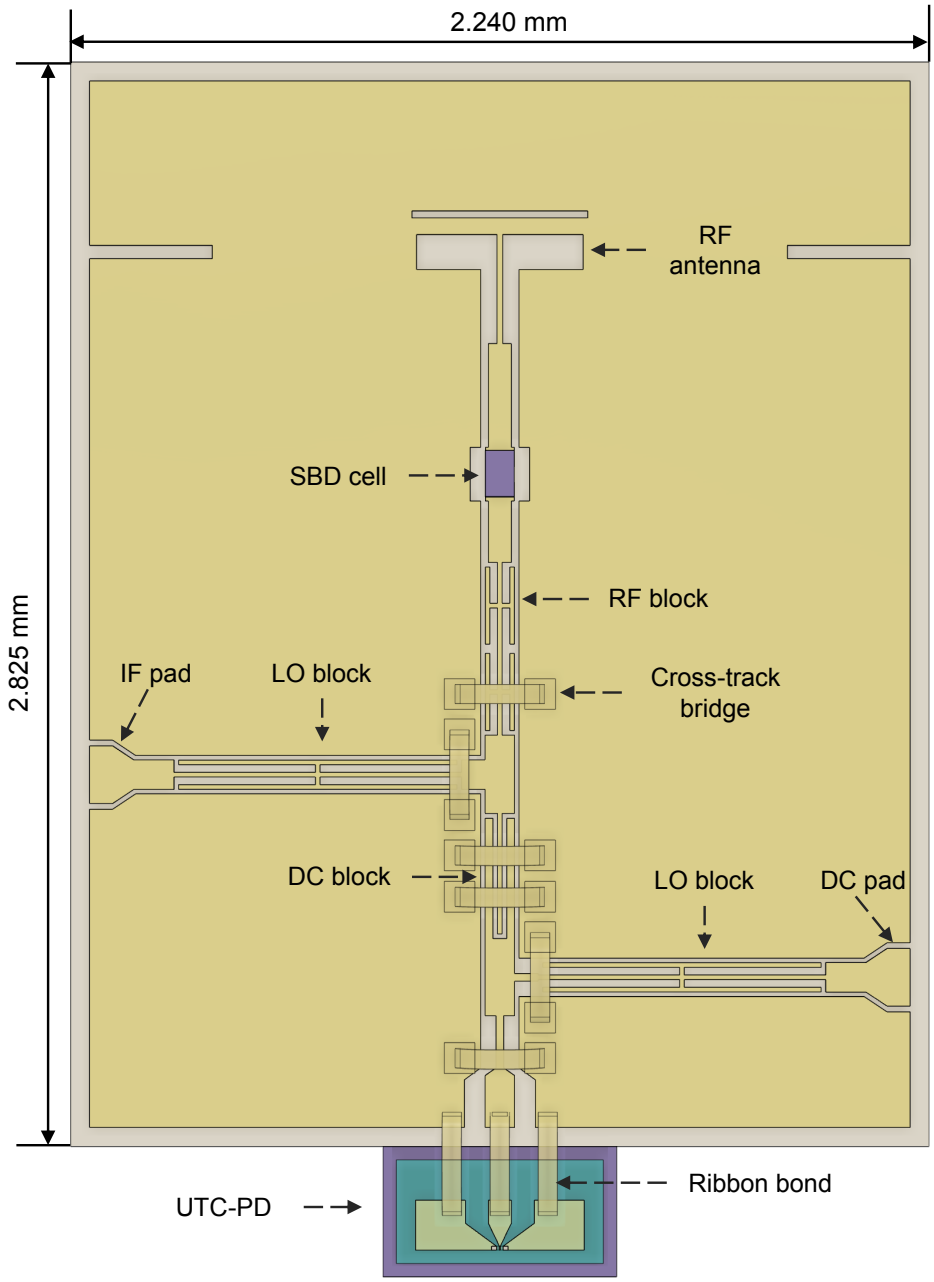

Figure 4.7: Top view of the hybrid integrated mixer circuit based on CPW on quartz, highlighting the key elements. Adapted from [4-1], under a CC-BY license.

RF signal coupling is achieved using a slot antenna, which also provides DC, IF, and LO short-circuit conditions. The simulated S11 magnitude is shown in Figure 4.9**a**. The return loss across the RF band exceeds 15 dB, while a reflection higher than -1.5 dB is maintained up to the edge of the LO band. The Smith chart

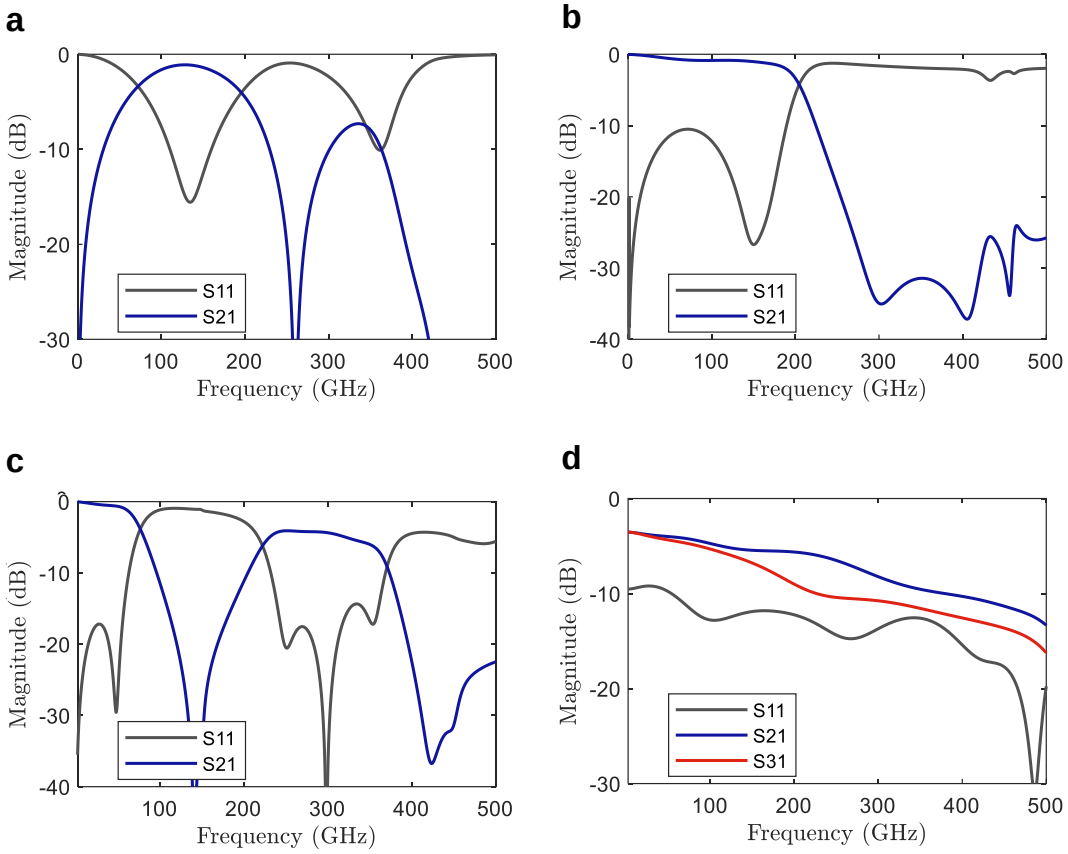

Figure 4.8: S-parameters of key components of the hybrid integrated mixer. **a** DC block. **b** RF block. **c** LO block. **d** T-junction. Adapted from [4-1], under a CC-BY license.

plot in Figure 4.9**b** shows that near short-circuit conditions are provided at IF frequencies, transitioning to an open circuit at 53 GHz. Near short-circuit conditions are then achieved again at the LO band.

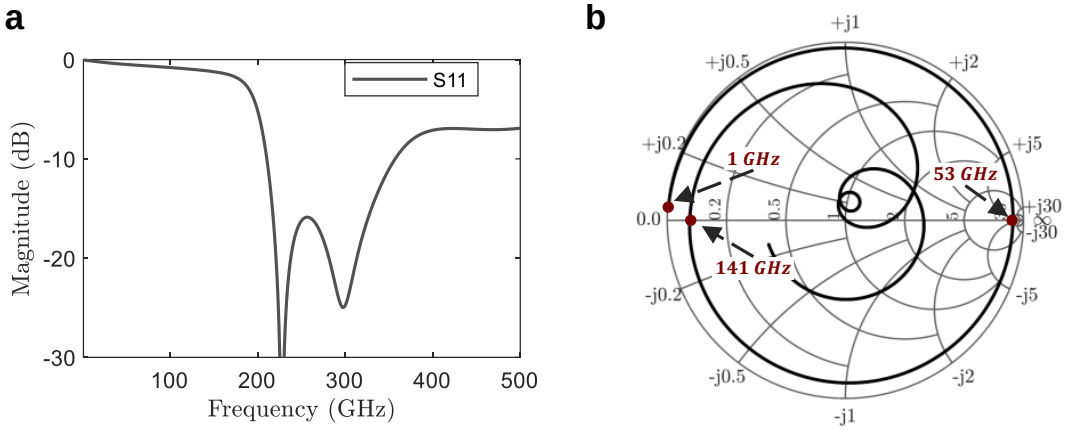

Figure 4.9: S11 of the hybrid integrated mixer antenna. **a** Magnitude plot in dB. **b** Smith chart plot. Adapted from [4-1], under a CC-BY license.

The completed mixer circuit was simulated together, producing five-port (RF, IF, LO, and SBDs) S-parameters, which are then incorporated into the HB simulations to predict the subharmonic mixer performance, following the procedures described in Chapters 2 and 3. A summary of the results is shown in Figure 4.10, illustrating the conversion loss and noise temperature as functions of RF frequency for different pumping photocurrents (Figure 4.10**a-b**), the conversion loss as a function of UTC-PD photocurrent at different frequencies (Figure 4.10**c**), and the IF response (Figure 4.10**d**).

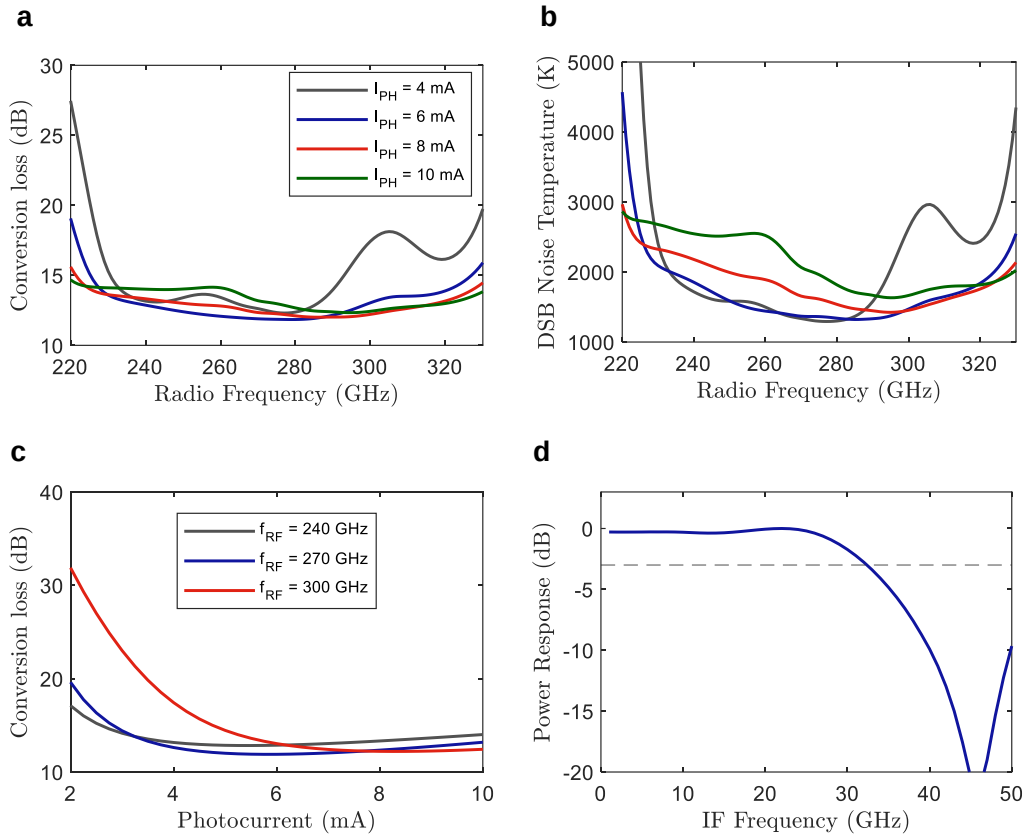

Figure 4.10: Predicted performance of the hybrid integrated mixer based on CPW on quartz. **a-b** Conversion loss and DSB noise temperature as a function of RF frequency for different pumping photocurrents. **c** Conversion loss as a function of pumping photocurrent for different RF frequencies. **d** IF response. Adapted from [4-1], under a CC-BY license.

A minimum conversion loss of 11.85 dB is achieved at 276 GHz with a photocurrent of 6 mA. At this photocurrent, the conversion loss remains below 20 dB across the entire band and below 15 dB from 225 GHz to 325 GHz. However, at

lower frequencies, overpumping causes a degradation of approximately 2 dB as the photocurrent increases from 6 to 10 mA. Compared to the monolithically integrated receiver, the LO power requirements are significantly reduced due to the lower barrier height of the InGaAs Schottky contacts relative to InP. Regarding noise temperature, a minimum of 1293 K is achieved at 276 GHz with just 4 mA of photocurrent. Under optimal pumping conditions, the noise temperature remains below 3000 K across the band and below 2000 K from 234 to 323 GHz. The conversion loss versus photocurrent analysis confirms the reduced LO power demand at the better impedance-matched frequencies of 240 and 270 GHz, achieving a conversion loss below 20 dB with only 2 mA of photocurrent. However, at 300 GHz, an 8 mA photocurrent is needed for optimal performance. Lastly, the IF response exhibits a 3-dB bandwidth of approximately 30 GHz.

4.2.4 Antenna-lens simulations

Similar to the monolithic receiver, the hybrid integrated receiver was mounted on a 6 mm silicon hyper-hemispherical lens for quasi-optical coupling. To estimate the coupling efficiency and obtain the radiation patterns, the same approach described in Chapter 3 was used, simulating the complete antenna-lens system in CST. Figure 4.11 presents the resulting S11 and radiation efficiency, considering the radiated power directed towards the lens (downwards).

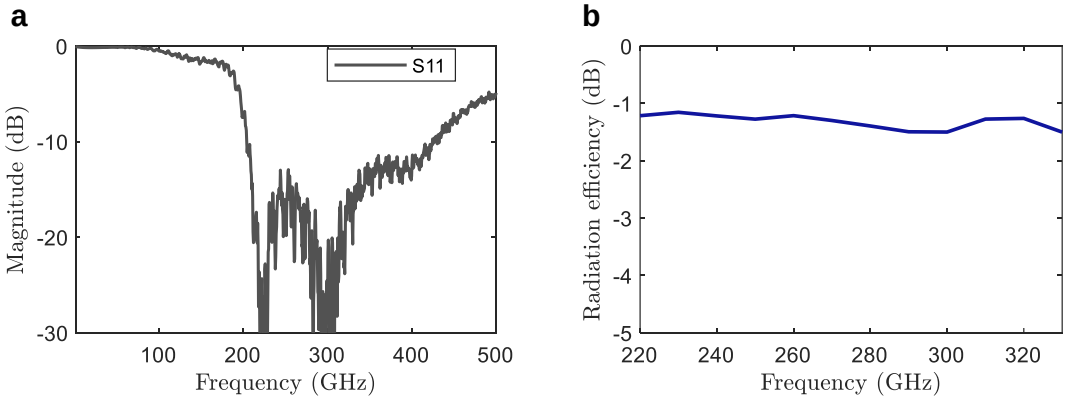

Figure 4.11: Antenna-lens system simulation results. **a** S11. **b** Radiation efficiency. Adapted from [4-1], under a CC-BY license.

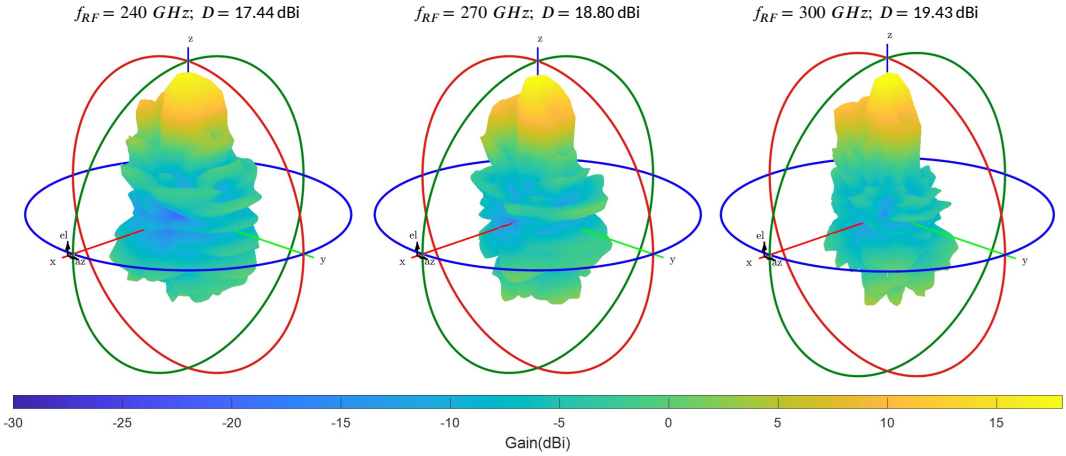

Figure 4.12: 3D radiation patterns of the antenna-lens system at 240, 270, and 300 GHz for the hybrid integrated mixer. Adapted from [4-1], under a CC-BY license.

The S11 exhibits characteristic ripple features arising from reflections at the quartz-silicon and silicon-air interfaces. A slight deterioration can be observed compared to the simulation without the lens, although the return loss remains below 10 dB from 205 GHz to 432 GHz. This demonstrates that the antenna could be employed for designs exceeding the 220–330 GHz range. The radiation efficiency has maximum and minimum values of -1.5 dB and -1.15 dB at 330 GHz and 230 GHz, respectively. The 3D radiation patterns are depicted in Figure 4.12 at frequencies of 240 GHz, 270 GHz, and 300 GHz. In all cases, the maximum radiation occurs in the +z-direction, corresponding to the downward direction toward the lens. The calculated directivities are 17.44 dBi, 18.80 dBi, and 19.43 dBi at 240 GHz, 270 GHz, and 300 GHz, respectively.

4.2.5 Quasi-optical receiver package

Among the different mixers developed in this work, the hybrid receiver design based on quasi-optical coupling was extended because of plans of fabrication and testing. Consequently, a receiver package is required to accommodate the components, provide mechanical support, and facilitate IF and DC connections. For this purpose, we designed a brass package, shown in Figure 4.13. The receiver integrates the quartz mixer circuit, UTC-PD, silicon lens, and IF and DC printed circuit boards (PCBs) with connectors. The PCBs use I-TERA MT40 [4-6] (IF) and FR4 [4-7] (DC) substrates, soldered to IF (K-type) and DC (SMA) connectors. The package also

includes a cylindrical groove to accommodate a fibre ferrule for fibre packaging. A closer view (Figure 4.13) shows an optical lensed fibre positioned at the edge of the UTC-PD's optical facet. To equalise the heights of the UTC-PD and quartz chips, an additional unprocessed 75 µm quartz substrate was used.

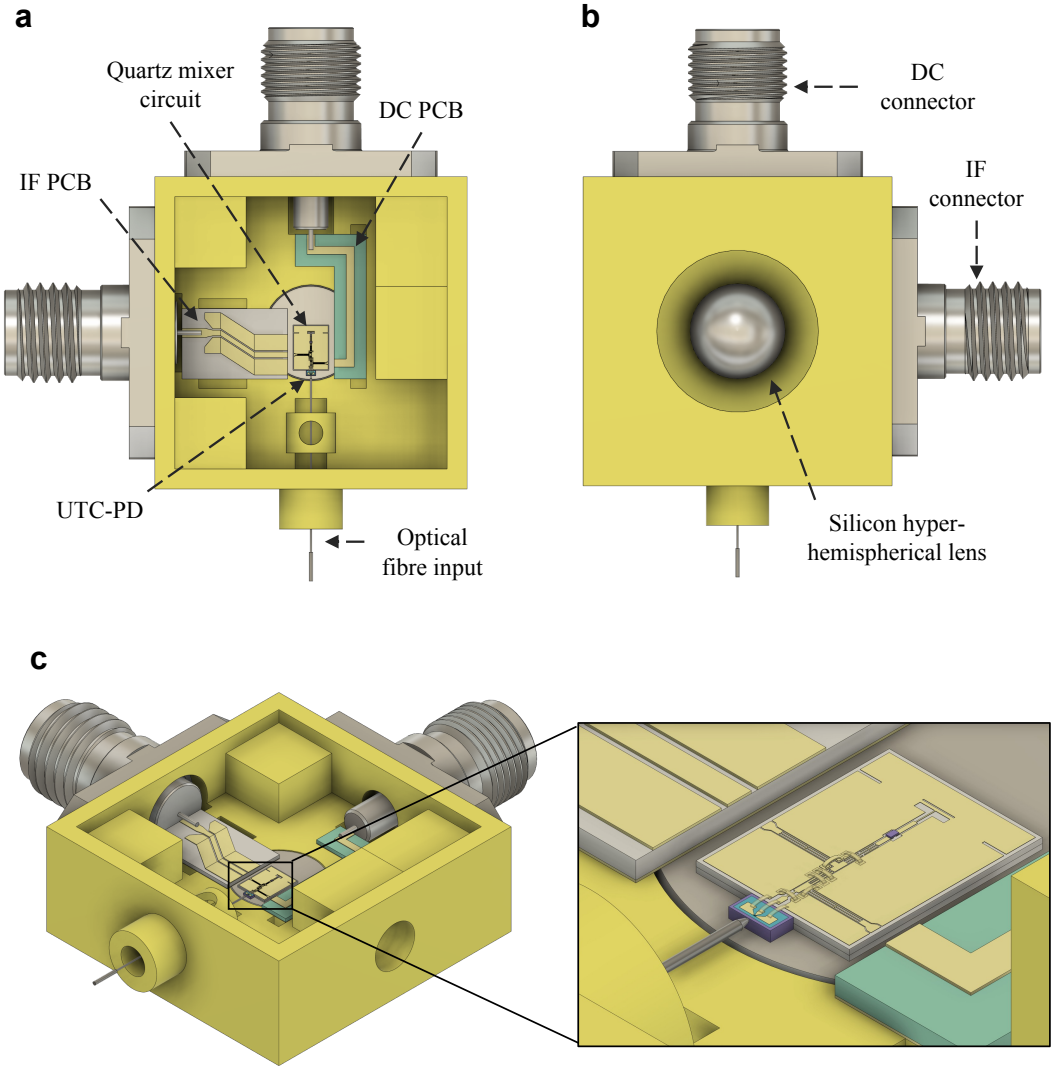

Figure 4.13: Hybrid integrated quasi-optical receiver package. **a** Top view. **b** Bottom view. **c** Perspective view. Adapted from [4-1], under a CC-BY license.

The IF response in Figure 4.10**d** does not account for the effects of ribbon bonds, the IF PCB, or the connector transition. To analyse these effects, we simulated separately: (1) the PCB, (2) the quartz-to-PCB connection using ribbon bonds, (3) the PCB-to-connector transition, and (4) a full model including all these components. The model, shown in Figure 4.14, is a simplified version of the receiver

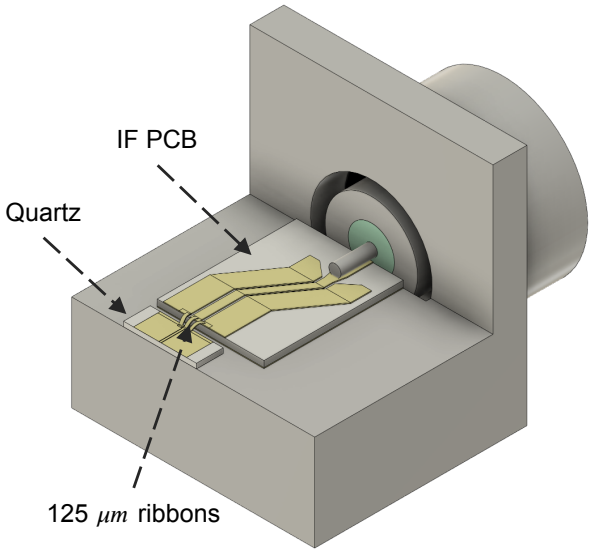

Figure 4.14: Model used to analyse the frequency response of the IF path including ribbon bonding, the IF PCB, and the transition to the K-type connector.

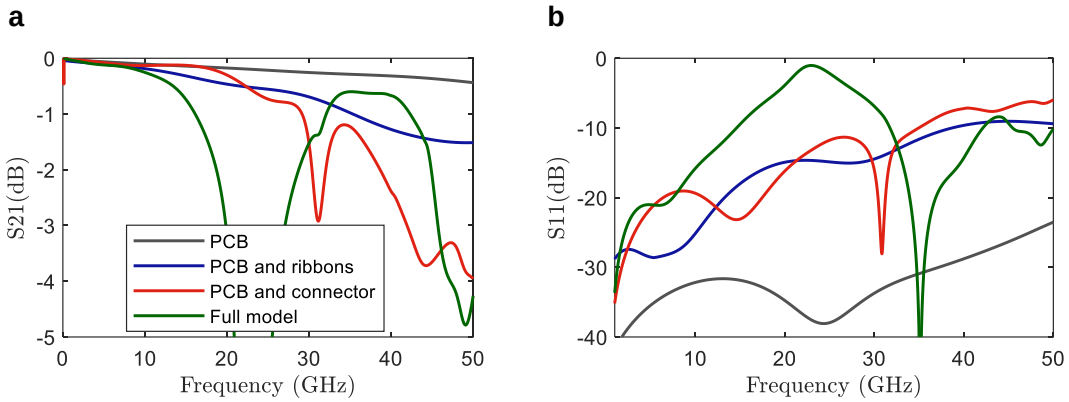

Figure 4.15: S-parameters of the external including the effect of PCB, quartz-to-PCB transition uing ribbons, PCB-to-connector transition, and the full model. **a** S21. **b** S11.

package, which includes the mentioned components.

The IF PCB is based on a grounded CPW with 0.3 mm diameter vias, transitioning into a microstrip waveguide. This transition facilitates soldering to the connector pin, though alternative implementations are possible. The S-parameters of the PCB up to 50 GHz are shown in Figure 4.15. The return loss exceeds 23 dB, with a maximum insertion loss of 0.43 dB at 50 GHz, demonstrating the PCB's capability to operate at high frequencies. Figure 4.15 also presents the frequency response for different cases, including the effects of ribbon bonding and the con-

nector. When considering the quartz-to-PCB transition with ribbons, the return loss increases, particularly at high frequencies, but remains above 10 dB. This increase is due to the inductance introduced by the ribbons, resulting in a maximum insertion loss of 1.51 dB. The PCB-to-connector transition exhibits a 3-dB bandwidth of 42 GHz, with a minor resonance at 30 GHz. Simulating all components together, as represented in Figure 4.14, reveals a strong resonance at 23 GHz. The 3-dB bandwidth in this case is 19.9 GHz, which remains acceptable. While this resonance was not optimised in the initial prototype, future designs should refine the IF path to extend the IF bandwidth.

4.3 250-320 GHz rectangular-waveguide receiver

A receiver based on CPW with quasi-optical coupling offers the main advantage of being easier and more cost-effective to fabricate and assemble compared to rectangular waveguide-based designs, which require precise micromachining with extremely low tolerances. However, rectangular waveguide designs with suspended microstrip lines deliver the best performance for THz mixers [4-8], [4-9]. Rectangular waveguide to microstrip transitions can be fabricated with ultra-low insertion loss, and suspended microstrip lines on waveguide channels exhibit very low propagation losses. Additionally, a receiver designed in rectangular waveguide can be connected to standard components, such as horn antennas. These reasons motivated us to design a 300 GHz rectangular waveguide optoelectronic receiver, which is presented here.

4.3.1 Microstrip and WR3 waveguide

The cross-section of the microstrip waveguide used in this mixer is shown in Figure 4.16**a**. As in the CPW-based mixer, a 75 µm-thick and 200 µm-wide quartz substrate with 3 µm gold metallisation was used. For a 50 Ω line, a signal width of 87 µm is required, which also depends on the channel dimensions, here 153 by 250 µm. Notice that the quartz substrate was directly mounted on top of the lower channel wall, instead of being suspended, which was done for simplicity of assembly. The Quasi-TEM mode of the waveguide is shown in Figure 4.16**c**, where

the channel walls act as a ground. The simulated attenuation is presented in Figure 4.16**d**, showing values below 0.64 dB/mm even at 500 GHz, a significant improvement over the CPW lines used in the other mixers. The dimensions of the waveguide channel are important to avoid the excitation of cavity modes at high-frequencies, relevant for the mixer operation, especially LO harmonics [4-10].

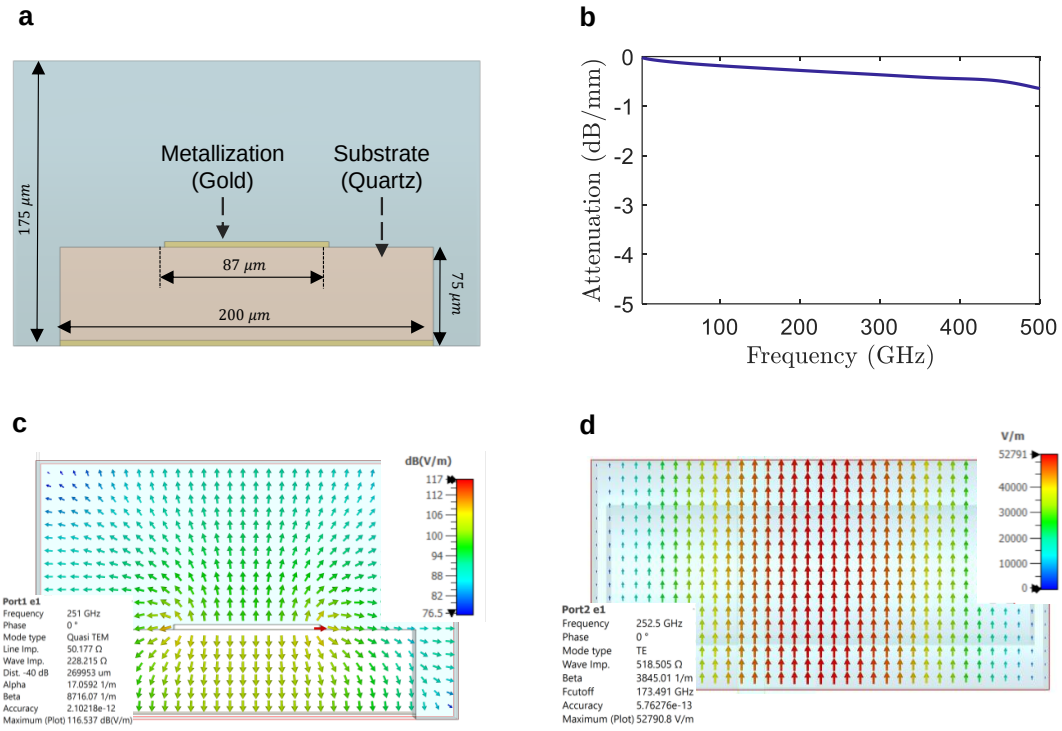

Figure 4.16: Insights into the microstrip and WR3 waveguide used in the rectangular-waveguide-based mixer. **(a)** Cross-section of the microstrip line on a waveguide channel, designed for a 50Ω line impedance. **(b)** Attenuation of the microstrip waveguide in dB/mm. **(c)** E-field distribution of the suspended microstrip quasi-TEM mode. **(d)** E-field distribution of the WR3 TE_{10} mode.

As the target frequency of the mixer is the 300 GHz band, the RF input waveguide was designed to meet standard WR3 specifications [4-11], with dimensions of 864 µm by 432 µm. The simulated TE_{10} E-field distribution is shown in Figure 4.16**d**, exhibiting a wave impedance of 518 Ω.

4.3.2 Mixer design

Following the previous considerations, a WR3 receiver with the same architecture as shown in Figure 4.7 was designed. The 3D model of the full receiver is presented in Figure 4.17. In the quasi-optical receiver, ribbon bonding was used to connect the

UTC-PD and quartz mixer circuit for easier assembly. However, flip-chip bonding was chosen in this receiver to reduce coupling losses. The primary goal of this receiver is to assess the optimal performance the optoelectronic receiver can achieve in terms of down-conversion efficiency and LO power requirements.

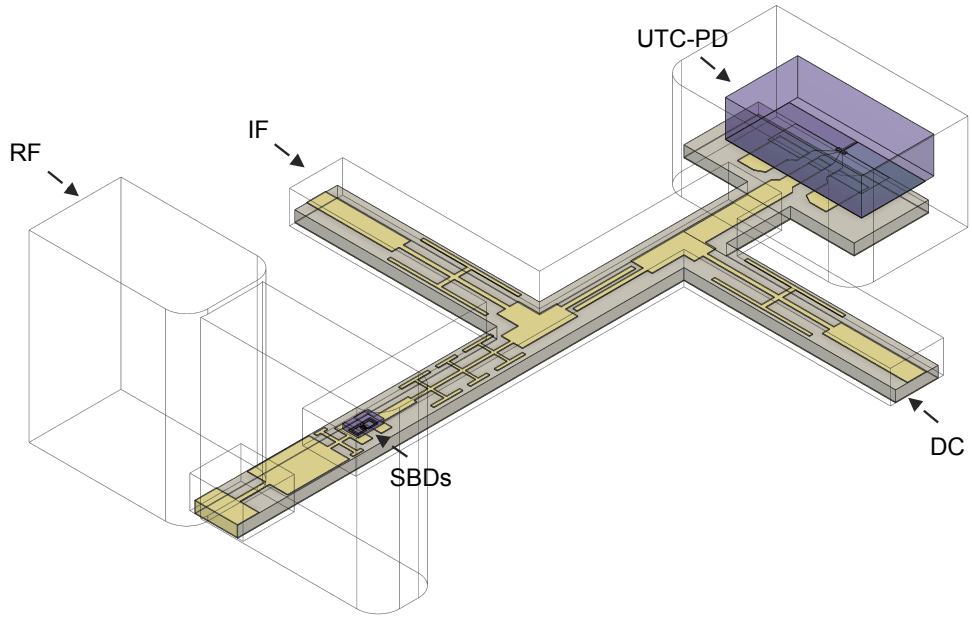

Figure 4.17: 3D model of the complete WR3 hybrid integrated receiver.

A more detailed view is shown in Figure 4.18, highlighting the receiver components. The S-parameters of the key elements are depicted in Figure 4.19. Since the mixer circuit uses microstrip lines, a tapered CPW-to-microstrip transition is required to convert the mode and minimise losses compared to an abrupt transition. A maximum insertion loss of 2.8 dB is achieved at 165 GHz, accounting for propagation losses in the InP CPW, flip-chip bonding, and the transition itself. For the RF and LO blocks, hammerhead-type low-pass filters are used, providing rejection ratios greater than 30 dB and 17 dB at the RF and LO bands, respectively.

Unlike the quasi-optical mixer design, an additional filter was included to suppress the third LO harmonic ($3f_{LO}$), which is necessary due to waveguide cavity modes at high frequencies, as evidenced in the S-parameter resonances beyond 300 GHz. The stopband of the filter is centred at 450 GHz. The DC block was implemented with quarter-wavelength gap-coupled lines [4-12]. The insertion loss at the LO band remains below 0.4 dB. An H-plane probe was used to implement the

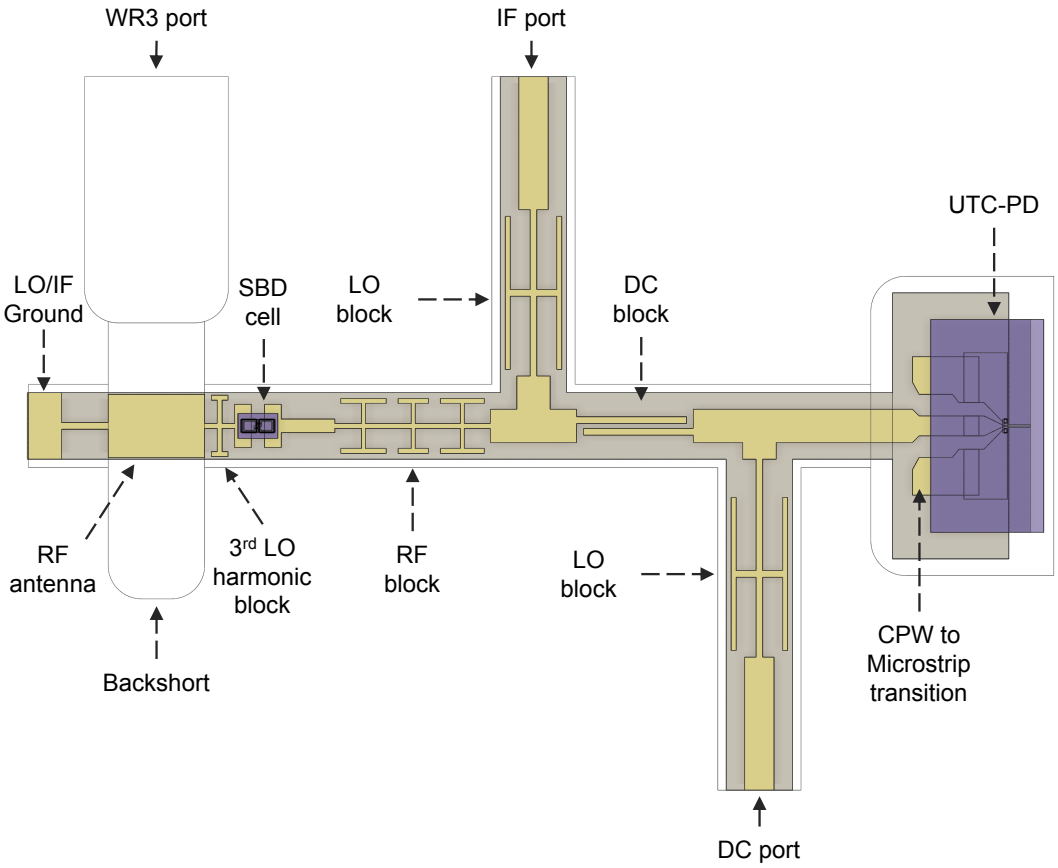

Figure 4.18: Top view of the complete hybrid integrated WR3 receiver, highlighting the key components.

WR3-to-microstrip transition, with LO and IF signals grounded on the right side of the RF probe. To optimise the return loss and signal coupling, the waveguide dimensions, position of the probe and backshort distance were carefully adjusted. From 250 to 325 GHz, the insertion loss remains below 1 dB, with a return loss greater than 10 dB.

The S-parameters of the T-junction used for the Bias T and IF extraction are shown in Figure 4.20**a**. Compared to CPW-based T-junctions, this design achieves S-parameters closer to the ideal case at higher frequencies without requiring cross-track bridges. The energy balance (Figure 4.20**b**) indicates that the T-junction remains nearly lossless up to approximately 300 GHz, beyond which cavity modes are excited in the waveguide channel. To mitigate this effect in the mixer, the RF block filter prevents RF propagation through the T-junction.

The final predicted performance of the optimised mixer structure, obtained

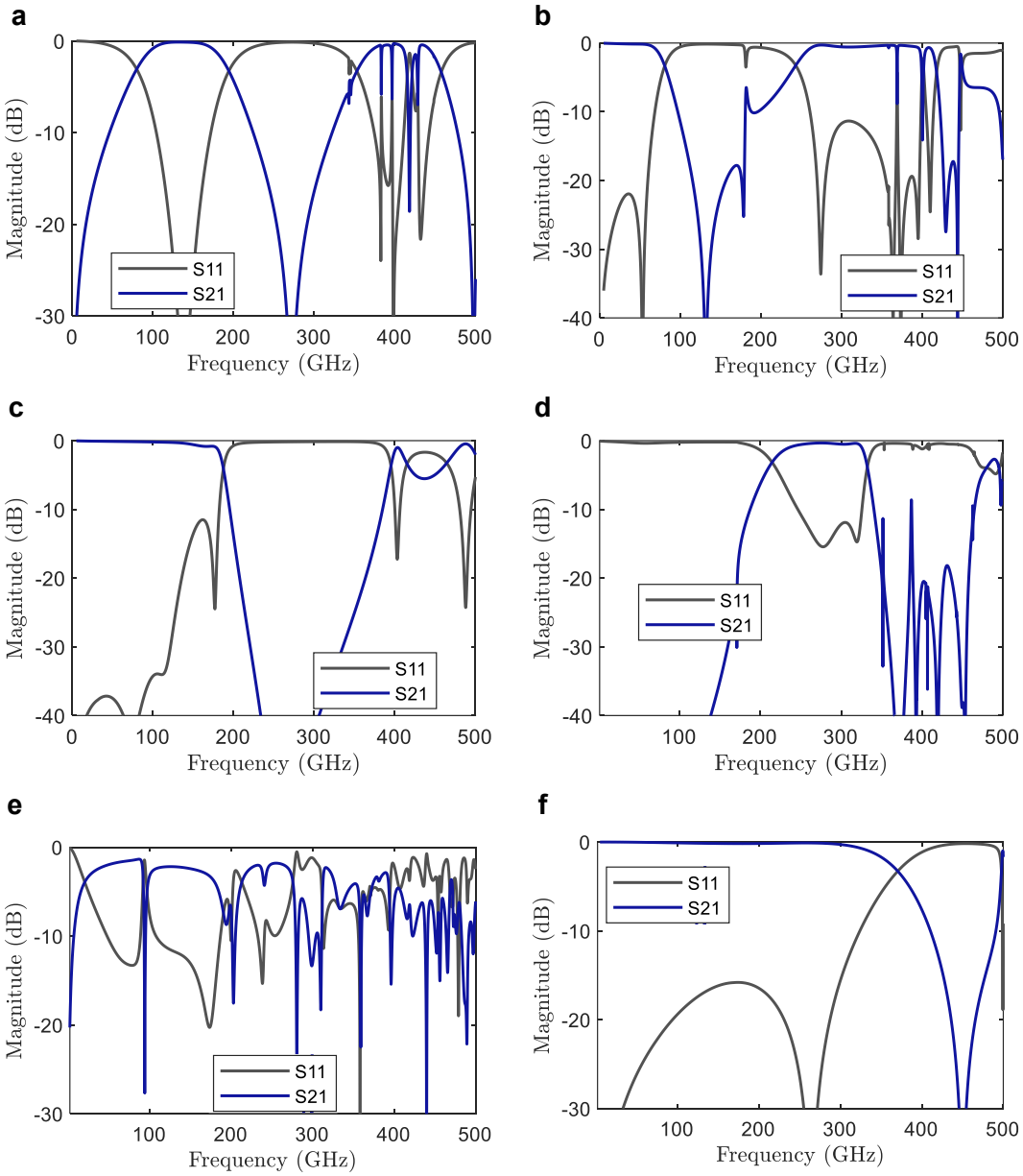

Figure 4.19: S-parameters of the WR3 mixer key components. **a** DC block. **b** LO block. **c** RF block. **d** WR3 to microstrip transition. **e** CPW to microstrip transition. **f** 3rd LO harmonic block.

from HB simulations, is summarised in Figure 4.21. A minimum conversion loss of 10.3 dB is achieved at 285 GHz with 6 mA of photocurrent. Even with only 2 mA, a conversion loss of 14.4 dB is obtained at 280 GHz. For 6 mA, the conversion loss remains below 15 dB from 252 to 310 GHz. Regarding noise temperature, a minimum of 694 K is reached at 6 mA, while at 2 mA, 1300 K is achieved at 280 GHz. The conversion loss versus photocurrent highlights the benefit of suspended microstrip,

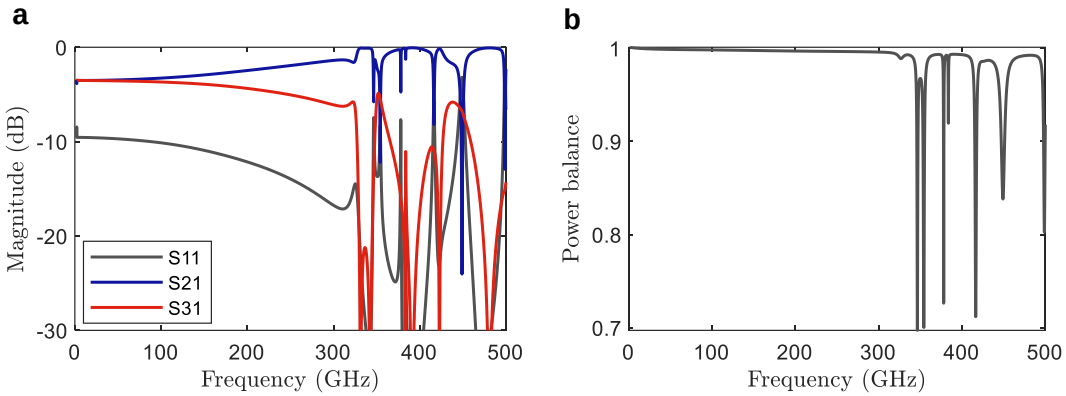

Figure 4.20: T-junction in microstrip waveguide. **a** S-parameters. **b** Energy balance.

as 20.3 dB conversion loss is attainable with only 1 mA. The lower LO power requirements are also influenced by the use of a narrow-band design, which improves impedance matching between the UTC-PD and SBD. Finally, the IF response exhibits a 3 dB bandwidth of 41 GHz.

4.4 Summary and discussion

This chapter has presented the design of both a quasi-optical and a WR3 optoelectronic receiver, employing hybrid integration of UTC-PDs and low-barrier SBDs. Hybrid integration enables independent design and optimisation of device structures and fabrication processes, allowing each component to achieve optimal performance while minimising design trade-offs. In this work, this applies to the SBD, UTC-PD, and mixer circuit. A key advantage is evident when comparing the InGaAs SBDs used in the hybrid receivers with the InP diodes of the monolithic approach. Since the doping and diode structure were optimised independently of the UTC-PD, the cut-off frequency is approximately an order of magnitude higher. This not only improves the minimum achievable conversion loss but also enables the realisation of receivers at higher frequencies. Although the designs here are optimised for 300 GHz, where InP diodes provide reasonable performance, the benefits of hybrid integration extend beyond this frequency range.

First, a quasi-optical receiver based on CPW-on-quartz was designed for operation across the full 220–330 GHz band, achieving near state-of-the-art simulated performance. This mixer implementation is particularly attractive for prototyping

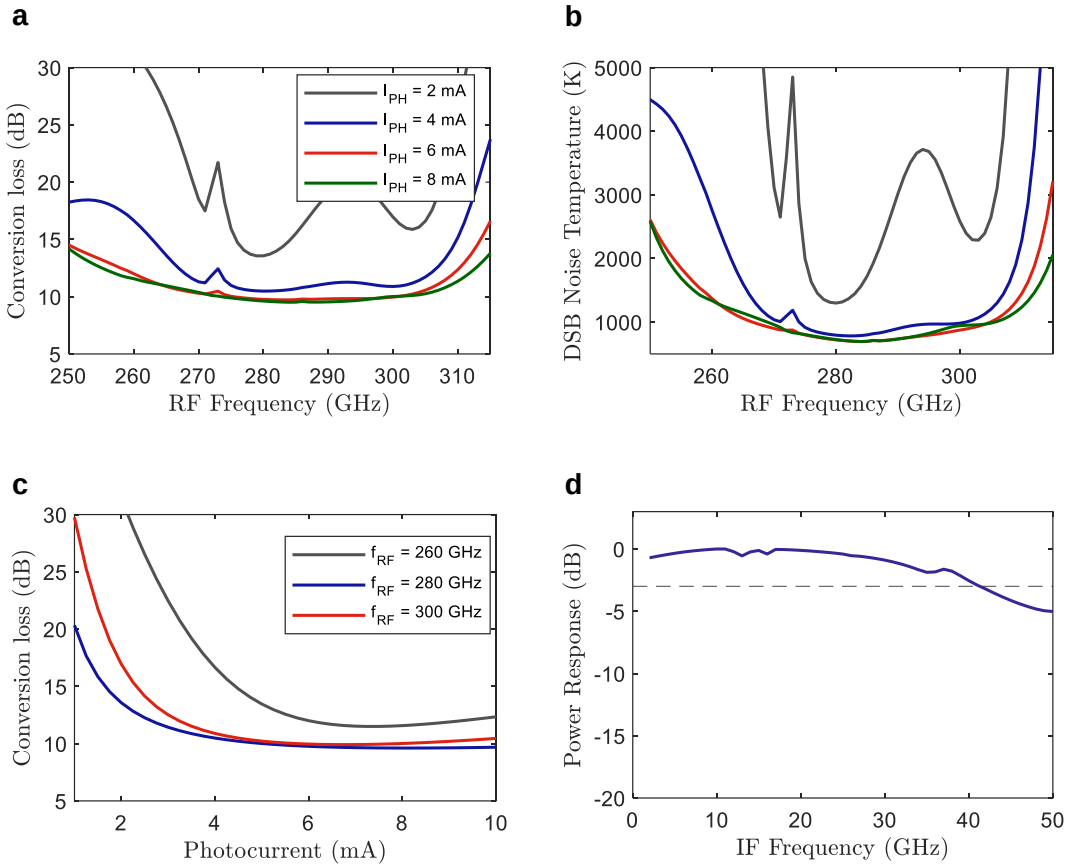

Figure 4.21: Predicted performance of the hybrid integrated mixer based on WR3 waveguide and microstrip line on quartz. **a-b** Conversion loss and DSB noise temperature as a function of RF frequency for different pumping photocurrents. **c** Conversion loss as a function of pumping photocurrent for different RF frequencies. **d** IF response.

due to its ease of assembly and fabrication, which motivated its fabrication and testing, as discussed in the next chapter. The predicted performance indicates that optimal conversion loss and noise temperature are achieved at a photocurrent of approximately 4 mA, well below the saturation regime of the UTC-PD. This key result demonstrates the feasibility of integrating UTC-PDs and low-barrier SBDs, paving the way for receiver designs at even higher frequencies. This receiver serves as a first prototype with room for improvement. For example, increasing the IF bandwidth, which is primarily limited by the mixer architecture and IF path, including the ribbon bonds and PCB-to-connector transition. Additionally, miniaturising the CPW lines could further reduce propagation losses, particularly at the T-junctions.

To determine the best achievable simulated performance with our proposed ap-

proach, a WR3 mixer with microstrip lines was designed, demonstrating superior performance with a minimum noise temperature of 700 K. This highlights the advantage of rectangular waveguide technology for high-performance terahertz mixers, despite the increased fabrication and assembly complexity and costs. While this design improves performance, further optimisation is needed to enhance the RF bandwidth and mitigate issues related to high-order cavity modes. Nevertheless, with optimised impedance matching, the WR3 receiver achieves a reasonable conversion loss of 20 dB with just 1 mA of photocurrent. Comparing the minimum achievable conversion loss across the three receivers presented, the WR3 design improves by approximately 4 dB over the monolithic receiver and 3 dB over the quasi-optical receiver.

References

[4-1] I. Belio-Apaolaza, J. Seddon, H. Wang, *et al.*, "Integrated 300 GHz optoelectronic mixer based on photonically-pumped low-barrier Schottky diodes," *J. Lightwave Technol.*, pp. 1–10, 2025.

[4-2] S. Adachi, *Physical Properties of III-V Semiconductor Compounds*, en. John Wiley & Sons, Nov. 1992.

[4-3] N. Daghestani, K. Parow-Souchon, D. Pardo, *et al.*, "Room temperature ultrafast InGaAs Schottky diode based detectors for terahertz spectroscopy," en, *Infrared Phys. Technol.*, vol. 99, pp. 240–247, Jan. 2019.

[4-4] D. A. Williams, "Millimeter-wave components and subsystems built using microstrip technology," *IEEE Trans. Microw. Theory Tech.*, vol. 39, no. 5, pp. 768–774, May 1991.

[4-5] A. E. Maestrini, J. V. Siles, C. Lee, R. Lin, and I. Mehdi, "A 2 THz room temperature bias-able Schottky mixer," *IEEE Transactions on Terahertz Science and Technology*, vol. 15, no. 2, pp. 169–180, 2025.

[4-6] Isola Group, *I-tera MT40*, version Revision No: F, Oct. 2024.

[4-7] Isola Group, *FR408HR*, version Revision No: F, Jul. 2024.

[4-8] I. Mehdi, J. V. Siles, C. Lee, and E. Schlecht, "THz diode technology: Status, prospects, and applications," *Proceedings of the IEEE*, vol. 105, no. 6, pp. 990–1007, 2017.

[4-9] A. Maestrini, B. Thomas, H. Wang, *et al.*, "Schottky diode-based terahertz frequency multipliers and mixers," *Comptes Rendus Physique*, vol. 11, no. 7-8, pp. 480–495, 2010.

[4-10] D. M. Melgar, "Design and optimization at the highest frequency of a heterodyne receiver at 1.2 THz for the JUICE-SWI instrument," en, Ph.D. dissertation, Université Pierre et Marie Curie-Paris VI, 2017.

[4-11] IEEE Standards Association, *IEEE standard for rectangular metallic waveguides and their interfaces for frequencies of 110 GHz and above— part 1: Frequency bands and waveguide dimensions*.

[4-12] S.-H. Choi, J.-Y. Lee, K.-B. Lee, and D.-H. Shin, "Design of miniaturized symmetric microstrip DC block," in *2007 Asia-Pacific Microwave Conference*, IEEE, Dec. 2007, pp. 1–4.

Chapter 5

Experimental work

The UTC-PDs used in the experiments were fabricated by C. Graham, while J. Seddon packaged the antenna-integrated devices. The WR3.4 low-barrier subharmonic mixer for the non-integrated experiments was provided by ACST GmbH. The InGaAs SBDs used in the hybrid integrated receiver were supplied by Teratech Components, and its assembly was conducted by N. Brewster at the Rutherford Appleton Laboratory (RAL). Mixer characterisation experiments were performed by I. Belio-Apaolaza. The high-speed multi-channel wireless link was developed in collaboration with the University of Duisburg-Essen, which provided the equipment and MUTC-PDs. The setup was designed by I. Belio-Apaolaza, and assembled by I. Belio-Apaolaza, J. Martinez-Gil, and J. Tebart. Multi-channel wireless transmission measurements were conducted by I. Belio-Apaolaza.

This chapter presents the experimental work on photonically-pumped SBD-based mixers. To validate the concept, a non-integrated receiver using discrete components was first tested. The results presented here are reproduced with permission from [5-1] © Optica Publishing Group. We then detail the fabrication, assembly, and characterisation of the hybrid integrated quasi-optical receiver introduced in Chapter 4. The receiver characterisation results are reproduced with permission from [5-2] under a CC-BY license. To demonstrate the applicability of the optoelectronic receiver concept, we also discuss a multi-channel 300 GHz link. The wireless link results are reproduced with permission from [5-3], under a CC-BY license.

5.1 Receiver characterisation setups

5.1.1 THz power measurements

First, the characterisation methods used for the optoelectronic receivers are discussed. For the two receivers analysed in this work, three figures of merit are evaluated: (1) conversion loss as a function of RF frequency, (2) conversion loss as a function of pumping photocurrent, and (3) IF response. These are determined through a series of calibrated power measurements, varying the RF and LO frequencies as well as the optical power at the UTC-PD LO signal generator input to adjust the photocurrent. The first step involves measuring the THz power of the source. In our experiments, we used an in-house antenna-integrated UTC-PD [5-4], [5-5]. To calibrate its output power, the setup shown in Figure 5.1 was used.

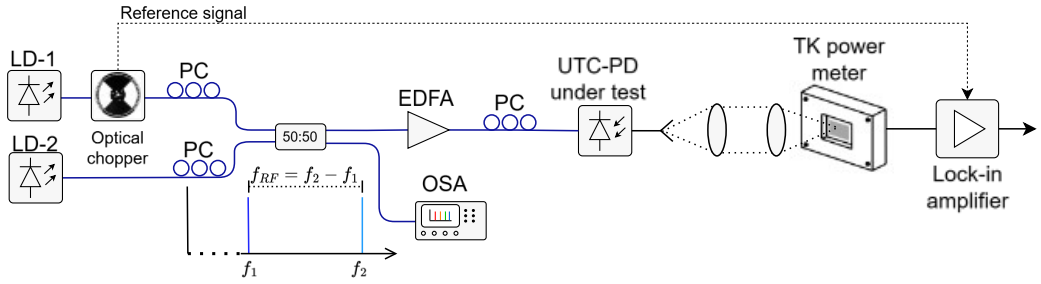

Figure 5.1: Schematic of the RF power measurement setup using a Thomas Keating power meter. PC: Polarization controller, LD: Laser diode, OSA: Optical spectrum analyser, EDFA: Erbium-doped fibre amplifier. Adapted with permission from [5-1] © Optica Publishing Group.

The power of the radiated wave was detected using a Thomas Keating absolute power meter with a NEP of $5\,\mu W/\sqrt{Hz}$. Two 1550 nm CW lasers, one fixed at 1553.73 nm (RIO Orion Series) and one tuneable (Agilent 81682A or PurePhotonics PPCL550), were used generate optical tones separated by the desired THz frequency (f_{RF}). The tuneable laser signal was chopped at 15 Hz, and the reference chopping signal was sent to a lock-in amplifier connected to the power detector. To compensate for optical losses and maximise the input power to the UTC-PD, an erbium-doped fibre amplifier (EDFA) (Thorlabs EDFA100S) was placed before the transmitter, with an output power of the order of 20 dBm. A set of three polarization controllers (PCs) ensured that the laser signals' polarisations are aligned with each

other and with the photodiode's optical waveguide mode. A bias voltage of approximately -3 V was supplied to the UTC-PD transmitter with a programmable voltage source (Keithley 2400), and the input optical power was adjusted to generate a photocurrent of approximately 10 mA.

Two different antenna-integrated UTC-PDs were used for characterising the non-integrated and integrated receivers: a bow-tie antenna for the former and a slot-antenna for the latter. Both devices were assembled in a brass package similar to the hybrid integrated receiver, using a 6 mm diameter hyper-hemispherical silicon lens. Figure 5.2 shows the quasi-optical package, along with microscope images of the antenna-integrated UTC-PDs.

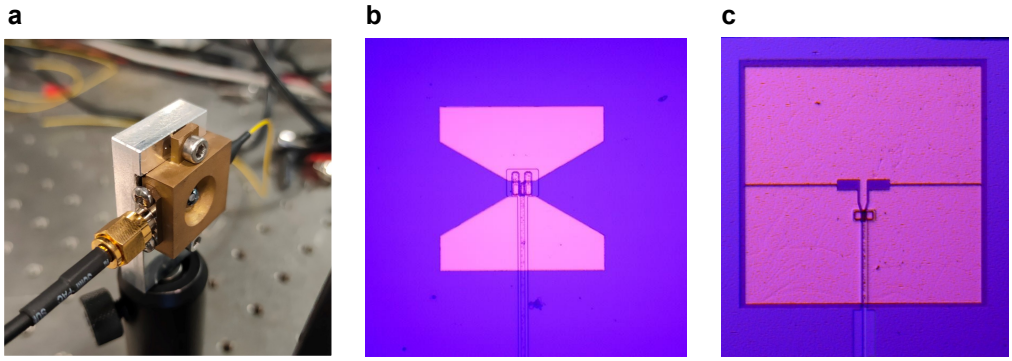

Figure 5.2: Antenna-integrated UTC-PDs used for mixer characterisation. **a** Packaged device. **b-c** Microscope photographs of bow-tie and slot antenna devices, respectively.

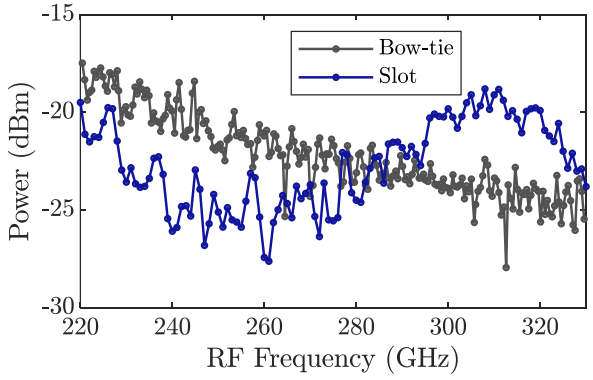

Figure 5.3: Measured RF power of the antenna-integrated UTC-PDs used as calibrated THz sources for receiver characterisation. Adapted with permission from [5-1] © Optica Publishing Group, with added data from the slot antenna device.

The radiated THz wave propagates over a short (<50 cm) free-space path. This path was replicated in the setup with the optoelectronic receiver to ensure that the power at the receiver input matches the measured value. Two different free-space paths were used for the non-integrated and integrated receiver characterisations. In the first case, two 5 cm diameter polytetrafluoroethylene (PTFE) lenses (Thorlabs PTFE LAT075) were employed, while in the second case, two 90° off-axis parabolic mirrors (MPD229-M03 and MPD269-M03) were used. These elements collect the radiated THz power and focus it onto the power meter or optoelectronic receiver input. An infrared (IR) block (Tydex LPF8.8-35) was also used in both cases to prevent overestimating the measured power due to the intrinsic IR radiation from the UTC-PD. The measured power from 220 to 330 GHz of the UTC-PDs transmitters is shown in Figure 5.3.

5.1.2 Down-converted power measurements

After measuring the RF power, the three figures of merit introduced earlier were measured using the setup shown in Figure 5.4. In this setup, the emitted THz power from the calibrated transmitter is down-converted by the optoelectronic receiver under test, allowing the IF power to be measured. This enables the extraction of the conversion loss and the IF response.

The optical path for optical heterodyning of the UTC-PD transmitter was replicated from the setup used for the RF power characterisation. Since the same photomixing principle is used in the optoelectronic receiver, the same components were employed: two free-running lasers (LD-3 and LD-4 in the schematic) with frequency separation equal to the LO frequency, and an EDFA to boost the optical power. The power and frequencies of the lasers were monitored with the optical spectrum analyser (OSA), as shown in Figure 5.4. The down-converted signal was amplified by a low-noise amplifier (LNA) with a frequency range of 0.01 to 30 GHz and a typical gain of 40 dB. The down-converted IF power and frequency were measured using an electrical spectrum analyser (ESA). Table 5.1 provides a list of the models used for each component and receiver.

To measure conversion loss across the RF band (220–330 GHz), the laser fre-

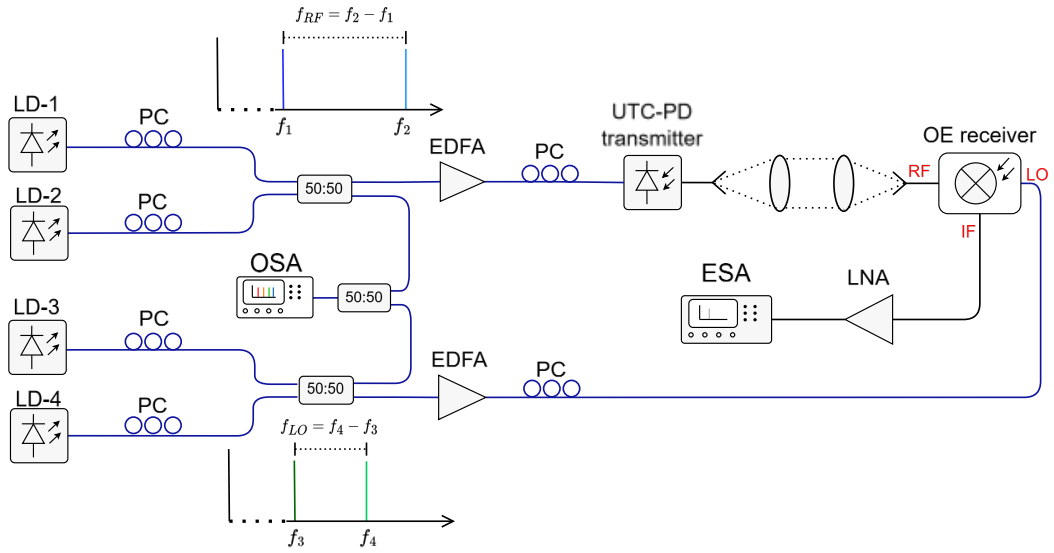

Figure 5.4: Schematic of the optoelectronic receiver characterisation setup. LNA: low noise amplifier, OE: Optelectronic, ESA: Electrical spectrum analyser. PC: Polarization controller, LD: Laser diode, OSA: Optical spectrum analyser, EDFA: Erbium-doped fibre amplifier. Adapted with permission from [5-1] © Optica Publishing Group.

	Model	
Component	Non-integrated receiver	Integrated receiver
LD-1	RIO Orion Series	RIO Orion Series
LD-2	PurePhotonics PPCL550	PurePhotonics PPCL550
LD-3	RIO Orion Series$^{(*)}$	RIO Orion Series
LD-4	Agilent 81640A	PurePhotonics PPCL550
EDFA	Thorlabs EDFA100S	Thorlabs EDFA100S
LNA	RF-Lambda RLNA00G30GA	RF-Lambda RLNA00G30GA
ESA	Rohde&Schwarz FSU-26	Rohde&Schwarz FSW-50
OSA	Aragon Photonics BOSA	Agilent 86142B
Voltage source	Keithley 2400	Keithley 2400

$^{(*)}$ In the non-integrated receiver setup, LD-3 and LD-1 were the same laser, split into two paths.

Table 5.1: Models of components used in the receiver characterisation setups for both the non-integrated and integrated cases.

quencies were adjusted to sweep the band while maintaining a fixed IF frequency between 0.5 and 1 GHz, and the down-converted power was recorded. Conversion loss was also measured as a function of the UTC-PD LO signal generator photocurrent to analyse mixer saturation by adjusting the EDFA output power at a fixed RF

frequency, repeating the process at different frequencies. A maximum photocurrent of 15 mA was used to prevent photodiode damage. The IF response was characterised by sweeping the LO frequency at a fixed RF frequency. Conversion loss was extracted by normalizing the gain of the full IF chain, including cables and connectors, using a calibrated VNA.

5.2 Non-integrated WR3.4 receiver

As discussed, the first optoelectronic receiver investigated in this work was implemented in a non-integrated fashion, with the motivation of proving the feasibility of photonically-pumped Schottky mixers. For this purpose, we used a prototype low-barrier subharmonic 270-320 GHz mixer, based on InGaAs Schottky contacts. The SBDs and the mixer were fully designed and fabricated at ACST GmbH, employing a proprietary Film-Diode (FD) technology process [5-6]. A photograph of the mixer block is shown in Figure 5.5. The RF, LO and IF ports are based on rectangular waveguide WR-3.4, WR-6.5, and an SMA connector respectively. A pyramidal antenna is used to couple the incoming RF signal. The LO power required to drive the mixer is approximately -7 dBm, which aligns closely to the power requirements of the InGaAs-based mixers presented in Chapter 4.

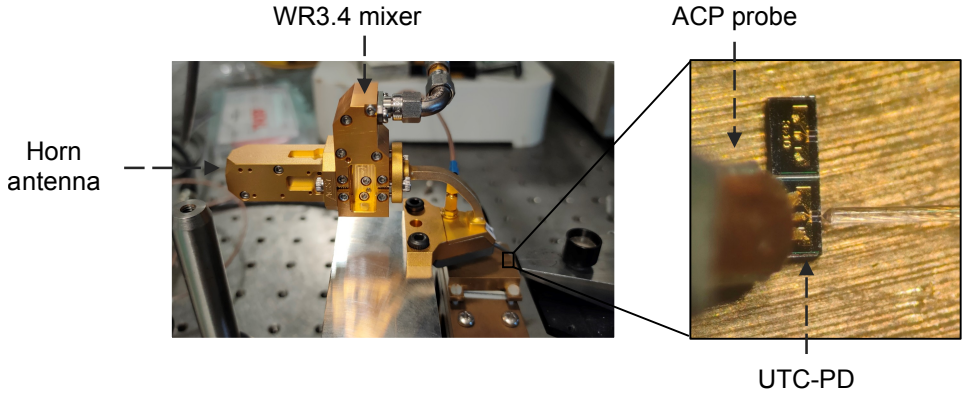

Figure 5.5: Non-integrated 270-320 GHz optoelectronic receiver based on a subharmonic WR3.4 mixer with InGaAs antiparallel SBDs, and a 3x10μm^2 GSG-probed UTC-PD. Adapted with permission from [5-1] © Optica Publishing Group.

To pump the mixer, we used our waveguide-integrated UTC-PDs with CPW pads, as presented in Chapters 2 and 3 [5-7]. The UTC-PD structure was fabricated using optical lithography in six mask steps, achieving the desired features through

dry etching. Ohmic contacts to the p-type and n-type sides were formed by sputtering a Ti/Pt/Au stack, followed by RTA. A detailed fabrication description can be found in [5-7]. The UTC-PD used in this work has an active area of 3x10 μm^2. Figure 5.6 shows two images of a fabricated 3x15 μm^2 photodiode. A GSG probe, shown in Figure 5.5, was used to couple the photodiode's output power to the Schottky mixer. The probe, a Cascade Microtech air co-planar (ACP) WR-8 model, has a 90–140 GHz bandwidth and incorporates a bias T, allowing the UTC-PD's DC voltage to be set. It is important to note that the rectangular waveguide size does not match the LO input port, and its cut-off frequency is lower than the maximum required LO frequency. This results in lower power delivered to the mixer's diodes. However, as shown later, the power was sufficient to drive the mixer at optimal conditions across most of the operating band.

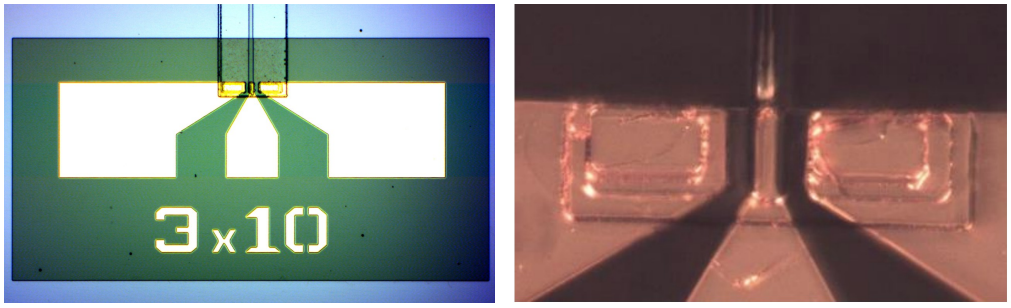

Figure 5.6: Photographs of UTC-PD devices with CPW pads used in the non-integrated and integrated optoelectronic receivers.

In Figure 5.7, a close view of the THz setup used for the mixer characterisation is depicted, highlighting the antenna-integrated UTC-PD used as the calibrated transmitter, the two PTFE THz lenses, and the optoelectronic receiver. The THz path was approximately 20 cm long.

The measured conversion loss as a function of RF frequency is shown in Figure 5.8**a**. The bias voltage was set to -3 V, and the optical power was adjusted to produce a photocurrent of 15 mA. The minimum measured conversion loss is 14.4 dB at 270 GHz, remaining typically below 20 dB. Two key features are observed in the response. First, at 293.5 GHz, a peak in the conversion loss reaches 30.6 dB, attributed to insufficient LO power, which will be discussed later. Second, at the band edge, the conversion loss increases due to the cut-off behaviour inherent to the

mixer's narrowband design. The IF response is shown in Figure 5.8**b**, revealing a 3-dB bandwidth of 19.5 GHz, primarily limited by the use of an SMA connector.

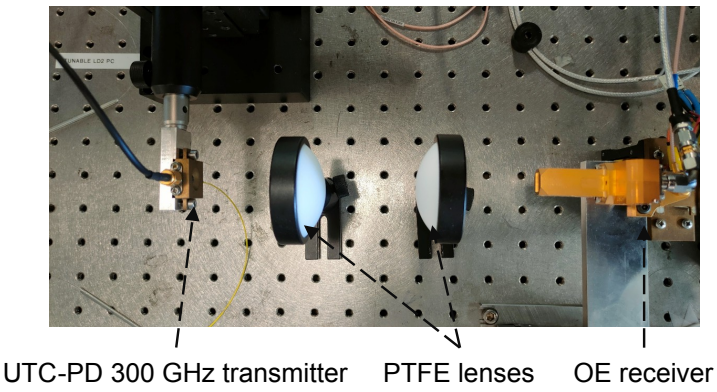

Figure 5.7: Non-integrated receiver characterisation setup. Adapted with permission from [5-1] © Optica Publishing Group.

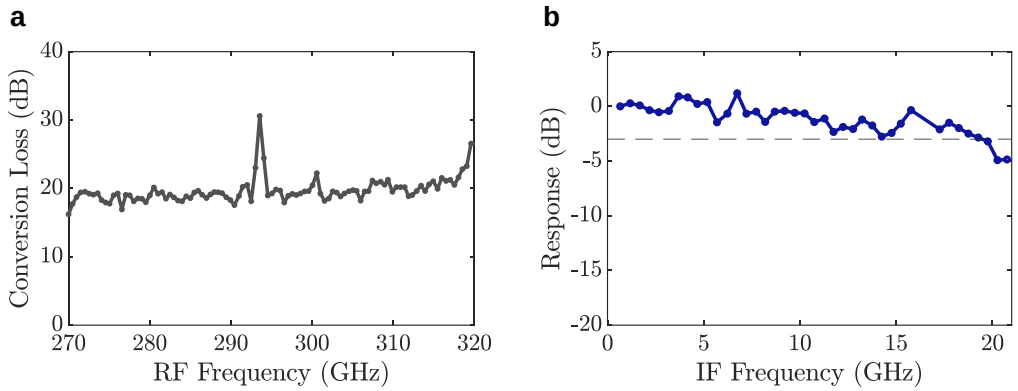

Figure 5.8: Non-integrated receiver characterisation results. **a** Conversion loss as a function of RF frequency. **b** IF power response. Adapted with permission from [5-1] © Optica Publishing Group.

The second set of measured results is shown in Figure 5.9, depicting the conversion loss as a function of pumping photocurrent for different frequencies. We measured the conversion loss for various bias voltages to further investigate the LO pumping conditions. Three main effects influence the measured response: (1) the power response of the UTC-PD, (2) saturation of the SBD mixer diodes, and (3) the effective LO power coupled to the mixer. A key insight is provided by the response at 293.5 GHz, corresponding to an LO frequency of 146.25 GHz. As previously discussed, the ACP probe is rated for up to 140 GHz, leading to an expected power decay and possible resonances at higher frequencies. This was confirmed by LO

power measurements [5-1], where we recorded an LO power of -14.23 dBm at -3 V and 15 mA, insufficient to pump the mixer.

The curves at 293.5 GHz reveal the point at which the UTC-PD output power saturates. As expected, the saturation threshold increased with bias voltage, occurring at approximately 8, 10, and 15 mA. Beyond this point, the conversion loss rises as the delivered LO power decreases. In contrast, at 270 GHz (LO frequency of 134.5 GHz), the conversion loss saturates at a photocurrent below 5 mA, indicating sufficient LO power. Beyond this, the conversion loss slightly degrades due to mixer diode overpumping. A similar trend is observed at other frequencies, with saturation occurring at moderately higher photocurrents, attributed to the combined frequency response of the UTC-PD and ACP probe.

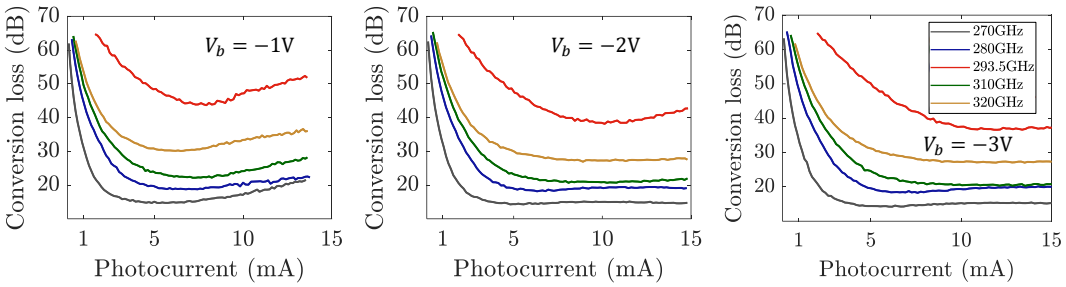

Figure 5.9: Non-integrated receiver characterisation results: Conversion loss as a function of pumping photocurrent for different RF frequencies and bias voltages (V_b). Adapted with permission from [5-1] © Optica Publishing Group.

5.3 Integrated quasi-optical receiver

Among the integrated optoelectronic receivers designed in this work, the hybrid integrated quasi-optical receiver was selected for fabrication and testing. As discussed in Chapter 4, this choice was motivated by the simpler fabrication and assembly process compared to a monolithic integration approach or a hybrid integration using costly rectangular waveguide blocks. Photographs of the complete assembled receiver are shown in Figure 5.10.

First, the brass package was fabricated using CNC machining. The quartz CPW mixer chip was fabricated by depositing a 3 µm gold layer and patterned via optical lithography using direct laser writing. The silicon lens, quartz chip, and

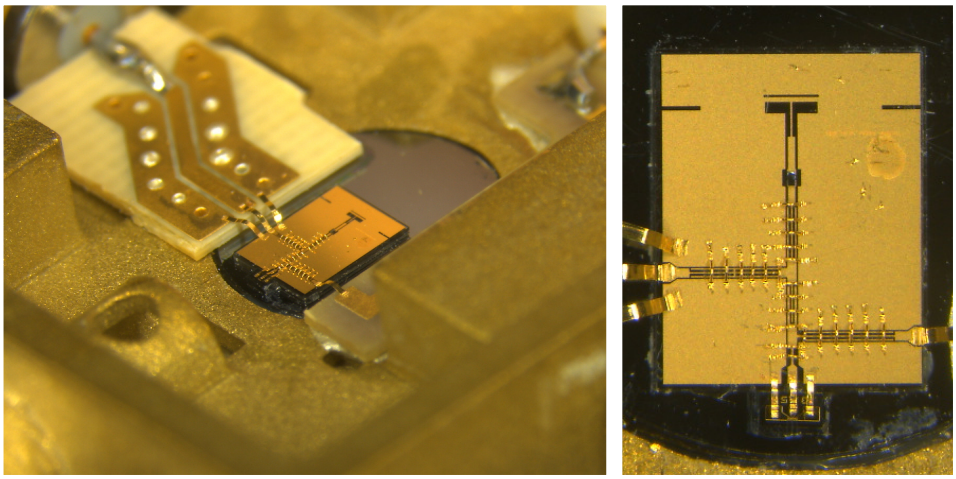

Figure 5.10: Photographs of the optoelectronic quasi-optical receiver after assembly completion. Adapted from [5-2], under a CC-BY license.

UTC-PD were glued to the package, with an additional 75 µm unprocessed quartz substrate to align the heights of the UTC-PD and mixer chip. The SBD chip was then flip-chip bonded to the mixer circuit. The PCBs were positioned and soldered to the connectors using silver epoxy. Connections between the PCBs and the quartz circuit were made with 125 µm wide gold ribbons, while the UTC-PD was bonded to the quartz circuit using 50 µm wide gold ribbons. Cross-track bridges were implemented with 25 µm diameter wire bonds. In the design stage, 50 µm ribbons were considered for cross-track bridges, but wire bonds were found to be easier and more reproducible during assembly. Simulations confirmed that this modification had a negligible impact on performance.

The setup used to characterise the hybrid-integrated quasi-optical receiver is shown in Figure 5.11. As discussed, parabolic mirrors were employed in the THz path to collect and couple the output THz radiation into the optoelectronic receiver. The measured conversion loss is presented in Figure 5.12**a**, with a minimum of 18.1 dB at 250 GHz and a maximum of 29.3 dB at 325 GHz. The measured response exhibits two distinct regions: a relatively flat region between 225 and 260 GHz, where the conversion loss remains close to or below 20 dB, and a higher-frequency range where the loss increases. For comparison, the predicted performance, including simulated coupling losses, is also shown. At 250 GHz, simulations predict a

conversion loss of 13.6 dB, indicating a measured offset of 4.5 dB. The IF response is shown in Figure 5.12**b**, where a 3-dB bandwidth of approximately 23 GHz was measured. Simulations estimate a bandwidth of 19.9 GHz, accounting for the IF PCB, ribbon bonds, and the PCB-to-connector transition. The predicted resonant behaviour is observed, though it occurs at a slightly higher frequency, likely due to simulation inaccuracies.

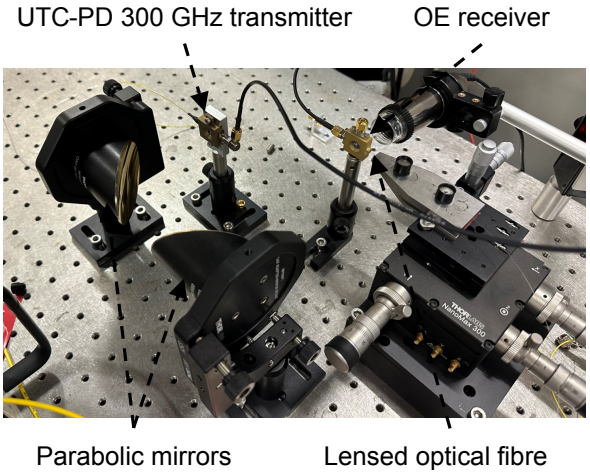

Figure 5.11: Hybrid integrated receiver characterisation setup. Adapted from [5-2], under a CC-BY license.

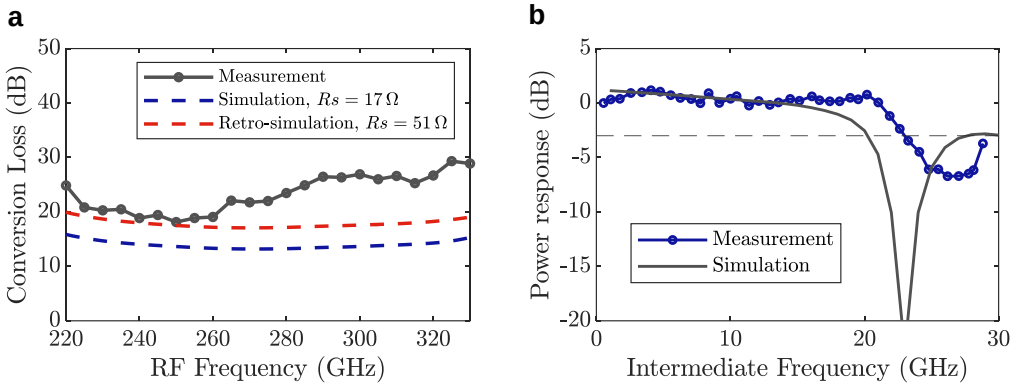

Figure 5.12: Hybrid integrated receiver characterisation results. **a** Conversion loss as a function of RF frequency. **b** IF power response, including simulated results. Adapted from [5-2], under a CC-BY license.

To account for non-idealities contributing to the offset between simulated and measured conversion loss, a common approach in THz Schottky mixer design is to perform retro-simulations by increasing the SBD series resistance [5-8]. This

increase can be partially attributed to the fact that the value extracted from DC measurements ($R_s = 17\,\Omega$) does not account for high-frequency effects, such as skin effects, which increase diode resistance [5-9]. Additionally, simulations may underestimate the RF coupling loss of the antenna-lens system, while fabrication and assembly imperfections are expected to degrade mixer performance. The predicted conversion loss with a three-fold increase in series resistance ($R_s = 51\,\Omega$) is also shown, demonstrating that the predicted performance aligns with measurements in the lower-frequency region (220–330 GHz). However, a larger offset persists at higher frequencies. Figure 5.13 provides insights into this behaviour, presenting the normalised conversion loss response as a function of pumping photocurrent at multiple frequencies.

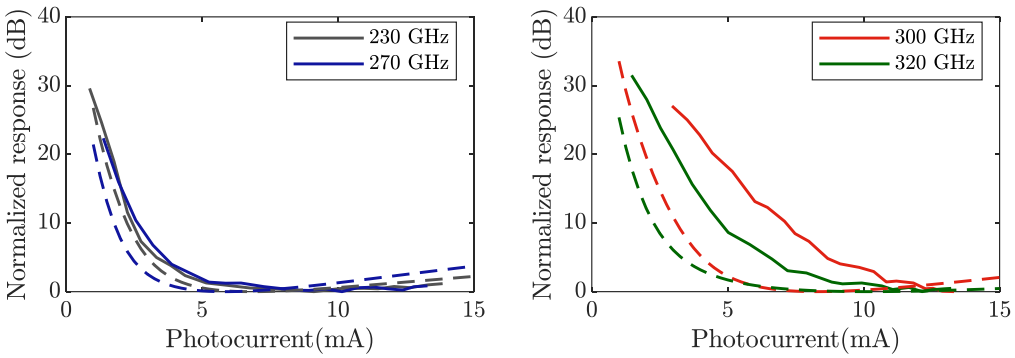

Figure 5.13: Characterisation results of the hybrid integrated receiver, showing the normalised conversion response as a function of pumping photocurrent at different frequencies. Simulated results are indicated by dashed lines. Adapted from [5-2], under a CC-BY license.

At 230 and 270 GHz, the mixer response approaches saturation at approximately 5 mA, achieving optimum performance around 8 mA. Beyond this point, the response slightly degrades due to overpumping of the SBDs. The comparison with predicted performance shows reasonable agreement, though a moderate offset shows a higher photocurrent (LO power) is required in practice. In contrast, at 300 and 320 GHz, saturation occurs at higher photocurrents, and overpumping is not observed. These UTC-PDs, when biased at -3 V and uncooled, saturate at a photocurrent of 10–15 mA [5-7], which is not accounted for in our simulations. The measured response reflects a combination of saturation effects in both the UTC-PD

and SBDs without reaching the optimum LO power, explaining the conversion loss offset at higher frequencies. This suggests that the LO path exhibits higher insertion loss than predicted and a lower UTC-PD cut-off frequency.

5.4 Multi-channel link at 300 GHz

As highlighted in Chapter 1, the target application of this work is 300 GHz wireless communications. To complete the experimental work and show the applicability of photonically-pumped low-barrier Schottky mixers, a fully optoelectronic high-speed multi-channel wireless link was demonstrated using the non-integrated receiver presented in section 5.2. The demonstration was developed in collaboration with the University of Duisburg-Essen (UDE). The following section has been adapted from [5-3], under a CC-BY license.

5.4.1 Wireless link experimental methods

Transmitter and receiver setups

The transmitter setup schematic of the 300 GHz link is depicted in Figure 5.14. The data to be transmitted was generated with a field-programmable gate array (FPGA) board with 88 Gsamples/s digital-to-analogue converters (DACs), designed for use in optical networks. The data consists of a random sequence of 10000 symbols encoded in 16-quadrature amplitude modulation (QAM) Gray format which was sampled at the FPGA rate, and raised-cosine (RC) filtered with a roll-off factor (α) of 0.1. The complex baseband IQ waveform was then digitally upconverted to a frequency $f_{up} = R_s/2 + 1.5\,\text{GHz}$ where R_s is the baseband data bandwidth in GHz which is equal to the baud rate. A pre-emphasis digital filter was used to boost the high frequencies and compensate for the roll-off of RF cables. After the digital-to-analog conversion, the signal was amplified by 28 dB to drive a Mach-Zehnder modulator (MZM) with 40 GHz RF bandwidth.

To generate the different frequency channels, up to three free-running tuneable external cavity lasers (ECLs) with 80 kHz linewidth were modulated by the MZM. All modulated lasers transport the same data to reduce the complexity of the setup. The use of optical heterodyning and coherent reception allows the bias of the MZM

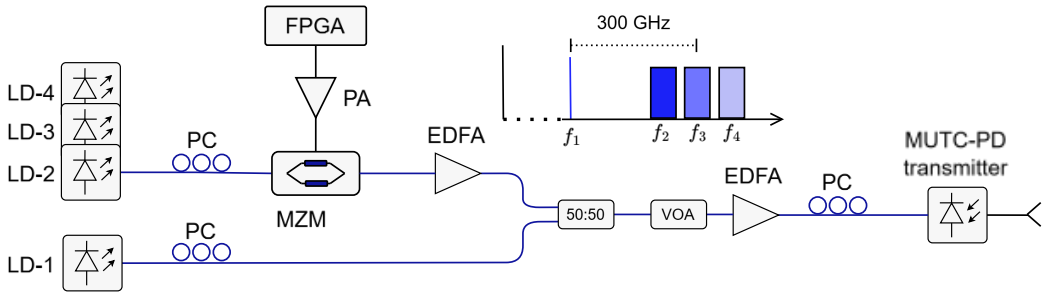

Figure 5.14: Transmitter schematic of the fully-optoelectronic multi-channel 300 GHz communications experiment. LD: Laser diode, PC: Polarization controller, FPGA: Field programmable gate array, PA: Power amplifier, EDFA: Erbium-doped fibre amplifier, VOA: Variable optical attenuator, MUTC-PD: Modified uni-travelling-carrier photodiode. Adapted from [5-3], under a CC-BY license.

to be set near the null point, exploiting a greater signal excursion. After modulation, the optical signals went through an EDFA and then combined with an additional laser, i.e. the photonic local oscillator, separated by the desired THz frequency.

The power of the combined optical signals was adjusted with a variable optical attenuator (VOA) and then amplified again by a second EDFA resulting in 20 dBm of optical power. The VOA also allowed us to monitor and limit the input power of the second EDFA. This amplifier fed the optical-to-terahertz converter, which was based on a 5x30 μm^2 MUTC-PD chip probed with a GSG WR-3.4 probe (Cascade InfinityProbe). MUTC-PDs differ from normal UTC-PD typically by including additional layers for charge compensation, which can enhance carrier transport and power saturation [5-10]. MUTC-PD device design and fabrication details used in this work can be found in [5-11]. A WR-3.4 horn antenna was used at the output of the probe followed by a 5 cm diameter PTFE lens (Thorlabs PTFE LAT100). The bias voltage of the MUTC-PD was fixed at -2 V. The power of the specific MUTC-PD used was not measured, but measurements on same batch devices reveal a power of approximately -18 dBm at 280 GHz and 10 mA of photocurrent [5-12]. The photocurrent was limited to 10 mA to avoid saturating the low-barrier mixer, as will be discussed later. Finally, laser frequency separation and power were monitored in an OSA.

The receiver is based on the non-integrated optelectronic receiver presented in

section 5.2. Figure 5.15 shows the receiver schematic. In this case, a second probed MUTC-PD device was used to pump the mixer, driven with a pair of tuneable ECLs separated by the corresponding LO frequency. The bias of the MUTC-PD is set at -2 V. The optical power at the input of the lensed fibre after the EDFA was measured at 23 dBm. In this case, we used a GSG WR6 probe connected to the input LO port of the low-barrier mixer. The incoming RF signal was coupled to the mixer after propagating 1.5 m with a 5 cm PTFE lens and WR3.4 horn antenna. The down-converted IF signal was amplified with a 40 dB gain LNA and then digitised with an 80 Gsamples/s digital storage oscilloscope (DSO), capturing sequences of 25 μs length. That results in a minimum measurable bit-error-rate (BER) of $4 \cdot 10^{-6}$ for a 10 Gbps signal.

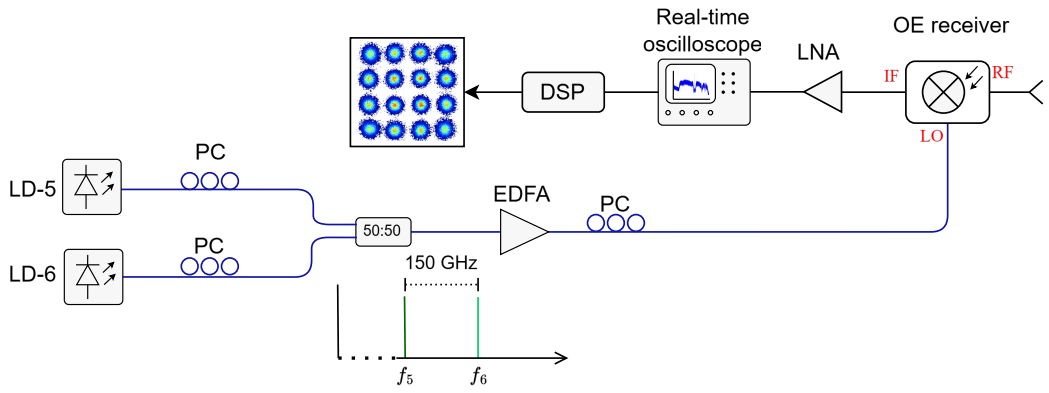

Figure 5.15: Receiver schematic of the fully-optoelectronic multi-channel 300 GHz communications experiment. LD: Laser diode, PC: Polarization controller, EDFA: Erbium-doped fibre amplifier, LNA: Low-noise amplifier, DSP: Digital signal processing, OE: optoelectronic. Adapted from [5-3], under a CC-BY license.

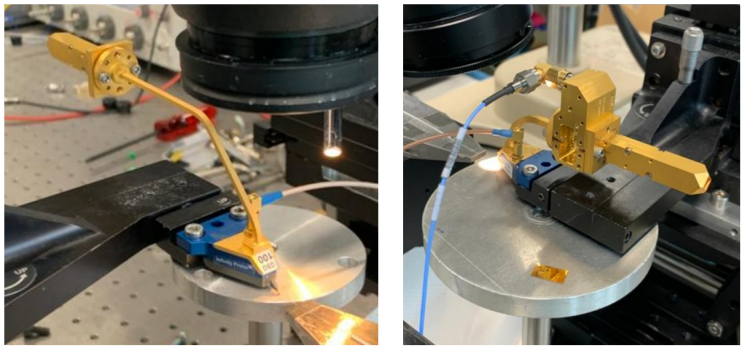

Figure 5.16: Photographs of the 300 GHz transmitter based on a GSG probed MUTC-PD (left) and the photonically-pumped non-integrated receiver (right). Adapted from [5-3], under a CC-BY license.

In Figure 5.16, photographs of the optoelectronic transmitter and receiver are shown, based on the GSG-probed MUTC-PD and the photonically-pumped low-barrier SBD mixer, respectively. Table 5.2 collects the models of the main instruments and equipment used for the transmitter and receiver setups.

Component	**Model**
LD-1, LD-2, LD-3, LD-4	PurePhotonics PPCL200
LD-5, LD-6	IDPhotonics CoBrite DX2-S
EDFA-1	Thorlabs EDFA100P
EDFA-2	IPG Laser GmbH EAD-500-CL
EDFA-3	Keopsys CEFA-CE-BO-HP
MZM	FUJITSU FTM 7938 EZ
PA	SHF 810
LNA	RF-Lambda RLNA00G30GA
FPGA	Fujitsu ROTTA OOLA
DSO	Agilent DSO-X 933304Q
OSA	Photonetics 3651 HR 12 or Apex Technologies AP2683A

Table 5.2: Models of main instruments and equipment used in the 300 GHz communications experiment.

Examples of the resulting optical and IF spectra are depicted in Figure 5.17, The optical spectra corresponds to the case of using three frequency channels (Figure 5.17**a**), and the IF spectra corresponds to a down-converted 10 Gbaud signal (Figure 5.17**b**). In this sense, the spectra reveals four aspects: the signal-signal-beating interference (SSBI) [5-13], the out-of-band IF effects, the cut-off of the scope (33 GHz), and spurious tone from the DAC.

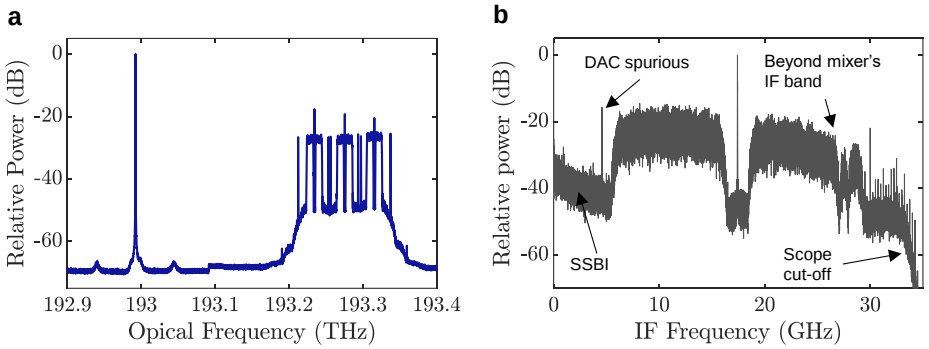

Figure 5.17: Transmission spectra. **a** optical spectra for a three channel transmission. **b** IF of a down-converted 300 GHz signal of 10 Gbaud. Adapted from [5-3], under a CC-BY license.

DSP routine

The digitised IF signal went through a coherent DSP routine (offline) to retrieve the data sequence. The steps are summarised in Figure 5.18. First, the clock of the signal was recovered by performing a cross-correlation with the digital IQ upconverted waveform used in the transmitter DSP. Then the signal was down-converted to baseband. In this case frequency-offset corrections are not needed because the centre frequency is accurately known thanks to the presence of the carrier. This down-conversion was done considering the lower sideband (LSB) by default, but it can also be done by adding the upper sideband (USB). The baseband signal was filtered with an inverse RC filter ($\alpha = 0.1$) and resampled at 2 samples per symbol.

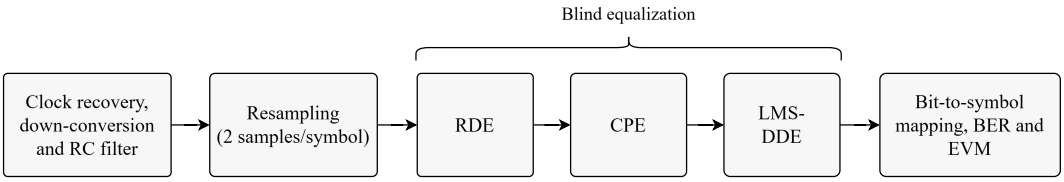

Figure 5.18: DSP routine with blind equalization to decode the received data signal in the multi-channel wireless communications link. Adapted from [5-3], under a CC-BY license.

A set of three blind digital equalisers were used: radius-directed equalizer (RDE), carrier phase estimation (CPE), and the classic least mean square decision-directed equalizer (LMS-DDE). The RDE algorithm was used due to its overall better performance than other techniques like the constant modulus algorithm (CMA) in 16-QAM signals [5-14]. The LMS-DDE helps to further reduce the bit error

rate. For instance, we measured a 150 % BER improvement when including the LMS-DDE for 100 Gbps transmission. Finally, the CPE algorithm is critical as it needs to compensate for the combined phase noise of the free-running lasers used in the transmitter and the receiver. For this purpose, we used the algorithm proposed in [5-15] which is based on a feed-forward architecture. The algorithm is robust against laser line widths of several MHz.

After the equalisers, the recovered symbols were mapped to bits and synchronised with the transmitted sequence. In the last step, the BER and error vector magnitude (EVM) were calculated and the SNR is estimated from the BER result.

Measurements

Using the experimental configuration previously outlined, we performed a set of measurements as detailed here. The transmitted RF frequencies for each case are summarised in table 5.3. The minimum frequency channel separation, denoted by Δf, is established as $\Delta f = 3\,(R_s + 1.5)$ GHz to prevent image frequency interference. In the scenario with two channels, frequency separation of $\Delta f = 2\,(R_s + 1.5)$ GHz could suffice to avoid interference. We maintained the additional separation to utilise the optimal LO range of the low-barrier mixer in the receiver, approximately ranging from 130 to 150 GHz. Furthermore, in the two-channel scenario, the centre frequencies were adjusted for faster signals (symbol rate greater than 10 Gbaud) to accommodate their bandwidth.

Number of channels	RF frequency (GHz)	LO frequency (GHz)*
1	270	145
2	250, 300 ($R_s \leq$ 10 Gbaud) 240, 315 ($R_s >$ 10 Gbaud)	135, 140 130, 147.5
3	240, 280, 320	130, 140, 150

*The LO frequency corresponds to a down-converted IF frequency of 10-20 GHz.

Table 5.3: Summary of frequencies used in the multi-channel link.

For each multi-channel scenario, we transmitted 16-QAM waveforms of increasing data rates as follows: 10 to 100 Gbps in 10 Gbps steps for one channel, 10 to 90 Gbps in 10 Gbps steps for two channels, and 5, 10, 20, 30, and 35 Gbps

for three channels. Each channel was received and sampled sequentially by tuning the photonic LO of the receiver. In addition, the photocurrent at both the MUTC-PD at the transmitter and receiver was optimised. At the transmitter, the goal is to achieve a balance between emitted power and non-linearities in the system. On the receiver side, optimum photocurrent means providing sufficient LO power to saturate conversion loss, leading to improved receiver sensitivity and overall performance. In addition to BER and EVM, which are measured by comparing retrieved and transmitted sequences, the SNR was estimated from the BER result as follows for 16-QAM format [5-16]

$$SNR(dB) = 20 log_{10}\left(\sqrt{10 \cdot erfc^{-1}(8/3 \cdot BER)}\right) \tag{5.1}$$

where $erfc^{-1}$ is the inverse error function.

5.4.2 Wireless transmission results

The main results of the experiments are summarised in Figure 5.19. Some retrieved constellations are plotted in Figure 5.19**b**, showing two examples for each multi-channel scenario. In Figure 5.19**a** the BER results are shown, where the hard decision (HD)-forward error correction (FEC) ($3.84 \cdot 10^{-3}$, 6.7 % overhead) [5-17] and soft decision (SD)-FEC ($1.94 \cdot 10^{-2}$, 15.3 % overhead) [5-18] thresholds are highlighted.

For the single channel case, data rates up to 80 Gbps remain below the HD-FEC limit and we are able to transmit a 100 Gbps signal below SD-FEC. In the two-channel scenario, up to 180 Gbps under the SD-FEC limit are transmitted, resulting in a maximum net data rate of 156 Gbps. The performance is better for the lower frequency channel, up to 100 Gbps, due to the equal power of the two modulated lasers. This results in the higher THz channel having reduced power due to the MUTC-PD roll-off. However, beyond 100 Gbps, the power of the modulated lasers was tuned to compensate for this effect and achieve equal BER. When employing three channels, up to an aggregate 105 Gbps rate is achieved under the SD-FEC limit. In this case, the power of the modulated lasers was compensated for all data

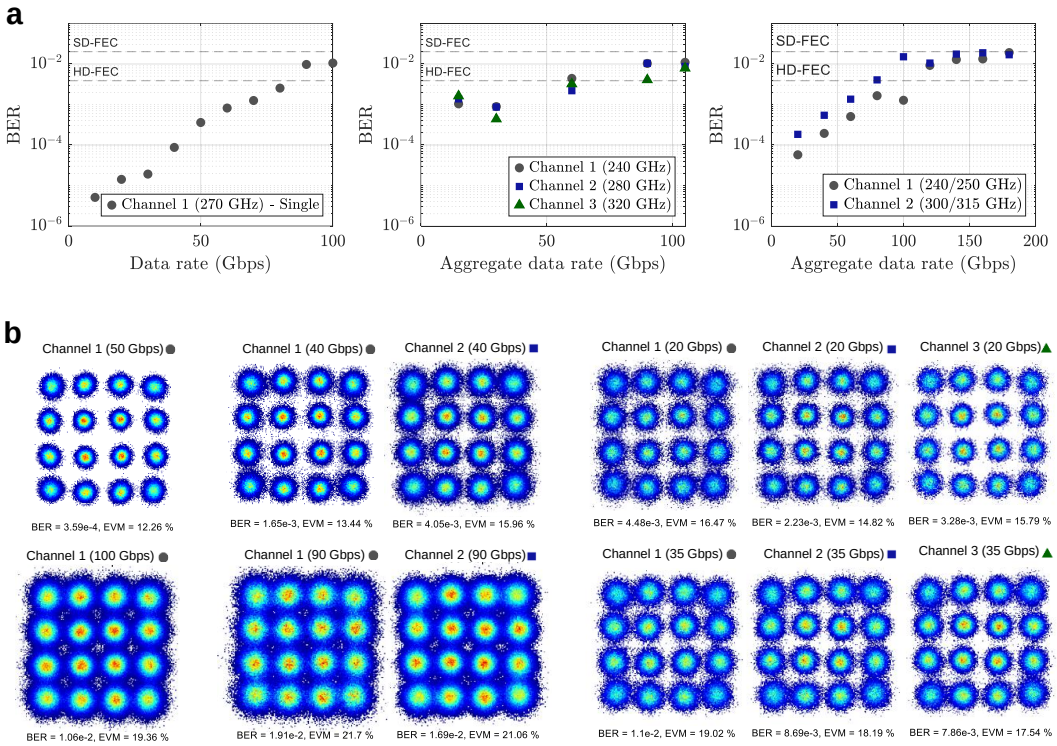

Figure 5.19: Main results of the 300 GHz communications experiment. **a** BER vs data rates for the different multi-channel scenarios. **b** examples of recovered constellations at two data rates for each scenario (single, dual, and triple channel from left to right). Adapted from [5-3], under a CC-BY license.

rates.

The photocurrent of the MUTC-PD transmitter was set to 10 mA for single and dual channel scenarios by keeping the same the input optical power. In the triple channel case, the photocurrent was reduced to 8 mA to mitigate non-linear effects. The photocurrent was limited due to the saturation of the low-barrier mixer, which occurs when the RF power is about 10 dB lower than the LO power. Since we were driving the mixer with approximately -7 dBm of LO power to achieve optimal conversion loss, the received RF power is estimated to be around -18 dBm, as FSPL is compensated with the THz lenses. The 1 dB power compression point for 5x30 μm^2 MUTC-PD devices has been measured to be at approximately 15 mA for 320 GHz [5-19]. Even though the MUTC-PD transmitter is expected be in linear regime at 10 mA, a certain level of non-linearity in the transmission can be attributed to it.

In Figure 5.20**a** and 5.20**b** the average SNR and EVM are shown for each

case. A degradation of performance for the same data rate can be observed when increasing the number of channels, particularly when looking at the SNR at low baud rates. This is expected as a result of non-linearities, and its effects can be visually noticed at the compression of higher energy symbols (Figure 5.19**b**). A better evaluation of this impairment is extracted from the penalty calculation, shown in Figure 5.20**b** based on SNR comparison. A maximum penalty of 1 and 2.5 dB are obtained for the two-channel and three-channel scenarios respectively. This degradation is less significant for increasing data rate, exhibiting a negative penalty for rates beyond 80 Gbps. This occurs because, for increasing data rate, the IF signal approaches or goes beyond the IF bandwidth of the low-barrier mixer, e.g. in the 100 Gbps case, the IF signal occupies frequencies higher than 25 GHz. The performance degradation when using three channels is also associated with extending the maximum operating frequency to 320 GHz, which negatively impacts the mixer's performance.

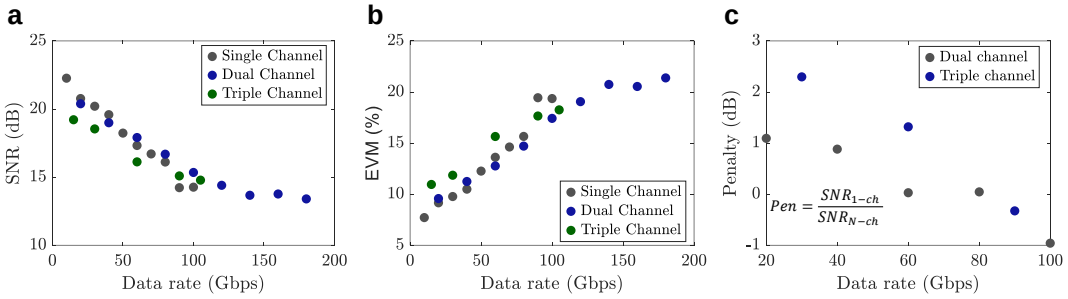

Figure 5.20: Additional 300 GHz communications experiment results. **a** SNR comparison (estimated from the BER measurements). **b** EVM comparison. **c** penalties associated with the transmission of multiple channels. Adapted from [5-3], under a CC-BY license.

The data rates demonstrated in this work represent a state-of-the-art achievement for fully-optoelectronic THz communication systems employing heterodyne detection. Table 5.4 summarises the most relevant prior demonstrations of comparable systems, highlighting the performance gap bridged by this work.

Reference	Centre frequency (GHz)	Modulation format	Total rate (Gbps)	Wireless distance (m)	Optical distance (km)	THz amplification	Real-time	Receiver type
[5-20]	80 to 320	BPSK	0.1	0.1	-	No	Yes	Photoconductor
[5-21]	90 to 310	QPSK	3.2	1	-	No	Yes	Photoconductor
[5-22]	120	QPSK	10	1	-	No	No	Photoconductor
[5-23]	120/320	QPSK	12/4	1	-	No	No	Photoconductor
[5-24]	306	QPSK	30[(1)]	58	-	Yes	No	Photoconductor
[5-25]	300	QPSK	40	52	-	Yes	No	ZBD + photonic LO
[5-26]	262	8/16-QAM	45	1	5	No	No	GaAs Schottky mixer + photonic LO
[5-27]	355	16-QAM	60	4	25	No	No	GaAs Schottky mixer + photonic LO
This work	280	16-QAM	100[(2)]/180[(1)]	1.5	-	No	No	InGaAs Schottky mixer + photonic LO

[(1)] Multi-channel transmission with sequentially received channels. [(2)] Single-channel transmission.

Table 5.4: Comparison of fully-optoelectronic terahertz links with a heterodyne receiver. ZBD: Zero bias detector. Adapted from [5-3], under a CC-BY license.

5.5 Summary and discussion

In this chapter, we have experimentally confirmed the feasibility and potential of optoelectronic receivers based on photonically pumped Schottky mixers. First, by demonstrating the receiver concept at 300 GHz with non-integrated components, we have shown that the conversion loss is typically below 20 dB, with a minimum measured value of approximately 14 dB at 270 GHz. A key outcome is that this performance is achieved with a moderately low photocurrent of 5 mA, enabling the design of higher-frequency receivers. This initial demonstration was followed by the development of an integrated quasi-optical receiver. Its characterisation confirms similar performance, with a minimum measured conversion loss of 18.1 dB, and an IF bandwidth of 23 GHz. A key result is the agreement between measured and predicted performance, validating the modelling and design process proposed in this work and allowing accurate receiver performance prediction, despite some discrepancies discussed. Again, optimal performance is achieved with a low photocurrent of approximately 5 mA, confirming the feasibility of integrating UTC-PDs with low-barrier InGaAs SBD.

The results presented here demonstrate the potential of the optoelectronic receiver concept, achieving a minimum conversion loss at least an order of magnitude lower than other photonic-based receivers in the 220–330 GHz band, such as photoconductor mixers. Compared to GaAs SBD mixers, performance is reduced by approximately 5–10 dB, partly due to the lower maturity of these designs relative to state-of-the-art GaAs Schottky mixers. Possible improvements to the receiver

design and implementation are discussed in the future work section of Chapter 6. Beyond device characterisation, we demonstrated the optoelectronic receiver in a 300 GHz communications system fully enabled by photonics. We showed that the receiver supports data rates comparable to electronic-based receivers, achieving an aggregate rate of up to 180 Gbps.

Compared to receivers based on photoconductors, the main limitation of the optoelectronic receiver approach is frequency tuneability. However, extreme tuneability is arguably unnecessary for communications, as future terahertz links will likely operate within a defined frequency range, such as 252–325 GHz in IEEE 802.15.3d [5-28]. In this context, the multi-channel link demonstration covers nearly the full bandwidth of the standard, with the primary limitation arising from the low-barrier mixer design rather than the technology itself. Additionally, long-distance links, such as fronthaul or backhaul, will likely require amplification, inherently restricting the operational frequency range. We argue that the key advantages of photonics-enabled systems in terahertz communications are: (1) the agility of signal generation, enabling multiple channel signals over a wide bandwidth, and (2) the distribution of both transmitter and receiver LOs via optical fibre.

References

[5-1] I. Belio-Apaolaza, J. Seddon, D. Moro-Melgar, *et al.*, "Photonically-driven schottky diode based 0.3 THz heterodyne receiver," en, *Opt. Express*, vol. 30, no. 24, pp. 43 223–43 236, Nov. 2022.

[5-2] I. Belio-Apaolaza, J. Seddon, H. Wang, *et al.*, "Integrated 300 GHz optoelectronic mixer based on photonically-pumped low-barrier Schottky diodes," *J. Lightwave Technol.*, pp. 1–10, 2025.

[5-3] I. Belio-Apaolaza, J. Martinez-Gil, J. Tebart, *et al.*, "Fully-optoelectronic 300 GHz multi-channel wireless link using a photonically-pumped low-barrier mixer for up to 180 Gbps," *J. Lightwave Technol.*, vol. 43, pp. 19–28, Jan. 2025.

[5-4] C. C. Renaud, M. Natrella, C. Graham, J. Seddon, F. Van Dijk, and A. J. Seeds, "Antenna integrated THz uni-traveling carrier photodiodes," *IEEE J. Sel. Top. Quantum Electron.*, vol. 24, no. 2, pp. 1–11, Mar. 2018.

[5-5] J. P. Seddon, M. Natrella, X. Lin, C. Graham, C. C. Renaud, and A. J. Seeds, "Photodiodes for terahertz applications," *IEEE J. Sel. Top. Quantum Electron.*, vol. 28, no. 2, pp. 1–12, 2022.

[5-6] O. Cojocari, I. Oprea, H. Gibson, and A. Walber, "SubMM-wave multipliers by film-diode technology," in *2016 46th European Microwave Conference (EuMC)*, IEEE, 2016, pp. 337–340.

[5-7] X. Lin, M. Natrella, J. Seddon, *et al.*, "High performance waveguide uni-travelling carrier photodiode grown by solid source molecular beam epitaxy," en, *Opt. Express*, vol. 27, no. 25, pp. 37 065–37 086, Dec. 2019.

[5-8] A. E. Maestrini, J. V. Siles, C. Lee, R. Lin, and I. Mehdi, "A 2 THz room temperature bias-able Schottky mixer," *IEEE Transactions on Terahertz Science and Technology*, vol. 15, no. 2, pp. 169–180, 2025.

[5-9] S. A. Maas, *Nonlinear microwave and RF circuits*, en, 2nd ed. Norwood, MA: Artech House, Jan. 2003.

[5-10] Z. Li, H. Pan, H. Chen, A. Beling, and J. C. Campbell, "High-saturation-current modified uni-traveling-carrier photodiode with cliff layer," *IEEE J. Quantum Electron.*, vol. 46, no. 5, pp. 626–632, May 2010.

[5-11] M. Grzeslo, S. Dülme, S. Clochiatti, *et al.*, "High saturation photocurrent THz waveguide-type MUTC-photodiodes reaching mW output power within the WR3.4 band," en, *Opt. Express*, vol. 31, no. 4, pp. 6484–6498, Feb. 2023.

[5-12] E. Abacioglu, M. Grzeslo, T. Neerfeld, J. L. F. Estevez, and A. Stoehr, "High output power broadband 1.55 μm waveguide-integrated terahertz MUTC-photodiodes," in *2023 23rd International Conference on Transparent Optical Networks (ICTON)*, IEEE, Jul. 2023, pp. 1–4.

[5-13] Z. Li, M. S. Erkılınç, S. Pachnicke, *et al.*, "Signal-signal beat interference cancellation in spectrally-efficient WDM direct-detection Nyquist-pulse-shaped 16-QAM subcarrier modulation," en, *Opt. Express*, vol. 23, no. 18, pp. 23 694–23 709, Sep. 2015.

[5-14] I. Fatadin, D. Ives, and S. J. Savory, "Blind equalization and carrier phase recovery in a 16-QAM optical coherent system," *J. Lightwave Technol.*, vol. 27, no. 15, pp. 3042–3049, Aug. 2009.

[5-15] T. Pfau, S. Hoffmann, and R. Noe, "Hardware-efficient coherent digital receiver concept with feedforward carrier recovery for M -QAM constellations," *J. Lightwave Technol.*, vol. 27, no. 8, pp. 989–999, Apr. 2009.

[5-16] X. Liu, "High-capacity long-haul optical fibre transmission," en, in *Optical Communications in the 5G Era*, Academic Press, Oct. 2021, pp. 185–232.

[5-17] E. Agrell and M. Secondini, "Information-theoretic tools for optical communications engineers," in *2018 IEEE Photonics Conference (IPC)*, Sep. 2018, pp. 1–5.

[5-18] C. Schow, M. Filer, and C. Doerr, "Coherent interconnects for data centers," in *Integrated Photonics for Data Communication Applications*, M. Glick, L. Liao, and K. Schmidtke, Eds., Elsevier, Jan. 2023, pp. 201–232.

[5-19] E. Abacioglu, M. Grzeslo, T. Neerfeld, J. L. F. Estevez, and A. Stoehr, "High output power broadband 1.55 um waveguide-integrated terahertz MUTC-photodiodes," in *2023 23rd International Conference on Transparent Optical Networks (ICTON)*, IEEE, Jul. 2023, pp. 1–4.

[5-20] A. Morales, G. Nazarikov, S. Rommel, C. Okonkwo, and I. T. Monroy, "Highly tunable heterodyne sub-THz wireless link entirely based on optoelectronics," *IEEE Transactions on Terahertz Science and Technology*, vol. 11, no. 3, pp. 261–268, May 2021.

[5-21] E. Andrianopoulos, N. K. Lyras, E. Pikasis, *et al.*, "Real-time sub-THz link enabled purely by optoelectronics: 90–310 GHz seamless operation," *IEEE Photonics Technol. Lett.*, vol. 35, no. 5, pp. 237–240, Mar. 2023.

[5-22] M. Deumer, L. Liebermeister, O. Stiewe, *et al.*, "Purely photonic wireless link at 120 GHz with a photoconductive antenna as heterodyne receiver," in *2023 48th International Conference on Infrared, Millimeter, and Terahertz Waves (IRMMW-THz)*, IEEE, Sep. 2023, pp. 1–2.

[5-23] M. Deumer, O. Stiewe, S. Nellen, *et al.*, "Optoelectronic heterodyne THz receiver for 100–300 GHz communication links," *IEEE Access*, vol. 12, pp. 27 158–27 166, 2024.

[5-24] T. Harter, S. Ummethala, M. Blaicher, *et al.*, "Wireless THz link with optoelectronic transmitter and receiver," en, *Optica*, vol. 6, no. 8, p. 1063, Aug. 2019.

[5-25] J. Dittmer, J. Tebart, C. Füllner, C. Koos, A. Stöhr, and S. Randel, "200 gbit/s wireless THz transmission over 52m using optoelectronic signal generation," pp. 134–137, Sep. 2023.

[5-26] S. Cho, S.-R. Moon, M. Sung, S.-H. Cho, T. Kawanishi, and H.-J. Song, "A 262-GHz wireless IFoF uplink with remote down-conversion using optically generated sub-THz LO," *IEEE Trans. Microw. Theory Tech.*, vol. 71, no. 5, pp. 2276–2285, May 2023.

[5-27] P. T. Dat, I. Morohashi, N. Sekine, A. Kanno, N. Yamamoto, and K. Akahane, "Fiber-terahertz-fiber bridge system in the 355-GHz band using a simple optical frequency comb and a photonics-enabled receiver," en, *Opt. Lett.*, vol. 48, no. 8, pp. 2190–2193, Apr. 2023.

[5-28] V. Petrov, T. Kurner, and I. Hosako, "IEEE 802.15.3d: First standardization efforts for sub-terahertz band communications toward 6G," *IEEE Commun. Mag.*, vol. 58, no. 11, pp. 28–33, Nov. 2020.

Chapter 6

Conclusions and future work

6.1 Conclusions

The research goal of this work, defined in Chapter 1, was to advance optoelectronic terahertz receivers and bridge the performance gap between electronic and optoelectronic solutions. Through the development, fabrication, and characterisation of integrated UTC-PD and SBD-based receivers, this goal has been successfully achieved, demonstrating near state-of-the-art down-conversion efficiency.

A key conclusion is that the modelling and design process presented in Chapter 2 provides a reliable tool for predicting receiver performance with reasonable accuracy, a non-trivial task. This methodology was first applied to design a monolithically integrated receiver, with a predicted minimum conversion loss of 12.46 dB and a noise temperature of 1548 K at approximately 250 GHz. We have demonstrated that this performance can be achieved by fabricating an SBD using the standard UTC-PD epitaxy and employing a compatible fabrication process with minimal modifications.

The main drawback of monolithic integration is the trade-off between UTC-PD, SBD, and mixer performance. Optimising the epitaxial structure to enhance both active devices is challenging and may not always be feasible. In addition, monolithic integration of the mixer circuit forces the use of an InP substrate and CPW waveguides, though other materials and waveguide architectures are more suitable for THz operation, both to minimise circuit losses and to reduce the Schot-

tky contact barrier height. Despite these challenges, the designed receiver and its simulated performance validate the concept, achieving remarkable conversion loss and noise temperature in the 300 GHz band.

In the second part of this work, we have developed hybrid integrated solutions using ready-to-assemble UTC-PDs and low-barrier SBDs. The quasi-optical receiver design achieves a simulated minimum intrinsic conversion loss and noise temperature of 11.86 dB and 1293 K at 276 GHz, demonstrating an improvement primarily attributed to the use of optimised air-bridged InGaAs Schottky contacts, with a cut-off frequency of 11.42 THz, compared to 1.62 THz for the InP monolithically integrated SBDs. The quasi-optical receiver offers advantages in fabrication and assembly over rectangular waveguide receivers, facilitating proof-of-concept implementation. Additionally, we introduced a WR3 receiver with microstrip waveguides, achieving a predicted conversion loss and noise temperature as low as 10.3 dB and 694 K at approximately 280 GHz, demonstrating that state-of-the-art performance is achievable with our approach.

Characterisation of both non-integrated and integrated receivers have experimentally confirmed the feasibility of the proposed concept, with measured conversion losses at least an order of magnitude lower than existing optoelectronic receivers, reaching $\sim$15–20 dB under optimal LO pumping. A key finding is that UTC-PDs can provide sufficient power to saturate the mixer diodes, in some cases with only $\sim$5–6 mA of photocurrent. The LO power requirement varies with frequency due to impedance mismatch, UTC-PD frequency response, and THz circuit losses. Integrating the UTC-PD and SBD increases LO path losses, primarily due to lossy T-junctions in CPW for the bias T and IF signal extraction. To mitigate these non-idealities, using InGaAs as the Schottky contact material to reduce barrier height is key. Narrow-band designs with reduced LO power coupling losses could enable the use of GaAs Schottky contacts for further performance enhancement. However, for higher-frequency operation where UTC-PD power is more limited, InGaAs remains the preferred option.

Finally, we have demonstrated a record-breaking 180 Gbps multi-channel link,

showcasing the potential of this solution compared to other photonics-based THz receivers. Even though this demonstration was carried out with the non-integrated receiver, the measured conversion loss and IF bandwidth of the integrated receiver indicates that similar data rates may be achieved. Unlike power-hungry electronic multiplier chains, optoelectronic receivers offer an efficient and compact alternative. This work demonstrates that a fully-optoelectronic link can compete with electronic LO-based systems, enabling multi-channel 300 GHz communications with reduced THz front-end power consumption and complexity, while ensuring seamless integration with fibre networks. These advantages make photonically-pumped Schottky receivers a strong candidate for wireless fronthaul and backhaul in future 6G and beyond networks. Beyond communications, the benefits of optoelectronic receivers extend to other applications, such as radio-astronomy telescope arrays, as discussed in Chapter 1.

6.2 Future work

Future research directions can be categorised into five main areas: (1) monolithic integration solutions, (2) hybrid integration solutions, (3) modelling improvements, (4) FMBD-based receivers, and (5) further experimental characterisation and system demonstrations.

6.2.1 Monolithic integration

In this work, the monolithic receiver remained at the design stage despite the promising simulated results. A natural continuation of this research involves fabricating and testing the receiver, which can be divided into three stages: (1) fabrication and characterisation of the InP SBD, (2) fabrication and characterisation of both the UTC-PD and SBD, and (3) fabrication and characterisation of the fully integrated receiver. The first step is essential for optimising InP Schottky contact fabrication, understanding process limitations, and validating model predictions of I-V and C-V characteristics. The second step focuses on developing a fabrication process capable of producing both active devices while ensuring performance is not degraded compared to their dedicated fabrication. Finally, the complete mixer cir-

cuit can be fabricated and assembled, potentially using the quasi-optical packaging employed for the hybrid integrated receiver.

As discussed, the current UTC-PD epitaxy lacks an appropriate n-type layer to form a high cut-off frequency THz Schottky contact with a reduced barrier height. Therefore, an interesting research direction, related to monolithic receivers, would be to redesign the epitaxy to incorporate such a layer. While InGaAs offers high electron mobility and a low barrier height, it also absorbs 1550 nm light, which could lead to excess noise. A promising alternative could be InGaAsP, which is used for the optical waveguide and, with adjusted doping, could provide better capacitance-resistance trade-off with lower barrier height than InP. However, modifying the epitaxial structure would impact UTC-PD capacitance and carrier transport. To assess these effects, a semiconductor model, such as a DD model similar to that used for the SBD, would be necessary for analysing UTC-PD behaviour. Additionally, the SBD fabrication process could be further improved, for example, by implementing an air-bridged structure to minimise parasitic effects, or by using micro transfer printing techniques [6-1] to replace the InP substrate with better alternatives in terms of heat dissipation and dielectric losses.

6.2.2 Hybrid integration

Despite the satisfactory measured performance of the quasi-optical receiver, further improvements could enhance down-conversion efficiency and IF bandwidth. Ribbon bonding was used to connect the UTC-PD to the mixer circuit for ease of implementation; however, adopting a flip-chip approach would improve coupling efficiency and increase LO power delivery to the SBDs, particularly at higher frequencies. Additionally, the laser writing process used for the quartz circuit limited the ground-to-signal gap to approximately 10 µm. Enhancing this resolution would enable further circuit miniaturisation, reducing propagation losses and minimising odd-mode excitation at T-junctions. Nevertheless, fabricating and testing the WR3 receiver or other rectangular waveguide designs remains of high interest to demonstrate state-of-the-art sensitivity with the optoelectronic receiver. Moreover, exploring higher frequency designs would be valuable, targeting bands relevant not only

for communications but also for radio astronomy. These designs could benefit from alternative mixer configurations, such as higher order harmonic mixers, to overcome LO power limitations.

6.2.3 Modelling improvements

The modelling framework proposed in this work can be further refined in several ways. Regarding the SBD model, tunnelling was not included as it is negligible at low doping levels and room temperature [6-2]. However, if the Schottky contact layer doping is increased, this effect would require consideration. Another key assumption in the SBD model is the quasi-static approximation, which remains valid at lower THz frequencies (below 500 GHz). For higher frequencies, this assumption may no longer hold, necessitating a revision of the model. In this context, DD models assume a static relationship between carrier velocity and the electric field [6-3]–[6-5], meaning carriers are considered to respond instantly to local conditions. As a result, these models cannot capture nonlocal effects such as velocity overshoot, which become significant in micron- and submicron-scale Schottky diodes [6-6], essential for higher-frequency operation. Implementing more complex semiconductor models that consider more moments of the BTE, like hydrodynamic models, or models based in the Monte Carlo method [6-6] would be of interest. Additionally, incorporating self-heating effects [6-7] would be an interesting enhancement.

For the UTC-PD model, a primary limitation is its reliance on impedance measurements of fabricated devices. A promising research direction would be the development of a semiconductor/electromagnetic model capable of accurately predicting impedance for a given epitaxial structure. Similarly, the current model assumes a perfect quadratic relationship between photocurrent and output power, neglecting UTC-PD saturation at high photocurrent levels. A more advanced semiconductor/electromagnetic model could incorporate this effect alongside self-heating considerations to improve power prediction accuracy.

For mixer non-linear simulations, the main improvement would be in noise estimation. The current approach considers only shot noise and thermal noise in harmonic balance simulations. However, hot-electron noise is known to be an im-

portant contributor when current densities are high [6-8], [6-9], which may occur when the diodes operate under optimal conditions. Including this effect would enhance the accuracy of the noise analysis.

6.2.4 FMBD-based receivers

The receivers presented in this work employ mixer diodes based on InP or InGaAs Schottky contacts. As discussed in Chapter 1, an alternative approach for resistive THz mixer diodes involves the use of FMBDs. Due to the all-semiconductor characteristic, they provide key advantages, including precise control over the barrier height, and enhanced reproducibility, as they are not susceptible to surface states that may alter the diode's rectifying characteristics [6-10], [6-11]. Moreover, the barrier height can be even lower than InGaAs Schottky contacts, leading to reduced LO power requirements. Given these benefits, the integration of UTC-PDs and FMBDs, whether through monolithic or hybrid approaches, constitutes a promising direction for future research. In this sense, existing UTC-PD and FMBD materials are already compatible for epitaxial growth, making monolithic integration a feasible and compelling solution.

6.2.5 Experimental work

The primary remaining task in mixer characterisation is the measurement of noise temperature, which was not performed for the receivers discussed in this work. This can be achieved using standard Y-factor measurements, where, at THz frequencies, room-temperature and liquid nitrogen-cooled absorbers serve as hot and cold loads [6-12]. Noise temperature characterisation would enable validation and refinement of noise estimations in mixer simulations, while also allowing conversion loss to be extracted from them, providing verification of the conversion loss measurements. For these experiments, the choice of photonic local oscillator sources is critical, as LO noise directly impacts the measured noise figure. Employing ultra-low-noise lasers and avoiding optical amplification would be recommended.

Beyond noise temperature, phase noise of the down-converted signal is another key figure of merit that was not evaluated. In this work, free-running lasers

were used, which are unsuitable for applications where phase noise is critical. A fair comparison would require locked optical sources, such as filtered optical frequency combs [6-13], [6-14], to assess and compare the phase noise performance of optoelectronic down-conversion against electronic solutions.

Regarding system demonstrations, the multi-channel link experiment validated the applicability of the optoelectronic receiver concept but was conducted with the non-integrated receiver. Extending this demonstration to the integrated receiver would be of interest. The demonstrated 1.5 m link was limited by the optical table size, but longer distances could be achieved using larger lenses and commercially available 300 GHz amplifiers, potentially extending the range to the kilometre scale [6-15]. Additionally, optoelectronic receivers could be employed in alternative system architectures, such as real-time wireless bridges interconnecting optical fibre networks [6-16], [6-17]. Although communications was the primary focus of this work, demonstrating their viability for other applications, such as radio-astronomy, would further highlight the advantages of photonically-pumped Schottky mixers.

References

[6-1] T. Nagatsuma, W. Gao, Y. Kawamoto, T. Ohara, H. Ito, and T. Ishibashi, "Si- and SiC-based integration platforms for generation, transmission, and detection of THz signals," in *2024 International Topical Meeting on Microwave Photonics (MWP)*, IEEE, Sep. 2024, pp. 1–4.

[6-2] M. T. Faber, J. Chramiec, and M. Adamski, *Microwave and Millimeter-wave Diode Frequency Multipliers*. Artech House, Jan. 1995.

[6-3] W. L. Schroeder and I. Wolff, "Monte-Carlo study of high-frequency, large-signal transport parameters for physics based device simulation," *IEEE Trans. Electron Devices*, vol. 42, no. 5, pp. 819–827, May 1995.

[6-4] M. S. Lundstrom, "Fundamentals of carrier transport, 2nd edn," *Measurement Science and Technology*, vol. 13, pp. 230–230, Feb. 2002.

[6-5] S. Selberherr, *Analysis and simulation of semiconductor devices*, en, 1984th ed. Vienna, Austria: Springer, Dec. 2012.

[6-6] D. Pardo Santos, "Analysis and design of multipliers and mixers via Monte Carlo modelling at THZ bands," en, Ph.D. dissertation, 2019.

[6-7] A. Y. Tang, "Modelling and characterisation of terahertz planar Schottky diodes," Ph.D. dissertation, 2013.

[6-8] G. M. Hegazi, A. Jelenski, and K. S. Yngvesson, "Limitations of microwave and millimeter-wave mixers due to excess noise," *IEEE Trans. Microw. Theory Tech.*, vol. 33, no. 12, pp. 1404–1409, Dec. 1985.

[6-9] T. W. Crowe and R. J. Mattauch, "Analysis and optimization of millimeter-and submillimeter-wavelength mixer diodes," *IEEE Trans. Microw. Theory Tech.*, vol. 35, no. 2, pp. 159–168, Feb. 1987.

[6-10] H. Ito and T. Ishibashi, "InP/InGaAs Fermi-level managed barrier diode for broadband and low-noise terahertz-wave detection," en, *Jpn. J. Appl. Phys.*, vol. 56, no. 1, p. 014 101, Dec. 2016.

[6-11] H. Ito and T. Ishibashi, "Highly sensitive terahertz-wave detection by Fermi-level managed barrier diode," en, in *Optical Sensing, Imaging, and Photon Counting: From X-Rays to THz 2019*, vol. 11088, SPIE, Sep. 2019, pp. 15–22.

[6-12] A. E. Maestrini, J. V. Siles, C. Lee, R. Lin, and I. Mehdi, "A 2 THz room temperature bias-able Schottky mixer," *IEEE Transactions on Terahertz Science and Technology*, vol. 15, no. 2, pp. 169–180, 2025.

[6-13] E. J. Tough, M. J. Fice, G. Carpintero, C. C. Renaud, A. J. Seeds, and K. Balakier, "InP integrated optical frequency comb generator using an amplified recirculating loop," *Opt. Express, OE*, vol. 30, no. 24, pp. 43 195–43 208, Nov. 2022.

[6-14] D.-C. Shin, B. Kim, H. Jang, Y.-j. Kim, and S.-W. Kim, "Photonic comb-rooted synthesis of ultra-stable terahertz frequencies," *Nat. Commun.*, vol. 14, Feb. 2023.

[6-15] I. Belio-Apaolaza, J. Martinez-Gil, J. Tebart, *et al.*, "Fully-optoelectronic 300 GHz multi-channel wireless link using a photonically-pumped low-barrier mixer for up to 180 Gbps," *J. Lightwave Technol.*, vol. 43, pp. 19–28, Jan. 2025.

[6-16] A. Kanno, P. T. Dat, N. Sekine, *et al.*, "Seamless fiber-wireless bridge in the millimeter- and terahertz-wave bands," *Journal of Lightwave Technology*, vol. 34, no. 20, pp. 4794–4801, 2016.

[6-17] L. Gonzalez-Guerrero, H. Shams, I. Fatadin, *et al.*, "Pilot-tone assisted 16-QAM photonic wireless bridge operating at 250 GHz," *J. Lightwave Technol.*, vol. 39, no. 9, pp. 2725–2736, May 2021.

Appendix A

Physics-based modelling of SBDs

A.1 Drift-diffusion model equations

Modelling the behaviour of any semiconductor device fundamentally requires describing carrier transport. This is commonly achieved using the semi-classical Boltzmann Transport Equation (BTE). The solution to the BTE is the carrier distribution function $f(\vec{r},\vec{k},t)$, where $\vec{r}$ and $\vec{k}$ represent position and momentum spaces, respectively, at time t [A-1]. The implicit form of the BTE arises from the fact that the total derivative of the distribution function vanishes, in accordance with Liouville's theorem [A-2].

$$\frac{d}{dt}f(\vec{r},\vec{k},t) = 0 \tag{A.1}$$

The implicit form of the BTE can be expanded as

$$\frac{\partial f}{\partial t} + \nabla_{\vec{k}} f \frac{d\vec{k}}{dt} + \nabla f \frac{d\vec{r}}{dt} = 0 \tag{A.2}$$

where $\nabla_{\vec{k}}$ and ∇ denote the gradient operators with respect to the momentum and spatial coordinates, respectively. To derive the explicit form of the BTE, we first consider the forces acting on a particle. The total force can be expressed as

$$\vec{F} = \hbar \frac{d\vec{k}}{dt} \tag{A.3}$$

where $\hbar$ is the Planck constant. These forces can be classified into electro-

magnetic ($\vec{F}_e$) and internal lattice collision forces ($\vec{F}_i$). Since the laws of dynamics cannot directly determine internal forces [A-2], statistical methods are employed, leading to the collision integral [A-1]

$$\begin{aligned}\nabla_{\vec{k}} f \frac{\vec{F}_i}{\hbar} &= \int_{Vk'} (f(\vec{r},\vec{k},t)\cdot(1-f(\vec{r},\vec{k}',t))\cdot S(\vec{k},\vec{k}') \\ &\quad - f(\vec{r},\vec{k}',t)\cdot(1-f(\vec{r},\vec{k},t))\cdot S(\vec{k}',\vec{k}))d\vec{k}' \\ &= \left(\frac{\partial f}{\partial t}\right)_{col}\end{aligned} \tag{A.4}$$

where $S(\vec{k},\vec{k}')$ represents the probability per unit time for a carrier to scatter from state $\vec{k}$ to $\vec{k}'$. Substituting Equations A.3-A.4 into Equation A.2, and noting that the group velocity of carriers is given by $\vec{v} = d\vec{r}/dt$, the explicit form of the BTE can be obtained as [A-3]

$$\frac{\partial f}{\partial t} + \frac{\vec{F}_i}{\hbar}\nabla_{\vec{k}} f + \vec{v}\nabla f = \left(\frac{\partial f}{\partial t}\right)_{col} \tag{A.5}$$

Equation A.5 holds under several implicit assumptions: scattering is independent of external forces and occurs instantaneously, carrier-carrier interactions are negligible, and band theory along with the effective mass theorem applies to the semiconductor [A-1]. Solving for the carrier distribution f allows the derivation of key parameters such as carrier concentrations, energy densities, current, and diffusion coefficients. However, this is highly challenging, as Equation A.5 represents an integro-differential equation with seven independent variables and no closed-form solution [A-1].

A common approach to solving the BTE is the method of moments [A-4]. This involves multiplying the BTE by a generic scalar function and integrating over the momentum space. The key is to choose functions that enforce the conservation of specific physical quantities. Drift-diffusion (DD) models simplify the BTE by retaining only the first two moments, corresponding to electron and momentum conservation. Based on these principles, the DD model equations can be derived. First, the continuity equations for electrons and holes, representing electron conservation, can be expressed as

$$\nabla \cdot \vec{J}_n - q\frac{\partial n}{\partial t} = q(R_n - G_n) \tag{A.6}$$

$$\nabla \cdot \vec{J}_p - q\frac{\partial p}{\partial t} = q(R_p - G_p) \tag{A.7}$$

where q, n, p, J_n, and J_p denote the elementary charge, electron concentration, hole concentration, electron current density, and hole current density, respectively. The terms $R_{n,p}$ and $G_{n,p}$ represent the generation and recombination rates of electrons and holes. For momentum conservation, the DD model assumes that electrons remain in thermal equilibrium, carrier velocity updates instantaneously with respect to the local electric field, and current remains constant over the momentum relaxation time [A-1], [A-4]. Under these approximations, the current flow equations of the DD model can be expressed as

$$\vec{J}_n = -q\mu_n\vec{E} + qD_n\nabla_n \tag{A.8}$$

$$\vec{J}_p = -q\mu_p\vec{E} + qD_p\nabla_p \tag{A.9}$$

where μ_n, μ_p, D_n, D_p, and $\vec{E}$ denote the electron mobility, hole mobility, electron diffusion coefficient, hole diffusion coefficient, and electric field, respectively. To complete the DD model, the Poisson equation describes the effect of an external electrostatic potential ϕ on charge distribution, given by [A-1]

$$-\nabla^2\phi = \frac{q}{\varepsilon}(N_D^+ - n + p - N_A^-) \tag{A.10}$$

where N_D^+ and N_A^- are the ionised donor and acceptor impurity concentrations, respectively. Equations A.6 to A.10 can then be solved self-consistently to obtain the transport characteristics of the semiconductor.

A.2 Metal and semiconductor interfaces

The equations presented so far describe carrier transport within a semiconductor. However, to model a Schottky barrier diode (SBD), the boundary conditions at metal-semiconductor and semiconductor-semiconductor interfaces are also crucial. In a simplified 1D SBD model (see Figure A.1), three interfaces are relevant: the Schottky contact interface, the epilayer-buffer layer interface, and the Ohmic contact interface.

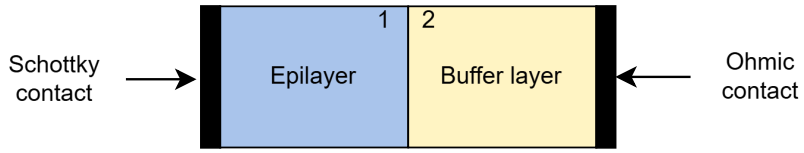

Figure A.1: 1D schematic of a physics-based SBD model.

To model the Schottky contact interface, it can be treated as a surface recombination mechanism, expressed as [A-5], [A-6]

$$\vec{J}_n \cdot \vec{n} = -qv_n(n - n_0) \tag{A.11}$$

$$\vec{J}_p \cdot \vec{n} = -qv_p(n - p_0) \tag{A.12}$$

where v_n and v_p are the recombination velocities for electrons and holes, respectively, $\vec{n}$ is the outward normal of the semiconductor domain, and n_0 and p_0 are the quasi-equilibrium carrier densities. Assuming a non-degenerate semiconductor, these are given by [A-6], [A-7]

$$n_0 = N_c \exp\left(-\frac{\phi_B}{k_B T}\right) \tag{A.13}$$

$$p_0 = N_v \exp\left(-\frac{E_g - \phi_B}{k_B T}\right) \tag{A.14}$$

where ϕ_B is the barrier height, E_g is the bandgap energy, N_c and N_v are the effective density of states in the conduction and valence bands, respectively, k_B is the Boltzmann constant, and T is the temperature. The recombination velocities v_n and

v_p are determined by thermionic emission across the junction (metal-semiconductor interface), which can be written as [A-5], [A-6]

$$v_n = \frac{A_n^* T^2}{qN_c} \tag{A.15}$$

$$v_p = \frac{A_p^* T^2}{qN_v} \tag{A.16}$$

where A_n^* and A_p^* are the effective Richardson constants for electrons and holes, respectively. Equations A.11 to A.16 specify boundary conditions for the current. The boundary condition for voltage is expressed as [A-6]

$$V = -(\phi_B + \chi) - \frac{\Delta E_f}{q} + V_0 \tag{A.17}$$

where χ, ΔE_f, and V_0 are the semiconductor affinity, the difference in Fermi level energies between the metal and semiconductor, and the applied voltage, respectively. At the boundary between two semiconductor layers, it is typically assumed that the semiconductor junction has negligible resistivity, which is modelled by the assumption that the quasi-Fermi levels at both sides are equal [A-6]

$$E_{fn1} = E_{fn2} \tag{A.18}$$

$$E_{fp1} = E_{fp2} \tag{A.19}$$

where E_{fn1}, E_{fp1}, E_{fn2}, and E_{fp2} are the electron and hole quasi-Fermi levels at the left and right sides, respectively. For the Ohmic contact boundary, local equilibrium is assumed, meaning the hole and electron quasi-Fermi levels are equal, and charge neutrality implies no band bending. The voltage at the Ohmic contact is given by

$$V = V_{eq} + V_0 \tag{A.20}$$

where V_0 is the applied voltage and V_{eq} is the built-in voltage at equilibrium, expressed as [A-6]

$$V_{eq} = \frac{k_B T}{q}\left(\ln\left(\frac{n_{eq}}{\gamma_n n_{i,eff}}\right) + \frac{1}{2}\ln\left(\frac{N_v}{N_c}\right) - \frac{1}{q}\left(\Delta E_f + \frac{1}{2}E_g\right)\right) - \chi \tag{A.21}$$

where n_{eq} is the equilibrium carrier concentration given by

$$n_{eq} = \gamma_n n_{i,eff} \exp\left(\frac{E_f - E_i}{k_B T}\right) \tag{A.22}$$

where $n_{i,eff}$ is the effective intrinsic carrier concentration and E_i is the intrinsic Fermi level energy. Finally, γ_n is a scaling factor related to the carrier statistics of the semiconductor, and for non-degenerate semiconductors, $\gamma_n = 1$.

References

[A-1] S. Selberherr, *Analysis and simulation of semiconductor devices*, en. Vienna, Austria: Springer, Dec. 2011.

[A-2] P. S. Kireev, *Semiconductor Physics*. Mir Publishers, 1978.

[A-3] D. Pardo Santos, "Analysis and design of multipliers and mixers via Monte Carlo modelling at THZ bands," en, Ph.D. dissertation, 2019.

[A-4] M. S. Lundstrom, "Fundamentals of carrier transport, 2nd edn," *Measurement Science and Technology*, vol. 13, pp. 230–230, Feb. 2002.

[A-5] C. R. Crowell and V. L. Rideout, "Normalized thermionic-field (T-F) emission in metal-semiconductor (schottky) barriers," *Solid-state Electronics*, vol. 12, pp. 89–105, Feb. 1969.

[A-6] COMSOL, *Semiconductor module user's guide 6.2*, 2023.

[A-7] C. R. Crowell and V. L. Rideout, "Normalized thermionic-field (T-F) emission in metal-semiconductor (Schottky) barriers," *Solid-state Electronics*, vol. 12, pp. 89–105, Feb. 1969.

Appendix B

UTC-PD transit-time response

To determine the transit-time limited response of the UTC-PD, a simplified model consisting of the absorber and collector layers can be employed [B-1], [B-2], as depicted in Figure B.1.

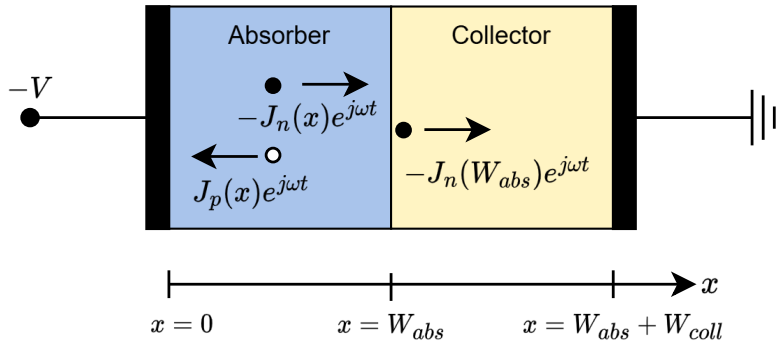

Figure B.1: 1D schematic of the UTC-PD model for transit-time response calculation. Adapted from [B-1].

By applying the drift-diffusion equations and Poisson's equation under short circuit conditions, the total frequency-dependent ($\omega = 2\pi f$) photocurrent density $J_{ph}(\omega)$ can be expressed as [B-2]

$$J_{ph}(\omega) = J_{coll}(\omega) + j\frac{\omega\varepsilon_{coll}}{W_{coll}}V_{coll}(\omega) \tag{B.1}$$

where $J_{coll}(\omega)$ and $V_{coll}(\omega)$ are the photocurrent density and voltage drop in the collector, respectively, W_{coll} is the collector thickness, and ε_{coll} its permittivity. Enforcing current continuity across the absorber and collector layers, the photocurrent also satisfies [B-2]

$$J_{ph}(\omega) = J_{abs}(\omega) + j\frac{\omega\varepsilon_{abs}}{W_{abs}}V_{Abs}(\omega) + J_{adj}(\omega) \tag{B.2}$$

where $J_{abs}(\omega)$ and $V_{abs}(\omega)$ are the photocurrent density and voltage drop in the absorber, W_{abs} is the absorber thickness, ε_{abs} is the permittivity of the absorber layer, and J_{adj} is an additional current component to ensure current continuity is satisfied [B-2]. The current densities $J_{abs}(\omega)$ and $J_{coll}(\omega)$ can be expanded to [B-3]

$$J_{abs}(\omega) = -qG(\omega)\frac{1}{1+\omega\tau_{adj}} \tag{B.3}$$

$$J_{coll}(\omega) = -qG(\omega)\frac{1}{1+\omega\tau_{abs}}\frac{sin(\frac{\omega\tau_{coll}}{2})}{\frac{\omega\tau_{coll}}{2}}e^{-j\frac{\omega\tau_{coll}}{2}} \tag{B.4}$$

where $G(\omega)$ is the electron-hole pair generation rate. τ_{adj}, τ_{abs}, and τ_{coll} are the adjustment current, absorber and collector time constant, respectively. The adjustment current can be approximated by

$$J_{adj}(\omega) = -j2\frac{\omega\varepsilon_{abs}}{W_{abs}}V_{abs}(\omega) \tag{B.5}$$

Assuming that the absorber current term is considerably greater than the adjustment current, it can be rewritten as [B-2]

$$J_{adj}(\omega) = -j2\frac{\omega\varepsilon_{abs}}{W_{abs}}J_{abs}(\omega)\frac{R_{abs}}{2} = -j\omega C_{abs}R_{abs}J_{abs}(\omega) = -j\omega\tau_{adj}J_{abs}(\omega) \tag{B.6}$$

where R_{abs} and C_{abs} are the resistance and capacitance of the absorber layer, respectively. Now, since a short-circuit condition is assumed, the following condition must hold

$$j\frac{\omega\varepsilon_{coll}}{W_{coll}}V_{coll}(\omega) = -j\frac{\omega\varepsilon_{abs}}{W_{abs}}V_{abs}(\omega) \tag{B.7}$$

.

The total photocurrent can be rewritten as

$$J_{ph}(\omega) = J_{coll}(\omega) - 2j\omega\tau_{adj}J_{abs} \tag{B.8}$$

Considering a p-InGaAs absorber, the adjustment current time constant is of the order of femtoseconds, which means the product $\omega\tau_{adj} << 1$ even at several hundred GHz. Therefore, the second term in Equation B.8 can be neglected, and the total photocurrent density $J_{ph}(\omega)$ is approximated by $J_{coll}(\omega)$. Then, assuming a constant generation rate, the photocurrent frequency as a function of frequency I_{ph} can be expressed as

$$I_{ph}(f) = I_{ph0}\frac{1}{1+j2\pi f\tau_{abs}}\frac{sin(\frac{2\pi f\tau_{coll}}{2})}{\frac{2\pi f\tau_{coll}}{2}}e^{-j\frac{2\pi f\tau_{coll}}{2}} \tag{B.9}$$

where I_{ph0} is the reference DC photocurrent. The time constants τ_a and τ_c can be calculated by [B-3]

$$\tau_{abs} = \frac{W_{abs}^2}{3D_e} + \frac{W_{abs}}{v_{th}} \tag{B.10}$$

$$\tau_{coll} = \frac{W_{coll}}{v_{coll}} \tag{B.11}$$

where D_e is the diffusion constant of electrons in the absorber, v_{th} is the thermionic emission velocity at the absorber-collector interface, and v_{coll} is the carrier saturation velocity in the collector.

References

[B-1] T. Ishibashi, N. Shimizu, S. Kodama, H. Ito, T. Nagatsuma, and T. Furuta, "Uni-traveling-carrier photodiodes," in *Ultrafast Electronics and Optoelectronics*, Optica Publishing Group, Mar. 1997, UC3.

[B-2] T. Ishibashi and H. Ito, "Uni-traveling-carrier photodiodes," en, *J. Appl. Phys.*, vol. 127, no. 3, p. 031 101, Jan. 2020.

[B-3] D. Guendouz, "Development of the first compact model for ultra-fast UTC (uni-travelling carrier) photodiodes towards monolithic integration of photonic and nanoelectronic technologies," Ph.D. dissertation, Universite de Bordeaux, 2022.

Appendix C

Material parameters

This appendix presents the material parameters and physical constants used in the simulations conducted in this thesis.

C.1 Semiconductor parameters

Table C.1 lists the semiconductor parameters required for the physics-based InP Schottky diode model, corresponding to each relevant layer of the UTC-PD epitaxy. These include the energy bandgap (E_g), electron affinity (χ), effective density of states in the conduction band (N_c), electron mobility (μ_n), effective electron mass ratio (m_n^*/m_0), and relative permittivity (ε_r). These parameters are obtained from references [C-1]–[C-7].

Layer	Material	N_D (1/cm^3)	E_g (eV)	χ (eV)	N_c (1/cm^3)	μ_n (cm^2/Vs)	m_n^*/m_0	ε_r
Collector	$n-InP$	$1\cdot10^{16}$	1.344	4.38	$3.7\cdot10^{17}$	4,392	0.078	12.50
Waveguide	$n^+-Q_{1.3}$	$2.5\cdot10^{18}$	0.925	4.53	$3.4\cdot10^{17}$	2,500	0.060	13.36
Contact	$n^{++}-InP$	$>1\cdot10^{19}$	1.295	4.38	$5.7\cdot10^{17}$	1,174	0.078	12.50

Table C.1: Semiconductor material parameters used of the InP SBD COMSOL model.

The energy bandgap is obtained considering bandgap narrowing effects from high doping, using a Jain-Roulston model [C-8]

$$\Delta E_g = A_{BGN}\cdot N_D^{1/3} + B_{BGN}\cdot N_D^{1/4} + C_{BGN}\cdot N_D^{1/2}, \tag{C.1}$$

where A_{BGN}, B_{BGN}, and C_{BGN} are model coefficients, and N_D is the doping concentration in cm^{-3}. The coefficients used in this work, listed in Table C.2, are taken

from previous studies [C-4], [C-5]. A 50:50 distribution between conduction and valence bands ($\alpha_{BGN} = 0.5$) is assumed, as it has demonstrated reasonable agreement with experimental results [C-9].

Material	A_{BGN}	B_{BGN}	C_{BGN}
InP	$2.25 \cdot 10^{-8}$	0	0
InGaAsP	$2 \cdot 10^{-8}$	0	0

Table C.2: Jain-Roulston model parameters for bandgap narrowing in n-type InP and InGaAsP.

The electron affinity of Q1.3 is derived from the conduction band discontinuity at the InP-InGaAsP heterojunction. For lattice-matched InGaAsP, this can be approximated by [C-1].

$$\Delta E_c = 0.39 \Delta E_g \tag{C.2}$$

For the electron mobility of the InP layers, a doping-dependent model was used [C-7]. The low-field electron mobility can be calculated as

$$\mu_n = \mu_{n_{min}} + \frac{\mu_{n_{max}}^{\theta_1} - \mu_{n_{min}}}{1 + \left(N_D / N_{ref}^{\theta_2}\right)^{\lambda}}, \tag{C.3}$$

where $\mu_{n,min}$ and $\mu_{n,max}$ are the mobilities at low and high doping concentrations, respectively, N_{ref} is the doping concentration at which the mobility is $\mu_{n,max}/2$, and θ_1, θ_2, and λ are additional fitting parameters. The values used in this study [C-7] are listed in Table C.3. For the Q1.3 layer, mobility data are obtained from experimental results in [C-6]. Finally, the effective electron mass ratio for the Q1.3 layer is calculated from [C-2].

$$m_n^*/m_0 = 0.080 - 0.049y \tag{C.4}$$

where y represents the arsenic mole fraction, which is 0.57 for lattice-matched $Q_{1.3}$.

$\mu_{n_{max}}(cm^2/Vs)$	$\mu_{n_{min}}(cm^2/Vs)$	$N_{ref}(cm^{-3})$	λ	θ_1	θ_2
5200	400	$1.3 \cdot 10^{17}$	0.47	2	3.25

Table C.3: InP doping-dependent electron mobility model parameters.

C.2 Electromagnetic parameters

The parameters used in CST EM simulations to obtain the S-parameters of the mixer components are listed in Table C.4.

Material	ε_r	$tan\,\delta$	σ
n - InP (collector layer)	12.5[C-3]	-	704
n^+-$Q_{1.3}$ (waveguide layer)	13.36[C-2]	-	100,125
n^{++}-InP (contact layer)	12.5[C-3]	-	188,070
S.I InP (substrate)	12.5[C-3]	0.0013[C-10]	-
SiON (passivation)	2.7(1)	0.004[C-11](2)	-
InGaAs (epilayer)	13.9[C-1]	0	-
SiO2 (passivation)	3.9[C-12]	0.0012[C-13]	-
Quartz (substrate)	3.75(3)	0.0004(3)	-
High-resistivity silicon (lens)	11.9(3)	0.00025(3)	-
Gold (metallization)	-	-	$4.561 \cdot 10^7$(3)

(1) Value found empirically to provide consistency between UTC-PD simulations and experimental measurements.
(2) Value from SiN due to the lack of available data.
(3) From CST material library.

Table C.4: Electromagnetic used in CST simulations for mixer design.

The parameters are the relative permittivity (ε_r), the dielectric loss tangent ($tan\,\delta$), and the conductivity (σ). In a dielectric material, $tan\,\delta$ and σ are related through the complex dielectric constant. While $\tan\delta$ is typically specified, for the materials in the UTC-PD layers used in the InP diode cell simulation, conductivity is employed instead, calculated as

$$\sigma = q\mu_n N_d \tag{C.5}$$

where q is the electron charge, μ_n is the electron mobility, and N_d is the doping concentration. This approach is used since these layers are used to electrically connect the diode finger to the Ohmic contact, allowing us to take into consideration the high-frequency spreading resistance in the simulations. The mobility and doping

concentrations specified in Table C.1 are used. Other parameters are sourced from various studies, with preference given to those within the 100-300 GHz frequency range [C-1]–[C-3], [C-10]–[C-13].

C.3 UTC-PD transit-time response parameters

The parameters used for calculating the UTC-PD photocurrent frequency response (Equation B.9) are listed in Table C.5. These include the absorber thickness (W_{abs}), the collector thickness (W_{coll}), the electron diffusion constant in the absorber (D_e) [C-14], [C-15], the thermionic emission velocity at the absorber-collector interface (v_{th}) [C-14], [C-15], and the carrier saturation velocity in the collector (v_{coll}), assumed to be equal to the overshoot velocity [C-16], [C-17].

$W_{abs}(nm)$	$W_{coll}(nm)$	$D_e(cm^2/s)$	$v_{th}(cm/s)$	$v_{coll}(cm/s)$
120	300	103	$2.5 \cdot 10^7$	$4 \cdot 10^7$

Table C.5: Parameters used in Equation B.9 to calculate the UTC-PD photocurrent frequency-dependent response.

References

[C-1] S. Adachi, *Physical Properties of III-V Semiconductor Compounds*, en. John Wiley & Sons, Nov. 1992.

[C-2] Y. A. Goldberg and N. M. Shmidt, "Gallium Indium Arsenide Phosphide ($Ga_xIn_{1-x}As_yP_{1-y}$)," in *Handbook Series on Semiconductor Parameters*, World Scientific, Nov. 1996, pp. 153–179.

[C-3] N. M. Shmidt, "Indium Phosphide (InP)," in *Handbook Series on Semiconductor Parameters*, World Scientific, Nov. 1996, pp. 169–190.

[C-4] B. Beaumont, G. Nataf, J. C. Guillaume, and C. Verie, "Low temperature photoluminescence of *n*-type GaInAsP layers grown on InP by liquid phase epitaxy," en, *J. Appl. Phys.*, vol. 54, no. 9, pp. 5363–5368, Sep. 1983.

[C-5] J. C. Li, M. Sokolich, T. Hussain, and P. M. Asbeck, "Physical modeling of degenerately doped compound semiconductors for high-performance HBT design," *Solid State Electron.*, vol. 50, no. 7, pp. 1440–1449, Jul. 2006.

[C-6] K. Tappura, "Electrical and optical properties of GaInAsP grown by gas-source molecular beam epitaxy," en, *J. Appl. Phys.*, vol. 74, no. 7, pp. 4565–4570, Oct. 1993.

[C-7] M. Sotoodeh, A. H. Khalid, and A. A. Rezazadeh, "Empirical low-field mobility model for III–V compounds applicable in device simulation codes," *J. Appl. Phys.*, vol. 87, no. 6, pp. 2890–2900, 2000.

[C-8] S. Jain and D. Roulston, "A simple expression for band gap narrowing (BGN) in heavily doped *Si*, *Ge*, *GaAs* and Ge_xSi_{1-x} strained layers," *Solid State Electron.*, vol. 34, pp. 453–465, May 1991.

[C-9] J. M. Lopez-Gonzalez and L. Prat, "The importance of bandgap narrowing distribution between the conduction and valence bands in abrupt HBTs," *IEEE Trans. Electron Devices*, vol. 44, no. 7, pp. 1046–1051, Jul. 1997.

[C-10] L. N. Alyabyeva, E. S. Zhukova, M. A. Belkin, and B. P. Gorshunov, "Dielectric properties of semi-insulating Fe-doped InP in the terahertz spectral region," en, *Sci. Rep.*, vol. 7, no. 1, p. 7360, Aug. 2017.

[C-11] Z. Pan, P. S. Barry, T. Cecil, *et al.*, "Measurement of dielectric loss in silicon nitride at centimeter and millimeter wavelengths," *IEEE Trans. Appl. Supercond.*, vol. 33, no. 5, pp. 1–7, Aug. 2023.

[C-12] T. R. Lenka and A. K. Panda, "AlGaN/GaN-based HEMT on SiC substrate for microwave characteristics using different passivation layers," en, *Pramana - J Phys*, vol. 79, no. 1, pp. 151–163, Jul. 2012.

[C-13] C. A. T. Garcia, N. Bailey, C. Kirby, *et al.*, "Disentangling superconductor and dielectric microwave losses in submicrometer Nb/SiO_2 interconnects using a multimode microstrip resonator," en, *Phys. Rev. Appl.*, vol. 21, no. 2, Feb. 2024.

[C-14] T. Ishibashi, S. Kodama, N. S. N. Shimizu, and T. F. T. Furuta, "High-speed response of uni-traveling-carrier photodiodes," *Japanese journal of applied physics*, vol. 36, no. 10R, p. 6263, 1997.

[C-15] T. Ishibashi, N. Shimizu, S. Kodama, H. Ito, T. Nagatsuma, and T. Furuta, "Uni-traveling-carrier photodiodes," in *Ultrafast Electronics and Optoelectronics*, Optica Publishing Group, Mar. 1997, UC3.

[C-16] K. Kurishima, H. Nakajima, T. Kobayashi, Y. Matsuoka, and T. Ishibashi, "Fabrication and characterization of high-performance InP/InGaAs double-heterojunction bipolar transistors," *IEEE Trans. Electron Devices*, vol. 41, no. 8, pp. 1319–1326, 1994.

[C-17] M. Natrella, "Photonic terahertz emitters and receivers," Ph.D. dissertation, University College London, Mar. 2015.